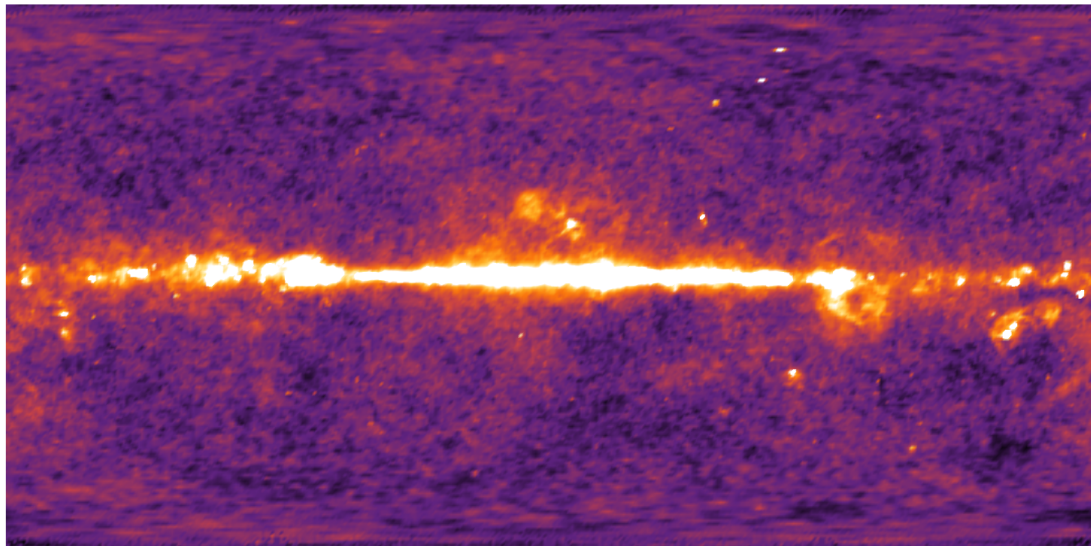




MULTI-MESSENGER CONSTRAINTS
AND
PRESSURE FROM DARK MATTER
ANNIHILATION INTO e^- - e^+ PAIRS



MANEENATE WECHAKAMA

Published online at the
Institutional Repository of the University of Potsdam:
URL <http://opus.kobv.de/ubp/volltexte/2013/6740/>
URN urn:nbn:de:kobv:517-opus-67401
<http://nbn-resolving.de/urn:nbn:de:kobv:517-opus-67401>

Cover illustration: An all-sky map from WMAP data at 33 GHz. It is one of 18 all-sky maps which we used in our calculation to impose constraints on the dark matter annihilation cross-section. Image produced by Maneenate Wechakama.

ABSTRACT

Despite striking evidence for the existence of dark matter from astrophysical observations, dark matter has still escaped any direct or indirect detection until today. Therefore a proof for its existence and the revelation of its nature belongs to one of the most intriguing challenges of nowadays cosmology and particle physics. The present work tries to investigate the nature of dark matter through indirect signatures from dark matter annihilation into electron-positron pairs in two different ways, pressure from dark matter annihilation and multi-messenger constraints on the dark matter annihilation cross-section. We focus on dark matter annihilation into electron-positron pairs and adopt a model-independent approach, where all the electrons and positrons are injected with the same initial energy $E_0 \sim m_{\text{dm}} c^2$. The propagation of these particles is determined by solving the diffusion-loss equation, considering inverse Compton scattering, synchrotron radiation, Coulomb collisions, bremsstrahlung, and ionization.

The first part of this work, focusing on pressure from dark matter annihilation, demonstrates that dark matter annihilation into electron-positron pairs may affect the observed rotation curve by a significant amount. The injection rate of this calculation is constrained by INTEGRAL, Fermi, and H.E.S.S. data. The pressure of the relativistic electron-positron gas is computed from the energy spectrum predicted by the diffusion-loss equation. For values of the gas density and magnetic field that are representative of the Milky Way, it is estimated that the pressure gradients are strong enough to balance gravity in the central parts if $E_0 < 1$ GeV. The exact value depends somewhat on the astrophysical parameters, and it changes dramatically with the slope of the dark matter density profile. For very steep slopes, as those expected from adiabatic contraction, the rotation curves of spiral galaxies would be affected on kiloparsec scales for most values of E_0 . By comparing the predicted rotation curves with observations of dwarf and low surface brightness galaxies, we show that the pressure from dark matter annihilation may improve the agreement between theory and observations in some cases, but it also imposes severe constraints on the model parameters (most notably, the inner slope of the halo density profile, as well as the mass and the annihilation cross-section of dark matter particles into electron-positron pairs).

In the second part, upper limits on the dark matter annihilation cross-section into electron-positron pairs are obtained by combining observed data at different wavelengths (from Haslam, WMAP, and Fermi all-sky intensity maps) with recent measurements of the electron and positron spectra in the solar neighbourhood by PAMELA, Fermi, and H.E.S.S.. We consider synchrotron emission in the radio and microwave bands, as well as inverse Compton scattering and final-state radiation at gamma-ray energies. For most values of the model parameters, the tightest constraints are imposed by the local *positron* spectrum and synchrotron emission from the central regions of the Galaxy. According to our results, the annihilation cross-section should not be higher than the canonical value for a thermal relic if the mass of the dark matter candidate is smaller than a few GeV. In addition, we also derive a stringent upper limit on the inner logarithmic slope α of the density profile of the Milky Way dark matter halo ($\alpha < 1$ if $m_{\text{dm}} < 5$ GeV, $\alpha < 1.3$ if $m_{\text{dm}} < 100$ GeV and $\alpha < 1.5$ if $m_{\text{dm}} < 2$ TeV) assuming a dark matter annihilation cross-section into electron-positron pairs $\langle \sigma v \rangle_{e^\pm} = 3 \times 10^{-26} \text{ cm}^3 \text{ s}^{-1}$, as predicted for thermal relics from the big bang.

ZUSAMMENFASSUNG

Trotz vieler Hinweise auf die Existenz von dunkler Materie durch astrophysikalische Beobachtungen hat sich die dunkle Materie bis heute einem direkten oder indirekten Nachweis entzogen. Daher gehört der Nachweis ihrer Existenz und die Enthüllung ihrer Natur zu einem der fasziniersten Herausforderungen der heutigen Kosmologie und Teilchenphysik. Diese Arbeit versucht die Natur von dunkler Materie durch indirekte Signaturen von der Paarzerstrahlung dunkler Materie in Elektron-Positronpaare auf zwei verschiedene Weisen zu untersuchen, nämlich anhand des Drucks durch die Paarzerstrahlung dunkler Materie und durch Grenzen des Wirkungsquerschnitts für die Paarzerstrahlung dunkler Materie aus verschiedenen Beobachtungsbereichen. Wir konzentrieren uns dabei auf die Zerstrahlung dunkler Materie in Elektron-Positron-Paare und betrachten einen modellunabhängigen Fall, bei dem alle Elektronen und Positronen mit der gleichen Anfangsenergie $E_0 \sim m_{dm}c^2$ injiziert werden. Die Fortbewegung dieser Teilchen wird dabei bestimmt durch die Lösung der Diffusions-Verlust-Gleichung unter Berücksichtigung von inverser Compton-Streuung, Synchrotronstrahlung, Coulomb-Streuung, Bremsstrahlung und Ionisation.

Der erste Teil dieser Arbeit zeigt, dass die Zerstrahlung dunkler Materie in Elektron-Positron-Paare die gemessene Rotationskurve signifikant beeinflussen kann. Die Produktionsrate ist dabei durch Daten von INTEGRAL, Fermi und H.E.S.S. begrenzt. Der Druck des relativistischen Elektron-Positron Gases wird aus dem Energiespektrum errechnet, welches durch die Diffusions-Verlust-Gleichung bestimmt ist. Für Werte der Gasdichte und des magnetischen Feldes, welche für unsere Galaxie repräsentativ sind, lässt sich abschätzen, dass für $E_0 < 1$ GeV die Druckgradienten stark genug sind, um Gravitationskräfte auszugleichen. Die genauen Werte hängen von den verwendeten astrophysikalischen Parametern ab, und sie ändern sich stark mit dem Anstieg des dunklen Materie-Profils. Für sehr große Anstiege, wie sie für adiabatische Kontraktion erwartet werden, werden die Rotationskurven von Spiralgalaxien auf Skalen von einem Kiloparsek für die meisten Werte von E_0 beeinflusst. Durch Vergleich der erwarteten Rotationskurven mit Beobachtungen von Zwerggalaxien und Galaxien geringer Oberflächentemperatur zeigen wir, dass der Druck von Zerstrahlung dunkler Materie die Übereinstimmung von Theorie und Beobachtung in einigen Fällen verbessern kann. Aber daraus resultieren auch starke Grenzen für die Modellparameter - vor allen für den inneren Anstieg des Halo-Dichteprofils, sowie die Masse und den Wirkungsquerschnitt der dunklen Materie-Teilchen.

Im zweiten Teil werden obere Grenzen für die Wirkungsquerschnitte der Zerstrahlung der dunkler Materie in Elektron-Positron-Paare erhalten, indem die beobachteten Daten bei unterschiedlichen Wellenlängen (von Haslam, WMAP und Fermi) mit aktuellen Messungen von Elektron-Positron Spektren in der solaren Nachbarschaft durch PAMELA, Fermi und H.E.S.S. kombiniert werden. Wir betrachten Synchrotronemission bei Radio- und Mikrowellenfrequenzen, sowie inverse Compton-Streuung und Final-State-Strahlung bei Energien im Bereich der Gamma-Strahlung. Für die meisten Werte der Modellparameter werden die stärksten Schranken durch das lokale *Positron*-Spektrum und die Synchrotronemission im Zentrum unserer Galaxie bestimmt. Nach diesen Ergebnissen sollte der Wirkungsquerschnitt für die Paarzerstrahlung nicht größer als der kanonische Wert für thermische Relikte sein, wenn die Masse der dunklen Materie-Kandidaten kleiner als einige GeV ist. Zusätzlich leiten wir eine obere Grenze für den inneren logarithmische Anstieg α des Dichteprofils des dunklen Materie Halos unserer Galaxie ab.

Leibniz-Institut für Astrophysik Potsdam
Kosmologie

MULTI-MESSENGER CONSTRAINTS
AND
PRESSURE FROM DARK MATTER
ANNIHILATION INTO e^- - e^+ PAIRS

Dissertation
zur Erlangung des akademischen Grades
Doktor der Naturwissenschaften (Dr. rer. nat.)
in der Wissenschaftsdisziplin Astrophysik

eingereicht an der
Mathematisch-Naturwissenschaftlichen Fakultät
der Universität Potsdam

von
MANEENATE WECHAKAMA
aus Thailand

Potsdam, Februar 2013

...for my parents and Frank...

CONTENTS

1	Introduction	1
2	Dark Matter	3
2.1	What is dark matter?	3
2.1.1	Classical astronomical evidence for dark matter	3
2.1.2	Dark matter distribution	7
2.1.3	Particle candidates	12
2.2	Dark matter detection	15
2.2.1	Accelerator searches	15
2.2.2	Direct detection	17
2.2.3	Indirect detection	20
3	e^- and e^+ from Dark Matter Annihilation	25
3.1	Dark matter annihilation	25
3.1.1	Annihilation channels	26
3.1.2	The Galactic positron excess	28
3.2	Electron-Positron propagation	31
3.2.1	Diffusion-loss equation	32
3.2.2	Loss rates	33
3.2.3	Source term	36
3.3	Astrophysical signatures from photons	36
3.3.1	Gamma-rays	37
3.3.2	Radio and microwaves	40
3.3.3	Surface brightness profile	40
4	Pressure from Dark Matter Annihilation	45
4.1	Dark matter pressure	45
4.1.1	The injection energy	46
4.1.2	Results for the canonical Milky Way model	48
4.1.3	Effect of the astrophysical parameters	51
4.2	Rotation curves	54
4.2.1	Results for the Milky Way model	54
4.2.2	Low surface brightness galaxies	57
4.3	Conclusions	58
5	Multi-messenger constraints	67
5.1	Astrophysical parameters	68
5.2	Observational data	68
5.3	Constraints on the dark matter cross-section	70
5.4	Effect of the astrophysical parameters	75
5.5	Constraints on the inner slope of the density profile	79

5.6 Conclusions	80
6 Summary and Future Prospects	95
6.1 Summary	95
6.1.1 Pressure from dark matter annihilation	95
6.1.2 Multi-messenger constraints	96
6.2 Future prospects	97
Bibliography	99

LIST OF FIGURES

2.1	Rotation curve of NGC 6503	4
2.2	Bullet Cluster	5
2.3	Rotation curve inferred for the 7 THINGS dwarf galaxies	10
2.4	Upper limits on WIMP annihilation cross-section from ATLAS	16
2.5	Cross-sections for spin-independent coupling versus WIMP mass diagrams	19
2.6	Upper limits on dark matter annihilation cross-section from gamma-rays measurement by Fermi compared to the limits from electron-positron searches by PAMELA and Fermi	23
3.1	Tree level diagrams for neutralino annihilation into fermion pairs	27
3.2	Feynman diagrams for the first Kaluza-Klein excitation of the hypercharge gauge boson $B^{(1)}B^{(1)}$ annihilation into fermion pairs	27
3.3	Antiproton flux, positron fraction, and sum of electron and positron spectrum	29
3.4	Global fit to the PAMELA, Fermi and H.E.S.S. data, and the boost factor	30
3.5	Energy losses, equilibrium time scales, and characteristic diffusion lengths	35
3.6	γ -particles created by final state radiation at the very moment of lepton pair creation in a process of $B^{(1)}B^{(1)}$ annihilation	41
4.1	Exclusion regions and production rates at the position of the Sun	47
4.2	Electron-positron spectrum	49
4.3	Dark matter pressure for the canonical Milky Way model	50
4.4	Effect of varying magnetic field intensity, ionization fraction and the ISM gas density	52
4.5	Dark matter pressure for different values of the inner logarithmic slope α	53
4.6	Dark matter acceleration for different values of the inner logarithmic slope α	55
4.7	Effect of dark matter annihilation on the rotation curve	56
4.8	Rotation curves of U1230, U5005 and F5631	62
4.9	Rotation curves of U4173, U3371 and N1560	63
4.10	Rotation curves of DDO189, N4395 and N3274	64
4.11	Rotation curves of N4455, N2366 and U4325	65
4.12	Rotation curves of DDO47 and DDO185	66
5.1	Theoretical photon spectra of synchrotron radiation, ICS and FSR for the canonical model	71
5.2	Angular separation θ that provides the upper limits for synchrotron, ICS and FSR emission	71
5.3	Surface brightness profiles of synchrotron radiation as a function of the angular separation θ from the Galactic centre	72
5.4	Surface brightness profiles of ICS and FSR as a function of the angular separation θ from the Galactic centre	73
5.5	Upper limits on the dark matter annihilation for the canonical model	75

5.6	Upper limits on the dark matter annihilation cross-section for different values of the magnetic field, interstellar radiation field, and diffusion coefficient	77
5.7	Upper limits on the dark matter annihilation cross-section for different values of the inner logarithmic slope α of the dark matter density profile	78
5.8	Upper limits on the inner logarithmic slope α of dark matter density profile	80
5.9	Haslam and WMAP intensity maps in Galactic coordinates, masked residual maps, and spherically-averaged intensities of 408 MHz, 23 GHz and 33 GHz	82
5.10	WMAP intensity maps in Galactic coordinates, masked residual maps, and spherically-averaged intensities of 41 GHz, 61 GHz and 94 GHz	83
5.11	Fermi intensity maps in Galactic coordinates, masked residual maps, and spherically-averaged intensities of 0.3-0.5 GeV, 0.5-0.9 GeV and 0.9-1.7 GeV	84
5.12	Fermi intensity maps in Galactic coordinates, masked residual maps, and spherically-averaged intensities of 1.7-3.0 GeV, 3.0-5.3 GeV and 5.3-9.5 GeV	85
5.13	Fermi intensity maps in Galactic coordinates, masked residual maps, and spherically-averaged intensities of 9.5-16.9 GeV, 16.9-30.0 GeV and 30.0-53.3 GeV	86
5.14	Fermi intensity maps in Galactic coordinates, masked residual maps, and spherically-averaged intensities of 53.3-94.9 GeV, 94.9-168.7 GeV and 168.7-300.0 GeV	87

LIST OF TABLES

4.1	Initial Lorentz factors, energies, cross-sections and production rates at the position of the Sun	47
4.2	Characteristic density and radius of the dark matter density profile	54
4.3	Galaxy name, characteristic dark matter density and radius, and reduced χ^2 values for the maximum disk models	60
4.4	Galaxy name, characteristic dark matter density and radius, and reduced χ^2 values for the constant mass-to-light ratio models	61
5.1	Three different models of the diffusion coefficient	69
5.2	Normalization of the grey-body models describing the interstellar radiation field	69
5.3	Haslam and WMAP (408 MHz, 23 GHz and 33 GHz): Original observational mean intensity, final mean intensity after discard the outliers and standard deviation	88
5.4	WMAP (41 GHz, 61 GHz and 94 GHz): Original observational mean intensity, final mean intensity after discard the outliers and standard deviation	89
5.5	Fermi (0.3-0.5 GeV, 0.5-0.9 GeV and 0.9-1.7 GeV): Original observational mean intensity, final mean intensity after discard the outliers and standard deviation (1)	90
5.6	Fermi (1.7-3.0 GeV, 3.0-5.3 GeV and 5.3-9.5 GeV): Original observational mean intensity, final mean intensity after discard the outliers and standard deviation (2)	91
5.7	Fermi (9.5-16.9 GeV, 16.9-30.0 GeV and 30.0-53.3 GeV): Original observational mean intensity, final mean intensity after discard the outliers and standard deviation (3)	92
5.8	Fermi (53.3-94.9 GeV, 94.9-168.7 GeV and 168.7-300.0 GeV): Original observational mean intensity, final mean intensity after discard the outliers and standard deviation (4)	93

Chapter

1

INTRODUCTION

The identity of “dark matter” is one of the most outstanding open problems in modern cosmology and particle physics. Although cosmological observations are providing compelling evidence that dark matter is the building block of structures in the Universe, the exact nature of this elusive component remains a mystery. Many different strategies have been devised to reveal its properties. Up to now, the results of experiments to confirm dark matter by direct detection in particle accelerators and recoil experiments are still unclear. Alternatively, a promising approach to the problem relies on the possibility that dark matter particles annihilate or decay into observable products such as photons, neutrinos, protons, anti-protons, electrons, and positrons. Thus one can aim for indirect dark matter detection by looking for signatures of the annihilation or decay products.

The present thesis focuses on the astrophysical signatures of dark matter annihilation into electron-positron pairs, neglecting other processes, such as dark matter decay, or other annihilation products, such as protons and antiprotons. We investigate the contribution of dark matter annihilation to the total gas pressure and consider the possibility that it has a significant effect on the rotation curve of spiral galaxies. We also try to impose robust, yet stringent constraints on the relevant cross-section by comparing the predictions of an analytic model of particle propagation with a multi-wavelength set of observational data obtained from the literature. We consider synchrotron emission in the radio and microwave bands, as well as inverse Compton scattering and final-state radiation at gamma-ray energies. Upper limits on the relevant cross-section are obtained by combining observational data at different wavelengths (from Haslam, WMAP, and Fermi intensity maps) with recent measurements of the electron and positron spectra in the solar neighbourhood by PAMELA, Fermi, and H.E.S.S..

The thesis is organized in five parts: dark matter, electrons and positrons from dark matter annihilation, pressure from dark matter annihilation, multi-messenger constraints, and a summary with a discussion of future prospects. Let us briefly present here a detailed overview of the thesis contents:

Chapter 2 is devoted to a review of the evidence for dark matter at all length scales and the current understanding of its distribution in the Universe, based on numerical simulations and astrophysical observations. Dark matter candidates as well as dark matter direct and indirect detection experiments are also discussed here.

Chapter 3 focuses on the physics of electrons and positrons arising from dark matter annihilation, the assumptions made in this work and the methods that we use in our

calculations. We discuss different annihilation channels and the Galactic positron excess. The diffusion-loss equation that determines electron-positron propagation, including the relevant energy loss rates and the source term, is introduced here. The discussion includes astrophysical signatures of dark matter annihilation from photons (i.e. gamma-rays, radio and microwaves), and the procedure followed to compute surface brightness profiles of inverse Compton scattering, synchrotron radiation and final state radiation is described in detail.

The first part of our results (Wechakama and Ascasibar, 2011), i.e. pressure from dark matter annihilation and the rotation curve of spiral galaxies are presented in Chapter 4. We show that dark matter annihilation into electron-positron pairs may affect the observed rotation curve by a significant amount. The pressure of the relativistic electron-positron gas is determined by solving the diffusion-loss equation, considering inverse Compton scattering, synchrotron radiation, Coulomb collisions, bremsstrahlung, and ionization. The role of each astrophysical parameter (gas density and ionization fraction of the interstellar medium, intensity of the magnetic field, and dark matter density profile) is investigated. We also present the results and discussions by comparing the predicted rotation curves with observations of dwarf and low surface brightness galaxies.

Chapter 5 is dedicated to the second part of our results concerning multi-messenger constraints on dark matter annihilation into electron-positron pairs (Wechakama and Ascasibar, 2012). Our analysis of the observational data, the constraints on the dark matter annihilation cross-section, and the effect of the different astrophysical parameters are fully described and discussed here. We also impose constraints on the dark matter density profile by assuming that dark matter particles are produced as thermal relics in the primordial universe. Finally, we summarise the main conclusions of this thesis and prospects for future work in Chapter 6.

Chapter

2

DARK MATTER

2.1 What is dark matter?

Eight decades ago, the term “Dark matter” was first suggested by Oort (1932) to account for the orbital velocities of stars in the Milky Way and followed by Zwicky (1933, 1937) in order to explain the velocity dispersion of galaxies in the Coma cluster by the presence of non-luminous matter. Up to now, although the contribution of dark matter particles to the total energy density can be precisely measured by current observational data, the exact nature of dark matter remains one of the most fundamental unsolved problems in cosmology and particle physics. We give here a review of the concept of dark matter, beginning with the evidence for dark matter, its distribution, and particle candidates.

2.1.1 Classical astronomical evidence for dark matter

The first convincing evidence for dark matter came from the velocity dispersion of galaxies in the Coma cluster observed by Zwicky (1933, 1937). He measured velocities of galaxies in the cluster and applied the virial theorem to infer the total gravitational mass of the system. He noticed that, in order to hold the galaxies together, the cluster must contain a large amount of mass in addition to that inferred from the luminous mass of the galaxies, i.e. most of the matter must be invisible matter, called “dark matter”. Zwicky’s results were confirmed by the velocity measurements of 30 galaxies in the Virgo cluster (Smith, 1936).

Rotation curves

The idea of dark matter become more attractive after the measurements of galactic *rotation curves* of spiral galaxies by Rubin and collaborators (Rubin and Ford, 1970; Rubin et al., 1978, 1985). The rotation curve of a galaxy is the graph of circular velocities of stars and gas as a function of their distance from the galactic center. Similar to the galaxies in the outer region of galaxy clusters, the circular velocities of stars in the outer reaches of spiral galaxies are seen to be faster than would be expected from the gravitational potential due to the visible gas and stars.

The observed rotation curves of spiral galaxies, including the Milky Way, usually rises slowly with increasing distance from the galactic center and remains almost constant, *flat*,

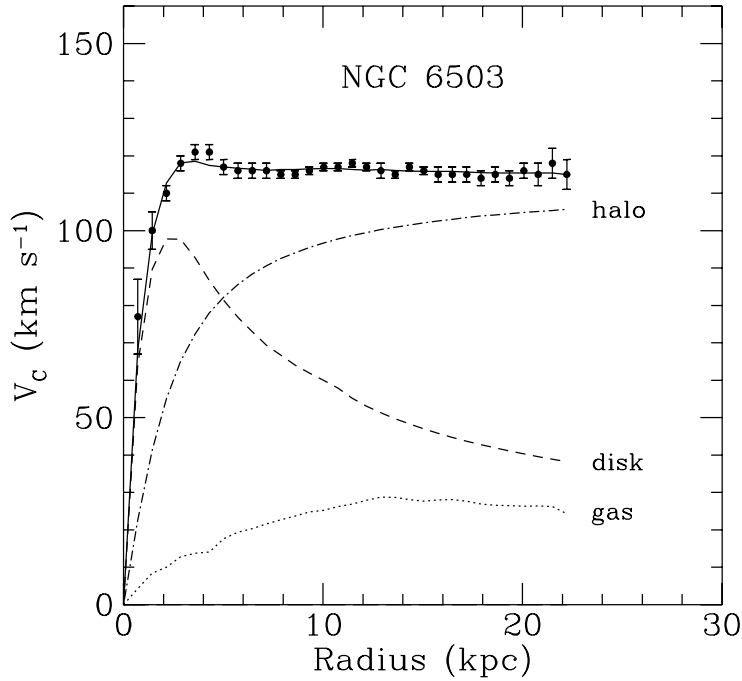


Figure 2.1: Rotation curve of NGC 6503 (Begeman et al., 1991). The dotted, dashed and dash-dotted lines are the contributions of gas, disk and dark matter, respectively.

at large distance (see e.g. Sofue and Rubin, 2001; Xue et al., 2008). The characteristic flat behaviour can be explained by the presence of an additional “dark matter halo”. The rotation curve data allow us to determine the mass-to-light ratio M/L , i.e. the comparison of the distribution of mass and light in the galaxies. In the outer region of spiral galaxies, the local value of M/L increases very rapidly outwards, since the luminosity drops rather rapidly while the circular velocities are almost constant. This leads to very high local values of $M/L > 200$ near the last points of the observed rotation curves. An example of such typical rotation curves is shown in Fig. 2.1 for a dwarf spiral galaxy, NGC 6503.

Gravitational lensing

According to Einstein’s theory of general relativity, the presence of any mass causes a curvature of space-time, which results in *lensing*, i.e. bending, of light rays around massive bodies. The gravitational fields of massive foreground objects can deflect the light and modify the apparent flux and shape of astronomical background sources. This allows the determination of the mass of the foreground objects without the need to speculate on the distribution and the properties of matter inside the gravitational potential (for a review, see Bartelmann and Schneider (2001) and Chapter 4 in Bertone (2010)).

The mass distribution and M/L of a foreground gravitational *lens* can be resolved by *weak* or *strong* gravitational lensing. The strong gravitational lensing only probes mass in a small region and happens very rarely, only when the background source, the lens, and the observer are aligned. Fortunately, weak gravitational lensing is able to resolve the mass distribution by using all distant background galaxies of deep astronomical images as lensed sources, which are distorted by the gravitational shear field of the foreground

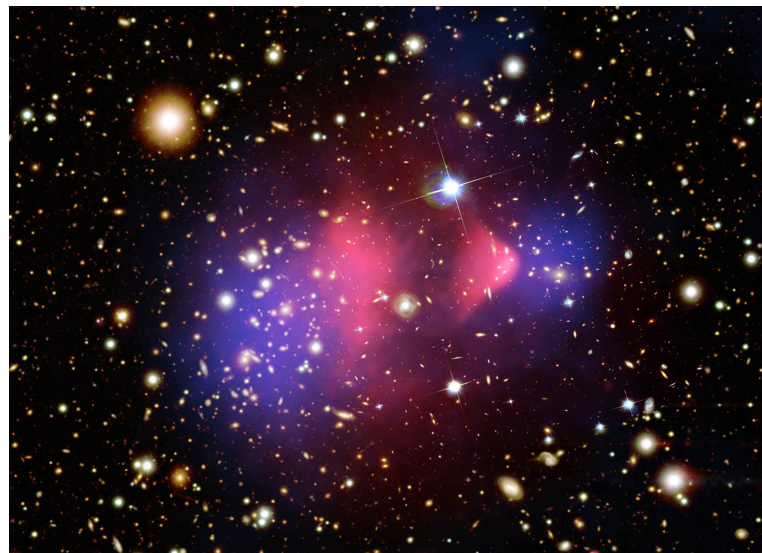


Figure 2.2: Bullet Cluster obtained by optical image, X-ray and weak gravitational lensing. The lensing mass map shown in blue represents the distribution of dark matter. The X-ray observations tracing the gas component are shown in red. During the collision of two clusters, the hot gas has interacted electromagnetically and created the bullet shape while the dark matter has just passed straight through both the gas clouds without interacting. The map also proves that the majority of the matter in the clusters is collisionless dark matter. X-ray data: NASA/CXC/CfA/ (Markevitch, 2006). Lensing Map: NASA/STScI; ESO WFI; Magellan/U.Arizona/ (Clowe et al., 2006). Optical data: NASA/STScI; Magellan/U.Arizona/ (Clowe et al., 2006).

gravitational lens. Although the distortion is very weak compared with the ellipticity of each source, the lensing signal can be derived from the average ellipticity of a large galaxy sample, while the mass distribution can be analysed statistically using the correlated signal induced in all of lensed sources (e.g. Tyson et al., 1990; Bonnet et al., 1994; Fahlman et al., 1994).

Another famous “smoking gun” for dark matter is the so-called “bullet cluster” (Clowe et al., 2006). The composite image of two clusters, which collided ~ 100 Myr ago, is shown in Fig. 2.2. The individual galaxies are seen in the optical image data. Two clouds of hot X-ray emitting gas, shown in red, represent the baryonic matter. The distribution of dark matter derived by weak gravitational lensing, shown in blue, represents even more mass than the optical galaxies and X-ray gas combined. During the titanic collision, the hot gas interacted electromagnetically and created the bullet shape while the dark matter has just passed straight through both the gas clouds without interacting. Such a behaviour is nearly impossible to explain by a theory without dark matter such as MOND (Modification of Newtonian Dynamics) which expects the lensing to follow the baryonic matter (see e.g. Milgrom, 1983; Sanders and McGaugh, 2002a; Bekenstein, 2004).

It is also possible to determine the three-dimensional mass distribution of large-scale structure of the Universe by using “cosmic shear” analysis which also needs redshift information. In fact, the results provided by the present day observations of gravitational lensing do agree with predictions of hierarchical cosmological models dominated by collisionless cold dark matter (CDM) and the most recent cosmic shear analysis seems to support the standard flat Λ CDM model with $\Omega_M = 0.25$ and $\Omega_b = 0.04$, where Ω_M and Ω_b denote the matter and the baryon density of the Universe, respectively, in terms of the critical density $\rho_c = 3H^2/(8\pi G)$ with the Hubble parameter H and Newton’s gravitational constant G (Kilbinger et al., 2009).

Big Bang nucleosynthesis and the cosmic microwave background

According to the Big Bang theory, nucleosynthesis began when the Universe had cooled down to a temperature of ~ 100 keV, sufficient to fuse protons and neutrons into light elements. The resulting elemental abundances depend on the nuclear reaction rates and the photon-to-baryon ratio at that time. With laboratory and theoretical nuclear reaction rates (e.g. Angulo et al., 1999), the primordial elemental abundances can be derived as a function of the photon-to-baryon ratio, providing $\Omega_b h^2$, where $h \equiv H_0/100 \text{ km s}^{-1} \text{ Mpc}^{-1} \approx 0.7$ is the dimensionless Hubble parameter (e.g. Alpher et al., 1948; Coc et al., 2004; Steigman, 2007; Iocco et al., 2009; Nakamura et al., 2010). Observations of the primordial Deuterium and Helium abundance consistently constrain the baryon abundance to $\Omega_b \approx 0.04$.

Furthermore, observations of the cosmic microwave background (CMB) give a snapshot of the Universe that reflects the situation shortly after the time of recombination (see e.g. Hu and Dodelson, 2002; Samtleben et al., 2007). The angular temperature anisotropies of the CMB are determined by the acoustic oscillations and diffusion damping of the coupled baryon-photon plasma in the early universe. The acoustic oscillations, created by the pressure of the photons and the gravitational attraction of the baryons, exhibit the characteristic peak structure of the CMB power spectrum. Therefore the angular power spectrum of the CMB observed today contains physical signatures of the components of the Universe that play an important role in the evolution of the baryon-photon oscillations, such as the large-scale geometry (i.e. the total energy density), the baryon density Ω_b , the dark matter density Ω_{DM} , and the spectral shape of the primordial perturbations n . The extremely high resolution of the 7-year Wilkinson Microwave Anisotropy Probe (WMAP)

data (Larson et al., 2011) provide the values $\Omega_m = 0.267 \pm 0.026$, $\Omega_b = 0.0449 \pm 0.0028$, $\Omega_{DM} = 0.222 \pm 0.026$ and $n = 0.963 \pm 0.014$.

The power spectrum of the CMB not only confirms the need for non-baryonic dark matter, but it also indicates the requirement of an additional form of “dark energy” to account for the remaining $\Omega_\Lambda = 0.734 \pm 0.029$. The need of dark energy was also suggested by observations of high redshift Type Ia supernovae which pointed to the accelerating expansion of the Universe (Riess et al., 1998; Perlmutter et al., 1999).

Structure formation

Large-scale surveys such as 2dFGRS (the 2-degree Field Galaxy Redshift Survey; Colless et al., 2001) and SDSS (the Sloan Digital Sky Survey; Tegmark et al., 2004) have revealed the cosmic scaffolding populated from small to large scale by galaxies, galaxy clusters and superclusters, arranged into large-scale sheets, filaments and voids. According to the concordance model, these structures have evolved from the perturbations of the gravitational field generated by the quantum fluctuations that led to the anisotropies in the CMB. Since at the time of recombination the density perturbations are rather small, and electromagnetic interactions also prevent the baryonic matter to start the structure formation through gravitational collapse before the time of recombination, the baryonic matter has had much too short a time to form the structures. The structure formation would have started by non-baryonic dark matter before the time of recombination. The description of the structure formation is complicated by the effect of gas dynamics, chemistry, radiative transfer and other astrophysical processes. The most accurate explanations of the structure formation have been provided by N -body simulations (e.g. Diemand et al., 2005a; Springel et al., 2005; Kuhlen et al., 2008) that require cold and non-dissipative dark matter.

The N -body simulations of the formation of CDM haloes have produced several robust results in explaining the above mentioned astrophysical as well as cosmological data. The properties of the haloes are being tested against observational data from scale of dwarf galaxies to galaxy clusters. Despite all the successes, there is a set of important problems which so far can not be explained by CDM, e.g. the “core-cusp” and “missing satellites” problems.

2.1.2 Dark matter distribution

If dark matter comprises the vast majority of matter in the Universe, then the formation and evolution of structures in the Universe must be determined by the properties of dark matter particles. Here, we discuss the distribution of large-scale structure and dark matter haloes, expected in the standard model of cosmological structure formation, which has been developed to describe the geometry and material content of the Universe (for recent reviews see e.g. Einasto, 2009; Diemand and Moore, 2011; Coil, 2012; Frenk and White, 2012).

Large-scale structure

The most precise observational information about large-scale structure comes from the “cosmic web”, presented in large galaxy redshift survey, such as the CfA (Davis et al., 1982), 2dFGRS (Colless et al., 2001) and SDSS (Tegmark et al., 2004). These observations reveal highly nonlinear structures, where galaxies are not uniformly distributed in space but reside in groups and clusters on scales of $\sim 1 - 3h^{-1}$ Mpc, which lie at the intersections

of long filaments of galaxies that are $> 10h^{-1}$ Mpc in length. Vast regions of relatively empty space, known as voids, contain very few galaxies and span the volume in between these structures (Coil, 2012, and references therein). This observed large-scale structure requires an explanation of its origin.

Large-scale cosmological N-body simulations have been used as a tool to study the growth of that nonlinear structure in an expanding Universe. the understanding of large-scale structure is led by two fundamental ideas: the theory of cosmic inflation (Guth, 1981; Linde, 1982a) and the dominance of non-baryonic dark matter. The gravitational field generated by quantum fluctuations during inflation seeds the Universe with adiabatic, scale-invariant density perturbations of very small amplitude and a power-law power spectrum, $P(k) \propto k^n$, where k is comoving wavenumber and n is close to, but smaller than unity (Guth and Pi, 1982; Hawking, 1982; Linde, 1982b; Starobinsky, 1982). The growth of the perturbations is regulated initially by the dominant radiation component and later by the dark matter. Characteristic masses of structures, formed by dark matter, are determined by random thermal motions below the free-streaming length λ_{fs} (i.e. the typical comoving distance that a particle travels in the age of the Universe) which varies inversely with particle mass m_X , i.e. $\lambda_{fs} \propto m_X^{-1}$.

According to their typical velocity, dark matter particles have been classified into three families: hot, warm and cold dark matter. The characteristic masses corresponding to the free-streaming length play an important role in structure formation for different families of dark matter particles. For hot dark matter (HDM) with $m_X \sim 30$ eV, the characteristic mass corresponding to the free-streaming length is roughly that of a large galaxy cluster, resulting in superclusters forming first and galaxies forming later. The characteristic masses of warm dark matter (WDM) (with $m_X \sim 2$ keV) and CDM (with $m_X \sim 100$ GeV) correspond to a dwarf galaxy and the Earth's mass, respectively. In both cases, small objects will form first and bigger systems grow later by merging and accretion. However, dark matter objects significantly smaller than galaxies can only form in CDM, not in WDM (Frenk and White, 2012).

Although the idea of the structures formed in a HDM universe was attractive when Lubimov et al. (1980) measured light neutrinos with a mass of ~ 30 eV, it is far from the Universe we observe since galaxies form only where the matter distribution has locally collapsed (White et al., 1983). The first set of simulations of structure formation in a CDM Einstein-de Sitter universe (e.g Davis et al., 1985; Frenk et al., 1985; White et al., 1987a,b; Frenk et al., 1988, 1990) gave far better results when compared to the observational data. However, an Einstein-de Sitter expansion history is finally excluded by supernova data (Riess et al., 1998; Perlmutter et al., 1999) and the first peak in the spectrum of CMB fluctuations, leading to the current standard Λ CDM model of the Universe (de Bernardis et al., 2000; Hanany et al., 2000).

In a Λ CDM universe, the structures start to grow by the collapse and hierarchical aggregation of dark matter “haloes”, seeded by fluctuations that were originally generated with a spectrum similar to the prediction of inflationary models (i.e. $P(k) \propto k^n$, $n \approx 1$). Halos typically form “inside out”, with a strongly bound core collapsing initially and material being gradually added on less bound orbits. The process is described by the phenomenological model of Press and Schechter (1974) and its extensions (Lacey and Cole, 1993) that combines the statistics of a hierarchical, Gaussian random field with the spherical, radial top-hat collapse model and predicts the abundance of collapsed objects as a function of mass. Small structures are the first to become nonlinear, larger structures form subsequently by mergers of pre-existing halos and by accretion of diffuse dark matter that has never been part of a nonlinear object. The gravity drives haloes to aggregate into

groups and clusters of galaxies. They are located and form nonlinear larger-scale pattern of filaments, sheets and voids in the Gaussian random field of initial fluctuations (Bond et al., 1996).

Recent large-scale cosmological N-body simulations, such as the Millennium simulation (e.g. Springel et al., 2005; Bower et al., 2006; Croton et al., 2006; De Lucia and Blaizot, 2007; Guo et al., 2011) have produced semi-analytic galaxy formation models that follow the evolution of millions of galaxies. Comparison of the observed galaxy clustering signatures with cosmological simulations allows one to model and understand the clustering of galaxies, as well as their formation and evolution within their parent dark matter haloes. The recent sets of simulations are able to construct mock surveys where the simulated galaxy population is ‘observed’ with a virtual telescope to produce a sample in which galaxy properties and the large-scale structure can be compared directly with those observed in real surveys. Indeed, the results from mock surveys closely match the observed galaxy population from CfA, 2dFGRS and SDSS (Springel et al., 2006). The comparisons of mock and real surveys are useful to test observational procedures for identifying galaxy groups and clusters, for measuring their masses (e.g. Eke et al., 2006; Li and White, 2008; Knobel et al., 2012), and constrain cosmological parameters and galaxy evolution models (e.g. Choi et al., 2010; Hilbert and White, 2010; Newman et al., 2011).

Dark matter haloes

The distribution of dark matter in a dark halo have been described by “dark matter density profiles”. Cosmological N-body simulations have predicted the dark matter density profile as a steep power law profile (e.g. Dubinski and Carlberg, 1991; Navarro et al., 1996b, 1997, 2004, 2010; Fukushige and Makino, 1997, 2001; Moore et al., 1998, 1999; Ghigna et al., 1998, 2000; Jing and Suto, 2000; Klypin et al., 2001; Power et al., 2003; Ascasibar et al., 2004; Fukushige et al., 2004; Hayashi et al., 2004; Reed et al., 2005; Diemand et al., 2005b, 2008; Ascasibar and Gottlöber, 2008; Gao et al., 2008). Over a mass range spanning from micro-halos to galaxy clusters, a near ‘universal’ spherically averaged density profile of haloes can be well expressed by a simple two-parameter formula that has become known as the “NFW profile” (Navarro et al., 1997):

$$\rho(r) = \frac{\rho_s}{(r/r_s)^\alpha (1+r/r_s)^{3-\alpha}}, \quad (2.1)$$

where the standard result is $\alpha = 1$, r_s and ρ_s are a characteristic radius and density, respectively. The density rises sharply, forming a ‘cusp’ near the center of the halo, and becomes infinite at the center. The scale radius r_s is used to define the halo concentration $c_{\text{vir}} = r_{\text{vir}}/r_s$, where the ‘virial’ radius r_{vir} is defined following an overdensity criteria such as r_{200} , which encloses a mean density 200 times the critical value required for closure. At this radius the period of a circular orbit is 63% of the Hubble time H_0^{-1} . The halo concentrations c_{vir} are related to the halo formation time: early forming halos tend to have higher c_{vir} and ρ_s at $z = 0$. The NFW profile was proposed as a fit to CDM density profiles in the radial range from 0.01 r_{200} to r_{200} (Navarro et al., 1997). Density profiles with this general form have been shown to arise even in the absence of hierarchical growth, for example from HDM initial conditions (e.g. Huss et al., 1999; Wang and White, 2009) or from sharply truncated initial power spectra (Moore et al., 1999). The physical origin of this near-universal shape is not well understood, although many attempts of explanation have been put forward (e.g. Syer and White, 1998; Dekel et al., 2003; Manrique et al., 2003; Ascasibar et al., 2004; Ascasibar, 2007; Salvador-Solé et al., 2012).

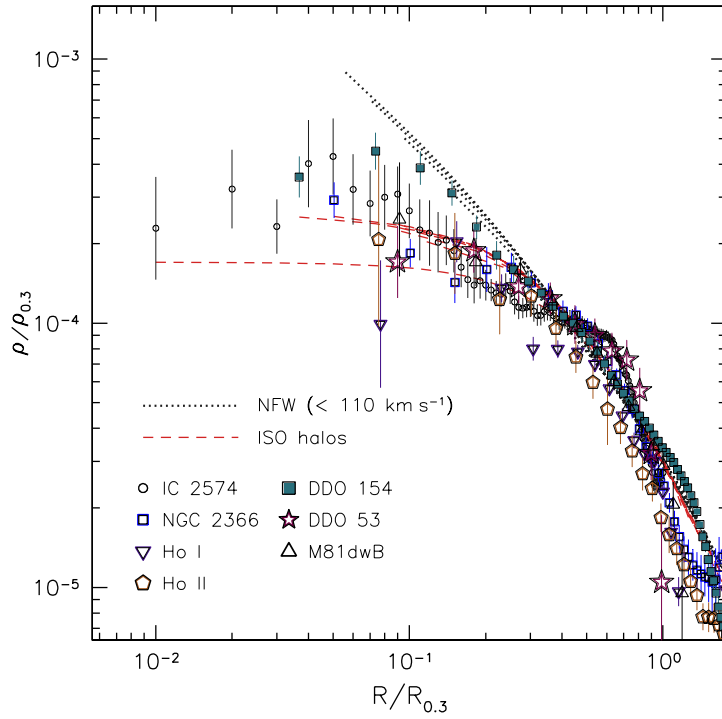


Figure 2.3: The dark matter density profiles of the 7 THINGS dwarf galaxies. The dotted lines represent the mass density profiles of NFW models ($\alpha \sim 1.0$) with V_{200} ranging from 10 to 110 km s^{-1} . The dashed lines indicate the mass density profiles of the best fit pseudo-isothermal halo models ($\alpha \sim 0.0$). Figure is taken from Oh et al. (2011b).

As more and higher resolution simulations were carried out, small but systematic deviations from the NFW profile became evident (e.g. Moore et al., 1999; Fukushige and Makino, 2003). Improved fits require an additional free parameter to account for the substantial halo-to-halo scatter. Good fits are obtained by letting the inner logarithmic slope α of the NFW function in equation 2.1 become a free parameter, instead of forcing $\alpha = 1$. To introduce the flexibility needed to account for these differences, Navarro et al. (2004) have proposed a new three-parameter fitting formula for the spherically averaged density profile:

$$\rho(r) = \rho_s e^{\frac{-2}{\gamma}[(r/r_s)^\gamma - 1]}, \quad (2.2)$$

where γ is a adjustable shape parameter that shows considerable scatter but it increases systematically with halo mass at $z = 0$ in the standard Λ CDM cosmology, reflecting small but real deviations from a truly universal profile (Gao et al., 2008). The functions in equation 2.1 and equation 2.2 only differ significantly at very small radii, i.e. below about 500 pc in a galaxy halo. Only very few simulations are currently able to resolve such small scales. The average Aquarius galactic halo has $\gamma = 0.159$ while the average Phoenix cluster has $\gamma = 0.175$ (Gao et al., 2012). No systematic studies have been carried out so far to test how γ varies with initial power spectrum, with cosmological parameters, or even with epoch in the standard Λ CDM cosmology. Since equation 2.2 had previously been used by Einasto (1965) to fit star counts in the Milky Way, this fitting function has come to be known as the “Einasto profile”.

Observationally, however, rotation curves are found to rise approximately linearly with

radius, consistent with a constant density ‘core’ profile rather than the ‘cusp’ profile provided by N-body simulations (e.g. Flores and Primack, 1994; Moore, 1994; Burkert, 1995; Kravtsov et al., 1998; Borriello and Salucci, 2001; de Blok et al., 2001; de Blok and Bosma, 2002; Marchesini et al., 2002; Gentile et al., 2004; Donato et al., 2004b; Spano et al., 2008; Kuzio de Naray et al., 2008; de Blok et al., 2008; Oh et al., 2011b). The first comparisons of the HI rotation curves of gas-rich dwarf galaxies with those predicted by CDM profiles have been presented in Flores and Primack (1994) and Moore (1994). The dynamics of these galaxies are dominated by dark matter, and they are therefore thought to be good probes of its distribution. The results showed that the haloes of these late-type dwarf galaxies are best characterized by an approximately constant-density core. The dark matter might be distributed in an isothermal sphere corresponding a “pseudo-isothermal profile”:

$$\rho(r) = \frac{\rho_0}{1 + (r/r_c)^2}, \quad (2.3)$$

where ρ_0 is the central dark matter density and r_c is the core radius (Gott, 1975; Gunn, 1977; Begeman et al., 1991). Moore (1994) has also suggested that it is conceivable that, during the galaxy formation process, gas settling in the halo will have affected the dark matter distribution. Usually this is thought to take place in the form of a process called “adiabatic contraction” (Blumenthal et al., 1986), which has the effect of contracting the inner dark matter distribution. If currently derived halo properties are the result of this process, then the initial halos must have been of even lower density, exacerbating the discrepancy. Although this profile provides better agreement with the observed rotation curves at the inner regions, it is not valid at very large radii where the density rises somewhat too fast.

After analysing the same four dwarf galaxies as investigated by Moore (1994), Burkert (1995) has introduced a one-parameter phenomenological profile for the halo density distribution that has become known as the “Burkert-profile”:

$$\rho(r) = \frac{\rho_0 r_0^3}{(r + r_0)(r^2 + r_0^2)}, \quad (2.4)$$

where ρ_0 is the central density and r_0 is the scale radius. This density law has a core radius of size r_0 , and, at large radii, converges to the NFW profile. The two parameters ρ_0 and r_0 are found to be correlated: $\rho_0 \sim r_0^{-2/3}$. Burkert (1995) has suggested that it is unlikely that baryonic blow-outs and mass-flows can cause this kind of behaviour, unless fine-tuned, and attributes the slow rise of the rotation curve to the intrinsic properties of the dark matter (i.e., a dark matter core).

By using N-body simulations, Navarro et al. (1996a) have suggested that baryonic processes might be the cause of the observed core distribution. A central dark matter core can be created if a large fraction of the baryons is suddenly expelled into the halo. For this process, star formation rates of up to $10 M_\odot \text{ yr}^{-1}$ occur over a dynamical time scale of the galaxy. The analysis of the baryonic blow-out process and its impact on the halo structure have been investigated in more details by Gelato and Sommer-Larsen (1999). The observed rotation curve of DDO 154 was reproduced by simulating NFW haloes, including the effect of violent gas outflows which are simulated by suddenly changing the disk potential in the simulations. In order to fit the simulated rotation curve to resemble the observed curve, 33 to 75 percent of the initial disk material needs to suddenly blow out. Moreover, they have suggested that the fine tuning argument put forward by Burkert (1995) may not be applicable.

However, the ‘‘core-cusp’’ problem has been a subject of many recent studies, especially for the inner regions of gas-rich dwarf and low surface brightness spiral galaxies (see e.g. de Blok, 2010, for a recent discussion). Figure 2.3 illustrates the dark matter density profiles of the 7 THINGS dwarf galaxies that represent ‘core’ profile, fit with pseudo-isothermal profile rather than NFW profile (Oh et al., 2011b). Several modifications to the standard CDM scenario, such as warm (Colín et al., 2000; Sommer-Larsen and Dolgov, 2001), repulsive (Goodman, 2000), fluid (Peebles, 2000), fuzzy (Hu et al., 2000), decaying (Cen, 2001), annihilating (Kaplinghat et al., 2000), or self-interacting (Spergel and Steinhardt, 2000; Yoshida et al., 2000; Davé et al., 2001) dark matter, and even alternative theories of gravitation (e.g. McGaugh and de Blok, 1998; Sanders and McGaugh, 2002b; Gentile et al., 2011) have been proposed in order to explain the discrepancy.

2.1.3 Particle candidates

The fundamental property of dark matter is mass. In Section 2.1.1, all the different pieces of evidence are based on the gravitational interaction of dark matter and therefore they constrain how this mass is distributed. However, astrophysical evidence also gives us hints on the properties of the dark matter particles. Firstly, in order to have persisted in significant numbers to explain the relic abundance observed at the present day ($\Omega_{\text{DM}} = 0.222 \pm 0.026$), the dark matter particle needs to be stable on cosmological time-scales, that is its lifetime must be larger than the age of the Universe. Secondly, null results of searches for exotic heavy nuclei on Earth constrain dark matter to be weakly interacting, since dark matter would form such states if it was interacting via strong or electromagnetic forces. We know then that it must be non-baryonic, because it does not couple to photons or baryons; this is spectacularly confirmed by the anisotropies in the CMB. As we have mentioned in Section 2.1.2, dark matter must be cold to be able to explain structure formation. This rules out the only known neutral and purely weakly interacting particles, neutrinos. Hence, none of the standard model (SM) particles can accommodate CDM, and this clearly hints at physics beyond the SM. Interestingly, many theories of new physics have been put forward for the identity of dark matter. A good candidate theory must fulfil all the requirements above, address the shortcomings of the SM and predict new particles, including some therefore well-motivated dark matter candidates. We exemplify here some of the many candidates proposed in the literature.

WIMPs

Although the process of chemical freeze-out generally allows dark matter to be a stable neutral particle around the electroweak scale, it brings a more serious question: How can stable particles exist around or just above the electroweak scale? One of the most elegant solutions to this problem is supersymmetry (SUSY) which mirrors each SM particle in a supersymmetric partner (sparticle) with a spin different by $1/2$. The new weakly interacting particles with mass m_{dm} close to the weak scale are the so-called weakly interacting massive particles (WIMPs). WIMPs have mass in the range $m_{\text{weak}} \sim 10 \text{ GeV} - \text{TeV}$ and tree-level interactions with the W and Z gauge bosons, but not with gluons or photons. Their relic density today as predicted from production by freeze-out, i.e. thermal decoupling (Chiu, 1966; Steigman, 1979; Lee and Weinberg, 1977; Dicus et al., 1977; Vysotskii et al., 1977), is in excellent agreement with the constraints from astrophysics and cosmology (in particular Ω_{DM} from the WMAP experiment, see above).

More precisely, in the early Universe, all particles, including dark matter, are in thermal equilibrium. As the Universe cools to temperatures T below the dark matter particle’s

mass m_{dm} , their density is being suppressed by the Boltzmann factor $\propto e^{-m_{\text{dm}}c^2/kT}$. However, apart from cooling, the Universe also expands, such that the rate of production/annihilation becomes smaller than the Hubble rate and then the WIMPs ‘freeze out’ with their number asymptotically approaching a constant, their thermal relic density. Quantitatively, the WIMP density n is governed by the Boltzmann equation (first given in Zeldovich, 1965),

$$\frac{dn}{dt} = -3Hn - \langle \sigma_{\text{ann}} v \rangle (n^2 - n_{\text{eq}}^2), \quad (2.5)$$

where H is the Hubble rate, $\langle \sigma_{\text{ann}} v \rangle$ is the thermal average of the WIMP annihilation cross section and relative velocity, and n_{eq} is the WIMP equilibrium density. In general, the thermal relic density is determined by solving the Boltzmann equation numerically but a simple analytical estimate, defining freeze out to be the time when $n\langle \sigma_{\text{ann}} v \rangle = H$, gives

$$\Omega_{\text{WIMP}} \sim \frac{x_f T_0^3}{\rho_c M_{\text{Pl}}} \langle \sigma_{\text{ann}} v \rangle^{-1}, \quad (2.6)$$

where $x_f = m_{\text{WIMP}}/T_f \approx 20$, T_f and T_0 are the temperature at freeze-out and at present day, respectively, and M_{Pl} is the Planck mass. A good approximation for particles with masses in the relevant range for WIMPs is

$$\Omega_{\text{WIMP}} h^2 = 0.1 \frac{3 \times 10^{-26} \text{ cm}^3 \text{ s}^{-1}}{\langle \sigma_{\text{ann}} v \rangle}. \quad (2.7)$$

Thus one finds an annihilation cross section corresponds to $\Omega_{\text{WIMP}} \sim \Omega_{\text{DM}}$ as

$$\langle \sigma_{\text{ann}} v \rangle \approx 3 \times 10^{-26} \text{ cm}^3 \text{ s}^{-1}. \quad (2.8)$$

The fact that WIMPs can provide the correct relic density has been called the ‘‘WIMP miracle’’.

An example of a WIMP is the lightest neutralino, a mixture of the supersymmetric partners of the hypercharge gauge boson, the neutral component of the W boson, and the neutral Higgs partners, which is the most compelling lightest supersymmetric particle (Goldberg, 1983; Ellis et al., 1984a). Depending on the region of the supersymmetric parameter space, its mass may vary from a few GeV (e.g. Feldman et al., 2010) to hundreds of TeV (e.g. Profumo, 2005). As a heavy, stable particle, the lightest neutralino is by far the most widely studied dark matter candidate. Neutralinos may annihilate, with a wide range of cross-sections and branching ratios, into SM fermion pairs (quarks and leptons), weak gauge boson pairs, and combinations containing Higgs bosons.

Theories of universal extra dimensions (Appelquist et al., 2001) also lead to new particles at the weak scale and thus WIMP dark matter candidates called Kaluza-Klein (KK) particles (Klein, 1926; Cheng et al., 2002; Servant and Tait, 2003). In most models, the lightest Kaluza-Klein particle (LKP) is the first KK state of the hypercharge gauge boson, B^1 . LKP could account for the observed relic density as long as its mass lies within $400 < m_{\text{dm}} < 1200$ GeV, well beyond current experimental constraints (Servant and Tait, 2003). Since there are less free parameters in the theory, the phenomenology of these particles is less rich than that of neutralinos. Most interestingly, the fermion (in particular, the lepton) channel is less suppressed, and they may efficiently annihilate into high-energy electron-positron pairs.

superWIMPs

Not only WIMP theories can predict the correct dark matter abundance, other mechanisms have been shown to be viable and lead to dark matter particles which have the desired relic density. We discuss one of them here: superWIMPs, superweakly-interacting massive particles that provide the right relic density but have interactions that are much weaker than weak. In the superWIMP framework, dark matter is produced in late decays. If every WIMP produced by thermal decoupling would decay to a “superWIMP”, the virtue of the right relic density can be saved (Feng et al., 2003a,b; Feng, 2010),

$$\Omega_{\text{superWIMP}} = \frac{m_{\text{superWIMP}}}{m_{\text{WIMP}}} \Omega_{\text{WIMP}}. \quad (2.9)$$

SuperWIMPs therefore inherit their relic density from WIMPs.

Another production mechanism is reheating after cosmic inflation (Krauss, 1983; Nanopoulos et al., 1983; Ellis et al., 1984b, 1985) in the context of gravitino which is in fact requires an extension of supersymmetry to supergravity (Ellis et al., 1985; Feng et al., 2003a,b; Buchmüller et al., 2004; Ellis et al., 2004; Wang and Yang, 2004; Roszkowski et al., 2005). If supersymmetry is made local and extended to supergravity, then the gravitinos interact only gravitationally. It easily fulfils the collisionless, non-dissipative and electrically-neutral requirements of a good dark matter candidate, but the very weakness of the interaction means that it is almost undetectable. Another possible example are axinos, the superpartner of axions (see below), and both could be possibly contributing in a multi-component dark matter scenario (Baer and Box, 2010). Like the gravitino, the axino is extremely weakly interacting. In contrast to the gravitino though, the axino should at least be detectable indirectly through the observation of the axion itself.

The extremely weak interactions of superWIMPs might be thought to be a nightmare for searches for dark matter. In fact, superWIMP scenarios predict signals from cosmic rays, at colliders, and in astrophysics that can be far more striking than in WIMP scenarios, making superWIMPs highly amenable to experimental investigation (Feng, 2010).

Axions

The axion was originally postulated to solve the so-called “strong CP problem” (Peccei and Quinn, 1977; Wilczek, 1978; Weinberg, 1978) and has been suggested as an extremely light and weakly interacting dark matter candidate (Preskill et al., 1983; Abbott and Sikivie, 1983; Dine and Fischler, 1983). The axion’s mass is determined by a new mass scale or the axion decay constant f_a ,

$$m_a \simeq 0.6 \text{ eV} \frac{10^7 \text{ GeV}}{f_a}. \quad (2.10)$$

A variety of searches constrains axions to be very light. Collider searches for rare decays $\pi^+ \rightarrow a(e^+e^-)e^+\nu_e$ rule out very short-lived (lifetime $< 10^{-11}$ s) axions with masses above 1 GeV. For long-lived axions (lifetime $> 10^{-11}$ s) production and interaction cross sections are constrained from beam dumps and rule out axions heavier than 50 keV (Eichler et al., 1986). Astrophysical constraints (Raffelt, 1990) like bounds on the lifetime of red giants limit the cooling due to axions and give $0.5 \text{ eV} \lesssim m_a \lesssim 200 \text{ keV}$. The duration of the neutrino burst observed from SN 1987a finally also limits the fraction of axion cooling and excludes $3 \times 10^{-3} \text{ eV} \lesssim m_a \lesssim 2 \text{ eV}$. Axions lighter than 10^{-6} eV are ruled out because they would over-close the Universe.

Furthermore, axions are expected to be extremely weakly interacting with ordinary particles, which implies that they were not in thermal equilibrium in the early universe.

The calculation of the axion relic density is uncertain, and depends on the assumptions made regarding the production mechanism. Nevertheless, it is possible to find an acceptable range where axions satisfy all present-day constraints and represent a possible dark matter candidate (e.g. Rosenberg and van Bibber, 2000).

Sterile neutrinos

SM neutrinos could have been considered as an excellent dark matter candidate, but recent experimental results have shown that they are simply not abundant enough to be the dominant component of dark matter. Furthermore structure formation constrains dark matter to be CDM. However, one or more gauge singlet right-handed (sterile) neutrinos with a mass $m_{\text{dm}} \sim \text{keV}$ can be a viable WDM candidate, with the correct relic abundance (e.g. Abazajian and Koushiappas, 2006; Viel et al., 2006; Laine and Shaposhnikov, 2008; Abazajian, 2009; Boyarsky et al., 2009). In some see-saw-inspired models, sterile neutrinos have large Majorana masses, which leads to three light active neutrinos and several heavier sterile neutrinos, the lightest of which is an attractive dark matter candidate (e.g. Asaka et al., 2007). Since this candidate necessarily decays into a light neutrino and a photon, to constitute the dark matter its lifetime must be much longer than the age of the Universe. Thus, this dark matter candidate might be detected through X-ray photons and neutrinos produced in its decay in the dark haloes of galaxies and may have other astrophysical effects, for example, on the velocity distribution of pulsars and on the formation of the first stars. Depending on the production mechanism in the early Universe, it is also possible to make sterile neutrino CDM (e.g. Gelmini et al., 2010).

2.2 Dark matter detection

2.2.1 Accelerator searches

A model-independent investigation of the production of WIMPs at the Large Hadron Collider (LHC) has been proposed recently (e.g. Beltrán et al., 2010; Rajaraman et al., 2011; Fox et al., 2012). Because WIMPs do not interact with the detector material, the most obvious collider WIMP signature is expected to be missing transverse momentum (p_T^{miss}), the magnitude of which is called E_T^{miss} . If the outgoing transverse momentum of a reaction does not sum to zero as in the original beam, this can be attributed to the production and escape of a massive particle with a very small interaction cross-section with the detector material. Although the particle must be stable enough to travel beyond the detector, the collider experiments cannot establish whether a WIMP candidate is stable on cosmological time scales. Therefore there would be no way to infer its relic abundance.

The masses of intermediate states in the decay chain and the mass of the missing particle leading to the missing E_T^{miss} can be derived by looking at kinematic endpoints in the momentum distributions of observed particles (Battaglia et al., 2004; White, 2007). However, it is very difficult to distinguish between different theories giving rise to the same observable decay products in a hadron collider like the LHC where collisions take place between bound-state quarks. Alternatively, the whole underlying theory can be reconstructed by using other channels, rather than missing E_T^{miss} , like a lepton collider. The International Linear Collider (ILC) could be used to search for direct pair production of WIMPs (Baltz et al., 2006). The masses and couplings could be constrained well enough to determine a particle's relic density to a similar level of accuracy as from the CMB (Battaglia, 2009).

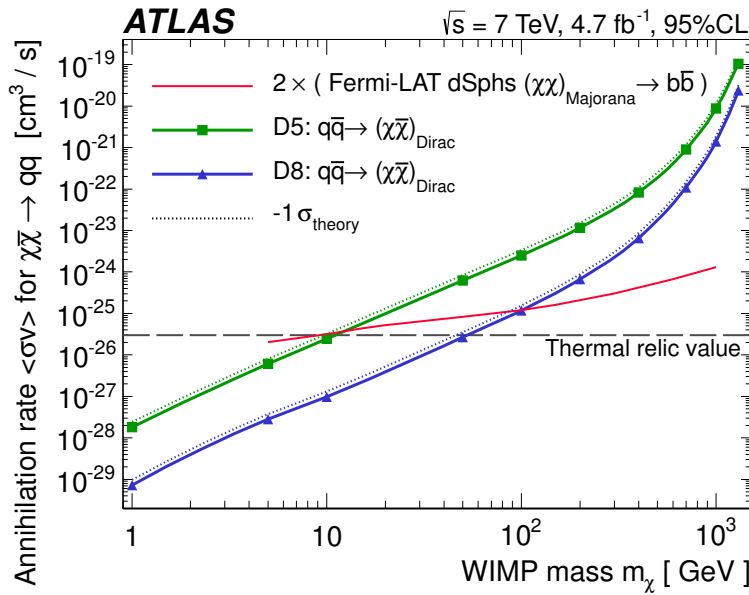


Figure 2.4: Upper limits on WIMP annihilation rates $\langle\sigma v\rangle$ versus mass m_χ . The thick solid lines are the observed upper limits without theoretical uncertainties. The thin dotted lines are the limits corresponding to the WIMP-parton cross section obtained from the $-1\sigma_{\text{theory}}$ lines. D5 and D8 describe different bilinear quark couplings to WIMPs, $qq \rightarrow \chi\chi$, by vector and axial-vector operators, respectively (see Goodman et al., 2010). High-energy gamma-ray limits from observations of Galactic satellite galaxies with the Fermi-LAT experiment (Ackermann et al., 2011) for Majorana WIMPs are shown here for comparison. The Fermi-LAT limits are scaled up by a factor of two to make them comparable to the ATLAS Dirac WIMP limits. The horizontal dashed line indicates the thermal cross-section value required for WIMPs to make up the relic abundance set by the WMAP measurement (The ATLAS Collaboration, 2012)

Searches for dark matter particles were performed in Run I and Run II at the Tevatron (Abazov et al., 2003; Abulencia et al., 2006; Altonen et al., 2012) and also in the LHC datasets by CMS (Chatrchyan et al., 2011, 2012) and ATLAS (The ATLAS Collaboration, 2012). None of the accelerators found evidence of dark matter particles. However, the dark matter annihilation rate can be constrained by these experiments. For instance, the recent upper limits of the average dark matter annihilation cross-section times the relative velocity $\langle \sigma v \rangle$ constrained by the full 2011 proton-proton LHC data set, recorded with the ATLAS detector at a centre-of-mass energy of $\sqrt{s} = 7$ TeV, and an integrated luminosity of 4.7 fb^{-1} , are shown in Figure 2.4 (The ATLAS Collaboration, 2012). For comparison, upper limits on dark matter annihilation into $b\bar{b}$ from dwarf spheroidal galaxies (dSphs) gamma-ray observations by the Fermi-LAT experiment (Ackermann et al., 2011) scaled up by a factor of two for comparison with the ATLAS limits for Dirac fermions (see for example the description of equation (34) in Cirelli et al., 2011, for an explanation of the factor of two) are also shown. Gamma-ray spectra and yields from WIMPs annihilating to $b\bar{b}$, where photons are produced in the hadronization of the quarks, are expected to be very similar to those from WIMPs annihilating to lighter quarks (Bergström et al., 1998; Fornengo et al., 2004). For low WIMP masses, i.e. $m_\chi < 10$ GeV, the ATLAS limits are below the thermal cross-section value needed for WIMPs to make up the cold dark matter abundance (see equation 2.8). In this case WIMPs would result in relic densities that are too large and hence incompatible with the WMAP measurements (The ATLAS Collaboration, 2012).

2.2.2 Direct detection

Even if a positive dark matter signal (i.e. missing energy) was detected in accelerators, further experiments would still be needed in order to assess the stability and relic abundance of the newly found part. The most promising idea of direct detection is based on the possibility that WIMPs interact with SM particles by the weak force. If WIMPs exist, the Earth should be passing through a flux of WIMPs in the Galactic dark matter halo. For these velocities, WIMPs interact with ordinary matter through elastic scattering with nuclei. Therefore an elastic scattering by a WIMP and a nucleus of large-volume target materials on Earth should produce a nuclear recoil that deposits an amount of energy which can be measured by a detector (Goodman and Witten, 1985).

The expected number of WIMP-nucleon scattering events dN per nuclear recoil energy window dE_r is given by (Gaitskell, 2004)

$$\frac{dN}{dE_r} = \frac{\sigma_0 \rho_\chi}{2\mu^2 m_\chi} F^2 \int_{v_{\min}(E_r)}^{v_{\text{esc}}} \frac{f(v)}{v} dv, \quad (2.11)$$

where σ_0 is the WIMP-nucleus cross-section, ρ_χ is the local WIMP density, m_χ is the WIMP mass, μ is the WIMP-nucleus reduced mass $(m_\chi m_N)/(m_\chi + m_N)$ (assuming a target nucleus mass m_N), and F is the nuclear form factor. The distribution of WIMPs in the halo with velocities v is given by $f(v)$, which is integrated over all possible velocities from v_{\min} to v_{esc} (v_{\min} is the minimum WIMP velocity that be able to generate a recoil energy of E_r , and v_{esc} is the maximum WIMP velocity set by the escape velocity in the halo model). Nuclear recoil searches attempt to measure $\frac{dN}{dE_r}$ directly. The relation between the WIMP mass and cross-section can be suggested by assuming a certain halo model. The standard properties of the dark matter halo are inferred from the rotational kinematics of the baryons with the mean WIMP velocity, typically $v_0 \approx 220 \text{ km s}^{-1}$, the WIMP escape velocity $v_{\text{esc}} \approx 544 \text{ km s}^{-1}$ (Smith et al., 2007), the velocity dispersion of the WIMPs

at the Earth’s location $v_{\text{rms}} \approx 270 \text{ km s}^{-1}$, and the local WIMP density 0.3 GeV cm^{-3} (Robin et al., 2003).

There are two types of scattering processes: a spin-dependent scattering where a WIMP couples to the spin of a target nucleus, and a spin-independent scattering where a WIMP couples to the nucleus mass. Due to coherence effects, the spin-independent cross section depends on the square of the nuclear mass, so higher mass nuclei, from Ge to Xe, are preferred for this search. The spin-dependent cross section depends on the nuclear spin factor, therefore the scattering happened only to target nuclei with an unpaired nucleon which provides non-zero nuclear spins, i.e. ^{19}F , ^{23}Na , ^{73}Ge , ^{127}I , ^{129}Xe , ^{131}Xe , and ^{133}Cs (see e.g. Jungman et al., 1996; Gondolo et al., 2004; Cerdeño and Green, 2010; Drees and Gerbier, 2012).

With expected WIMP masses in the range 10 GeV to 10 TeV, typical nuclear recoil energies are of order of 1 to 100 keV. Cross-sections calculated in some models, e.g. Minimal Supersymmetric Standard Model (Ellis et al., 2008), induce rates of at most 1 evt day $^{-1}$ kg $^{-1}$ of detector, much lower than the usual radioactive background. Due to the low rate of the extremely low energy events, all direct dark matter experiments are located in underground laboratories to reduce residual flux of high energy cosmic rays. The typical dark matter detector has an ‘onion-like’ shielding structure where each layer targets a specific background. The majority of present experiments use one of two detector technologies: cryogenic detectors, operating at temperatures below 100 mK with target atoms as Germanium, and noble liquid detectors with liquid Xenon or Argon as target atoms. Various combinations of detection methods are employed in different experiments. The discrimination techniques of nuclear recoils to search for evidence of WIMP scattering, based either on the shape of the pulses or on the use of multiple detection channels, are ionisation of target atoms caused by energy transfer from the recoiling nucleus, fluorescent radiation given off by excited electrons of target atoms, and scintillation light which measured phonon excitations generated in crystals by the nuclear recoils (see e.g. Saab, 2012; Arneodo, 2013, for recent reviews).

The proper motion of the Earth within the galactic halo should result in a diurnal modulation of WIMP-nucleus collisional directions, and an annual modulation of the total detection rate due to the non-perpendicularity of the solar ecliptic and galactic planes. The DAMA collaboration has reported results from a total of 6 years exposure involving 250 kg of detectors, plus the earlier 6 years exposure of the original DAMA/NaI experiment with 100 kg of detectors (Bernabei et al., 2010). They observe an annual modulation of the signal, with the expected period (1 year) and phase (maximum around June 2), at 8.9σ level. CoGeNT with Ge detectors has observed an unidentified excess of events below 3 keV and a hint (2.8σ) of seasonal modulation that could be compatible with DAMA (Aalseth et al., 2011, 2012). However, no other annual modulation analysis with comparable sensitivity has been reported by any experiment. KIMS, an experiment operating 12 crystals of CsI(Tl) with a total mass of 104.4 kg in Korea, has accumulated several years of continuous operation (Kim, 2005). They should soon be able to set an upper limit on annual modulation amplitude.

Exclusion limits placed upon the WIMP mass and spin-independent nuclear scattering cross-sections by various direct detection experiments are shown in Fig. 2.5. After operating 19 Germanium cryogenic detectors, CDMS provides limits on the spin-independent coupling of WIMPs (Ahmed et al., 2010). Two events were found in the pre-defined signal region, the expected background rate of event was 0.9. Given these figures, no observation of a signal is claimed. EDELWEISS has operated ten 400 g Germanium detectors equipped with different thermal sensors and an interdigitised charge collection electrode

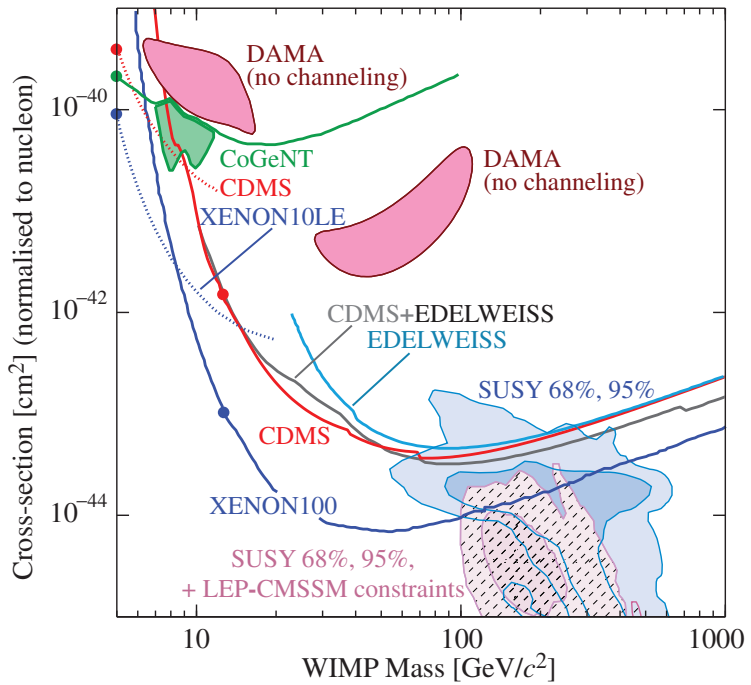


Figure 2.5: Cross-sections obtained from direct dark matter searches in the framework of spin-independent coupling. The big dots on some curves show the “WIMP safe” minimal mass for the corresponding experimental result, which is the minimal mass value defined as the maximum of the mass where the increase of sensitivity from infinite resolution to actual experimental resolution is not more than a factor two, and the mass where the experiment is sensitive to at least 1 % of the total WIMP signal recoil spectrum. Shaded 68 and 95 % regions are SUSY predictions by (Trotta et al., 2008), together with recent constraints (light gray 68 and 95 % contours) placed by LHC experiments, both on the CMSSM (Buchmueller et al., 2011). Figure is taken from Drees and Gerbier (2012).

scheme, for a duration of one year (Armengaud et al., 2011). A total of 5 events were observed, while 3 events were expected from backgrounds. No WIMP signal was claimed. The XENON collaboration has successfully operated the 161 kg XENON100 setup during a 100 day data collection period. Within a fiducial mass of 48 kg, 3 events were observed in the signal region, while 1.8 were expected, out of which 1.2 originate from a sizeable contamination of Krypton 85 in the liquid (Aprile et al., 2011). This allows them to set the best limits at all masses on spin-independent interactions of WIMPs, with a minimum cross section at 7.0×10^{-9} pb for a mass of 50 GeV. A reanalysis of part of the XENON10 data (Angle et al., 2011), using the ionization signal only, with an ionization yield of around 3.5 electron/keV at a threshold of 1.4 keV, sets a more convincing limit in the 7 GeV range, about one order of magnitude below the original CoGeNT claim. Recently, the cryogenic experiment CRESST uses the scintillation of CaWO4 as second variable for background discrimination. The observation of 67 events in the signal region does not match the about 40 expected background events (Angloher et al., 2012). The event excess is said to be compatible with WIMPs. A likelihood method provides two solutions, respectively for 12 and 25 GeV masses, stating also that the background hypothesis alone is more than 4 sigma away from the observed data. However, some other potential sources of background are insufficiently addressed, like “no-light” events, a category of events which previously plagued the sensitivity of this experiment.

2.2.3 Indirect detection

If the dark matter particles are thermal relics, then dark matter particles and antiparticles exist in equal amounts, and they could also annihilate or decay to SM particles that can be detected. As a two-body process, the rate of annihilation is proportional to the square of the dark matter density, whereas single-body decay process is proportional to the the dark matter density. The primary products of the annihilations or decays, i.e. cosmic ray protons, antiprotons, electrons, positrons, gamma-rays and neutrinos, could in principle be observed on or around the Earth, while secondary radiation like gamma-rays from inverse Compton scattering (ICS), and radio or microwaves from synchrotron could be detected in the Galactic halo (see e.g. Bertone et al., 2005).

The most commonly studied signature is the emission of gamma rays from the Galactic centre (e.g. Bergström et al., 1998; Baltz and Edsjö, 1999; Gondolo and Silk, 1999; Morselli et al., 2002; Ullio et al., 2002; Stoehr et al., 2003; Prada et al., 2004; Cesarini et al., 2004; Aharonian et al., 2006; Springel et al., 2008; Cirelli and Panci, 2009; Fornasa et al., 2009; Bernal and Palomares-Ruiz, 2010, among many others) as well as photons at other frequencies (e.g. Colafrancesco and Mele, 2001; Regis, 2008; Regis and Ullio, 2008; Bergström et al., 2009; Cholis et al., 2009a; Pato et al., 2009; Profumo and Ullio, 2010; Crocker et al., 2010). As the annihilation products travel through the surrounding medium, they heat and ionize the gas, potentially leaving an imprint on the cosmic microwave background (Chen and Kamionkowski, 2004; Colafrancesco, 2004; Padmanabhan and Finkbeiner, 2005; Mapelli et al., 2006; Zhang et al., 2006, 2007; Hooper et al., 2007; Cirelli et al., 2009a; Galli et al., 2009; Cumberbatch et al., 2009; Kanzaki et al., 2010) and the HI 21 cm spectral line (Furlanetto et al., 2006; Valdés et al., 2007; Chuzhoy, 2008). Heating and ionization of the surrounding baryonic gas can also affect the formation of the first stars (Iocco et al., 2008; Spolyar et al., 2008; Natarajan et al., 2009; Ripamonti et al., 2010) and the formation and evolution of galaxies (Ascasibar, 2007; Ripamonti et al., 2007; Natarajan et al., 2008).

The indirect dark matter detections aim to extract the signal of dark matter annihilation or decay from the astrophysical backgrounds and use their spectral or spatial information to constrain the particle physics models or properties of dark matter. The

most promising targets to search for annihilations or decays are those with large dark matter densities and/or low astrophysical backgrounds. The Galactic centre seems to be the most obvious target with large dark matter concentration, although the backgrounds are poorly-understood and the dark matter profile is uncertain. Dark matter dominated objects like dwarf galaxies are also a good option with a low background, but have the disadvantage of having rather low predicted fluxes. Galaxy clusters and the total integrated contribution to the extragalactic background have also been considered competitive targets.

In the following sections, we will briefly review the ideas, prospects and current status of dark matter indirect detection in different channels.

Photons

In general, photons can be produced by dark matter in different ways. Dark matter annihilation can proceed directly into $\gamma\gamma$ or γZ (e.g. Bergström and Snellman, 1988; Bergström and Ullio, 1997; Ullio and Bergström, 1998). Although loop-suppressed, this results in a monochromatic gamma-ray line with a very clean signature. A hard spectrum can also be produced by internal bremsstrahlung from one of the internal particles in the annihilation diagram (e.g. Bergström, 1989; Bringmann et al., 2008). This typically gives rise to a sharp feature that peaks at an energy corresponding to the dark matter mass. The annihilation into quarks, leptons and heavy gauge bosons generically give origin to a continuum of gamma-rays via π^0 and inverse Compton scattering as well as the emission of bremsstrahlung and synchrotron radiation to softer photons.

Indirect detection with photons is currently dominated by large air-Čerenkov gamma-ray telescopes and the Fermi Large Area Telescope (LAT; Atwood et al., 2009) that allow for various searches for possible dark matter signatures with a so far unprecedented accuracy. Limits on the total cross-section from dwarf galaxies (e.g. Lombardi et al., 2009; Essig et al., 2009; Abdo et al., 2010b), the isotropic diffuse background (e.g. Abdo et al., 2010c; Abazajian et al., 2010) and galaxy clusters (e.g. Ackermann et al., 2010b) are approaching the canonical thermal cross-section ($\langle\sigma v\rangle \approx 3 \times 10^{-26} \text{ cm}^3 \text{ s}^{-1}$). Claims have been made from outside the collaboration of excesses in public Fermi data in the inner Galaxy (Goodenough and Hooper, 2009; Dobler et al., 2010) and recently by the Fermi collaboration (Ackermann et al., 2012c), which have interpreted as signals of WIMP annihilation. Very recently, the claim of an indication of line emission in Fermi data (Weniger, 2012; Su and Finkbeiner, 2012) has drawn considerable attention. Weniger (2012) found a (trial corrected) 3.2σ significant excess at a mass of ~ 130 GeV.

Searches for secondary photons from WIMP annihilation or decay benefit from gamma-ray and longer-wavelength observations. ICS of CMB and interstellar radiation field photons by primary leptons injected in annihilations or decays can lead to substantial signals in gamma rays and X-rays, as well as in radio and microwave signals from synchrotron radiation of primary leptons in regions with significant magnetic fields, see Section 3.3 for more details.

Cosmic rays

Recent electron and positron cosmic ray data from the Fermi satellite (Abdo et al., 2009), the PAMELA satellite (Adriani et al., 2009a), the ATIC balloon mission (Chang et al., 2008; Panov et al., 2011) and the H.E.S.S. telescope (Aharonian et al., 2008) indicate a slight excess with respect to the astrophysical background. A substantial excess is also seen in the fraction of events due to positrons. The positron excess can be explained in

terms of conventional astrophysical sources like pulsars (see e.g. Serpico, 2012; Profumo, 2012), supernova remnants (Piran et al., 2009; Fujita et al., 2009), and possibly even standard secondary production (Katz et al., 2010). However, it also leads to several works explaining the data in terms of dark matter annihilation or decay that makes a sizeable contribution to the positron budget of the Milky Way. We will explain details of the positron excess in Section 3.1.2.

In the standard WIMP scenario, hadron production in WIMP pair annihilation is not forbidden either by kinematics or any symmetry enforcing WIMPs to be coupled with leptons only. In many models, WIMP annihilation produces a substantial number of antiprotons (e.g. see Section 3.1.1). However the PAMELA data (Adriani et al., 2010b) and the other indirect detection experiments in the solar neighbourhood show no excess in absolute antiproton flux. This results constrain severe limits on particle models which can be invoked to explain the PAMELA positron excess. It suggests that such models should annihilate predominantly to lepton-antilepton pairs rather than hadrons, which is suppressed for neutralinos but occurs frequently for the lightest Kaluza-Klein particles (Cheng et al., 2002; Servant and Tait, 2003; Cholis et al., 2009b; Bergström et al., 2009). Otherwise, antiproton measurements can give stringent constraints (Cirelli et al., 2009b; Donato et al., 2009) on a number of models invoking boost factors to explain the anomalies in the lepton channels.

Upper limits on dark matter annihilation cross-section times the relative velocity, $\langle\sigma v\rangle$, from diffuse gamma-rays measured in the Galactic halo by Fermi for an NFW profile and two different annihilation channels, compared to the upper limits from the electron and positron data in the solar neighbourhood measured by PAMELA (Adriani et al., 2009b) and FermiLAT (Abdo et al., 2009), are shown in Figure 2.6. The limits obtained from the gamma-rays are compatible with the limits obtained from the electron-positron measurements (Ackermann et al., 2012c).

Antideuterons are another promising indirect detection channel. The use of a signal of antideuterons to search for dark matter was first proposed by Donato et al. (2000). Although predicted yields from dark matter annihilation (Baer and Profumo, 2005) and decay (Ibarra and Tran, 2009b) are certainly smaller than those for antiprotons, it is a particularly convenient dark matter detection channel, since the expected astrophysical background at low energies is at a very low level. Therefore, antideuterons allow for an almost background-free search for an exotic dark matter component in certain parameter ranges. In fact, no cosmic-ray antideuterons have been observed so far. However, future experiments, such as the Alpha Magnetic Spectrometer(AMS-02) space shuttle mission (Choutko and Giovacchini, 2008) and the dedicated balloon mission General AntiParticle Spectrometer (GAPS) (Hailey, 2009), will greatly improve the sensitivity to low antideuteron fluxes.

Neutrinos

Neutrinos can be produced directly by WIMP annihilation in certain models, such as Kaluza-Klein dark matter in universal extra dimensions, and can also be produced indirectly in secondary decays and/or cascade interactions with baryonic matter. Although their weak interactions, small masses and atmospheric background make neutrinos a difficult indirect detection prospect, dark matter indirect detection with neutrinos benefits from the same advantage as indirect detection with gamma rays that neutrinos point directly back to their source. Their small interactions require detector volumes of cubic kilometre size and provide event rates of a few per year.

A particularly interesting idea for dark matter indirect detection is that a WIMP can

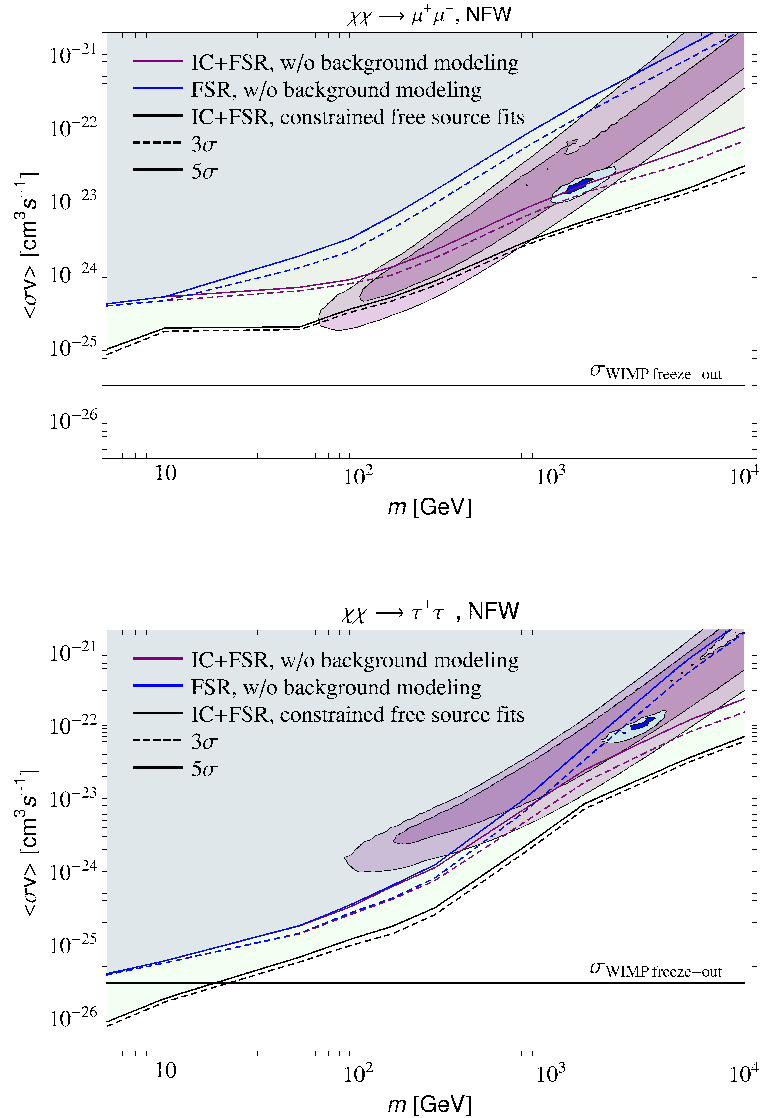


Figure 2.6: Upper limits on dark matter annihilation cross-section times to the relative velocity, $\langle\sigma v\rangle$, including a model of the astrophysical background compared with the limits obtained with no modeling of the background. Upper panel: Limits on models in which dark matter annihilates into $\mu^+\mu^-$, for a dark matter distribution given by the NFW distribution. The horizontal line marks the thermal decoupling cross section expected for a generic WIMP candidate. Lower panel: The same, for dark matter annihilation to $\tau^+\tau^-$. The region excluded by the analysis with no model of the astrophysical background is indicated in light blue, while the additional region excluded by the analysis with a modeling of the background is indicated in light green. The regions of parameter space which provide a good fit to PAMELA (Adriani et al., 2009b) (purple) and *Fermi* LAT (Abdo et al., 2009) (blue) cosmic rays electron and positron data are shown, as derived in Cirelli et al. (2010) and are scaled by a factor of 0.5, to account for different assumptions on the local dark matter density. Figures are taken from Ackermann et al. (2012c).

scatter elastically and become gravitationally trapped inside the Sun. After sinking to the core of the Sun, dark matter particles can annihilate at a significant rate, especially if equilibrium between capture and annihilation is reached. Neutrinos detected from the Sun with energies of tens to hundreds of GeV can be unambiguously assigned to dark matter annihilation processes and used to constrain WIMP annihilation cross sections and dark matter models. The detection is relatively robust against astrophysical uncertainties, especially at steady state, as the annihilation rate depends ‘almost exactly’ on the same product of local density and cross section entering the direct detection experiments. Since the Sun is mostly made of protons, bounds on spin-dependent cross-sections are comparatively stronger than those on spin-independent ones.

With observations of the Galactic centre (Bertone et al., 2004) and the inner Galactic halo (Yüksel et al., 2007), the SUPER-Kamiokande experiment, which has the best sensitivity for WIMP masses of about a GeV, has been used with some success to constrain the annihilation cross-section of traditional WIMP models. The cubic-kilometre telescopes such as IceCube, which can detect larger mass neutrinos, has already improved limits on the elastic scattering cross section by 2-3 orders of magnitude for the spin-dependent case (Abbasi et al., 2009). For spin-independent cross sections, however, the event rates inferred by direct detection limits are much too low to be discovered by IceCube. For recent results from IceCube, see Aartsen et al. (2012) and Abbasi et al. (2012).

Chapter

3

e^- AND e^+ FROM DARK MATTER ANNIHILATION

As we have discussed in the previous Chapter, in Section 2.2.3, dark matter can be indirectly detected through the signatures of standard model particles produced by its annihilation or decay. Recent results from indirect detection experiments in the solar neighbourhood have indicated the possibility that such a signature has been seen. In particular, the PAMELA satellite has found a significant excess of positrons above the expected smooth astrophysical background (Adriani et al., 2009a). These results can be interpreted as evidences of dark matter annihilations. If this excess does originate from dark matter annihilation, then an abundant population of high energy electrons and positrons is being created everywhere in the Galactic dark matter halo. These energetic electrons and positrons must have an impact on the Galactic halo and produce photons through synchrotron radiation in the Galactic magnetic field, and inverse Compton scattering of photons of the interstellar radiation field (ISRF), and final state radiation (FSR) which happens at the very moment of pair creation.

In this thesis, we focus on the electrons and positrons arising from dark matter annihilation, moreover we neglect other processes, such as dark matter decay, and other annihilation products, such as protons and antiprotons (whose contribution is severely constrained by recent observational data, as we will explain in Section 3.1.2).

In this Chapter, we discuss the assumptions and methods which we use. Section 3.1 reviews the detail of dark matter annihilation which relates to electron and positron production. Section 3.2 describes the procedure followed to estimate the electron-positron spectrum. Astrophysical signatures of dark matter annihilation from photons are described in Section 3.3.

3.1 Dark matter annihilation

In this section, we start with a review of the annihilation channels that relate to the production of electrons and positrons. Later we discuss the Galactic positron excess which has been suggested as a signature of dark matter annihilation (for reviews see e.g. Jungman et al., 1996; Bertone, 2010; Cirelli, 2012; Lavalle and Salati, 2012).

3.1.1 Annihilation channels

The dark matter particles that constitute the Galactic dark matter halo may annihilate directly into fermions, gauge bosons, Higgs boson and photons. The decaying of those primary annihilation products would subsequently give origin to fluxes of energetic cosmic rays (e^- , e^+ , p , \bar{p}), as well as γ -rays and neutrinos. Since we focus on electrons and positrons produced from dark matter annihilations, in this section we summarize only the most important annihilation channels which produce fermions from two of the most popular dark matter candidates, neutralinos and the lightest Kaluza-Klein particles (for a more complete list and details see e.g. Drees and Nojiri, 1993; Jungman et al., 1996; Nihei et al., 2001, 2002; Birkedal-Hansen and Jeong, 2003).

Neutralino annihilation

Fermion pairs can be produced through the annihilation of neutralinos by three tree level diagrams (Ellis et al., 1984a; Griest, 1988a,b; Drees and Nojiri, 1993). These processes, shown in Figure 3.1, consist of t-channel exchange of sfermions (\tilde{f}), s-channel exchange of Z^0 -bosons and pseudoscalar Higgs (A), respectively. The expected neutralino mass for the annihilations to a fermion-antifermion pair is of order or greater than 10 GeV, and the cross section of the annihilation channels can be expanded as

$$\sigma v = a + b(v/c)^2 + \dots \quad (3.1)$$

where a is the s-wave contribution at zero relative velocity, b is the contribution from both s and p waves, c is the speed of light, and v is the neutralino-neutralino relative velocity.

It is sufficient for indirect detection to consider the amplitudes and cross sections in the limit of zero velocity, i.e. the s-wave amplitude or the first term in the expansion (see e.g. Jungman et al., 1996; Bertone et al., 2005). The cross section for the annihilation in the limit of zero velocity is given in terms of the three contributions to the amplitude by

$$\sigma v(\chi\chi \rightarrow \bar{f}_i f_i)_{v \rightarrow 0} = \frac{c_f \beta_f}{128\pi m_\chi^2} |\mathcal{A}(\chi\chi \rightarrow \bar{f}_i f_i)_{v \rightarrow 0}|^2, \quad (3.2)$$

where

$$\mathcal{A}(\chi\chi \rightarrow \bar{f}_i f_i)_{v \rightarrow 0} = \mathcal{A}_{\tilde{f}} + \mathcal{A}_Z + \mathcal{A}_A \quad (3.3)$$

is the s-wave amplitude for annihilation to a fermion-antifermion pair (adding the contribution of six sfermion states, Z^0 -boson, and pseudoscalar Higgs) which is proportional to the fermion mass. m_χ is the neutralino mass, $\beta_f = \sqrt{1 - m_f^2/m_\chi^2}$ and c_f is a color factor which is equal to three for quark final states and one otherwise (Ellis et al., 1984a; Griest, 1988a,b; Drees and Nojiri, 1993).

The cross-section for the annihilation to fermion-antifermion pairs is proportional to the fermion mass by the three contributions to the amplitude. Therefore neutralino annihilation into light quarks (i.e. $u\bar{u}$, $d\bar{d}$, and $s\bar{s}$) and light leptons (i.e. e^-e^+ and $\mu^-\mu^+$) is negligible in comparison with annihilation to heavy final states, $b\bar{b}$, $\tau^-\tau^+$, and $t\bar{t}$. Furthermore, if the neutralino is heavy enough to annihilate to top-quark ($m_\chi > m_t$), the top-quark final state is the dominant annihilation channel in most models.

The lightest Kaluza-Klein particle annihilation

As mentioned in Section 2.1.3, direct annihilation into light charged leptons pairs, i.e. e^-e^+ and $\mu^-\mu^+$, occurs frequently for the lightest Kaluza-Klein particles (LKP) (Cheng

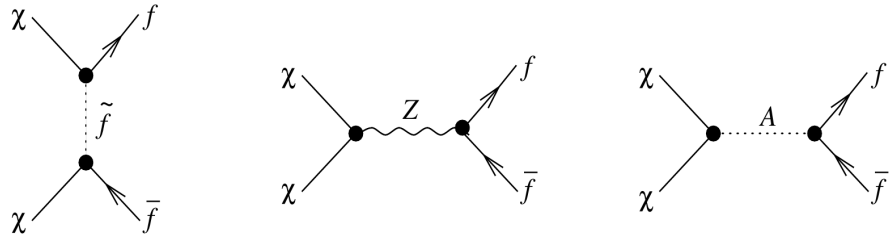


Figure 3.1: Tree level diagrams for neutralino annihilation into fermion pairs by t-channel exchange of sfermions (\tilde{f}), s-channel exchange of Z^0 -bosons and pseudoscalar Higgs (A), respectively. Figures are from Jungman et al. (1996).

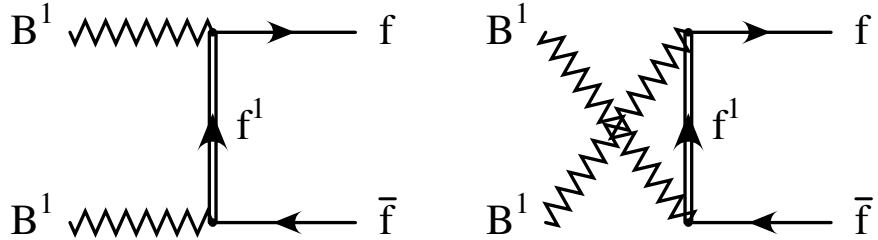


Figure 3.2: Feynman diagrams for the first Kaluza-Klein excitation of the hypercharge gauge boson $B^{(1)}$ annihilation into fermion pairs by t-channel and u-channel exchange of the first Kaluza-Klein excitation of the fermion f^1 . Figures are from Servant and Tait (2003).

et al., 2002; Servant and Tait, 2003), such as the first Kaluza-Klein excitation of the hypercharge gauge boson which referred as $B^{(1)}$.

The calculation of the relic density of the $B^{(1)}$ LKP was first performed by Servant and Tait (2003). Pairs of $B^{(1)}$ can annihilate into fermions, $f\bar{f}$, or pairs of Higgs bosons, $\phi\bar{\phi}^*$. The cross-section for $B^{(1)}B^{(1)} \rightarrow f\bar{f}$ is given in terms of contributions of both the $f_L^{(1)}$ and $f_R^{(1)}$ exchanged in the t-channel and u-channel as shown in Figure 3.2. The cross-section of $B^{(1)}B^{(1)}$ annihilation has been derived in Servant and Tait (2003) and is expressed in a short formula in Bertone et al. (2005) by

$$\langle\sigma v\rangle = \frac{95g_1^4}{324\pi m_{B^{(1)}}^2} \simeq \frac{0.6 \text{ pb}}{m_{B^{(1)}}^2 [\text{TeV}]}, \quad (3.4)$$

where g_1 is the U(1) gauge coupling and $m_{B^{(1)}}$ is the $B^{(1)}$ mass.

The annihilation cross section is almost independent of the particle mass of the final state. Therefore a large fraction of LKP annihilations produce charged lepton pairs. The branching ratios for $B^{(1)}$ annihilation are 35% into quark pairs, 59% into charged lepton pairs, 4% into neutral leptons, and 2% into Higgs. The mass of the LKP should lie in the range of 400 to 1200 GeV (Servant and Tait, 2003).

Charged leptons can also be produced by the first Kaluza-Klein excitation of neutrino $\nu^{(1)}$ and co-annihilations, e.g. $B^{(1)}$ co-annihilates with $e_R^{(1)}$ and $\nu^{(1)}$ co-annihilates with $e_L^{(1)}$, where $e_R^{(1)}$ and $e_L^{(1)}$ are the first Kaluza-Klein excitation of the right and left handed electron, respectively. It was shown in Servant and Tait (2003) that including co-annihilation effects can reduce the mass for the dark matter particle which is to be contrasted with the neutralino case where co-annihilation effects tend to push the prediction

for the mass of the neutralino to higher values (for more details about all co-annihilation channels see e.g. Kong and Matchev, 2006; Burnell and Kribs, 2006).

3.1.2 The Galactic positron excess

Dark matter annihilation can produce baryons and leptons that decay into the lightest (i.e. stable) members of the family (i.e. $p\bar{p}$ and e^\pm). This leads to an excess of either $p\bar{p}$ or e^\pm with respect to the astrophysical background. Data from PAMELA (Adriani et al., 2010b) showed no excess in the \bar{p}/p energy spectrum compared with the predicted background, as shown in the top panel of Figure 3.3. However, an excess of the positron measurement with respect to the astrophysical background was presented in the HEAT data (Barwick et al., 1997), AMS-01 (Aguilar et al., 2007), and has recently been confirmed by the PAMELA observation (Adriani et al., 2009a) of the positron fraction $e^+/(e^+ + e^-)$ and an independent measurement by the Fermi satellite (Ackermann et al., 2012b) (see the bottom panel of Figure 3.3). The positron excess lies above 10 GeV and extends to 200 GeV. The presence of a peak in the $e^+ + e^-$ energy spectrum has also been reported by the balloon experiments ATIC-2 (Chang et al., 2008; Panov et al., 2011) and PPB-BETS (Torii et al., 2008), the Fermi satellite (Abdo et al., 2009), and the H.E.S.S. telescope (Aharonian et al., 2008) which show a power law spectrum in agreement with the one from Fermi.

The attempt to explain this striking excess in terms of the background of secondary positrons produced from primary cosmic ray nuclei colliding in the interstellar medium (ISM), is far from trivial (Delahaye et al., 2009). The signal presented above implies the existence of an unknown new source of ‘primary’ positrons. Although currently the most favoured explanation for the origin of Galactic positrons, traced by the positron annihilation emission line at 511 keV (see Prantzos et al., 2011, for a recent review) is low-mass X-ray binaries (Weidenspointner et al., 2008), and the local positron excess at high energies is most likely due to the contribution of nearby pulsars (see e.g. Serpico, 2012; Profumo, 2012), several works have considered the possibility that dark matter annihilation makes a sizeable contribution to the positron budget of the Milky Way (e.g. Boehm et al., 2004; Boehm and Ascasibar, 2004; Beacom et al., 2005; Picciotto and Pospelov, 2005; Ascasibar et al., 2006; Beacom and Yüksel, 2006; Sizun et al., 2006; Finkbeiner and Weiner, 2007; Pospelov and Ritz, 2007; Barger et al., 2009; Bergström, 2009; Chen and Takahashi, 2009; Cholis et al., 2009a; Cirelli et al., 2009a; Donato et al., 2009; Grasso et al., 2009; Malyshev et al., 2009; Mertsch and Sarkar, 2009; Regis and Ullio, 2009; Yin et al., 2009; Chen et al., 2010; Meade et al., 2010; Cline et al., 2011; Vincent et al., 2012).

It has been suggested that the positron excess and the peak in the $e^+ + e^-$ energy spectrum could be the signal of dark matter annihilations within the context of supersymmetry (see e.g. Tylka, 1989; Turner and Wilczek, 1990; Kamionkowski and Turner, 1991; Baltz and Edsjö, 1999; Kane et al., 2002b; Baltz et al., 2002; Kane et al., 2002a; Bergström et al., 2008) and Kaluza-Klein dark matter (see e.g. Cheng et al., 2002; Hooper and Kribs, 2004; Hooper and Zurek, 2009). Interpreted in terms of dark matter annihilation, the datasets listed in Section 3.1.2 precisely restrict the dark matter annihilation scenarios. Since the antiproton data measured by the PAMELA collaboration (Adriani et al., 2010b) are consistent with the predicted background, they favour models where the dark matter species preferentially annihilate into leptonic channels rather than any hadronic annihilation channels, otherwise antiproton measurements would be exceeded (e.g. Bergström et al., 2009; Cholis et al., 2009a; Yin et al., 2009; Meade et al., 2010). According to Meade et al. (2010), dark matter annihilation into $\tau^+\tau^-$ provides the best fit to the data, while annihilation channels involving quarks, heavy vectors or the Higgs are

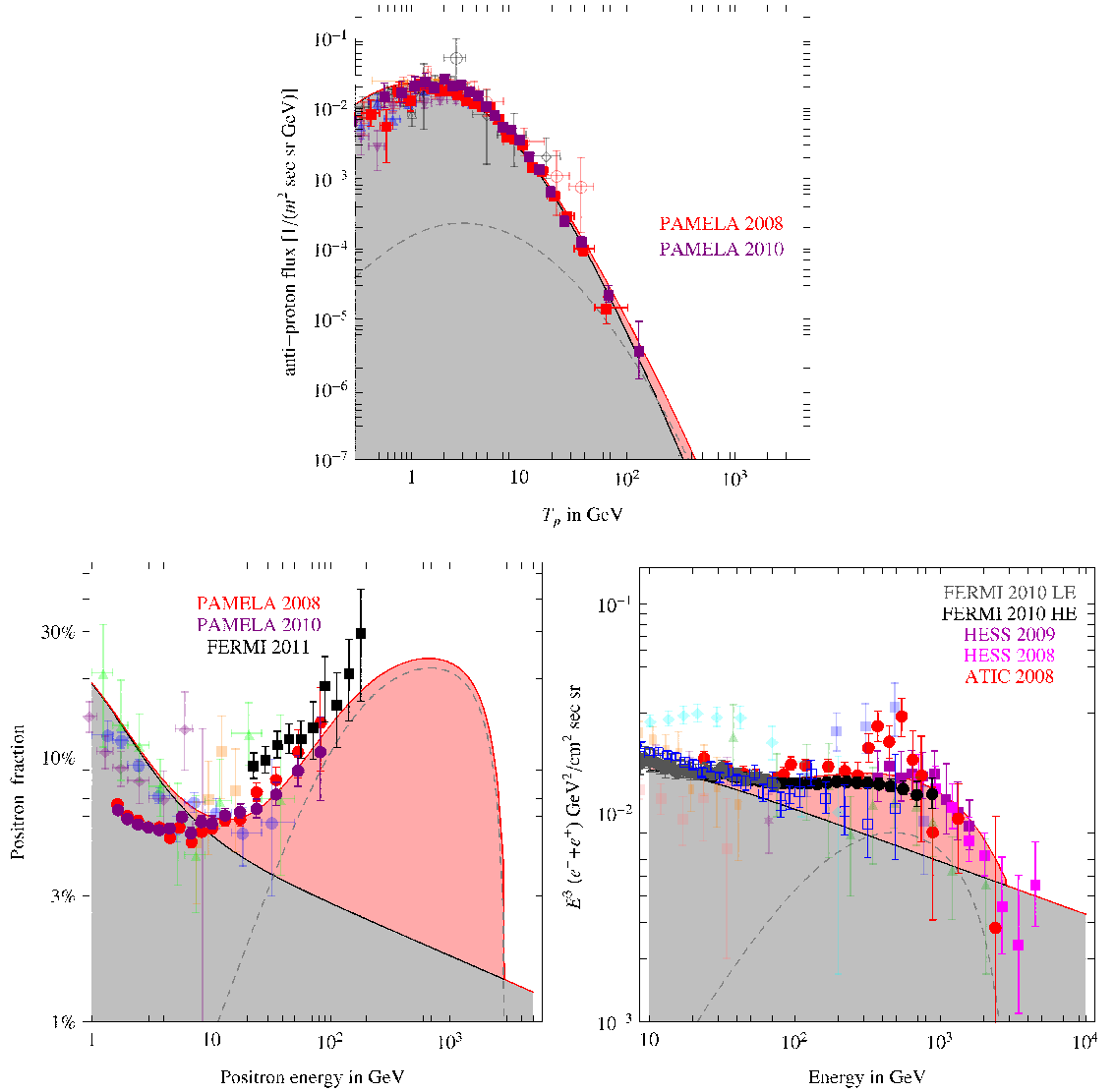


Figure 3.3: Antiproton flux (*top*), the positron fraction (*bottom-left*), and sum of electrons and positrons flux (*bottom-right*) compared with the expected astrophysical background (*gray areas*). The flux from the best fit dark matter candidate from Meade et al. (2010), a 3 TeV dark matter particle annihilating into $\tau^+\tau^-$ with a cross section of $\langle\sigma_{\text{ann}}v\rangle = 2 \times 10^{-22} \text{ cm}^3 \text{ s}^{-1}$, are represented in the lower dashed line. Sum of the flux from dark matter annihilation and the expected astrophysical background are represented in pink areas. Figures are from Cirelli (2012).

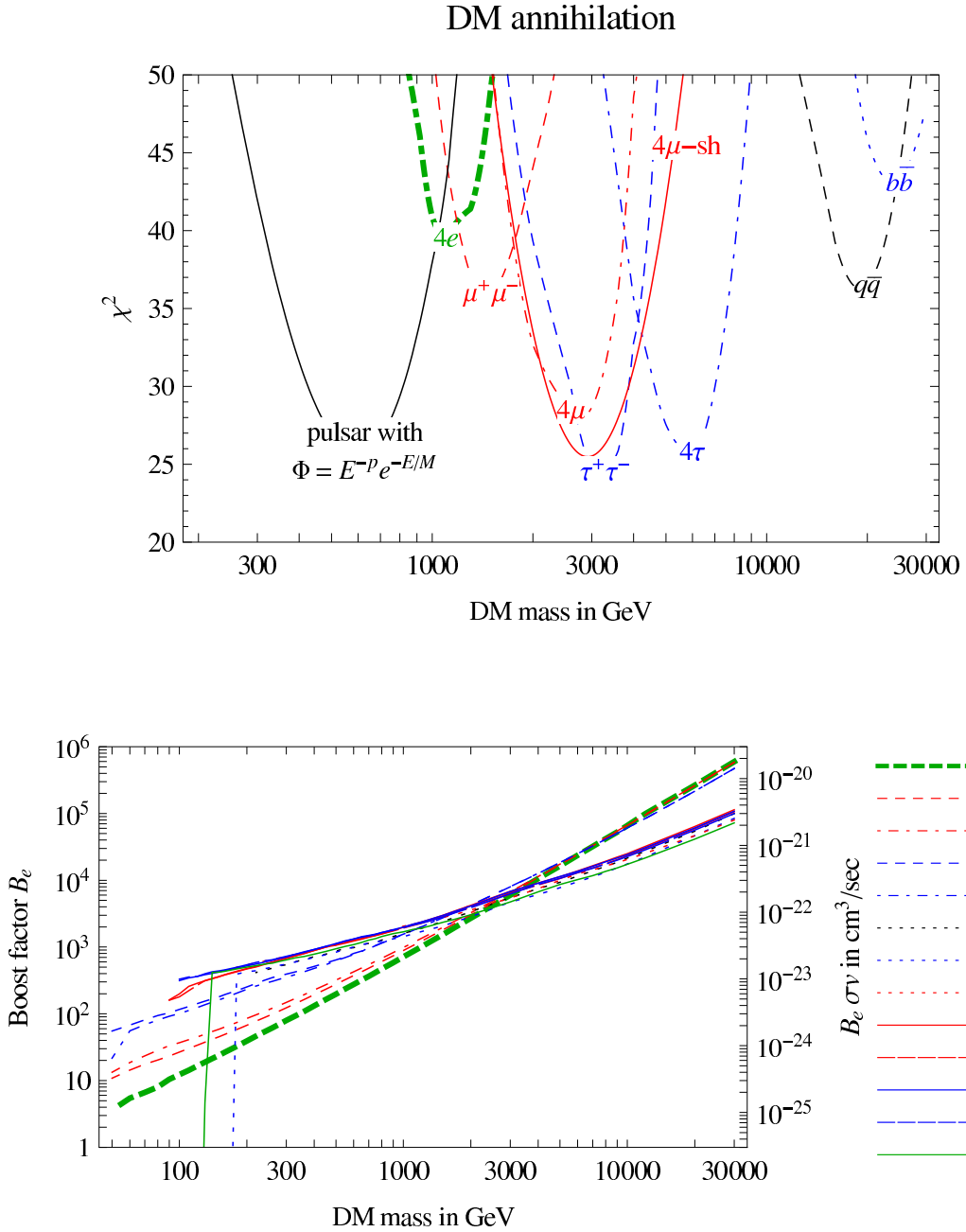


Figure 3.4: Global fit to the PAMELA, Fermi and H.E.S.S. data (top). The labels on each curve indicate the primary annihilation channel (Adopt from Meade et al., 2010). Values of $B_e \cdot \sigma v$ and of the boost factor B_e (for $\langle \sigma_{\text{ann}} v \rangle \sim 3 \times 10^{-26} \text{ cm}^3 \text{ s}^{-1}$) needed to fit the data have shown in the bottom panel (adopted from Cirelli et al., 2009b).

disfavored. The global fit of different dark matter annihilation channels to the PAMELA, Fermi and H.E.S.S. data is shown in the top panel of Figure 3.4. The actual best fit case of a candidate with a mass of 3 TeV and annihilating into $\tau^+\tau^-$ with a cross section of $2 \times 10^{-22} \text{ cm}^3 \text{ s}^{-1}$ is illustrated in Figure 3.3.

The excess can be generated by a particle with a mass in the range 100 GeV to a few TeV, in good agreement with theoretical expectations for WIMP masses. However, high energy positrons (and electrons) cannot diffuse on long distances, and those detected at the Earth must have been produced locally. With standard astrophysical assumptions of the dark matter halo, e.g. NFW (Navarro et al., 1996b, 1997) or isothermal (Bahcall and Soneira, 1980) profile, and a local dark matter density of $\rho_\odot \sim 0.3 \text{ GeV cm}^{-3}$, it turns out that a very large annihilation cross section is needed, of the order of $\langle \sigma_{\text{ann}} v \rangle \sim 10^{-23} \text{ cm}^3 \text{ s}^{-1}$ up to $10^{-20} \text{ cm}^3 \text{ s}^{-1}$ or more, depending on the mass of the candidate and the annihilation channel (Cirelli et al., 2009b). The numbers are much larger than the annihilation cross section at the decoupling time, $\langle \sigma_{\text{ann}} v \rangle \sim 3 \times 10^{-26} \text{ cm}^3 \text{ s}^{-1}$, and large enhancements need to be invoked, either from astrophysics and/or particle physics. The value of the required annihilation cross section and ‘boost factor’ as a function of the dark matter mass is illustrated in the bottom panel of Figure 3.4 (Cirelli et al., 2009b).

One can expect some ‘enhancement mechanism’ under certain assumptions, either from astrophysics or particle physics, which is effective at low redshift but not in the early universe. Astrophysical enhancements, or ‘boost factors’, can be the presence of a local dark matter substructure which would actually outshine the rest of the Galactic dark matter distribution. The probability of such a substructure close enough to the Earth to explain the excess is very small, as demonstrated in an analysis (Brun et al., 2009) based on the results of the cosmological N-body simulation Via Lactea II (Diemand et al., 2008). Particle physics enhancement can come from an elementary effect in non-relativistic quantum mechanics of the annihilation cross section, so-called Sommerfeld enhancement (e.g. electromagnetic potential enhance the annihilation cross section of an electron-positron annihilation by attracting the incident electron by the positron) (Sommerfeld, 1931; Hisano et al., 2004, 2007), and the annihilation via a resonance, for example by a resonance mass just below twice of dark matter mass (Cirelli et al., 2009b; Ibe et al., 2009; Guo and Wu, 2009; Feldman et al., 2009; An and Pospelov, 2012). Another possibility has been suggested by unstable dark matter candidates with very large lifetimes which required higher dimension operators to explain the positron excess (see e.g. Ibarra and Tran, 2009a; Ibarra et al., 2009; Garny et al., 2011). In any case, dark matter annihilation must be exclusive to leptonic channels to prevent antiprotons from being overproduced.

3.2 Electron-Positron propagation

If the electron and positron excess originates from dark matter annihilation, it would be very interesting to look for signatures of dark matter annihilation through those electrons and positrons. In order to do that, we need to investigate how electrons and positrons propagate throughout the dark matter halo. Here we focus on the energy density associated with electrons and positrons arising from dark matter annihilations. We adopt a model-independent approach, in which all particles are created with the same initial energy $E_0 \sim m_{\text{dm}} c^2$. Results for a particular dark matter candidate can be obtained by integrating over the appropriate source function.

Since the characteristic energies involved are on the order of the mass of the dark matter particle, and this mass is usually much larger than the rest mass of the electron, electrons and positrons will be relativistic at the moment of their creation. However,

they can efficiently lose their energy through different processes, such as ICS, synchrotron radiation, Coulomb collisions, bremsstrahlung, and ionization. Throughout this thesis, we will often use the Lorentz factor γ to express the energy $E = \gamma m_e c^2$, where m_e denotes the rest mass of electron, and c is the speed of light.

3.2.1 Diffusion-loss equation

The propagation of electrons and positrons through the interstellar medium (ISM) is determined by the diffusion-loss equation,

$$\frac{\partial}{\partial t} \frac{dn}{d\gamma}(\mathbf{x}, \gamma) = \nabla \left[K(\mathbf{x}, \gamma) \nabla \frac{dn}{d\gamma}(\mathbf{x}, \gamma) \right] + \frac{\partial}{\partial \gamma} \left[b(\mathbf{x}, \gamma) \frac{dn}{d\gamma}(\mathbf{x}, \gamma) \right] + Q(\mathbf{x}, \gamma). \quad (3.5)$$

We assume a diffusion coefficient of the form

$$K(\gamma) = K_0 \gamma^\delta \quad (3.6)$$

with $K_0 = 1.67 \times 10^{25} \text{ cm}^2 \text{s}^{-1}$ and $\delta = 0.7$, independent of Galactic location (MED model in Donato et al., 2004a). The energy loss rate

$$b(\mathbf{x}, \gamma) \equiv -\frac{d\gamma}{dt}(\mathbf{x}, \gamma) = \sum_i b_i(\mathbf{x}, \gamma) \quad (3.7)$$

is a sum over the relevant physical processes, and the source term $Q(\mathbf{x}, \gamma)$ represents the instantaneous electron-positron injection rate.

Given enough time, the electron-positron population will approach a steady-state distribution, $\frac{\partial}{\partial t} \frac{dn}{d\gamma}(\mathbf{x}, \gamma) = 0$. Assuming that $b(\mathbf{x}, \gamma)$ varies smoothly in space, the particle spectrum fulfills the relation

$$\frac{\partial y(\mathbf{x}, \gamma)}{\partial \gamma} + \frac{K(\gamma)}{b(\gamma)} \nabla^2 y(\mathbf{x}, \gamma) = -Q(\mathbf{x}, \gamma), \quad (3.8)$$

where

$$y(\mathbf{x}, \gamma) \equiv b(\gamma) \frac{dn}{d\gamma}(\mathbf{x}, \gamma). \quad (3.9)$$

Imposing $\frac{dn}{d\gamma}(\mathbf{x}, \gamma) = 0$ at infinity, one obtains the Green function

$$G(\mathbf{x}, \gamma, \mathbf{x}_s, \gamma_s) = \frac{\exp\left(-\frac{|\mathbf{x}-\mathbf{x}_s|^2}{2\Delta\lambda^2}\right)}{(2\pi\Delta\lambda^2)^{3/2}} \Theta(\gamma - \gamma_s) \quad (3.10)$$

and either the image charges method or an expansion over the eigenfunctions of the linear differential operator may be used to derive the Green function for other boundary conditions (see e.g. Baltz and Edsjö, 1999; Delahaye et al., 2009). The electron-positron spectrum is thus given by

$$\frac{dn}{d\gamma}(\mathbf{x}, \gamma) = \frac{1}{b(\mathbf{x}, \gamma)} \int_{\gamma}^{\infty} d\gamma_s \int_0^{\infty} d^3 \mathbf{x}_s \frac{\exp\left(-\frac{|\mathbf{x}-\mathbf{x}_s|^2}{2\Delta\lambda^2}\right)}{(2\pi\Delta\lambda^2)^{3/2}} Q(\mathbf{x}_s, \gamma_s), \quad (3.11)$$

where the quantity

$$\Delta\lambda^2 = \lambda^2(\gamma) - \lambda^2(\gamma_s) \quad (3.12)$$

is related to the characteristic diffusion length of the electrons and positrons, and γ_s denotes their initial energy. The variable λ is defined as

$$\lambda^2(\gamma) = \int_{\gamma}^{\infty} \frac{2K(\gamma)}{b(\gamma)} d\gamma. \quad (3.13)$$

Considering the dark matter halo as a spherically-symmetric source, the spatial integral can be reduced to one dimension, and the electron-positron spectrum is finally given by the expression

$$\begin{aligned} \frac{dn}{d\gamma}(r, \gamma) &= \frac{1}{b(\gamma)} \frac{\exp\left(-\frac{r^2}{2\Delta\lambda^2}\right)}{(2\pi r^2 \Delta\lambda^2)^{1/2}} \\ &\times \left\{ \int_{\gamma}^{\infty} d\gamma_s \int_0^{\infty} dr_s r_s \exp\left(-\frac{r_s^2}{2\Delta\lambda^2}\right) \right. \\ &\times \left. \left[\exp\left(\frac{rr_s}{\Delta\lambda^2}\right) - \exp\left(-\frac{rr_s}{\Delta\lambda^2}\right) \right] Q(r_s, \gamma_s) \right\}. \end{aligned} \quad (3.14)$$

3.2.2 Loss rates

Electrons and positrons can lose their energy by several physical processes as they move through the ISM. We consider ICS of cosmic microwave background (CMB), starlight and infrared photons, synchrotron radiation, bremsstrahlung, Coulomb collisions, and ionization of neutral hydrogen atoms.

The energy loss rates depend on the energy of the particle. High-energy electrons and positrons mainly lose energy by ICS (e.g. Sarazin, 1999). The relevant loss function is

$$b_{\text{ICS}}(\gamma) = \frac{4}{3} \frac{\sigma_T}{m_e c} \gamma^2 U_{\text{rad}}, \quad (3.15)$$

where σ_T is the Thomson cross section. The combined radiation energy density of the CMB, starlight (SL), and infrared (IR) light from thermal dust emission (see e.g. Porter and Strong, 2005; Porter et al., 2008) is represented by three grey bodies,

$$U_{\text{rad}} = \frac{4\sigma_{\text{SB}}}{c} (T_{\text{CMB}}^4 + \mathcal{N}_{\text{SL}} T_{\text{SL}}^4 + \mathcal{N}_{\text{IR}} T_{\text{IR}}^4) \quad (3.16)$$

where T_i and \mathcal{N}_i represent the effective temperature and the normalization of each component, respectively, and σ_{SB} is the Stefan-Boltzmann constant. The cosmic microwave background is modeled as a perfect black body with temperature $T_{\text{CMB}} = 2.726$ K (Fixsen, 2009), and we follow Cirelli and Panci (2009) for the two other components.

Synchrotron radiation is another important loss mechanism at high energies. The expression for the loss rate is similar to that of ICS, substituting the radiation energy density in equation (3.15) by the energy density of the magnetic field, $U_B = B^2/(8\pi)$, where B is the intensity of the magnetic field:

$$b_{\text{syn}}(\gamma) = \frac{4}{3} \frac{\sigma_T}{m_e c} \gamma^2 U_B. \quad (3.17)$$

For lower-energy electrons and positrons, Coulomb interactions with the thermal plasma must be taken into account. The loss rate is approximately (Rephaeli, 1979)

$$b_{\text{Coul}}(\gamma) \approx 1.2 \times 10^{-12} n_e \left[1 + \frac{\ln(\gamma/n_e)}{75} \right] \text{ s}^{-1} \quad (3.18)$$

where n_e is the number density of thermal electrons.

Collisions with thermal ions and electrons also produce radiation through bremsstrahlung. The loss rate due to bremsstrahlung can be approximated as (Blumenthal and Gould, 1970)

$$b_{\text{brem}}(\gamma) \approx 1.51 \times 10^{-16} n_e \gamma [\ln(\gamma) + 0.36] \text{ s}^{-1}. \quad (3.19)$$

Additional energy losses come from the ionization of hydrogen atoms. This loss rate is given in Longair (1981),

$$b_{\text{ion}}(\gamma) = \frac{q_e^4 n_H}{8\pi\epsilon_0^2 m_e^2 c^3 \sqrt{1 - \frac{1}{\gamma^2}}} \times \left[\ln \frac{\gamma(\gamma^2 - 1)}{2 \left(\frac{I}{m_e c^2} \right)^2} - \left(\frac{2}{\gamma} - \frac{1}{\gamma^2} \right) \ln 2 + \frac{1}{\gamma^2} + \frac{1}{8} \left(1 - \frac{1}{\gamma} \right)^2 \right], \quad (3.20)$$

where n_H is the number density of hydrogen atoms, q_e is the electron charge, ϵ_0 is the permittivity of free space and I is the ionization energy of the hydrogen atom. The number density of thermal electrons and neutral atoms can be expressed in terms of the total ISM gas density ρ_g and the ionization fraction X_{ion} as

$$n_e = \frac{\rho_g}{m_p} X_{\text{ion}} \quad (3.21)$$

and

$$n_H = \frac{\rho_g}{m_p} (1 - X_{\text{ion}}) \quad (3.22)$$

respectively.

The contribution of the individual loss terms is plotted on the top-left panel in Figure 3.5 for $\rho_g/m_p = 1 \text{ cm}^{-3}$, $B = 6 \mu\text{G}$, $U_{\text{rad}} \approx 0.9 \text{ eV cm}^{-3}$ and $X_{\text{ion}} = 0.5$ (in order to have a non-zero contribution from Coulomb collisions and bremsstrahlung). ICS and synchrotron emission, being proportional to γ^2 , dominate at high energies, $\gamma > 10^4$. Bremsstrahlung is important in the intermediate range $10^3 < \gamma < 10^4$, and Coulomb collisions and ionization, roughly independent on γ , dominate at low energies, $\gamma < 10^3$.

The time taken by the electron-positron population to reach equilibrium is on the same order as

$$t_{\text{rest}}(\gamma_0) = \int_1^{\gamma_0} \frac{1}{b(\gamma)} d\gamma, \quad (3.23)$$

the time that the particles take to loose all their energy, shown on the top-right panel in Figure 3.5 as a function of γ_0 . Although this may be larger than the orbital time at $r \sim 500 \text{ pc}$ ($T \sim 10 \text{ Myr}$, assuming $v \sim 220 \text{ km s}^{-1}$) for $m_{\text{dm}} > 100 \text{ MeV}$, a steady state will be reached as long as the conditions (dark matter and gas densities, magnetic field, etc.) evolve on timescales longer than $\sim 100 \text{ Myr}$, which is relatively short in astrophysical terms.

The characteristic diffusion scale $\Delta\lambda$, shown on the bottom panel of Figure 3.5, depends on the Lorentz factor of the electrons and positrons. It is zero at the injection energy, and it rapidly increases for lower energies until it saturates at a maximum value that depends on E_0 .

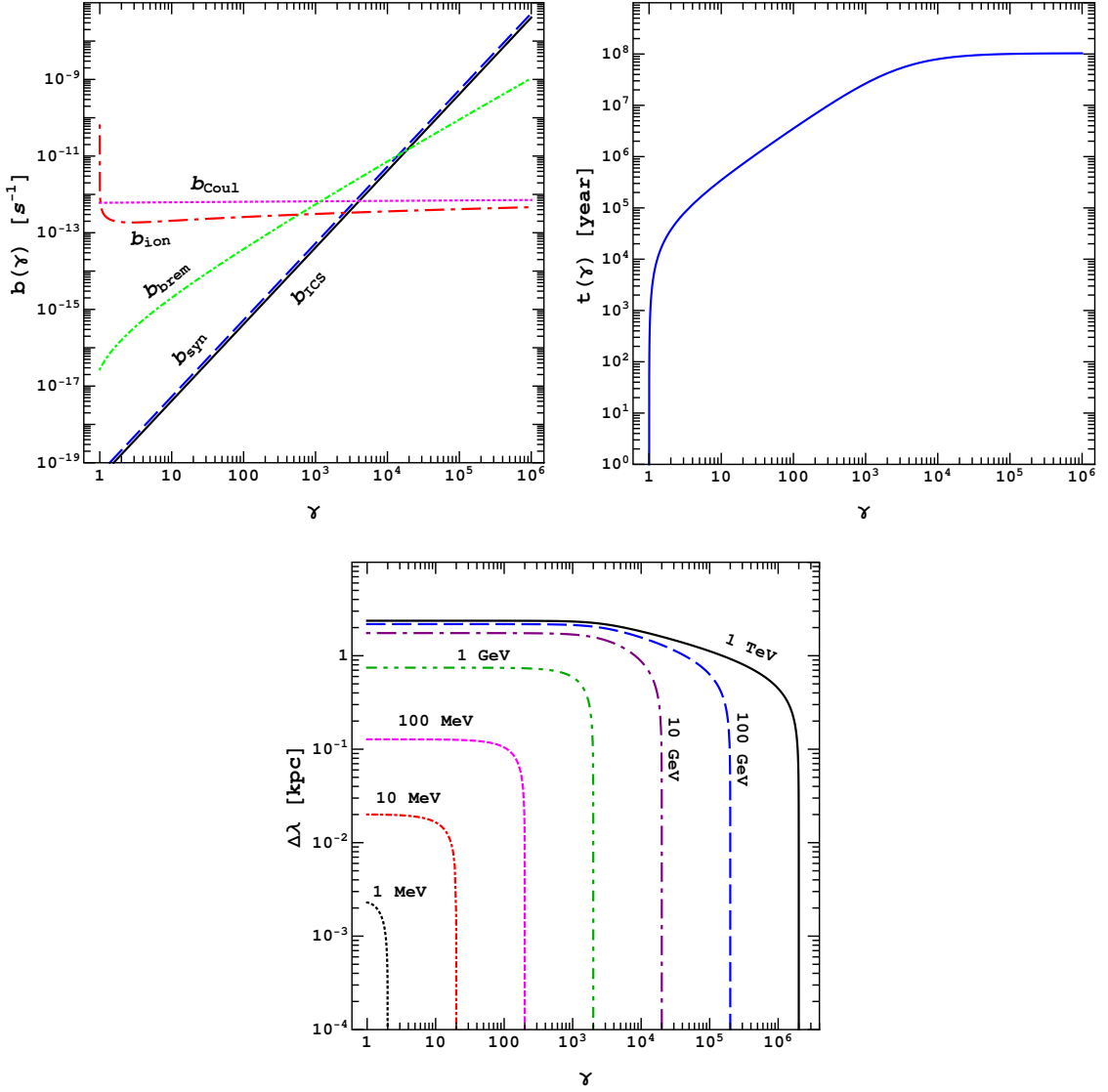


Figure 3.5: Energy losses (*top-left*), equilibrium time scales (*top-right*), and characteristic diffusion lengths (*bottom*) of electrons and positrons for $\rho_g/m_p = 1 \text{ cm}^{-3}$, $B = 6 \mu\text{G}$, $U_{\text{rad}} \approx 0.9 \text{ eV cm}^{-3}$ and $X_{\text{ion}} = 0.5$. On the top-left panel, Coulomb collisions, ionization, bremsstrahlung, synchrotron radiation, and inverse Compton scattering are represented by dotted, dot-long dashed, dot-short dashed, dashed, and solid lines, respectively (Wechakama and Ascasibar, 2011).

3.2.3 Source term

Since the electrons and positrons in our model originate from the annihilation of dark matter particles, the instantaneous production rate at any given point can be expressed as

$$Q(r, \gamma) = \eta \ n_{\text{dm}}(r) \ n_{\text{dm}^*}(r) \ \langle \sigma v \rangle_{e^\pm} \ \frac{dN_{e^\pm}}{d\gamma}(\gamma), \quad (3.24)$$

where n_{dm} and n_{dm^*} denote the number densities of dark matter particles and anti-particles, respectively, $\langle \sigma v \rangle_{e^\pm}$ is the thermal average of the annihilation cross-section times the dark matter relative velocity, and $\frac{dN_{e^\pm}}{d\gamma}$ is the injection spectrum of electrons and positrons in the final state. For self-conjugate dark matter particles, $n_{\text{dm}} = n_{\text{dm}^*} = \frac{\rho_{\text{dm}}}{m_{\text{dm}}}$ and $\eta = 1/2$ in order to avoid double counting; otherwise, $n_{\text{dm}} = n_{\text{dm}^*} = \frac{1}{2} \frac{\rho_{\text{dm}}}{m_{\text{dm}}}$ and $\eta = 1$.

We assume that each annihilation event injects one electron and one positron with roughly the same energy $\gamma_0 \sim m_{\text{dm}}/m_e$,

$$\frac{dN_{e^\pm}}{d\gamma}(\gamma) = 2 \ \delta(\gamma - \gamma_0), \quad (3.25)$$

where $\delta(\gamma - \gamma_0)$ denotes a Dirac delta function. Although this is a rather coarse approximation, it has the advantage of being model-independent. For self-conjugate dark matter particles, we obtain

$$Q(r, \gamma) = \left[\frac{\rho_{\text{dm}}(r)}{m_{\text{dm}}} \right]^2 \langle \sigma v \rangle_{e^\pm} \ \delta(\gamma - \gamma_0). \quad (3.26)$$

We consider a spherically-symmetric halo, described by a density profile of the form

$$\rho_{\text{dm}}(r) = \frac{\rho_s}{\left(\frac{r}{r_s} \right)^\alpha \left(1 + \frac{r}{r_s} \right)^{3-\alpha}}, \quad (3.27)$$

where r_s and ρ_s denote a characteristic density and radius of the halo, respectively, and α is the inner logarithmic slope of the density profile, as explained in Section 2.1.2. Local inhomogeneities that would boost the expected signal, such as small-scale clumpiness or the presence of subhaloes, are not taken into account. The shape of the dark matter density profile in the inner regions is far from being a settled question. N-body simulations suggest that, at least in the absence of baryons, the profile should be quite steep near the centre ($\alpha \sim 1$), in apparent contradiction with observations. Traditionally, it has been argued that the presence of gas and stars makes the profile even steeper due to the effects of adiabatic contraction (Blumenthal et al., 1986), although some recent claims have also been made in the opposite direction (e.g. El-Zant et al., 2001; Mashchenko et al., 2006; Oh et al., 2011a). Given the current uncertainties, we have left the inner slope of the density profile as a free parameter of the model.

3.3 Astrophysical signatures from photons

Although electrons and positrons injected from dark matter annihilations are deflected by magnetic fields, ISM and ISRF, as mentioned in Section 3.2.2, these energy loss processes also produce photons, resulting in a diffuse Galactic gamma-ray, radio and microwaves emission, that one can look for signatures of dark matter annihilation. An advantage of looking for the signatures through the photons is they are neutral and massless, they arrive at the Earth essentially undeflected and unattenuated. This allows to trace the directions

of their origins, mapping the dark matter distribution in the halo of the Milky Way as well as any other structures.

The most commonly studied dark matter signatures from photons are the emission of gamma rays from the Galactic centre (e.g. Berezinsky et al., 1994; Bergström et al., 1998; Baltz and Edsjö, 1999; Gondolo and Silk, 1999; Morselli et al., 2002; Ullio et al., 2002; Stoehr et al., 2003; Peirani et al., 2004; Prada et al., 2004; Cesarini et al., 2004; Bergström et al., 2005b,a; Profumo, 2005; Aharonian et al., 2006; Zaharijas and Hooper, 2006; Boyarsky et al., 2008a; Pospelov et al., 2008; Springel et al., 2008; Bell and Jacques, 2009; Cirelli and Panci, 2009; Fornasa et al., 2009; Bernal and Palomares-Ruiz, 2010; Abazajian et al., 2010; Cirelli et al., 2010; Papucci and Strumia, 2010; Hooper and Goodenough, 2011; Hooper and Linden, 2011a,b; Ackermann et al., 2012c, among many others), the Milky Way satellites (e.g. Baltz et al., 2000; Tyler, 2002; Baltz and Wai, 2004; Hooper and Kribs, 2004; Bergström and Hooper, 2006; Sánchez-Conde et al., 2007; Strigari et al., 2007, 2008; Wood et al., 2008; Martinez et al., 2009; Abdo et al., 2010b; Acciari et al., 2010; Essig et al., 2009, 2010; Ackermann et al., 2011; Abramowski et al., 2011c), and galaxy clusters (e.g. Colafrancesco et al., 2006; Jeltema et al., 2009; Ackermann et al., 2010b; Sánchez-Conde et al., 2011; Pinzke et al., 2011). Prospects for indirect dark matter detection in the microwave background have also been considered by several authors (e.g. Blasi et al., 2003; Colafrancesco, 2004; Padmanabhan and Finkbeiner, 2005; Mapelli et al., 2006; Zhang et al., 2006, 2007; Cholis et al., 2009c; Galli et al., 2009; Slatyer et al., 2009; Kanzaki et al., 2010; Lavalle, 2010; Hütsi et al., 2011; Galli et al., 2011; McQuinn and Zaldarriaga, 2011; Delahaye et al., 2012), as well as X-ray (e.g. Abazajian et al., 2001; Boyarsky et al., 2007, 2008b; Zavala et al., 2011), radio (e.g. Colafrancesco and Mele, 2001; Aloisio et al., 2004; LeZhang and Sigl, 2008; Bergström et al., 2009; Borriello et al., 2009; Ishiwata et al., 2009; Fornengo et al., 2012) and multi-wavelength signatures (e.g. Regis, 2008; Regis and Ullio, 2008; Bertone et al., 2009; Pato et al., 2009; Profumo and Ullio, 2010; Crocker et al., 2010).

In the following Sections, we will briefly review prospects and current status of astrophysical signatures of dark matter annihilation from gamma-rays, radio and microwaves, as we use them as tools to constrain the dark matter annihilation cross-section in Chapter 5. At the end, we will also explain the surface brightness profile that we use in our calculations.

3.3.1 Gamma-rays

As mentioned in Section 2.2.3, gamma-rays can be produced by dark matter annihilation in different physical processes. The possible contributions are prompt emission, (i.e. π^0 decays, FSR and virtual internal bremsstrahlung), and ICS of electrons and positrons interacting with the ISRF. The gamma-rays from these processes have continuous spectra with peaks at energies smaller than the mass of dark matter particles. They can also be produced directly by the annihilation or decay to $\gamma\gamma$ and γZ at loop level (although suppressed since dark matter is neutral), which provide a particular clear spectral line feature of monochromatic gamma-rays at the energy corresponding to the mass of dark matter particles.

To detect astrophysical signatures of dark matter, many observations are currently taking gamma-ray data, like large air-Čerenkov gamma-ray telescopes (e.g. H.E.S.S., MAGIC, CANGAROO and VERITAS) and the Fermi-LAT which is now taking exciting new data with an unprecedented accuracy. Dark matter indirect detection in gamma-rays have been studied in different targets, as we briefly review below.

Galactic centre

The flux of radiation produced in dark matter annihilations is proportional to the annihilation rate which depends on the square of dark matter density, $\rho_{\text{dm}}^2(r)$. Therefore the prime targets for dark matter search are the regions where dark matter density is highest. Of course, the Galactic centre is one of the best targets for detecting gamma-rays from dark matter annihilations. However, astrophysical backgrounds are also very bright close to the Galactic centre. To analyse the signals, one needs to model and subtract point sources, the diffuse Galactic emission and the extra-galactic background.

Compared to early estimates (e.g. Dodelson et al., 2008; Baltz et al., 2008), Fermi-LAT data have revealed a more complex structure of sources at the Galactic center. Although claims of excesses in the inner Galaxy have been made from outside the collaboration (Goodenough and Hooper, 2009), the Fermi-LAT collaboration analysis is in fact still in progress (see Morselli et al., 2010) and however concludes that better modeling of the galactic diffuse emission and possibly unresolved point sources is necessary before any excess can be confirmed. There are different interpretations of the gamma-ray excess at the inner Galactic region: e.g. signals from dark matter annihilation (Hooper and Linden, 2011b), standard diffuse emissions and known point sources (Boyarsky et al., 2011) and a millisecond pulsar population in the nuclear stellar cluster of the Milky Way (Abazajian, 2011).

Alternatively, in order to reduce the impact of the complex astrophysics at the Galactic center, a promising approach is to exclude the very center from the analysis. This strategy was followed, for example, to obtain the H.E.S.S. bound (Abramowski et al., 2011b) where a signal region close to the Galactic center was selected. The analysis results in the determination of upper limits on the dark matter annihilation cross-section $\langle\sigma v\rangle$. In particular, for a dark matter particle mass of ~ 1 TeV, values for $\langle\sigma v\rangle > 3 \times 10^{-25} \text{ cm}^3 \text{ s}^{-1}$ are excluded for the Einasto and NFW dark matter density profiles.

Galactic halo

Although the dark matter contribution to gamma-ray fluxes from the Galactic halo is comparatively lower than from the Galactic centre, the astrophysical backgrounds are also less strong. The spectrum from dark matter annihilation, with a sharp cut-off at the dark matter mass, is expected to be the same everywhere in the halo, and it is difficult to be explained by astrophysical backgrounds. The influence of the uncertainty of the halo profile in the inner regions is also reduced when regions around the Galactic centre or the Galactic plane are excluded.

A conservative analysis has been presented by Cirelli et al. (2010) without an attempt to subtract or fit any astrophysical backgrounds. Model-independent two-body annihilation or decay to leptonic and hadronic channels are considered. The resulting gamma-ray flux from FSR and π^0 -decay as well as from ICS of electrons and positrons are required not too exceed the Fermi-LAT measurements by more than 3σ . This gives already quite considerable constraints in the dark matter annihilation cross-section $\langle\sigma v\rangle$. The results indicate that the electron-positron excess by PAMELA and Fermi can be explained by dark matter annihilation and decay under very conservative assumptions, i.e. only models producing dominantly $\mu^+ \mu^-$ and a cored dark matter density profile with dark matter masses around 2 TeV.

With a different analysis (Dobler et al., 2010) based on template subtraction of foregrounds, an excess called the ‘Fermi haze’ is found up to $|b| \approx 40^\circ$ above the galactic centre. This is argued to be most likely due to ICS by relativistic electrons, and that the under-

lying electron distribution is compatible with the ‘WMAP haze’. However it was pointed out by Linden and Profumo (2010) that the template maps used in Dobler et al. (2010) are in fact inappropriate and underestimate both the π^0 decay and ICS contributions to the gamma-ray emission.

As shown in Figure 2.6, the Fermi collaboration (Ackermann et al., 2012c) has performed an analysis of the diffuse gamma-ray emission in the Galactic halo. Gamma-rays produced directly in the dark matter annihilation/decay and those produced by ICS of the electrons and positrons are considered. Conservative limits are derived requiring that the dark matter signal does not exceed the observed diffuse gamma-ray emission. More stringent limits are derived based on modeling the foreground astrophysical diffuse emission using the GALPROP code. The resulting limits impact the range of particle masses over which dark matter thermal production in the early Universe is possible, and challenge the interpretation of the electron-positron excesses by PAMELA and Fermi-LAT as annihilation of dark matter.

Dwarf spheroidal galaxies

Dwarf spheroidal (dSph) galaxies, particularly faint companion galaxies of the Milky Way or Andromeda, are known to be excellent targets for indirect dark matter detections since they are the most extremely dark matter dominated environments. From stellar kinematics it can be inferred that some have mass-to-light ratios of up to $\mathcal{O}(1000)$, that is many times more than in conventional types of galaxies. Furthermore, dSphs contain only little neutral or ionised gas which could otherwise contribute to its gamma-ray emission.

About 20 dSph satellites of our own Galaxy have been targeted by the main gamma-ray experiments. A recent study by the Fermi collaboration (Ackermann et al., 2011) of 10 satellite galaxies with 24 months of data does not detect any dark matter signal and sets upper limits on their gamma-ray fluxes. They can constrain the cross section for annihilation into gamma-rays by $b\bar{b}$, $\tau^+\tau^-$, as motivated from neutralino dark matter. The 95% confidence level upper limits range from about $10^{-26} \text{ cm}^3 \text{ s}^{-1}$ at 5 GeV to about $5 \times 10^{-23} \text{ cm}^3 \text{ s}^{-1}$ at 1 TeV, depending on the dark matter annihilation final state. The results rule out models with the thermal cross section ($\sim 3 \times 10^{-26} \text{ cm}^3 \text{ s}^{-1}$ for a purely s-wave cross section), without assuming additional boost factors. Geringer-Sameth and Koushiappas (2011) have presented upper limits on the dark matter annihilation cross section of WIMPs based on the joint analysis of seven Milky Way dwarfs. The results exclude generic WIMP candidates annihilating into $b\bar{b}$ with mass less than 40 GeV.

dSphs are also interesting targets for Čerenkov gamma-ray telescopes which have sensitivity to higher dark matter mass values. The recent bounds from MAGIC (Aleksić et al., 2011), H.E.S.S. (Abramowski et al., 2011a) and VERITAS (Acciari et al., 2010) should give a feeling on how far the sensitivity is from theoretically interesting values of parameters.

Line emission

Although dark matter is found to be electrically neutral and annihilation or decay to photons can therefore only occur at loop order, gamma-ray line has been suggested as a smoking gun signal for dark matter (Bergström and Snellman, 1988). Constraints on line emission have been presented using EGRET (Pullen et al., 2007) and Fermi-LAT (Abdo et al., 2010a; Ackermann et al., 2012a). However, very recently, the claim of an indication of line emission in Fermi-LAT data (Weniger, 2012; Su and Finkbeiner, 2012) has drawn considerable attention. By concentrating on energies between 20 and 300 GeV of 43 months of data and using a new data-driven technique to select optimized target

regions depending on the profile of the Galactic dark matter halo, Weniger (2012) found a 3.2σ significant excess at a mass of ~ 130 GeV. If interpreted in terms of dark matter particles annihilating into a photon pair, the observations imply a partial annihilation cross-section of $\langle\sigma v\rangle_{\chi\chi\rightarrow\gamma\gamma} \sim 10^{-27} \text{ cm}^3 \text{ s}^{-1}$ when using the Einasto dark matter profile (see also e.g. Bringmann and Weniger, 2012; Asano et al., 2012). The result is compatible with the upper limit presented in Abdo et al. (2010a) and later was confirmed by Su and Finkbeiner (2012), who even claimed a 5σ detection significance.

3.3.2 Radio and microwaves

Dark matter indirect detections by radio and microwave emission require careful subtraction of Galactic foregrounds which usually can be generated by different physical processes: i.e. free-free emission by thermal electrons of the gas in the ISM (see e.g. Finkbeiner, 2003), emission in the microwave range by dust grains vibrating in equilibrium with the surrounding radiation fields (see e.g. Schlegel et al., 1998; Draine and Lazarian, 1998; Finkbeiner et al., 1999; Dobler and Finkbeiner, 2008a), and Galactic synchrotron radiation by electrons and positrons in the Galactic magnetic field (see e.g. Hinshaw et al., 2007; Gold et al., 2009).

By using the template fitting technique and subtracting the known foregrounds, Finkbeiner (2004a) have claimed a presence of a new foreground that does not correlate spatially with any of the above processes. This residual, the so-called ‘WAMP haze’, spherically localises around the centre of the Galaxy and presents a harder spectrum (Dobler and Finkbeiner, 2008b) than synchrotron radiation by relativistic Galactic cosmic-ray electrons from standard astrophysical sources like supernova remnants. An independent analysis has confirmed the existence of the haze (Bottino et al., 2010), but others (Dickinson et al., 2009; Cumberbatch et al., 2009), including the analysis by the WMAP collaboration itself (Gold et al., 2011), do not find the significant evidence. However it was suggested later that the haze is in fact synchrotron emission from a new population of relativistic electrons and positrons, produced by dark matter annihilations (e.g. Finkbeiner, 2004b; Hooper et al., 2007; Cumberbatch et al., 2009; Linden et al., 2010). There were also attempts to describe the haze by electrons emitted by pulsars (Kaplinghat et al., 2009; Harding and Abazajian, 2010), and supernova remnants (Blasi, 2009; Ahlers et al., 2009) that would produce a less spherical haze since most pulsars and supernova remnants are in the galactic disk.

Furthermore, the ARCADE 2 collaboration reported measurements of the absolute sky temperature at a number of frequencies between 3 and 90 GHz (Fixsen et al., 2009). While these measurements are dominated by the CMB at frequencies above several GHz, they reveal the presence of significant excess power at the lowest measured frequencies (Seiffert et al., 2009) that can not easily be explained by astrophysical sources (see e.g. Singal et al., 2010; Kogut et al., 2011; Ponente et al., 2011; Vernstrom et al., 2011). This excess can be interpreted in term of dark matter annihilations (e.g. Fornengo et al., 2011; Hooper et al., 2012).

In general, conservative constraints on dark matter annihilation or decay can be derived by imposing that the possible contribution from dark matter does not exceed the observed signals in radio and microwaves (e.g. Borriello et al., 2009; LeZhang et al., 2009).

3.3.3 Surface brightness profile

It is one of our aims to look for photons produced by energetic electrons and positrons through three different processes:

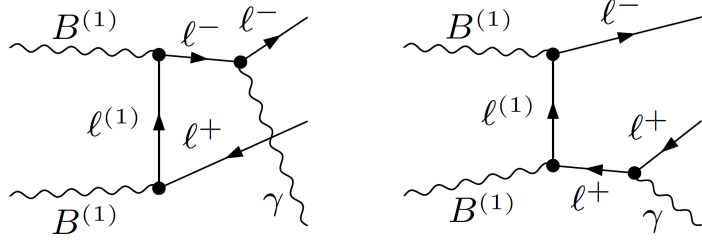


Figure 3.6: The tree level Feynmann diagrams which contribute to the process $B^{(1)}B^{(1)} \rightarrow l^+l^-\gamma$. The γ -particles are radiated by l^- or l^+ at the final states of annihilations. Figures are from Bergström et al. (2005a)

- I) **Final-state radiation (FSR):** γ -particles in the energy range of MeV to multi-TeV are radiated by the charged particles that are produced in the final states of annihilations. This process becomes particularly important for a sizable branching ratio into electron-positron pairs, as in the case of MeV dark matter (e.g. Beacom et al., 2005) or Kaluza-Klein inspired models (e.g. Bergström et al., 2005a). The spectra can be computed in a model independent way, since all one needs to know is the pair of primary standard model particles (Cirelli et al., 2011). An example of FSR is illustrated in Figure 3.6 which contribute to the process $B^{(1)}B^{(1)} \rightarrow l^+l^-\gamma$ (Bergström et al., 2005a). The γ -particles are radiated by l^- or l^+ at the very moment of lepton pair creation.
- II) **Inverse Compton scattering (ICS):** γ -particles can be indirectly produced by the inverse Compton scattering of the energetic electrons and positrons, created in the dark matter annihilation, onto the Galactic ISRF such as the CMB, the galactic star light and the infrared photons from thermal dust emission. Typically, they cover a wide range of energies from energies of a fraction of the dark matter mass to almost up to the dark matter mass itself. The γ -ray flux depends on the densities of the electrons and positrons which originate from dark matter and then diffuse out in the whole galactic halo. The ICS is very important for dark matter species which annihilate into charged leptons.
- III) **Synchrotron radiation:** Another signature of dark matter annihilation can be the synchrotron radiation originating from the propagation of electrons and positrons produced by dark matter annihilations in the Galactic magnetic field. The radiation in the range of MHz to GHz, e.g. radio and microwave band, can be emitted in the magnetic field of the Galaxy by the electrons and positrons of GeV to TeV energies. The most interesting target of choice is at the Galactic centre where most of the annihilation signal comes from and the magnetic field is highest.

The photon signals from dark matter annihilation can be investigated by the surface brightness profile of the different processes. For ICS and synchrotron radiation, once the electron-positron spectrum is computed, the emission coefficient¹ for photons of frequency ν is given by the integral

$$\epsilon_\nu(r, \nu) = \frac{1}{4\pi} \int_1^\infty \frac{dn}{d\gamma}(r, \gamma) j(\gamma, \nu) d\gamma, \quad (3.28)$$

¹Energy radiated per unit volume per unit frequency per unit time per unit solid angle.

of the electron-positron spectrum $\frac{dn}{d\gamma}(r, \gamma)$ times the specific luminosity $j(\gamma, \nu)$ emitted at frequency ν by a single electron or positron with Lorentz factor γ . The intensity from any given direction in the sky is simply the integral along the line of sight of the emission coefficient. Since we assume a spherically-symmetric source and boundary conditions, it will only depend on the angular separation θ with respect to the Galactic centre,

$$I_\nu(\theta, \nu) = \int_0^\infty \epsilon(r, \nu) \, ds, \quad (3.29)$$

where s represents the distance along the line of sight, and the radial distance r to the centre of the Milky Way at any point along the ray is

$$r = \sqrt{x^2 + y^2}, \quad (3.30)$$

with $x = s \sin \theta$, $y = s \cos \theta - R_\odot$, and $R_\odot = 8.5$ kpc (the distance from the Sun to the Galactic centre).

The contribution of synchrotron radiation, which dominates at low photon energies, can be estimated as (see e.g. Sarazin, 1999)

$$j_{\text{syn}}(\gamma, \nu) = \frac{\sqrt{3} q_e^3 B}{m_e c^2} R[\chi(\gamma)], \quad (3.31)$$

where m_e and q_e denote the electron mass and charge, respectively, B is the intensity of the magnetic field, and the function $R(\chi)$ is defined as (e.g. Ghisellini et al., 1988)

$$R(\chi) \equiv 2\chi^2 \left[K_{\frac{4}{3}}(\chi) K_{\frac{1}{3}}(\chi) - \frac{3}{5} \chi \left\{ K_{\frac{4}{3}}^2(\chi) - K_{\frac{1}{3}}^2(\chi) \right\} \right]. \quad (3.32)$$

In this expression, K refers to the modified Bessel function, and the normalized frequency

$$\chi \equiv \frac{\nu}{3\gamma^2 \nu_c} \quad (3.33)$$

is expressed in terms of the cyclotron frequency

$$\nu_c \equiv \frac{q_e B}{2\pi m_e c}. \quad (3.34)$$

At high photon energies (i.e. gamma rays), we consider the contributions of inverse Compton scattering and final-state radiation. For ICS (see e.g. Blumenthal and Gould, 1970)

$$j_{\text{ICS}}(\gamma, \nu) = \frac{3\sigma_{\text{TC}}}{4\gamma^2} \int_0^\infty \frac{n(\nu_0)}{\nu_0} \mathcal{F}(\Gamma, q) \, d\nu_0, \quad (3.35)$$

where $n(\nu_0)$ is the photon number density of the interstellar radiation field being scattered, which we represented as the sum of three grey bodies

$$n(\nu_0) = \frac{8\pi\nu_0^2}{c^3} \left[\frac{1}{\exp(h\nu_0/kT_{\text{CMB}}) - 1} + \frac{\mathcal{N}_{\text{SL}}}{\exp(h\nu_0/kT_{\text{SL}}) - 1} + \frac{\mathcal{N}_{\text{IR}}}{\exp(h\nu_0/kT_{\text{IR}}) - 1} \right] \quad (3.36)$$

and

$$\begin{aligned} \mathcal{F}(\Gamma, q) \equiv & 2q \ln q + (1+2q)(1-q) + \frac{(\Gamma q)^2 (1-q)}{2(1+\Gamma q)} \\ & \times \Theta(q - \frac{1}{4\gamma^2}) \Theta(1-q) \end{aligned} \quad (3.37)$$

with $\Gamma \equiv \frac{4\gamma h\nu_0}{m_e c^2}$, $\Gamma q \equiv \frac{h\nu}{\gamma_e c^2 - h\nu}$, σ_T the Thomson cross-section, h the Planck constant, k the Boltzmann constant, and the product of Heaviside functions ensures that only kinematically-allowed collisions $\frac{1}{4\gamma^2} \leq q \leq 1$ are taken into account.

For FSR, the emission coefficient for photons of frequency ν is given by

$$\epsilon_\nu(r, \nu) = \frac{h\nu}{4\pi} \left[\frac{\rho_{\text{dm}}(r)}{m_{\text{dm}}} \right]^2 \frac{d\langle\sigma v\rangle_{\text{FSR}}}{d\nu}. \quad (3.38)$$

with each annihilation event yielding a photon spectrum given by

$$\frac{d\langle\sigma v\rangle_{\text{FSR}}}{d\nu} = \langle\sigma v\rangle_{e^\pm} \frac{\alpha}{\pi} \frac{\kappa^2 - 2\kappa + 2}{\nu} \ln \left[\left(\frac{2m_{\text{dm}}}{m_e} \right)^2 (1 - \kappa) \right] \quad (3.39)$$

where α is the fine-structure constant and $\kappa = h\nu/m_{\text{dm}}c^2$ (see e.g. Peskin and Schroeder, 1995).

Chapter

4

PRESSURE FROM DARK MATTER ANNIHILATION

While rotation curves provided one of the first and most important pieces of evidence for the existence of dark matter (see e.g. Sofue and Rubin, 2001, and references therein), their shape in the inner regions of gas-rich dwarf and low surface brightness (LSB) spiral galaxies is one of the outstanding issues in modern cosmology (see e.g. de Blok, 2010, for a recent discussion). As was discussed in Section 2.1.2 observed rotation curves are found to rise approximately linearly with radius, consistent with a constant density core in the dark matter distribution rather than the steep power law predicted by cosmological N-body simulations, and several modifications to the standard cold dark matter scenario have been proposed in order to explain the so-called “cusp-core” discrepancy.

In the present Chapter, we investigate the contribution of dark matter annihilation to the total gas pressure and consider the possibility that it has a significant effect on the rotation curve of spiral galaxies (Wechakama and Ascasibar, 2011). It is our aim to show that, depending on the model parameters, the contribution of the pressure associated to the electrons and positrons from dark matter annihilation, hereafter referred to as “dark matter pressure”, to the rotation curve may not be negligible. The dark matter pressure, and its results for the canonical Milky Way model and the role of each astrophysical parameter (gas density and ionization fraction of the interstellar medium, intensity of the magnetic field, and dark matter density profile) are discussed in detail in Section 4.1. The effect on the rotation curve for the canonical Milky Way model and low surface brightness galaxies are investigated in Section 4.2. Our main conclusions are summarized in Section 4.3.

4.1 Dark matter pressure

The pressure associated to electrons and positrons arising from dark matter annihilations, i.e. dark matter pressure, can be expressed as

$$P_{\text{dm}}(r) = \frac{m_e c^2}{3} \int_1^\infty \frac{dn}{d\gamma}(r, \gamma) \left(\frac{\gamma^2 - 1}{\gamma} \right) d\gamma, \quad (4.1)$$

where m_e denotes the rest mass of electron, c is the speed of light, and the electron-positron spectrum $\frac{dn}{d\gamma}(r, \gamma)$, determined in equation 3.14, is the number density of particles with

Lorentz factor γ at a radius r from the centre of the dark matter halo. The pressure gradient induces an acceleration

$$a_{\text{dm}}(r) = -\frac{1}{\rho_g(r)} \frac{dP_{\text{dm}}(r)}{dr}, \quad (4.2)$$

where $\rho_g(r)$ is the gas density at radius r , that opposes the gravitational pull towards the centre, affecting observable quantities such as the circular velocity

$$v_c(r) = \sqrt{\frac{GM(r)}{r} + \frac{r}{\rho_g(r)} \frac{dP_{\text{dm}}(r)}{dr}} \quad (4.3)$$

that is measured by the rotation curve.

4.1.1 The injection energy

To calculate the electron-positron spectrum $\frac{dn}{d\gamma}(r, \gamma)$ we used equation 3.14. We consider the injection energy as a free parameter and investigate values of the initial Lorentz factor γ_0 between 2 and 2×10^6 , corresponding to energies $E_0 = \gamma_0 m_e c^2$ from about 1 MeV to 1 TeV. On the other hand, the production rate Q_0 in the solar neighbourhood is strongly constrained by different Galactic observations. At high energies, we consider observations of the local electron-positron spectrum by H.E.S.S. and the Large Area Telescope (LAT) on board the Fermi satellite (Aharonian et al., 2008; Abdo et al., 2009). More specifically, the predicted amount of electrons and positrons cannot exceed the observed values for *any* Lorentz factor γ . Given the energy dependence of the observed spectrum, $[\frac{dn}{dE}]_{\text{obs}} \sim E^{-3}$, and the energy losses, $b(E) \sim E^2$, the most restrictive constraint comes from the spectrum near the injection energy, where propagation can be safely neglected and $[\frac{dn}{dE}]_{\text{model}} \approx \frac{Q_0}{b} \propto E^{-2}$. The maximum production rate allowed by the data can then be expressed as

$$Q_0(r_\odot) < b(\gamma_0) \left[\frac{dn}{dE} \right]_{\text{obs}}(\gamma_0). \quad (4.4)$$

Another, completely independent upper limit, valid at all energies, can be obtained from the observed intensity of the 511 keV line that measures the positron annihilation rate at the Galactic centre. In order to fully explain the line with dark matter annihilations, it is necessary that (Ascasibar et al., 2006)

$$\frac{\langle \sigma v \rangle_{511}}{2.6 \times 10^{-30} \text{ cm}^3 \text{ s}^{-1}} = \left(\frac{m_{\text{dm}} c^2}{1 \text{ MeV}} \right)^2, \quad (4.5)$$

so one just has

$$Q_0(r_\odot) < \left[\frac{\rho_{\text{dm}}(r_\odot)}{m_{\text{dm}}} \right]^2 \langle \sigma v \rangle_{511} \quad (4.6)$$

in order not to overproduce the observed signal.

The corresponding exclusion regions are shown in Figure 4.1, together with the production rates used in our calculation at the position of the Sun, $r_\odot = 8.5$ kpc. These conditions constitute strict upper limits, since astrophysical sources will also contribute to the relativistic particle budget, but the annihilation cross-sections they imply are comparable to or larger than the ones required to explain the cosmic dark matter density in equation 2.8.

Therefore, we have set the injection rate according to equation (4.6) for $m_{\text{dm}} c^2 \leq 100$ MeV, while a cross-section compatible with the relic density constraint, $\langle \sigma v \rangle_{e^\pm} =$

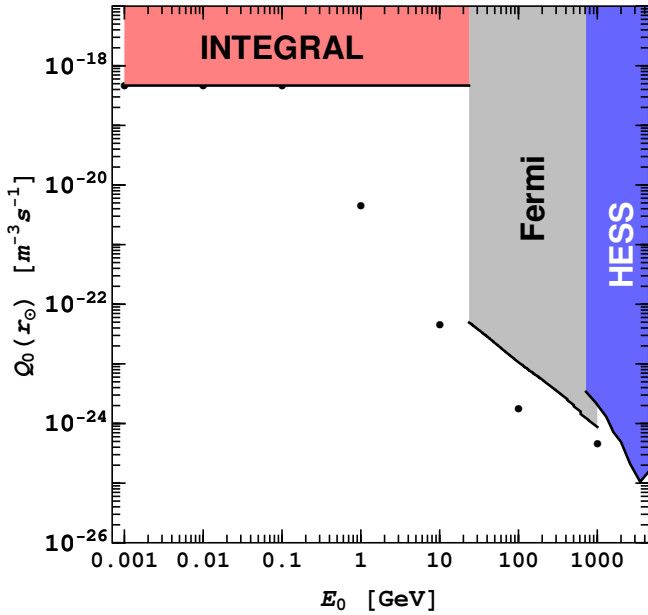


Figure 4.1: Exclusion regions and production rates at the position of the Sun: black dots are the adopted values of the instantaneous production rate Q_0 (see Table 4.1). Shaded regions above the black lines are excluded by INTEGRAL, Fermi and H.E.S.S. data.

$5 \times 10^{-26} \text{ cm}^3 \text{ s}^{-1}$, has been assumed for $100 \text{ MeV} \leq m_{\text{dm}} c^2 \leq 10 \text{ GeV}$, and slightly larger values (based on the positron excess observed by PAMELA; Adriani et al., 2009a) have been used for $m_{\text{dm}} c^2 \approx 100 \text{ GeV}$ and 1 TeV . Numeric values are given in Table 4.1.

Apart from the initial energy and injection rate of the electron-positron pairs, related to the nature of the dark matter particle, there are many astrophysical parameters that determine the contribution of dark matter annihilation to the total gas pressure. We will first define a canonical model based on observations of the Milky Way and then investigate the effect of each individual component by varying the values of the adopted parameters one by one. In all cases, we calculate the electron-positron spectrum as described in the previous Chapter, and then estimate the dark matter pressure according to expression (4.1).

γ_0	$E_0 \text{ [GeV]}$	$\langle \sigma v \rangle_{e^\pm} \text{ [cm}^3 \text{ s}^{-1}\text{]}$	$Q_0(r_\odot) \text{ [m}^{-3} \text{ s}^{-1}\text{]}$
2×10^0	1.022×10^{-3}	5×10^{-30}	4.7×10^{-19}
2×10^1	1.022×10^{-2}	5×10^{-28}	4.7×10^{-19}
2×10^2	1.022×10^{-1}	5×10^{-26}	4.7×10^{-19}
2×10^3	1.022×10^0	5×10^{-26}	4.7×10^{-21}
2×10^4	1.022×10^1	5×10^{-26}	4.7×10^{-23}
2×10^5	1.022×10^2	2×10^{-25}	1.8×10^{-24}
2×10^6	1.022×10^3	5×10^{-24}	4.7×10^{-25}

Table 4.1: Initial Lorentz factors, energies, cross-sections and production rates at the position of the Sun used in our calculations.

4.1.2 Results for the canonical Milky Way model

Our canonical model assumes a dark matter density profile with $\alpha = 1$ (Navarro et al., 1997), $r_s = 17$ kpc and $\rho_s = 6 \times 10^{-22}$ kg m $^{-3}$, consistent with dynamical models of the Milky Way (e.g. Dehnen and Binney, 1998; Klypin et al., 2002). The virial mass of the Galaxy is thus 10^{12} M $_{\odot}$, and the local dark matter density is $\rho_{\text{dm}}(r_{\odot}) c^2 = 0.3$ GeV cm $^{-3}$. The ISM is mainly composed by neutral hydrogen atoms ($X_{\text{ion}} = 0$) with number density $\rho_g/m_p \sim 1$ cm $^{-3}$ (Dehnen and Binney, 1998; Ferrière, 2001; Robin et al., 2003), and it is permeated by a uniform, tangled magnetic field whose intensity is $B \sim 6$ μ G throughout the Galaxy (Ferrière, 2001; Beck, 2001; Ascasibar and Díaz, 2010). For the radiation energy density in equation 3.15, we consider the CMB, starlight and thermal dust emission with $U_{\text{rad}} \approx 0.9$ eV cm $^{-3}$ (see e.g. Porter and Strong, 2005).

The steady-state electron-positron spectrum at the position of the Sun, $r_{\odot} = 8.5$ kpc, is shown on the top panel in Figure 4.2 for different values of the initial energy E_0 . As stated above, all of the electrons and positrons are generated with the same γ_0 , according to Table 4.1. Propagation through the Galaxy and energy losses are accounted for by equation (3.14). The shape of the resulting spectrum is determined by the value of γ_0 , the production rate $Q_0(r)$, the loss rates $b(\gamma)$ implied by the values of ρ_g , B , and X_{ion} , and the diffusion coefficient $K(\gamma)$. Nevertheless, some insight may be gained by neglecting diffusion. For $K_0 = 0$,

$$\frac{dn}{d\gamma}(r_{\odot}, \gamma) = \frac{Q_0(r_{\odot})}{b(\gamma)}; \quad (4.7)$$

the electron-positron spectrum is almost flat when ionization dominates the energy losses, and there is a transition at $\gamma \sim 10^3$ ($E \sim 1$ GeV) to the ICS-synchrotron regime, where $\frac{dn}{d\gamma} \propto \gamma^{-2}$. For low injection energies (1 MeV to 100 MeV), the normalizations of the spectra are identical because the value of Q_0 is only constrained by the INTEGRAL data, whereas other constraints impose lower values at higher energies (see Figure 4.1). In all cases, the spectra are cut at the injection energy γ_0 since no acceleration mechanism is included in our model.

The electron-positron spectrum closer to the centre of the Galaxy ($r = 10$ pc) is shown on the bottom panel in Figure 4.2. In general terms, the overall normalizations are higher than at the position of the Sun because of the higher dark matter density, and there is a sharp spectral feature near E_0 . The characteristic diffusion scale $\Delta\lambda$ plays an important role in both cases. As can be seen on the bottom panel of Figure 3.5, $\Delta\lambda$ depends on the Lorentz factor of the electrons and positrons. It is zero at the injection value, and it rapidly increases for lower energies until it saturates at a maximum value that depends on E_0 . The spectrum at a given γ probes the effective value of the production rate $Q(r)$, averaged over the diffusion scale. This is not very relevant at the position of the Sun because the dark matter density does not vary much on kpc scales, but it becomes more important as one moves towards the central density cusp. For $\gamma \ll \gamma_0$, $\Delta\lambda$, and thus the effective production rate, is independent on γ . The larger E_0 , the larger the smoothing scale, and therefore the smaller the average density and the contrast with respect to the normalization at 8.5 kpc. As long as $\Delta\lambda$ is constant, the shape of the spectrum remains the same, flat for low Lorentz factors and proportional to γ^{-2} in the inverse Compton regime. Near the injection energy, $\Delta\lambda$ becomes very small, the effective production rate approaches the local source term $Q_0(r)$, much higher than the smoothed value, and the spectrum rises steeply just before the cutoff.

Finally, the contribution of dark matter annihilations to the gas pressure at a given radius can be obtained by substituting the electron-positron spectrum in equation (4.1). Results for different values of γ_0 compared with gas and magnetic pressure in the galaxy

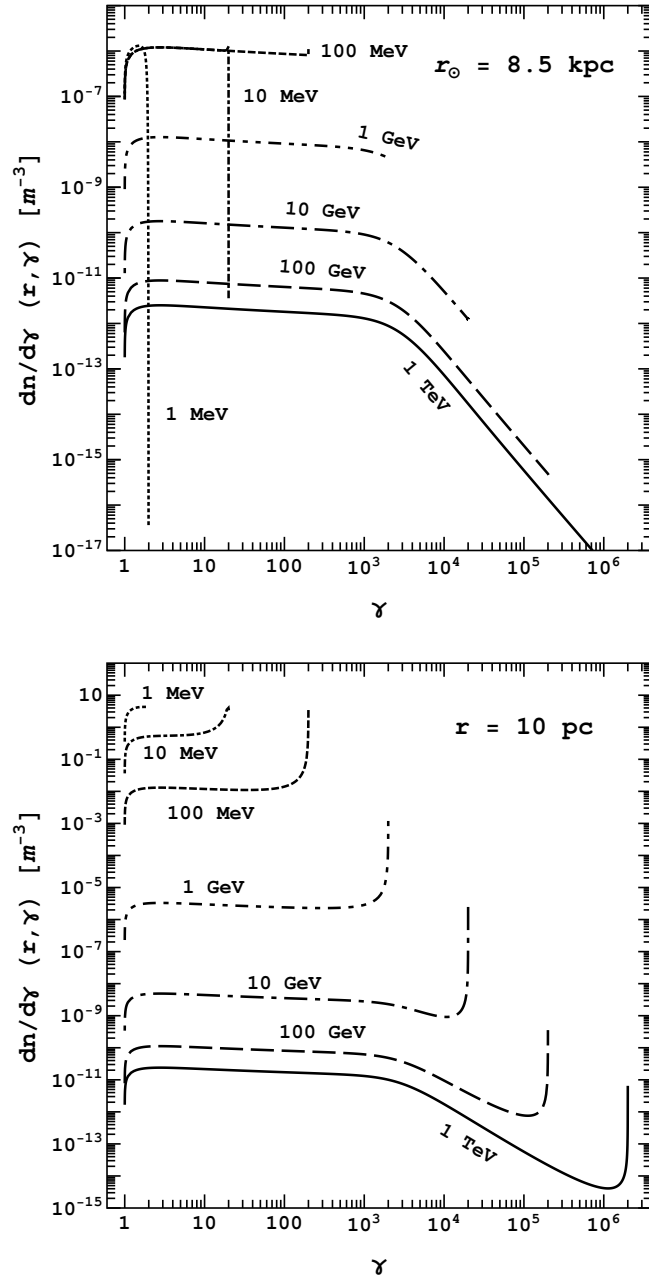


Figure 4.2: Electron-positron spectrum at the position of the Sun (*top*) and at $r = 10$ pc (*bottom*) for our canonical model of the Milky Way and different values of the injection energy E_0 .

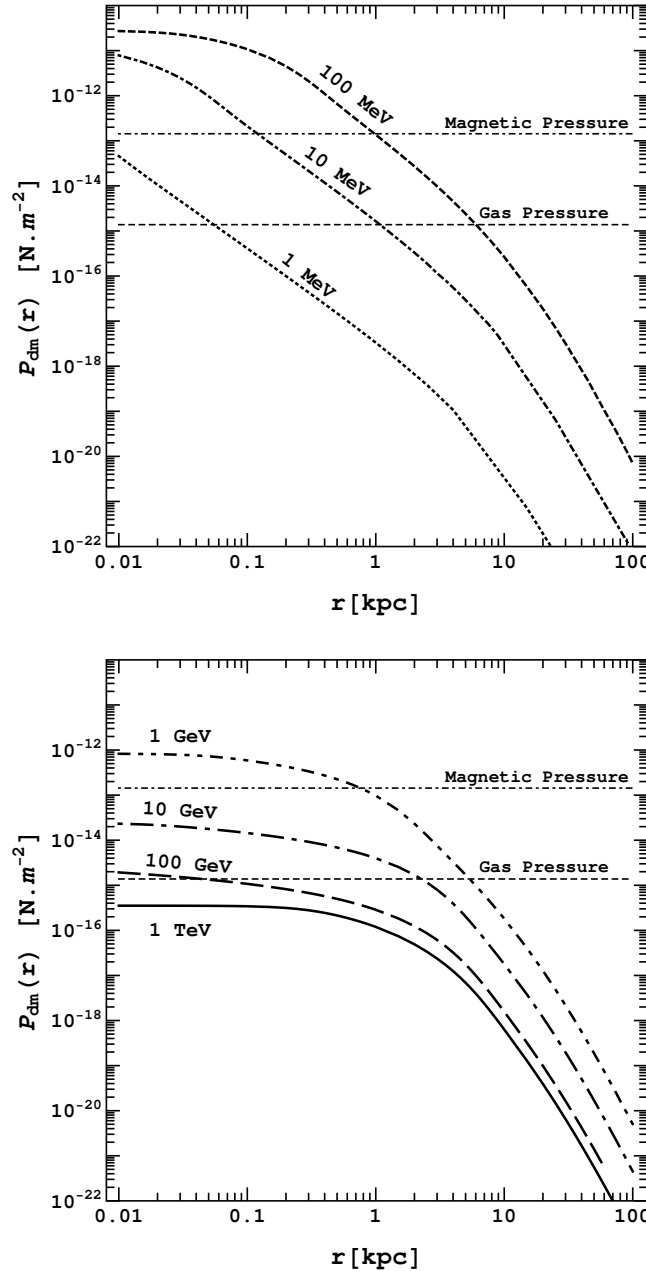


Figure 4.3: Dark matter pressure as a function of radius in our canonical model compared with gas and magnetic pressure.

are presented in Figure 4.3, compared to the thermal pressure of the gas $P_{\text{gas}} = nkT$ (where $n = \rho_g/m_p = 1 \text{ cm}^{-3}$ is the gas density, k is the Boltzmann constant, and we have assumed a temperature $T = 100 \text{ K}$, appropriate for the neutral gas in the Galactic disk) and the magnetic pressure $P_{\text{mag}} = B^2/8\pi$, with $B = 6 \mu\text{G}$.

For low injection energies, the pressure decreases sharply with distance from the Galactic centre. For $E_0 > 1 \text{ GeV}$, diffusion keeps the electron-positron spectrum (and the ensuing pressure) roughly constant within a radius of a few kpc. The highest values of the dark matter pressure are found for an initial energy $E_0 = 100 \text{ MeV}$. Although the spectra for $E_0 = 1$ and 10 MeV are similar (approximately constant up to the cutoff at γ_0 , because they are always dominated by ionization losses) and have a higher normalization near the centre, the smaller upper limits of the integral in (4.1) yield significantly lower pressures. At high ($E_0 \geq 1 \text{ GeV}$) injection energies, the dark matter pressure is also lower, due to the smaller number density of dark matter particles. The dark matter pressure at the Galactic centre is higher than the gas pressure for all values of the initial energy $E_0 < 1 \text{ TeV}$. For $E_0 = 10 \text{ MeV} - 1 \text{ GeV}$, the dark matter pressure is even higher than the pressure from magnetic fields.

4.1.3 Effect of the astrophysical parameters

We will now discuss the effect of the various astrophysical parameters that enter our calculation of the dark matter pressure, namely the intensity of the magnetic field, the density and ionization fraction of the ISM gas, and the inner slope of the dark matter density profile. As we did for the canonical model, we will compare the results obtained for different initial energies E_0 from $\sim 1 \text{ MeV}$ to 1 TeV and vary each of the astrophysical parameters in turn in order to assess how much they influence the results.

Magnetic fields affect the high-energy ($\gamma > 10^3$) tail of the electron-positron spectrum by setting the energy losses due to synchrotron radiation. As can be seen in Figure 3.5, in our canonical model with $B = 6 \mu\text{G}$, the synchrotron term in equation (3.17) is responsible for about 50 per cent of the energy loss at high energies, with ICS being responsible for most of the other 50 per cent. At low energies, energy losses are dominated by ionization of neutral hydrogen, and the contribution of synchrotron emission is negligible. The effect of varying B from 1 to $10 \mu\text{G}$ is plotted on the top panel in Figure 4.4. Not surprisingly, the results for an initial energy $E_0 < 1 \text{ GeV}$ are largely unaffected. At higher energies, the pressure at large radii decreases with the magnetic field intensity because of the more rapid energy losses. However, the diffusion length becomes shorter, increasing the effective production rate and yielding a larger pressure near the centre of the Galaxy.

As explained in Section 3.2.2, the density of the ISM gas and the ionization fraction X_{ion} regulate the energy losses by Coulomb interactions, bremsstrahlung, and ionization. For $X_{\text{ion}} = 0$ (our canonical model), the ISM gas is entirely composed of neutral hydrogen atoms, and the energy loss of the electrons and positrons with $\gamma < 10^3$ is dominated by the ionization process. At the other extreme, $X_{\text{ion}} = 1$, the ISM is already fully ionized, and the relevant energy losses are Coulomb collisions and bremsstrahlung. Since the total loss by these processes is higher than the loss by ionization, the maximum pressure happens when $X_{\text{ion}} = 0$ (mid panel of Figure 4.4). The effect of changing the gas density from 0.1 to 10 cm^{-3} is shown on the bottom panel. Higher densities yield lower dark matter pressures, simply because the energy losses are faster.

Finally, we calculate the dependence of dark matter pressure on the inner logarithmic slope α of the dark matter density profile. When varying α , we also modify the characteristic density and radius in expression (3.27) so that the dark matter density at the solar radius is equal to 0.3 GeV cm^{-3} and the virial mass of the Galaxy is 10^{12} M_\odot . The

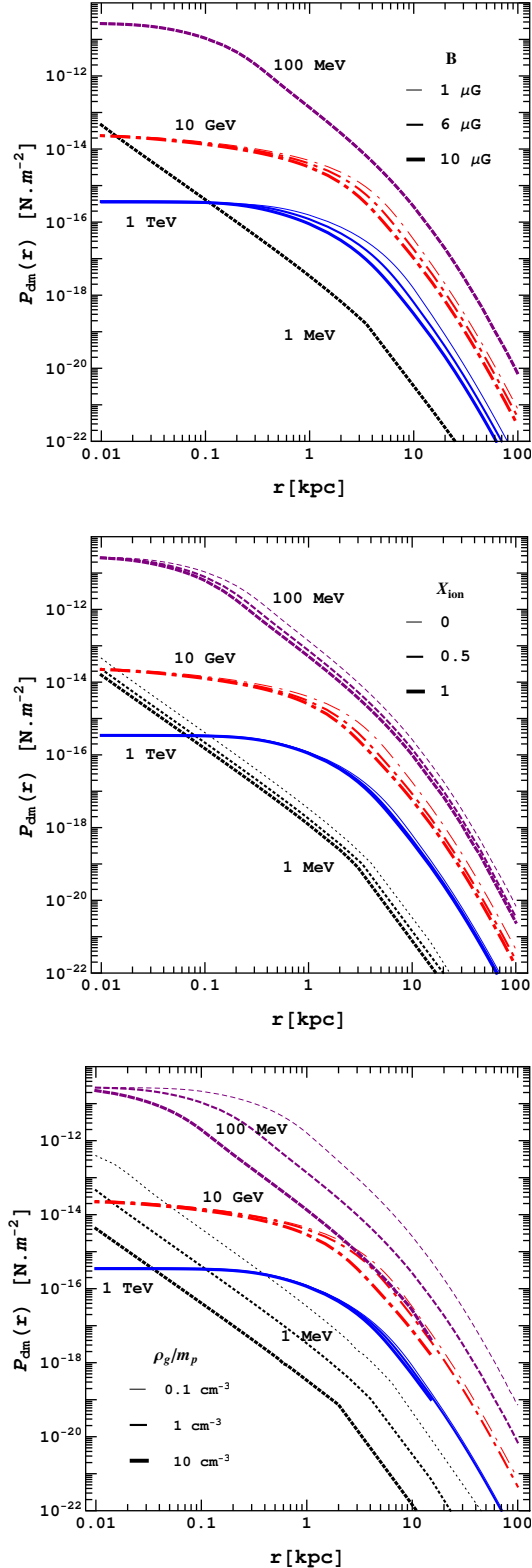


Figure 4.4: Effect of varying the magnetic field intensity B from 1 to $10 \mu\text{G}$ (top), the ionization fraction X_{ion} from 0 to 1 (middle), and the ISM gas density from $\rho_g/m_p = 0.1$ to 10 cm^{-3} (bottom). The pressure profiles for $E_0 = 1 \text{ MeV}$, 100 MeV , 10 GeV , and 1 TeV are represented by dotted, dashed, dot-dashed, and solid lines, respectively.

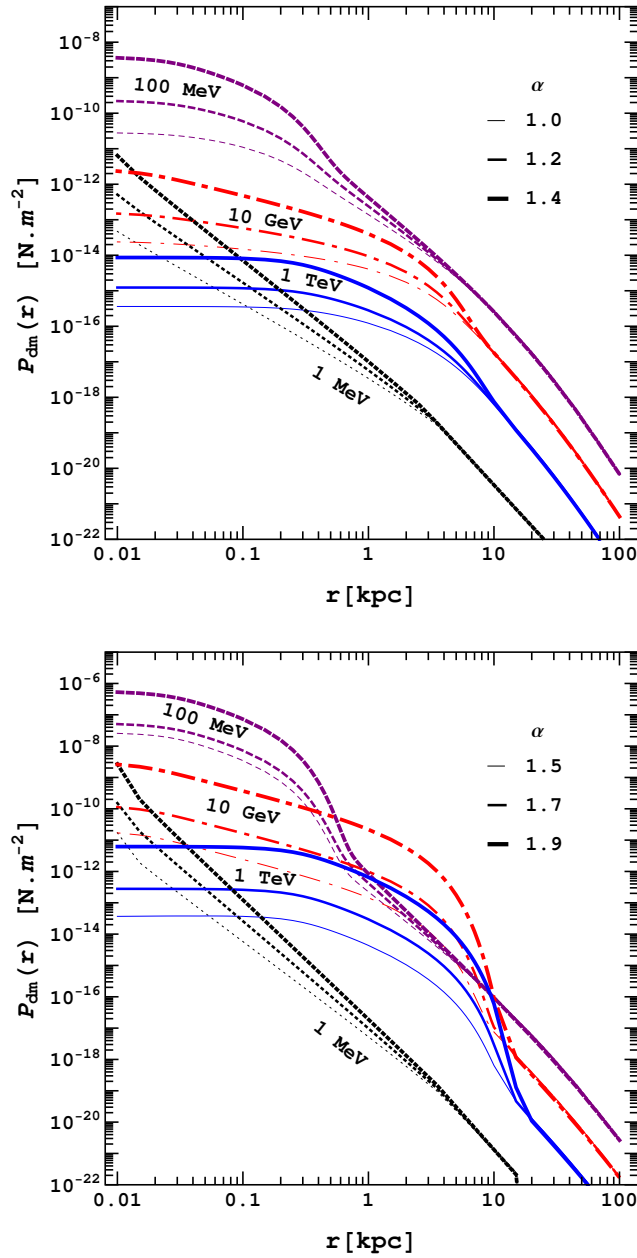


Figure 4.5: Dark matter pressure for different values of E_0 and the inner logarithmic slope α of the dark matter density profile.

α	$\rho_s c^2$ [GeV cm $^{-3}$]	r_s [kpc]
0.00	2.346	8.64
0.20	1.737	9.56
0.50	1.042	11.41
0.70	0.702	13.08
1.00	0.349	16.67
1.20	0.197	20.33
1.25	0.169	21.49
1.40	0.099	25.88
1.50	0.066	29.81
1.70	0.025	42.57
1.90	0.006	70.30
Einasto	0.17	20.00

Table 4.2: Characteristic density and radius of the dark matter density profile (3.27) as a function of its asymptotic logarithmic inner slope α .

appropriate values of ρ_s and r_s are quoted in Table 4.2 for several values of the inner slope. For $\alpha \geq 1.5$, the production rate Q_0 in equation (3.26) diverges rapidly at $r = 0$, so we add a cutoff based on the local annihilation rate $\Gamma(r)$,

$$Q_0(r) = \left[\frac{\rho_{\text{dm}}(r) \exp(-t_0 \Gamma(r))}{m_{\text{dm}}} \right]^2 \langle \sigma v \rangle_{e^\pm} \quad (4.8)$$

where $t_0 = 13.7$ Gyr is the age of the Universe and $\Gamma(r) = \frac{\rho_{\text{dm}}(r)}{m_{\text{dm}}} \langle \sigma v \rangle_{e^\pm}$.

The dark matter pressure profiles obtained for $\alpha = 1, 1.2, 1.4, 1.5, 1.7$ and 1.9 are compared in Figure 4.5. Since the central dark matter density increases dramatically with the value of the inner logarithmic slope, this is, by far, the most relevant astrophysical parameter, only second in importance to the injection energy E_0 which is related to the mass (and the precise nature) of the dark matter particle.

4.2 Rotation curves

4.2.1 Results for the Milky Way model

The gradient of the dark matter pressure induces an acceleration on the baryonic component that opposes the gravitational force. This acceleration, given by expression (4.2), is plotted in Figure 4.6 for all the injection energies considered in this work and compared to the gravitational acceleration $g(r) = GM(r)/r^2$ (represented by a thick solid black line). Each panel corresponds to a different value of the inner logarithmic slope of the dark matter density profile. For our canonical model with $\alpha = 1$, $g(r) \approx 2\pi G \rho_s r_s = 1.3 \times 10^{-10}$ m s $^{-1}$ in the innermost regions, whereas in the general case described by equation (3.27) gravity scales as $g(r) \propto r^{1-\alpha}$ for $r \ll r_s$.

Depending on the model parameters, the acceleration caused by the electron-positron gas may be comparable to (or even higher than) the gravitational one in the central parts of the halo. For our canonical model (top panel of Figure 4.6), the pressure gradient is strong enough to overcome gravity for $E_0 < 1$ GeV, and the radius at which both forces balance each other is of the order of 100 pc. The effect of dark matter annihilation is weaker, but

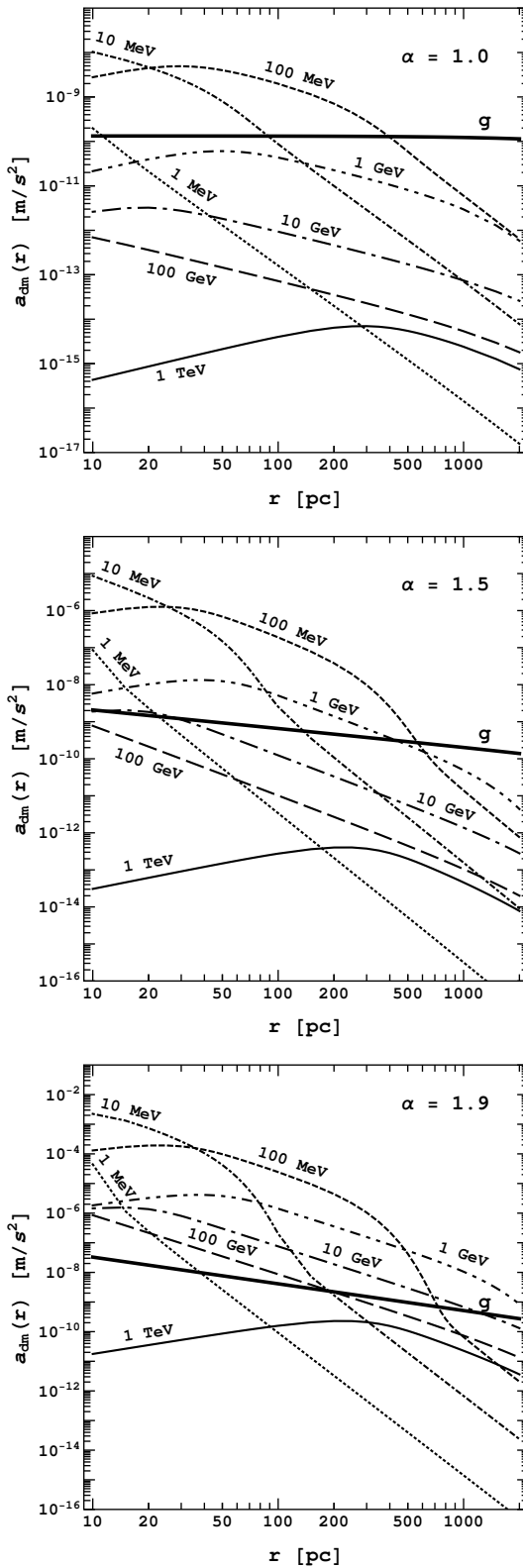


Figure 4.6: Dark matter acceleration for different values of the injection energy E_0 and the inner logarithmic slope α .

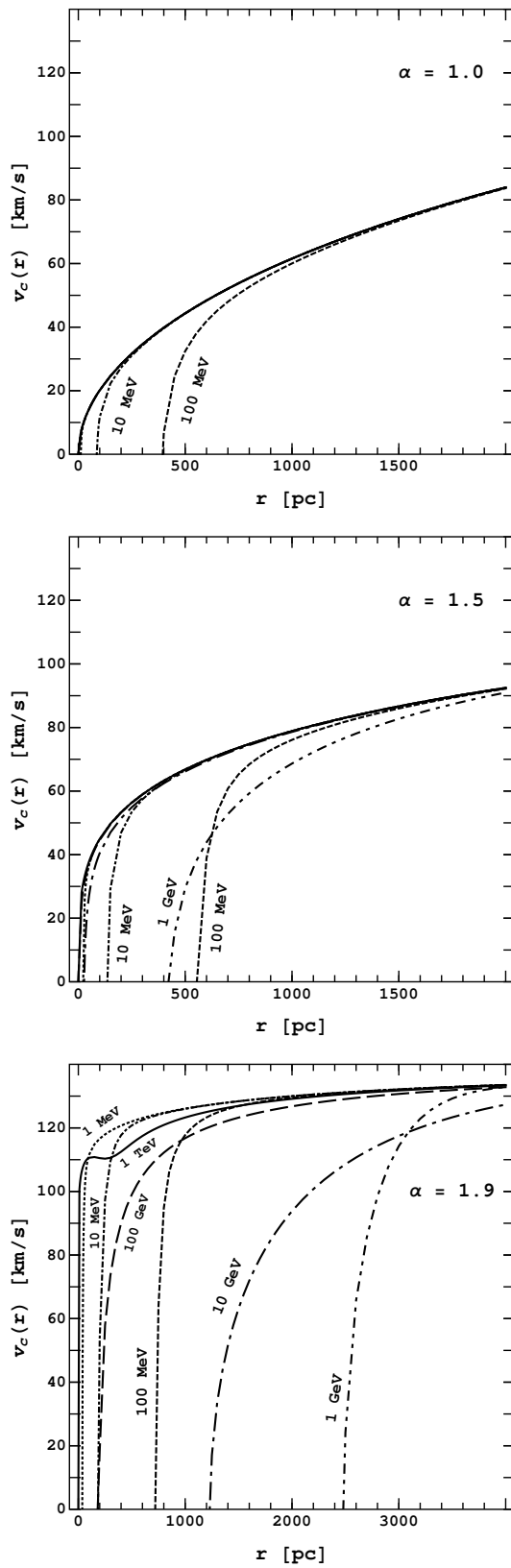


Figure 4.7: Effect of dark matter annihilation on the rotation curve. From top to bottom, panels correspond to $\alpha = 1.0$ (our canonical model), 1.5, and 1.9, respectively.

perhaps still measurable, for $E_0 \sim 1$ GeV. It would be extremely difficult to detect at 10 GeV, and completely negligible for larger particle masses. These conclusions are very robust with respect to variations in the ionization fraction of the gas or the intensity of the magnetic field. The exact density of the interstellar medium has a somewhat larger influence on the results, partly because of its effect on the dark matter pressure (see Figure 4.4) and partly through the presence of the gas density in equation (4.2). For the extreme case $E_0 = 100$ MeV and $\rho_g/m_p = 0.1$ cm $^{-3}$, dark matter pressure is able to prevent gravitational collapse within the inner 2 kpc, compared to 100 pc for a density of 10 cm $^{-3}$. However, the qualitative picture is not changed. For $E_0 > 10$ GeV, the gravitational acceleration dominates by several orders of magnitude at all radii, even for the most dilute gas.

As shown in the previous section, the logarithmic slope of the density profile plays a critical role on the pressure profile. The accelerations for $\alpha = 1.5$ and 1.9 are shown on the centre and bottom panels of Figure 4.6, respectively. When $\alpha = 1.9$, the radius at which the relativistic pressure balances gravity ranges from a few tens of parsec up to several kpc, and a sizable effect on the rotation curve of the Galaxy is expected for any value of the injection energy $E_0 < 1$ TeV.

Figure 4.7 shows the modified circular velocity profiles, according to expression (4.3), for different values of α and E_0 . In our canonical model, the rotation curve of the Galaxy changes significantly for $E_0 = 100$ MeV, it is slightly modified for $E_0 = 10$ MeV and almost imperceptibly for $E_0 = 1$ GeV. For higher values of the inner logarithmic slope, as those predicted, for instance, in the adiabatic contraction scenario (Blumenthal et al., 1986), it is more likely that the annihilation of dark matter particles leaves a clearly detectable imprint on the observed rotation curve. The scales on which such a signal would be visible, of the order of kpc in some cases, subtend several degrees on the sky for the Milky way, and may be observable as well in other nearby galaxies.

4.2.2 Low surface brightness galaxies

In order to quantify the effect on the rotation curves of low surface brightness galaxies, we compute the model predictions for the objects compiled by de Blok and Bosma (2002). Since it is not our aim to fit the data (which would require more careful modeling, beyond the scope of the present work), we simply take the observed rotation curves, as well as the quoted decomposition into stellar disk, gaseous disk, and dark matter halo. We consider their constant mass-to-light ratio and maximum disk models, adopting the corresponding best-fitting values of V_{200} and c_{200} (Table 4 in de Blok and Bosma, 2002). Values of ρ_s and r_s for the maximum disk and constant mass-to-light ratio cases are given in Tables 4.3 and Tables 4.4, respectively.

Figures 4.8 to 4.12 show the predicted rotation curves for $\gamma_0 = 200$ ($m_{dm}c^2 \sim 100$ MeV) and $\gamma_0 = 2000$ ($m_{dm}c^2 \sim 1$ GeV) with $\langle \sigma v \rangle_{e^\pm} = 5 \times 10^{-26}$ cm 3 s $^{-1}$ and all other parameters set to our canonical values.

Since these rotation curves have been computed (at least, in the innermost regions) from the H α line, we also plot the results obtained for a gas density $n = \rho_g/m_p = 0.01$ cm $^{-3}$ and $x_{ion} = 1$, appropriate for the hot, diffuse component responsible for the emission line. The original model of de Blok and Bosma (2002) without dark matter annihilation is shown for the sake of comparison, and the reduced χ^2 values associated to each model are listed in Tables 4.3 and Tables 4.4.

In general, the effect is not very significant for $n = 1$ cm $^{-3}$ (not even for $m_{dm}c^2 \sim 100$ MeV, except for a few exceptional cases, such as NGC 3274). For the adopted value of the logarithmic slope of the dark matter density profile near the centre, $\alpha = 1$, and

the extremely low values of the characteristic density ρ_s reported by de Blok and Bosma (2002), the circular velocity at the innermost point becomes reduced by an amount that is typically much smaller than the observational error bars. A more noticeable effect would be obtained for steeper profiles (see Figure 4.7), but also if one considers the typical density of the hot, ionized medium where the H α line originates. Using $n = 0.01 \text{ cm}^{-3}$, the rotation curves of *all* galaxies would be dramatically affected on $\sim \text{kpc}$ scales for $\alpha = 1$ and $E_0 \leq \text{GeV}$, both for the constant M/L and maximum disk models.

These results represent a double-edged sword for dark matter annihilation models. On the one hand, it might be possible to find a particular dark matter candidate that is able to explain the rotation curve data with a cuspy density profile. On the other hand, we also predict that, in that case, one should observe prominent differences in the kinematics of the stellar, neutral, and ionized components due to their different densities. The observed rotation curves provide thus an additional tool (complementary to radio and gamma-ray constraints) to rule out a broad class of models and hopefully help to identify the physical properties of dark matter particles.

4.3 Conclusions

In this Chapter, we have investigated the contribution to the total gas pressure arising from relativistic electrons and positrons produced in dark matter annihilations. The propagation of these particles through the ISM is determined by the diffusion-loss equation. We assume a uniform diffusion coefficient and consider inverse Compton scattering, synchrotron radiation, Coulomb collisions, bremsstrahlung and ionization of neutral hydrogen atoms as the main energy loss mechanisms. All the electrons and positrons are injected with an initial energy E_0 between 1 MeV and 1 TeV, and the injection rate is constrained by different Galactic observations.

We have evaluated the effect of this “dark matter pressure” for astrophysical conditions representative of the Milky Way and varied the adopted values of each parameter (intensity of the magnetic field, density and ionization fraction of the ISM gas, inner logarithmic slope of the dark matter density profile and the virial mass of the galaxy) to verify that our results hold in the general case. Our main conclusions can be summarized as follows:

1. For the canonical Milky Way model, the dark matter pressure gradient is able to offset the gravitational acceleration within the central $\sim 10 - 400 \text{ pc}$ as long as the injection energy is lower than 1 GeV. There would be an extremely weak signature if $E_0 \sim \text{GeV}$, and the effect would be completely negligible for larger values of E_0 .
2. The ionization fraction of the ISM and the intensity of the magnetic field determine the energy losses and the shape of the electron-positron spectrum at low and high values of the Lorentz factor, respectively. Although these details may have a strong impact on other observables, such as the emission at different wavelengths, they do not affect the rotation curve significantly. The precise value of the gas density plays a more important role, and it changes the results at the quantitative level.
3. Steep logarithmic slopes of the dark matter density profile yield much higher pressures in the central regions. For $\alpha \geq 1.9$, a clear signature of dark matter annihilation on the observed rotation curve is expected even for $E_0 \sim 1 \text{ TeV}$.
4. Comparison with publicly-available observational data shows that, while dark matter pressure may bring the predicted rotation curves into better agreement with

observations, it is arguably more likely that this effect is more useful as a constraint on the annihilation cross-section as a function of dark matter particle mass.

Name	$\rho_s c^2$ [GeV cm $^{-3}$]	r_s [kpc]	χ_{dBB}^2	$\chi_{100\text{MeV,HI}}^2$	$\chi_{1\text{GeV,HI}}^2$	$\chi_{100\text{MeV,HII}}^2$	$\chi_{1\text{GeV,HII}}^2$
UGC1230	9.2799×10^{-2}	15.152	0.723	0.713	0.720	49.825	0.430
UGC5005	8.5056×10^{-5}	4206.9	0.521	0.520	0.521	4.726	0.488
LSBCF563-01	4.5080×10^{-3}	188.61	0.383	0.381	0.383	27.368	0.345
UGC4173	8.5056×10^{-5}	1765.8	0.225	0.225	0.225	1.223	0.214
UGC'3371	8.5056×10^{-5}	7302.7	0.387	0.383	0.386	17.775	0.273
NGC1560	8.5056×10^{-5}	7131.5	8.914	9.183	8.896	659.459	8.720
DDO 189	3.9944×10^{-3}	135.71	0.173	0.171	0.173	40.124	0.135
NGC4395	3.8588×10^{-1}	5.8478	0.573	1.627	0.555	743.952	14.954
NGC3274	4.4477×10^{-1}	6.7189	1.787	7.139	1.731	2935.570	33.516
NGC4455	8.5056×10^{-5}	8252.1	1.428	1.694	1.419	320.260	1.643
NGC2366	1.7431×10^{-1}	2.3734	1.246	1.209	1.245	58.692	1.204
UGC4325	8.5056×10^{-5}	23618	1.326	1.294	1.300	748.686	4.459
DDO 47	8.5056×10^{-5}	14107	0.400	0.303	0.394	260.841	2.056
DDO 185	8.5056×10^{-5}	5245.2	2.036	2.024	2.026	141.203	1.896

Table 4.3: Galaxy name, characteristic dark matter density and radius, and reduced χ^2 values for the maximum disk models in de Blok and Bosma (2002). χ_{dBB}^2 refers to the original model without dark matter annihilation. The subscripts in the other columns denote the injection energy (100 MeV or 1 GeV) and the conditions in the baryonic medium ($n = 1$ cm $^{-3}$ and $x_{\text{ion}} = 0$ for HI, $n = 0.01$ cm $^{-3}$ and $x_{\text{ion}} = 1$ for HII).

Name	$\rho_s c^2$ [GeV cm $^{-3}$]	r_s [kpc]	χ^2_{dBB}	$\chi^2_{100\text{MeV,HI}}$	$\chi^2_{1\text{GeV,HI}}$	$\chi^2_{100\text{MeV,HI}}$	$\chi^2_{1\text{GeV,HI}}$
UGC1230	3.7001×10^{-1}	9.0973	1.091	1.032	1.072	257.449	5.447
UGC5005	9.1650×10^{-3}	75.759	0.175	0.172	0.174	18.571	0.102
LSBC F563-01	9.9553×10^{-2}	20.850	0.370	0.355	0.367	155.857	1.492
UGC4173	8.5056×10^{-5}	2413.7	0.124	0.123	0.124	3.687	0.110
UGC3371	8.5056×10^{-5}	10073	0.280	0.273	0.278	36.263	0.118
NGC1560	5.6447×10^{-3}	166.59	2.330	3.810	2.315	1905.660	17.378
DDO 189	2.2759×10^{-3}	7.4629	0.109	0.088	0.105	273.964	5.120
NGC4395	4.4477×10^{-1}	6.3057	0.644	2.476	0.613	1149.580	30.584
NGC3274	2.2174×10^{-0}	2.9131	0.941	29.406	0.808	9205.720	371.555
NGC4455	8.5056×10^{-5}	9702.7	0.614	1.078	0.605	466.972	2.482
NGC2366	3.8588×10^{-1}	4.1902	1.935	2.222	1.900	950.701	16.488
UGC4325	8.5056×10^{-5}	36371	1.096	1.081	1.047	1737.360	34.844
DDO 47	8.5056×10^{-5}	16137	0.272	0.180	0.265	344.709	3.186
DDO 185	8.5056×10^{-5}	7876.7	2.162	2.333	2.138	366.502	3.996

Table 4.4: Same as Table 4.3, for the constant mass-to-light ratio models in de Blok and Bosma (2002).

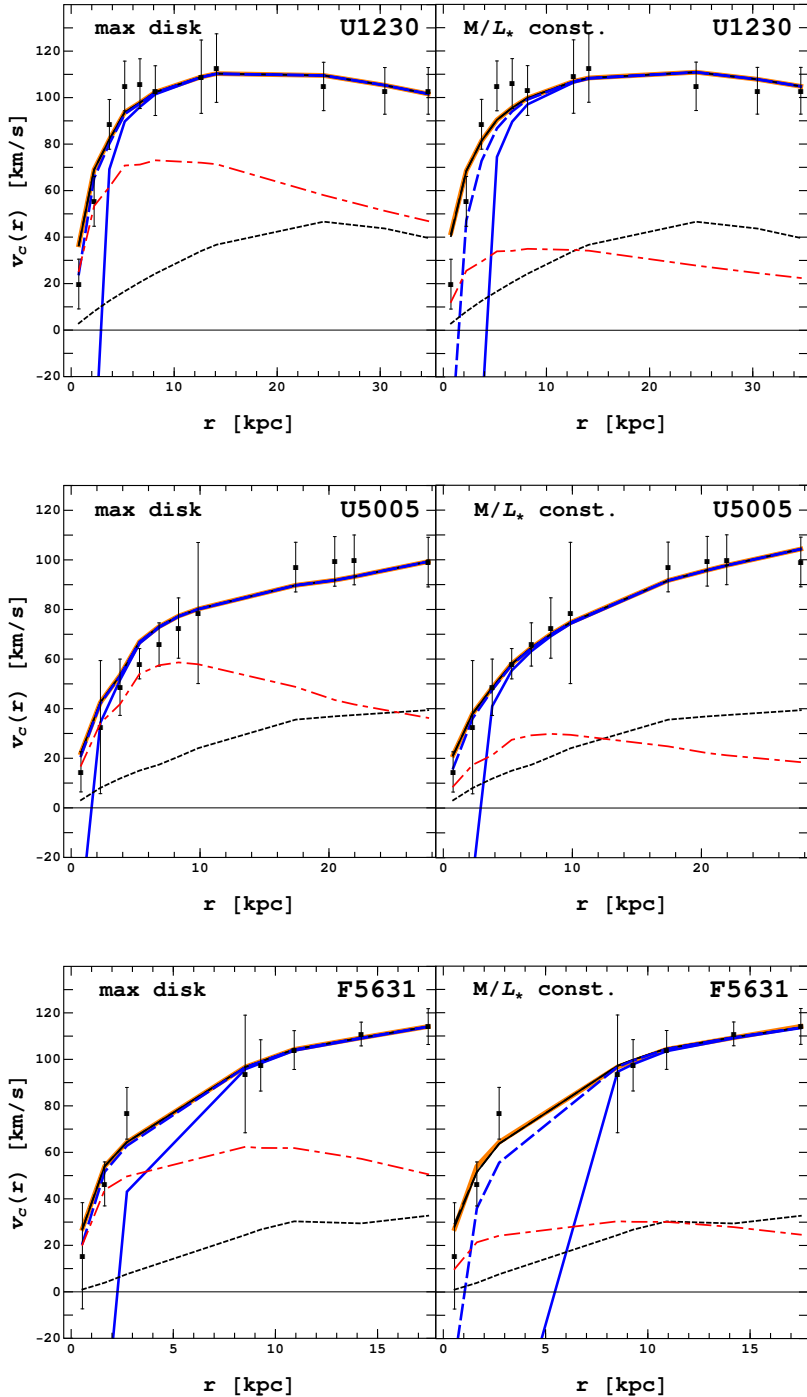


Figure 4.8: Model predictions for U1230, U5005 and F5631, compared to the observed rotation curves (data points with error bars). Solid lines are used for $E_0 = 100$ MeV and dashed lines for 1 GeV. Results for neutral and ionized gas are shown in black and blue colour, respectively. Orange lines depict the model without dark matter annihilation. The rotation curves by star and gas (data taken from de Blok and Bosma, 2002) are shown by red dot-dashed and black small dashed lines, respectively.

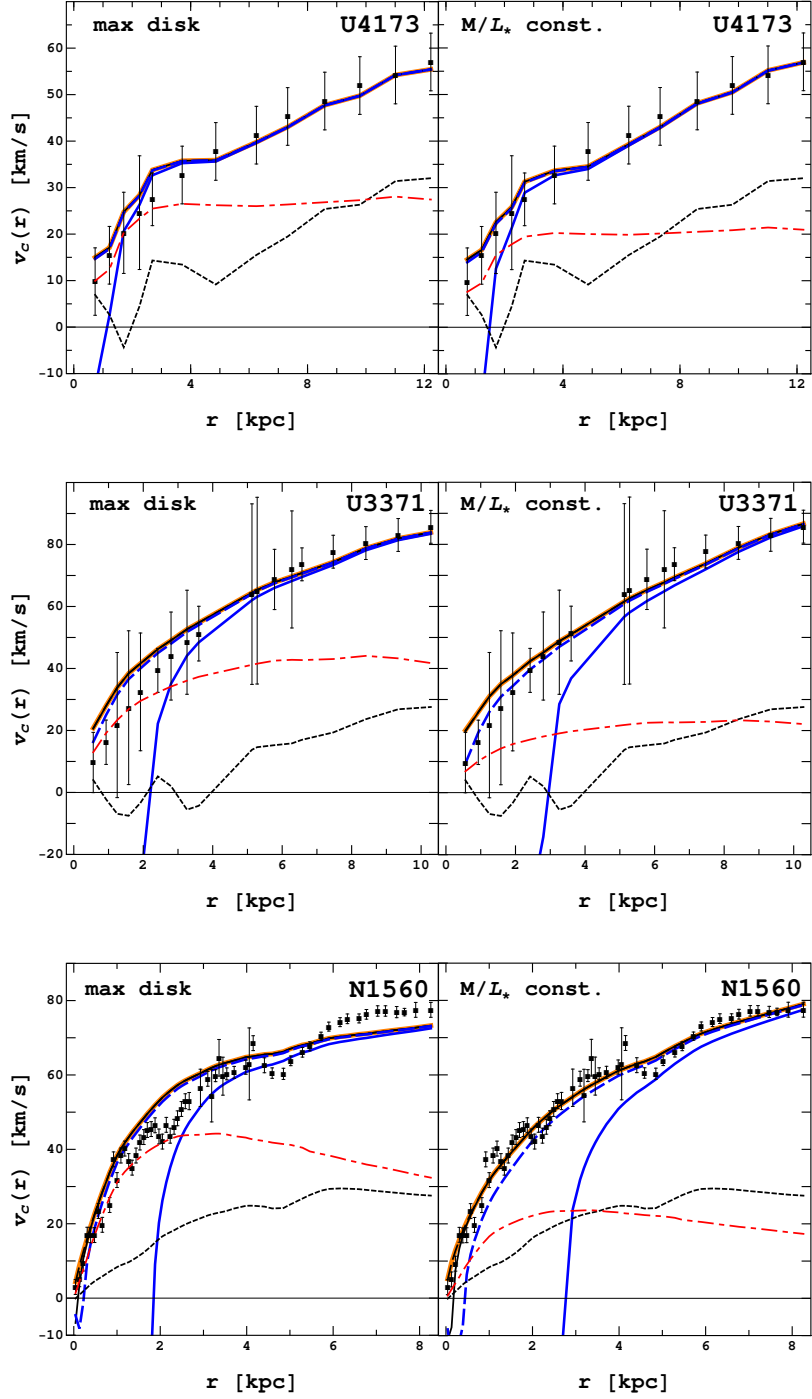


Figure 4.9: Model predictions for U4173, U3371 and N1560, compared to the observed rotation curves (data points with error bars). Solid lines are used for $E_0 = 100$ MeV and dashed lines for 1 GeV. Results for neutral and ionized gas are shown in black and blue colour, respectively. Orange lines depict the model without dark matter annihilation. The rotation curves by star and gas (data taken from de Blok and Bosma, 2002) are shown by red dot-dashed and black small dashed lines, respectively.

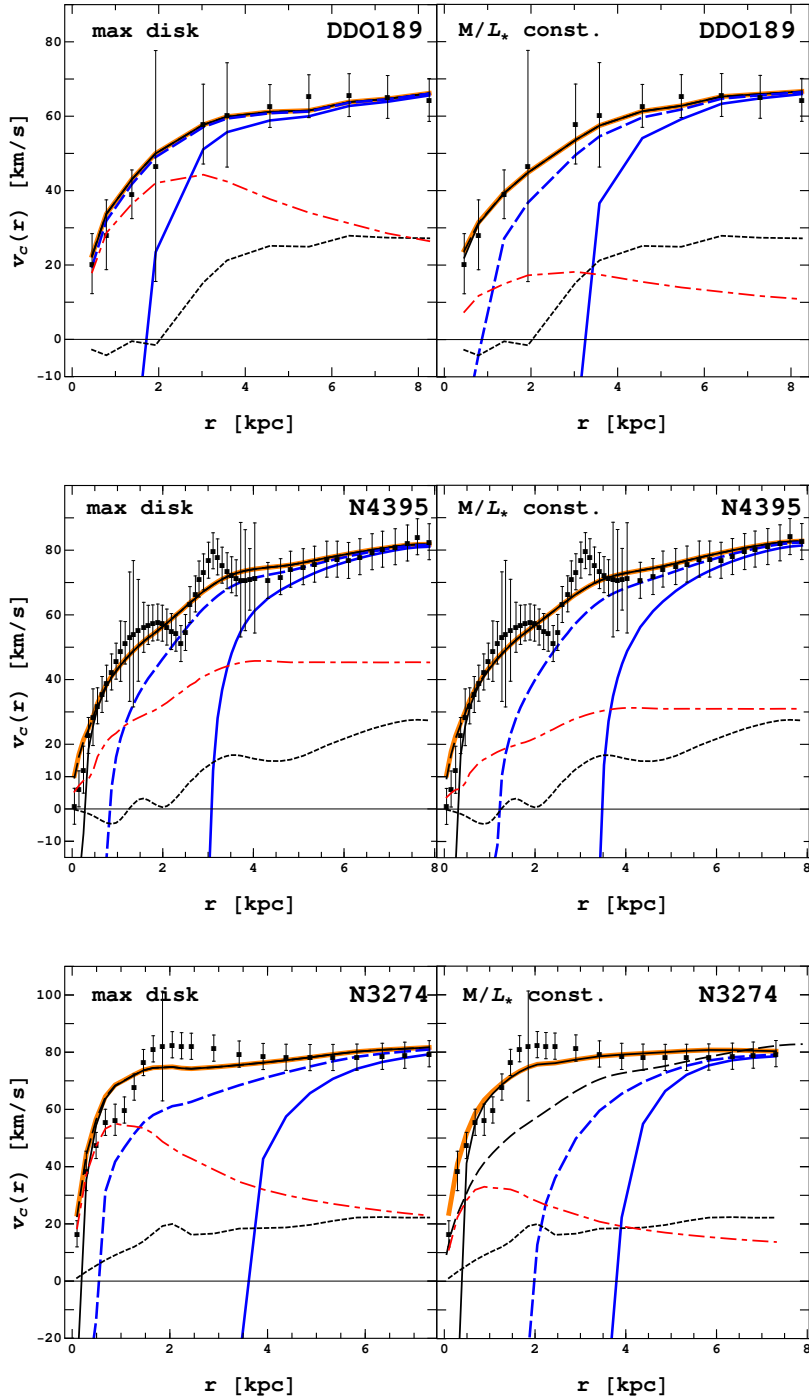


Figure 4.10: Model predictions for DDO189, N4395 and N3274, compared to the observed rotation curves (data points with error bars). Solid lines are used for $E_0 = 100$ MeV and dashed lines for 1 GeV. Results for neutral and ionized gas are shown in black and blue colour, respectively. Orange lines depict the model without dark matter annihilation. The rotation curves by star and gas (data taken from de Blok and Bosma, 2002) are shown by red dot-dashed and black small dashed lines, respectively.

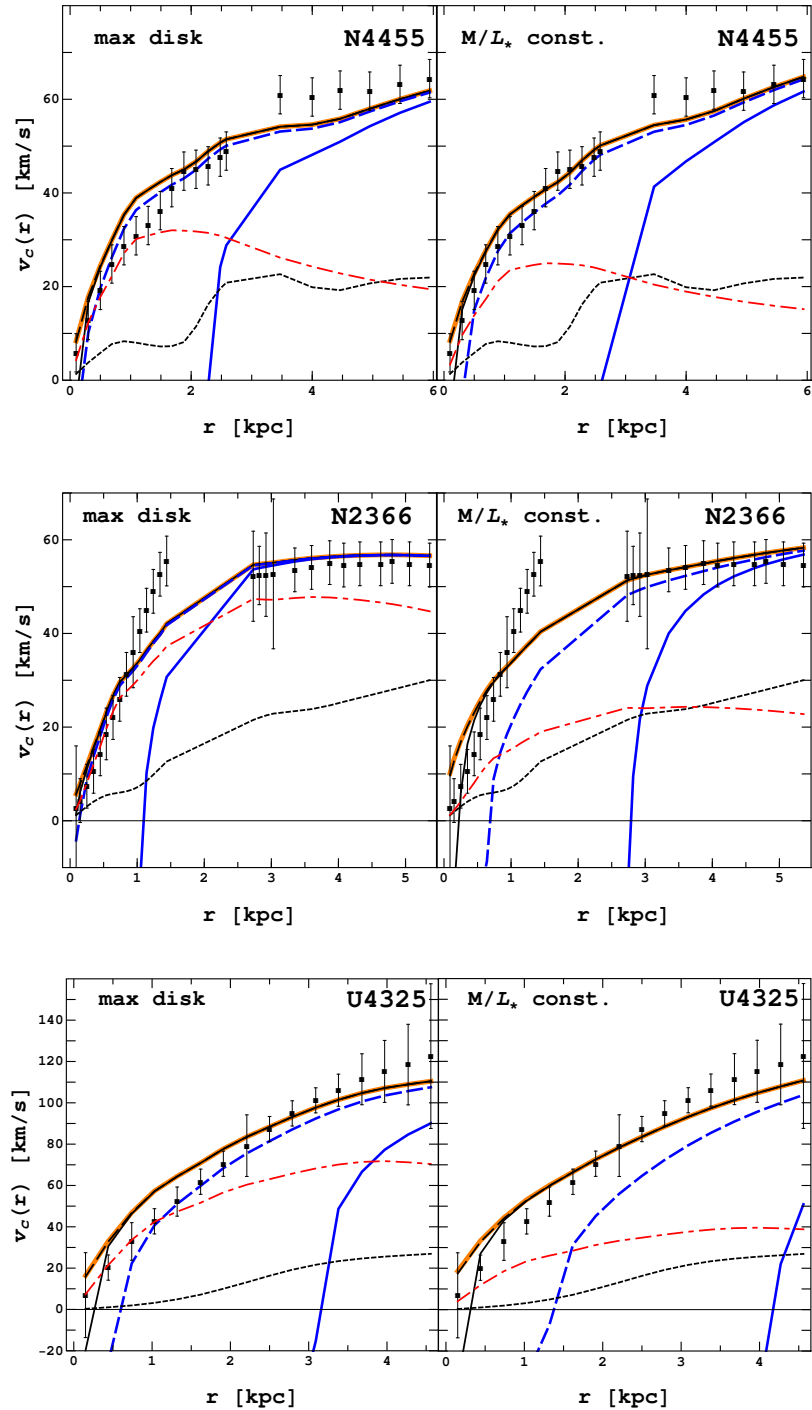


Figure 4.11: Model predictions for N4455, N2366 and U4325, compared to the observed rotation curves (data points with error bars). Solid lines are used for $E_0 = 100$ MeV and dashed lines for 1 GeV. Results for neutral and ionized gas are shown in black and blue colour, respectively. Orange lines depict the model without dark matter annihilation. The rotation curves by star and gas (data taken from de Blok and Bosma, 2002) are shown by red dot-dashed and black small dashed lines, respectively.

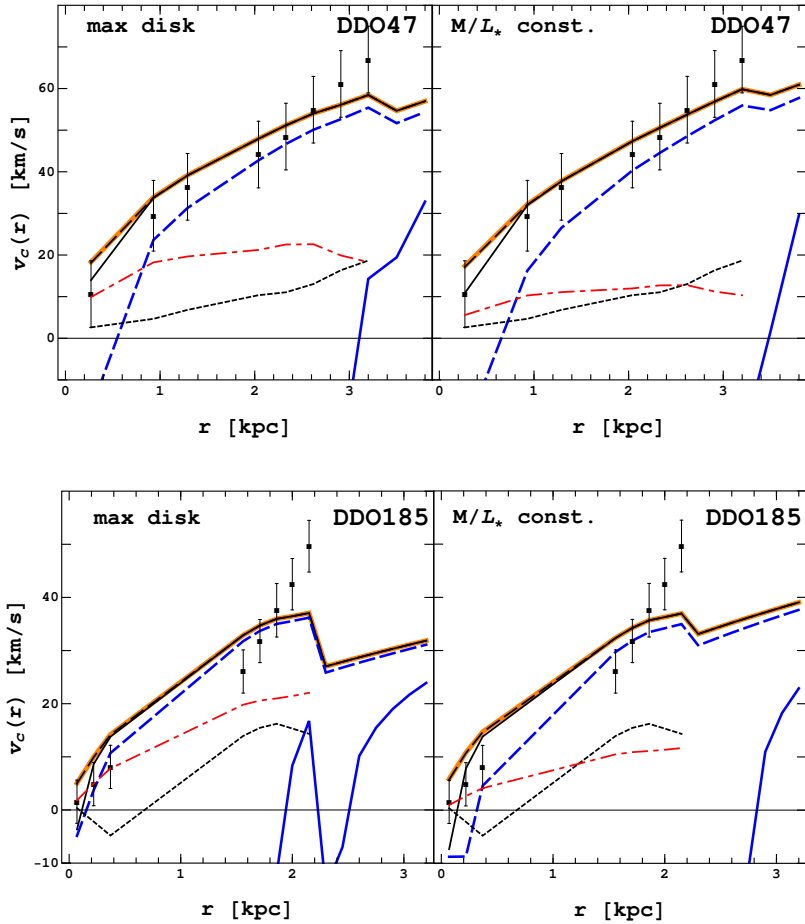


Figure 4.12: Model predictions for DDO47 and DDO185, compared to the observed rotation curves (data points with error bars). Solid lines are used for $E_0 = 100$ MeV and dashed lines for 1 GeV. Results for neutral and ionized gas are shown in black and blue colour, respectively. Orange lines depict the model without dark matter annihilation. The rotation curves by star and gas (data taken from de Blok and Bosma, 2002) are shown by red dot-dashed and black small dashed lines, respectively.

Chapter

5

MULTI-MESSENGER CONSTRAINTS

In this Chapter, we try to impose constraints on the cross-section of dark matter annihilation into electron-positron pairs by comparing the predictions of our analytic model of particle propagation with a multi-wavelength set of observational data obtained from the literature. More precisely, we compare the expected emission from synchrotron radiation, ICS and FSR within the Milky Way with 18 maps of the sky at different frequencies: the Haslam radio map at 408 MHz, the 7-year data from the Wilkinson Microwave Anisotropy Probe (WMAP) in its 5 bands (23 GHz, 33 GHz, 41 GHz, 61 GHz, and 94 GHz), and gamma-ray maps from the Fermi Large Area Telescope (LAT) binned in 12 different channels (from 0.3 to 300 GeV). A straightforward statistical criterion is used in order to mask the most obvious astrophysical signals (i.e. emission from the galactic disc and point sources), and observational upper limits are derived from the remaining spherically-symmetric component.

In addition to the photon data, we also consider the recent measurements of the local electron and positron spectra performed by PAMELA (Adriani et al., 2009a, 2010a, 2011), Fermi (Ackermann et al., 2010a, 2012b), and H.E.S.S. (Aharonian et al., 2008). As will be shown below, considering the positron spectrum separately (rather than the combined electron+positron spectrum) yields a significant improvement on the maximum value allowed for the positron injection rate or, equivalently, the dark matter annihilation cross-section.

We will first discuss the results obtained for a ‘canonical’ model of the Milky Way model and then explore the effects of varying the intensity of magnetic field, the diffusion coefficient, the ISRF, and the inner logarithmic slope of dark matter density profile.

The remainder of this Chapter is structured as follows: Section 5.1 describes the parameters of the Milky Way model. Our analysis of the observational data is fully described in Section 5.2 (tables with precise numeric values are provided at the end of the Chapter), and Section 5.3 is devoted to the constraints on the dark matter annihilation cross-section. The effect of the different astrophysical parameters is discussed in Section 5.4, while Section 5.5 focuses on the constraints that one can impose on the slope of the dark matter density profile by assuming that dark matter particles are produced as thermal relics in the primordial universe. Finally, our main conclusions are succinctly summarized in Section 5.6.

5.1 Astrophysical parameters

As discussed in Section 3.3.3, the emission coefficient associated to final-state radiation is fully specified by the initial energy and injection rate of the electron-positron pairs, related to the nature of the dark matter particle (mass and cross-section) and the parameters describing the density profile of the Galactic halo. In contrast, the photon intensity from the synchrotron and ICS emission also depends on the astrophysical parameters that determine the propagation and energy losses of the relativistic particles. Following the same procedure as in Chapter 4, we will first define a canonical model based on observations of the Milky Way and then investigate the effect of each individual component by varying the values of the adopted parameters. In all cases, we calculate the electron-positron spectrum as described in expression (3.14), and then estimate the photon intensity according to expression (3.29).

As explained in Section 4.1.2, our canonical model assumes a dark matter density profile with $\alpha = 1$, $r_s = 17$ kpc and $\rho_s c^2 = 0.35$ GeV cm $^{-3}$. The ISM is mainly composed of neutral hydrogen atoms ($X_{\text{ion}} = 0$) with number density $\rho_g/m_p \sim 1$ cm $^{-3}$, and it is permeated by a tangled magnetic field $B \sim 6$ μ G. Apart from the canonical model, we consider the effect that the magnetic field, the diffusion coefficient, and the interstellar radiation field have on the synchrotron and ICS emission. The intensity of the magnetic field B is varied from 1 to 100 μ G. For the diffusion coefficient (see equation 3.6), we consider the three models discussed by Donato et al. (2004a) and Delahaye et al. (2008), summarized in Table 5.1. We will also use three different models of the ISRF (adopted from Cirelli and Panci, 2009) where the photon intensity is represented by three grey-body components (see equations 3.16 and 3.36). The normalizations and effective temperatures of the light emitted by the Galactic stars and dust are quoted in Table 5.2.

Most importantly, we also investigate the effect of the inner slope of dark matter density profile on the production rate of electron-positron pairs. We vary the inner logarithmic slope α from 0.5 to 1.5. When varying α we also modify the characteristic density and radius in expression (3.27) so that the dark matter density at the solar radius is equal to 0.3 GeV cm $^{-3}$ and the virial mass of the Galaxy is 10^{12} M $_{\odot}$. The appropriate values of ρ_s and r_s are quoted in Table 4.2 for several values of the inner logarithmic slope α . In addition, we also consider the so-called Einasto profile

$$\rho(r) = \rho_s \exp \left[\frac{-2}{\alpha} \left(\left(\frac{r}{r_s} \right)^\alpha - 1 \right) \right], \quad (5.1)$$

where $\alpha = 0.17$.

5.2 Observational data

In order to constrain the production of relativistic electrons and positrons in the Milky Way, we consider observations of the whole sky at very different wavelengths. More precisely, the Haslam map in the radio band, the 5 WMAP channels at microwave wavelengths, and 12 energy bins of the Fermi LAT observations in the gamma-ray regime. The Haslam and WMAP maps are dominated by synchrotron emission, whereas Fermi traces ICS and FSR.

The Haslam 408 MHz radio continuum all-sky map (Haslam et al., 1981, 1982) combines data from four different surveys. The data were obtained from the archives of the NCSA ADIL in equatorial 1950 coordinates, and they were subsequently processed further in the Fourier domain to mitigate baseline striping and strong point sources. For

Model	K_0 [kpc 2 s $^{-1}$]	δ
M1	7.42×10^{-17}	0.46
MED (canonical)	1.76×10^{-18}	0.70
M2	2.92×10^{-18}	0.55

Table 5.1: Three different models of the diffusion coefficient, following the parameterization $K(\gamma) = K_0\gamma^\delta$. The model MED has been proposed by Donato et al. (2004a), and models M1 and M2 are adopted from Delahaye et al. (2008).

Model	\mathcal{N}_{SL}	\mathcal{N}_{IR}
	$T_{\text{SL}} = 3481$ K	$T_{\text{IR}} = 40.6$ K
ISRF (I)	2.7×10^{-12}	7.0×10^{-5}
Canonical	1.7×10^{-11}	7.0×10^{-5}
ISRF (II)	8.9×10^{-13}	1.3×10^{-5}

Table 5.2: Normalization of the grey-body models describing the interstellar radiation field, adopted from Cirelli and Panci (2009). In our canonical model, we use the values appropriate for the Galactic centre in order to compute the ICS and synchrotron emission. For the electron-positron spectrum at the Solar neighbourhood, we use ISRF(I).

the WMAP data, we take the full-resolution coadded temperature maps for each of the 5 frequency bands (23, 33, 41, 61, and 94 GHz) corresponding to the 7-year observations (Jarosik et al., 2011). The Fermi gamma-ray maps were computed by Dobler et al. (2010) from all “Class 3” (diffuse) photon events in the first-year data release. We use the 12 logarithmically-spaced frequency bands, from 0.3 to 300 GeV, of the smoothed maps without point source subtraction.

Since we are interested in a spherically-symmetric component, we may follow a simple, conservative procedure in order to mask the emission from the Galactic disk and individual point sources without relying on any particular foreground model. For each frequency, we compute the average intensity $I(\theta)$ in 180 bins as a function of the angular separation θ from the Galactic centre. We also estimate the standard deviation $\sigma(\theta)$ within each bin, as well as the average standard deviation

$$\sigma_{\text{ave}} = \frac{\sum_{i=1}^n \sigma(\theta_i)}{n}, \quad (5.2)$$

where $n = 180$ is the total number of the bins. We then start an iterative procedure, where all pixels more than $3\sigma_{\text{ave}}$ away from $I(\theta)$ are discarded until convergence is achieved.

This method seems to correctly identify and remove the most obvious structures in all but the two highest-energy Fermi bands, where the photon statistics is so poor that it is extremely difficult to distinguish diffuse emission from individual point sources. For these two bands, we opted to use the original average intensity $I_0(\theta)$ without applying any mask. Raw intensity maps, masked residual maps, i.e. $I - I(\theta)$, and the average intensity $I(\theta)$ for each wavelength are shown in Figures 5.9 to 5.14 at the end of the Chapter. Numeric values of $I_0(\theta)$, $I(\theta)$, and $\sigma(\theta)$ are quoted in Tables 5.3 to 5.8.

Besides these observational data, we also consider the energy spectra of cosmic-ray electrons and positrons in the solar neighbourhood; in particular, we use the combined electron+positron spectrum measured by the Fermi (Ackermann et al., 2010a) and H.E.S.S.

(Aharonian et al., 2008) collaborations, as well as the positron-only spectrum determined from Fermi data (Ackermann et al., 2012b). For PAMELA, we combine the electron-only spectrum obtained by Adriani et al. (2011) with the positron fraction discussed in Adriani et al. (2010a) in order to derive the positron spectrum.

5.3 Constraints on the dark matter cross-section

Once the emission from the galactic disc and the most prominent point sources is excluded, the remaining spherically-averaged component can be used to place upper limits on the cross-section for dark matter annihilation into electron-positron pairs.

First of all, model intensities are computed according to the scheme described in Section 3.2 and Section 3.3.3. We consider the injection energy (i.e. the mass of the dark matter particle) as a free parameter and investigate values of the initial Lorentz factor γ_0 between 2×10^3 and 2×10^7 , corresponding to injection energies $E_0 = \gamma_0 m_e c^2$ from 1 GeV to 10 TeV. As an example, Figure 5.1 displays the results of our canonical Milky Way model for the synchrotron, inverse Compton, and final-state radiation contributions to the photon intensity at 10° from the Galactic centre, assuming a dark matter annihilation cross-section of $\langle \sigma v \rangle_{e^\pm} = 3 \times 10^{-26} \text{ cm}^3 \text{ s}^{-1}$.

One can readily see that the Haslam radio map will be most sensitive to synchrotron emission by particles with an initial energy between 1 and 10 GeV, whereas WMAP data will cover the range $E_0 \sim 10 - 100$ GeV. On the other hand, the gamma rays observed by the Fermi LAT will constrain the maximum ICS and FSR emission allowed. The final-state radiation is sharply peaked at the injection energy, and it traces values of E_0 between 1 GeV and 1 TeV. The inverse Compton spectrum is broader, and it features three distinct emission peaks, due to the scattering of CMB, starlight, and infrared photons. It is best suited to probe injection energies between 10 and 100 GeV, although the maximum intensity is always much smaller than the FSR peak, and therefore the associated constraints are going to be weaker.

Since the value of the annihilation cross-section only sets the normalization of the spectra, and it does not alter its shape, it is relatively easy to set an upper limit by imposing that the model intensities do not exceed the observed values (red triangles in Figure 5.1) at *any* angular separation θ . Not surprisingly, the tightest constraint will always be provided by a small value of θ , i.e. close to the Galactic centre. The dark matter density, and thus the injection rate, are higher there than anywhere else in the Galaxy. However, the observed intensity also reaches a maximum at $\theta = 0$, and particles may diffuse from their injection point, effectively smoothing the density cusp. The angle that sets the maximum normalization that would be compatible with the observations (i.e. the upper limit of $\langle \sigma v \rangle_{e^\pm}$) is plotted in Figure 5.2, and the predicted surface brightness profiles of synchrotron, ICS, and FSR emission, normalized according to such prescription, are plotted in Figure 5.3 and Figures 5.4 together with the observational data.

Final-state radiation is produced at the very moment of pair creation, and thus it directly traces the positron injection profile, which is, in turn, proportional to the square of the dark matter density. Therefore, the intensity of the FSR emission does not depend on the injection energy of the particles or any astrophysical parameter other than the inner logarithmic slope α of the dark matter density profile. For this reason, the normalized surface brightness profiles of FSR depicted in Figure 5.4 do *not* depend on E_0 . In our canonical model (where $\alpha = 1$), and even more so if $\alpha > 1$, the tightest constraints on the final-state radiation come from the very centre of the Galaxy ($\theta < 1^\circ$) in almost all cases, yielding a null standard deviation in Figure 5.2 for most values of E_0 .

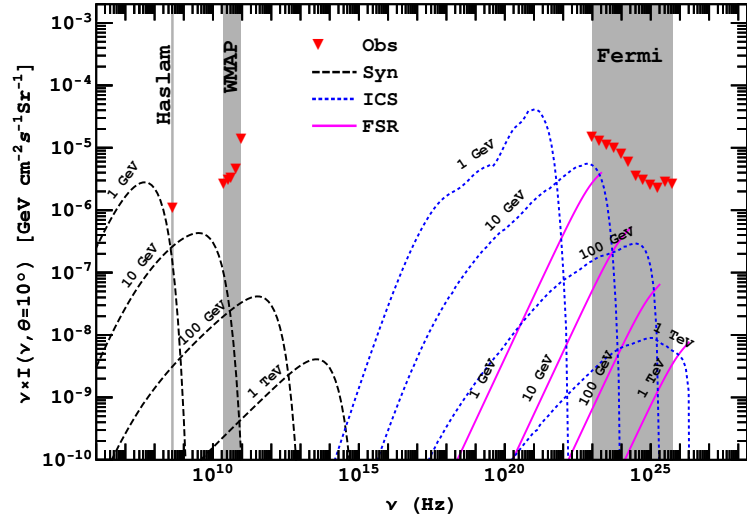


Figure 5.1: Theoretical photon spectra of synchrotron radiation (dashed black lines), ICS (dotted blue lines) and FSR (solid magenta lines) for our canonical model with $\langle \sigma v \rangle_{e^\pm} = 3 \times 10^{-26} \text{ cm}^3 \text{ s}^{-1}$ and different injection energies, evaluated at 10° from the Galactic centre. Grey bands illustrate the frequency ranges of Haslam, WMAP and Fermi. The observational data at $\theta = 10^\circ$ are plotted as red triangles.

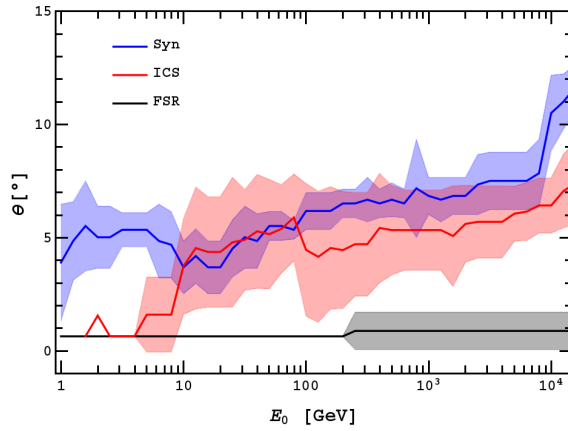


Figure 5.2: Angular separation θ that provides the upper limits for synchrotron, ICS and FSR emission. The optimal value is computed independently for each of the observed wavelengths. Solid lines and shadowed regions show the average $\langle \theta \rangle = 1/N_\lambda \sum_i \theta(\lambda_i)$ and standard deviation $\langle \theta^2 \rangle - \langle \theta \rangle^2$ across different channels, respectively.

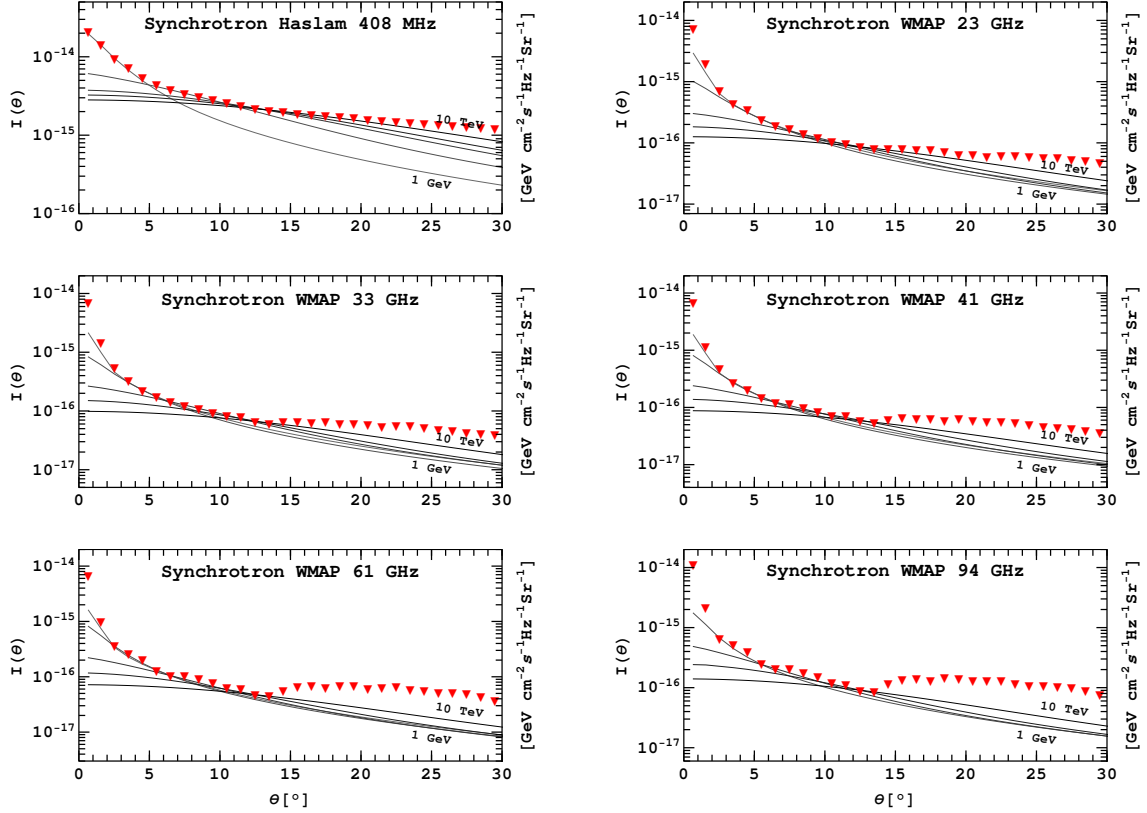


Figure 5.3: Surface brightness profiles of synchrotron radiation as a function of the angular separation θ from the Galactic centre. Red triangles correspond to the mean observational intensity after discarding the contribution of the Galactic disk and prominent point sources as discussed in Section 5.2. Theoretical profiles are normalized to the maximum value of the annihilation cross-section (see Figure 5.5) allowed by these data. The angular separation that provides the tightest constraint – i.e. the tangent point between models and observations – is depicted in Figure 5.2. The intensities of synchrotron radiation obtained for the canonical Milky Way model are expressed in grey to black lines, where a darker colour represents a higher value of the injection energy E_0 .

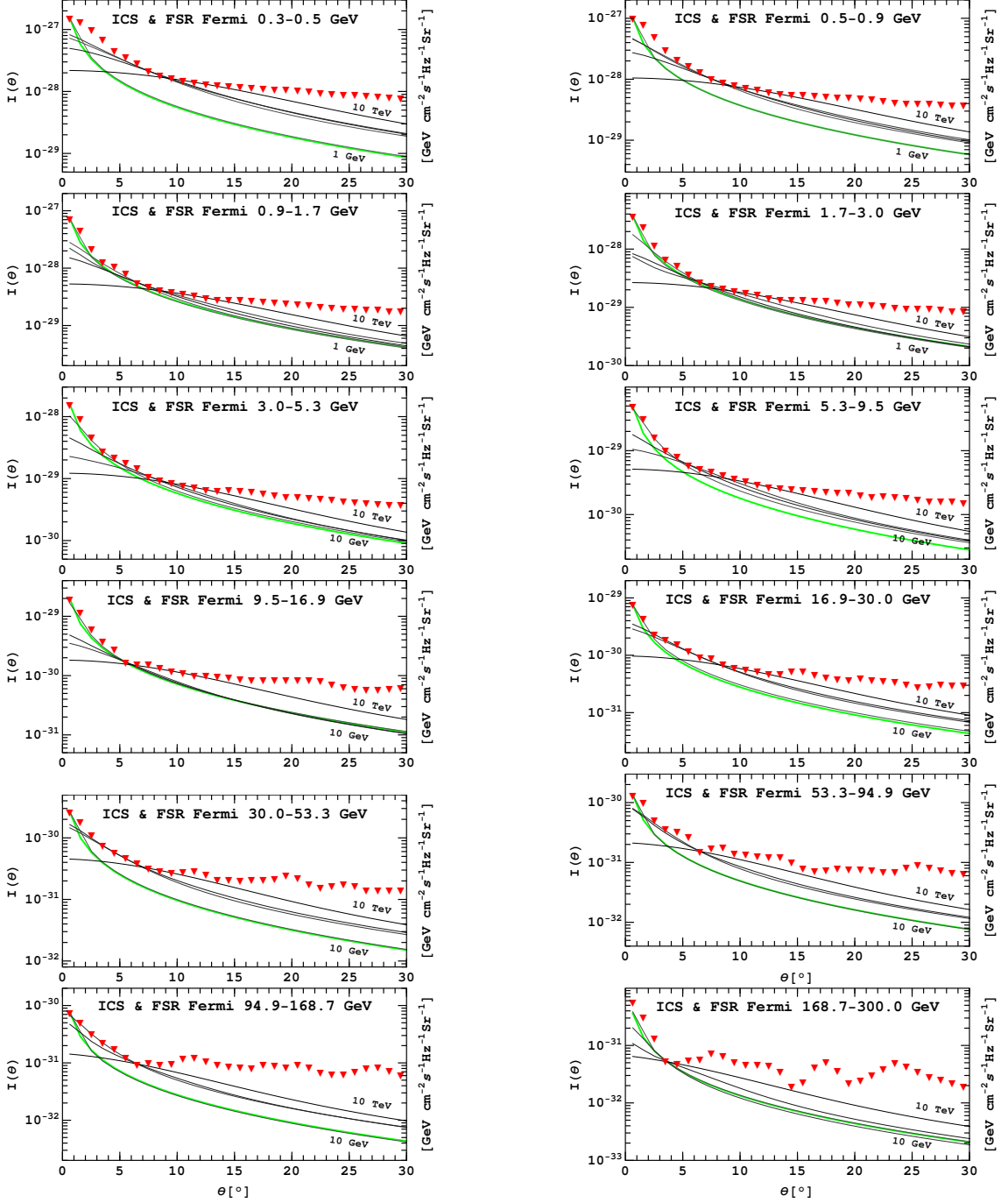


Figure 5.4: Surface brightness profiles of ICS and FSR as a function of the angular separation θ from the Galactic centre. Red triangles correspond to the mean observational intensity after discarding the contribution of the Galactic disk and prominent point sources as discussed in Section 5.2. Theoretical profiles are normalized to the maximum value of the annihilation cross-section (see Figure 5.5) allowed by these data. The angular separation that provides the tightest constraint – i.e. the tangent point between models and observations – is depicted in Figure 5.2. For ICS emission, the intensities obtained for the canonical Milky Way model are expressed in grey to black lines, where a darker colour represents a higher value of the injection energy E_0 . The normalized intensity of FSR, shown as a green solid line, does not depend on E_0 .

For synchrotron and ICS emission, particle diffusion makes the intensity profile shallower, especially at high injection energies. In general, one can say that photons of a given frequency trace electrons and positrons within a certain energy range. If that range is close to E_0 , these particles would have just been injected, and therefore the effects of particle propagation should be small, whereas, away from E_0 , these electrons and positrons would have traveled a significant distance from the point of injection, and the surface brightness profile will become considerably shallower.

This trend is indeed evident in Figure 5.3 and 5.4: surface brightness profiles become progressively shallower as one moves from $E_0 = 1$ GeV to 10 TeV, and the effect is more pronounced for those channels that trace low-energy particles, i.e. Haslam, WMAP, and the lowest-energy Fermi bands. In the most extreme cases, diffusion keeps the electron-positron spectrum (and the ensuing intensity) roughly constant within the innermost 10–20°. For inverse Compton scattering, the tightest constraints on the annihilation cross-section come from $\theta \sim 5^\circ$ at all but the highest injection energies, whereas for synchrotron emission the optimal angle increases steadily from 1 to 15° (see Figure 5.2).

In addition to the photons arriving from the centre of the Milky Way, the dark matter annihilation cross-section $\langle\sigma v\rangle_{e^\pm}$ is also strongly constrained by the observed abundance of relativistic electrons and positrons in the solar neighbourhood. In particular, we consider the recent measurements of the *positron* spectrum by the Fermi collaboration (Ackermann et al., 2012b) and the PAMELA experiment. The latter data have not been published as such in the literature, but they can be trivially derived from the quoted positron fraction (Adriani et al., 2010a) and electron spectrum (Adriani et al., 2011). Since the positron fraction is of the order of 10 percent or less at the energies below ~ 10 GeV, the constraints from the positron-only spectrum will be much tighter than those derived from the combined electron+positron data. For the sake of comparison, we also show these for PAMELA (Adriani et al., 2011), Fermi (Ackermann et al., 2010a), and H.E.S.S. (Aharonian et al., 2008). Note that, in the latter case, the measurements are able to probe higher (\sim TeV) energies, but it is not possible to discriminate between the electron and positron signatures.

Our constraints are derived by imposing that the predicted amount of electrons and/or positrons does not exceed the observed values for *any* Lorentz factor γ . Given the energy dependence of the observed spectrum, $\left[\frac{dn}{dE}\right]_{\text{obs}} \sim E^{-3}$, and the energy losses, $b(E) \sim E^2$, the most restrictive constraint comes from the spectrum near the injection energy, where propagation can be safely neglected and $\left[\frac{dn}{dE}\right]_{\text{model}} \approx \frac{Q_0}{b} \propto E^{-2}$. The maximum production rate allowed by the data can then be expressed as

$$Q_0(r_\odot) < b(\gamma_0) \left[\frac{dn}{dE} \right]_{\text{obs}}(\gamma_0), \quad (5.3)$$

and one arrives to the condition

$$\langle\sigma v\rangle_{e^\pm}(\gamma_0) < \left[\frac{m_{\text{dm}}}{\rho_{\text{dm}}(r_\odot)} \right]^2 b(\gamma_0) \left[\frac{dn}{dE} \right]_{\text{obs}}(\gamma_0) \quad (5.4)$$

in order not to overproduce the observed signal.

The results are plotted in Figure 5.5, together with the upper limits on the dark matter annihilation cross-section derived from the comparison of the predicted synchrotron, ICS and FSR emission, assuming our canonical Milky Way model for particle propagation, with multi-wavelength observations by Haslam, WMAP, and Fermi. As can be readily seen in the figure, the tightest constraints are provided by the final-state radiation and inverse Compton scattering for injection energies above 20–30 GeV, whereas the positron

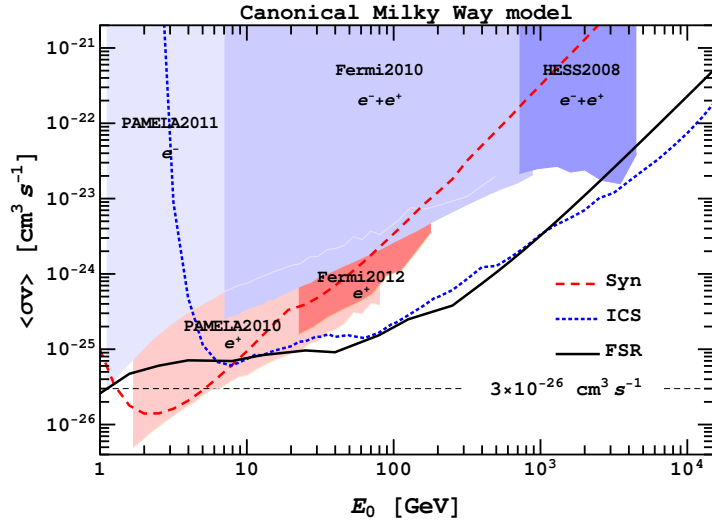


Figure 5.5: Upper limits on the dark matter annihilation cross-section derived by comparing the predicted synchrotron (red dashed line), ICS (blue dot-dashed line) and FSR (black solid line) emission with multi-wavelength observational data. The areas shaded in blue show the constraints obtained from the measurements of the combined electron+positron spectrum at the solar neighbourhood by PAMELA, Fermi and H.E.S.S.. The upper limits obtained from the positron spectrum are shown by the red areas. The horizontal dotted line indicates the value $\langle \sigma v \rangle_{e^\pm} = 3 \times 10^{-26} \text{ cm s}^{-1}$.

spectrum in the solar neighbourhood and synchrotron emission limits the production cross-section at lower energies.

The typical value for thermal relics, $\langle \sigma v \rangle_{e^\pm} = 3 \times 10^{-26} \text{ cm s}^{-1}$, is ruled out for particle masses lighter than a few GeV. Both particle physics processes and astrophysical boost factors have previously been advocated to increase the current annihilation rate in the Milky Way by more than a factor of 10 with respect to the early universe. According to Figure 5.5, such models are excluded for any dark matter candidate below the \sim TeV regime annihilating primarily into electron-positron pairs. Since our analysis involves a very conservative treatment of the astrophysical signal, merely excluding the emission from the disk and prominent point sources, it is expected that a deeper understanding of the astrophysical sources of electrons and positrons would make possible to probe the interesting region of the parameter space below $\langle \sigma v \rangle_{e^\pm} = 3 \times 10^{-26} \text{ cm s}^{-1}$.

5.4 Effect of the astrophysical parameters

All the constraints represented in Figure 5.5 are based on our ‘canonical’ Milky Way model. The final-state radiation from the Galactic centre and the local positron spectrum directly trace the instantaneous injection rate, and therefore they do not depend on the propagation parameters. However, the surface brightness profiles of synchrotron and ICS emission are sensitive to the precise values adopted for the intensity of the magnetic field, the diffusion coefficient, and the interstellar radiation field. The inner logarithmic slope of dark matter density profile has a very strong impact on the injection rate close to the centre, and thus it affects all the tracers considered in the present work except the positron spectrum in the solar neighbourhood.

Here we investigate the effect of the various astrophysical parameters of our propaga-

tion model on the upper limits obtained for the dark matter annihilation cross-section. Once again, we will consider different initial energies E_0 from 1 GeV to 10 TeV and compare the predicted emission with the full observational data set, varying each of the astrophysical parameters in turn in order to assess their influence on the results.

Let us start with the intensity of the magnetic field B . This parameter plays an important role in the energy losses, and it sets the total amount of energy that is radiated away as synchrotron emission. The top panel on Figure 5.6 shows the upper limits derived by combining the constraints obtained from synchrotron and inverse Compton scattering. The results obtained $B = 1, 6$ (our canonical model), 30 and $100 \mu\text{G}$ are plotted as dotted, solid, dash-dotted, and dashed lines, respectively. All the other constraints (FSR and local positron spectrum) are independent of B , and are shown by the shaded area.

Synchrotron constraints are most important at the lowest injection energies ($E_0 \sim 1 - 30$ GeV), while the upper limits at higher initial energies (from ~ 30 GeV to 10 TeV) are due to ICS in the gamma-ray regime. The intensity of the magnetic field affects both processes in an opposite way: for low values of the magnetic field, all energy is lost by inverse Compton scattering, and synchrotron emission is almost irrelevant; as one increases the value of B , synchrotron constraints become more important at the expense of ICS emission. In the most extreme case ($B = 100 \mu\text{G}$), gamma-ray constraints are negligible, and the upper limits derived from synchrotron radiation are well approximated by a pure power law. For large values of the magnetic field, the synchrotron constraints are more stringent than the upper limits derived from the positron spectrum.

In the middle panel of Figure 5.6, we investigate the upper limits of synchrotron and ICS for different models of the interstellar radiation field. As mentioned in Section 3.2.2 and 5.1, we adopted the parameterization proposed by Cirelli and Panci (2009) in terms of three black-body components. The temperatures and normalizations of each component are summarized in Table 5.2. The effect of the ISRF is similar to that of the magnetic field, but in the opposite direction: a higher photon density results in a larger amount of energy being lost by inverse Compton scattering rather than synchrotron emission. Nevertheless, for reasonable values of the model parameters, the upper limits on $\langle \sigma v \rangle$ do not vary by more than a factor of three.

As shown on the bottom panel of Figure 5.6, the effect of the diffusion coefficient is even smaller. The upper limits are slightly more stringent when the electrons and positrons are allowed to travel a shorter distance from the place where they were injected, but the difference between the three propagation models discussed by Donato et al. (2004a) is barely noticeable. Thus, we conclude that our results are not severely affected by the astrophysical uncertainties associated to particle propagation. In particular, synchrotron and inverse Compton constraints are weaker than the upper limits from final-state radiation and the local positron spectrum for any value of the magnetic field, the interstellar radiation field, or the diffusion coefficient.

In contrast, the exact value of the inner slope α of the dark matter density profile plays a very important role in setting the actual constraints on $\langle \sigma v \rangle$. We have investigated several values in the interval $0 < \alpha < 2$ (the appropriate values of ρ_s and r_s are quoted in Table 4.2) as well as the Einasto profile given by equation (5.1). We report in Figure 5.7 the upper limits obtained from the comparison of the predicted final-state radiation, synchrotron, and inverse Compton scattering emission for $\alpha = 0.50, 1.00, 1.25$, and 1.50 with our multi-wavelength observational data set. Results for FSR and the combination of synchrotron and ICS emission are plotted separately. Constraints from the local positron spectrum are independent of α and are shown as a solid area.

The top panel of the figure shows the upper limits obtained by the same procedure

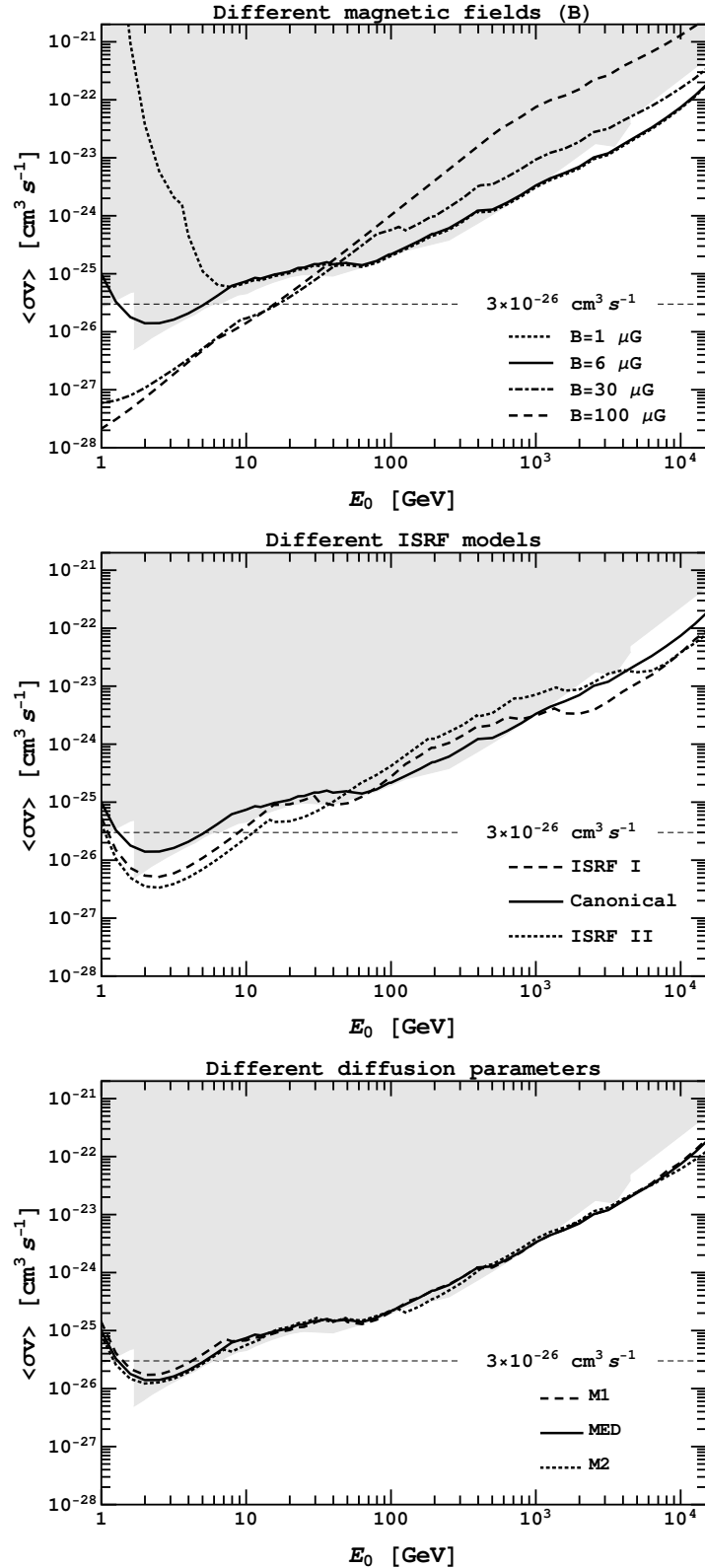


Figure 5.6: Upper limits on the dark matter annihilation cross-section from synchrotron and ICS, for different values of the magnetic field (top), interstellar radiation field (middle), and diffusion coefficient (bottom). Constraints from FSR and the local positron spectrum are indicated by the shaded area.

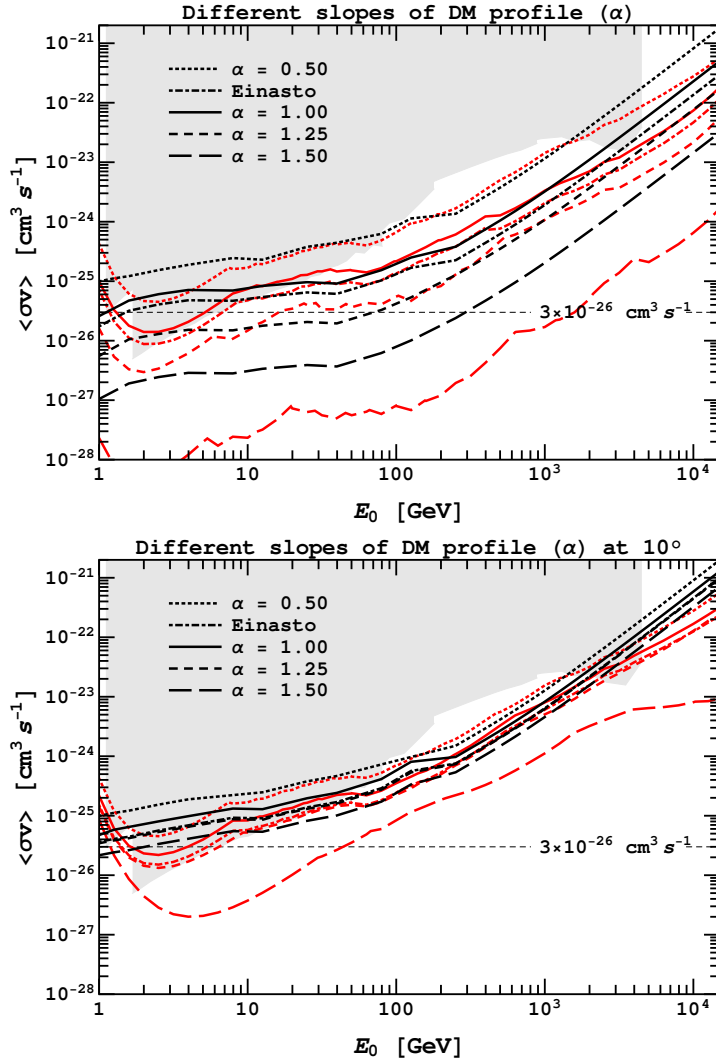


Figure 5.7: Upper limits on the dark matter annihilation cross-section for different values of the inner logarithmic slope α of the dark matter density profile. On the top panel, the constraints are derived from the angle that provides the most stringent limit (see Figure 5.2 for the canonical case $\alpha = 1$), whereas all the constraints on the bottom panel are obtained from the observed emission at $\theta = 10^\circ$ from the Galactic centre. In both cases, black and red lines represent the limits associated to FSR and Synchrotron+ICS emission, respectively. The constraints from the local positron spectrum (independent on α) are shown by the shadowed areas.

applied to the canonical model, i.e. choosing the angular separation θ that provides the tightest constraint. Not surprisingly, larger values of α result in lower values of θ . The constraints from FSR and Synchrotron+ICS emission come from innermost 1° for $\alpha > 0.5$ and $\alpha > 1.25$, respectively.

Since the particle production rate near the centre of the Milky Way increases dramatically with the value of the inner slope of the density profile, this is, by far, the most relevant astrophysical parameter. For $\alpha > 1.25$, the upper limits from final-state radiation are always stronger than the constraints provided by the local positron spectrum, and they rule out a cross-section larger than $3 \times 10^{-26} \text{ cm}^3 \text{ s}^{-1}$ is rule out for any dark matter candidate lighter than $\sim 100 \text{ GeV}$. On the contrary, if the dark matter density profile of the Milky Way was shallow, with a logarithmic slope significantly below $\alpha = 1$, the positron spectrum in the solar neighbourhood would provide the most stringent limits on dark matter annihilation, and therefore the constraints would not depend at all on the actual value of the logarithmic slope.

One may remove the dependency of the results on the precise shape of the dark matter density profile by fixing $\theta = 10^\circ$ when comparing model predictions with observational data. As shown in the bottom panel of Figure 5.7, we find, in agreement with previous work (e.g. Serpico and Zaharijas, 2008; Ackermann et al., 2012c), that the uncertainty associated to the precise value of α reduces to about a factor of 2 when the comparison is restricted to the photon intensity at $\theta = 10^\circ$. While this is therefore a good choice when the goal is to provide a conservative upper limit on the dark matter annihilation cross-section, we would like to stress that any prior knowledge of the dark matter density profile may lead to much stronger constraints if the inner slope was steeper than $\alpha = 1$, as evidenced in the upper panel.

5.5 Constraints on the inner slope of the density profile

As pointed out in Ascasibar et al. (2006), the photons from the central region of the Galaxy contain information on *both* the dark matter annihilation cross-section and the shape of the density profile. By assuming a given value of the cross-section, one can constrain the value of α from the total intensity and the morphology of the observed surface brightness.

In this work, we will focus only on the total intensity from the central bin (i.e. one degree around the Galactic centre) in order to derive a robust upper limit. More detailed constraints could be obtained from the shape of the surface brightness profiles at different wavelengths once the astrophysical contribution is adequately subtracted. We set the dark matter annihilation cross-section into electron-positron pairs to the value expected for a thermally-produced relic, $\langle \sigma v \rangle_{e^\pm} = 3 \times 10^{-26} \text{ cm}^3 \text{ s}^{-1}$, and compute the value of α for which the predicted emission rises above the observed level.

The corresponding upper limits are plotted in Figure 5.8 as a function of the initial energy E_0 associated to the mass of dark matter candidate. Our results show that, for a thermal relic with $m_{\text{dm}} < 100 \text{ GeV}$, the dark matter density profile of the Milky Way *must* be shallower than $\alpha \sim 1.3$ in order not to overproduce the observed signal. It is worth noting that, since final-state radiation only depends on the injection rate, this constraint on the inner logarithmic slope α is independent on the other astrophysical parameters. Synchrotron and inverse Compton scattering yield stronger limits than FSR at low and high injection energies, respectively, although of course these results depend much more on the details of the adopted propagation model (most notably, the intensity of the magnetic field). For our canonical set-up, synchrotron radiation imposes extremely tight constraints for a limited range of dark matter masses, around a few GeV (observational data at

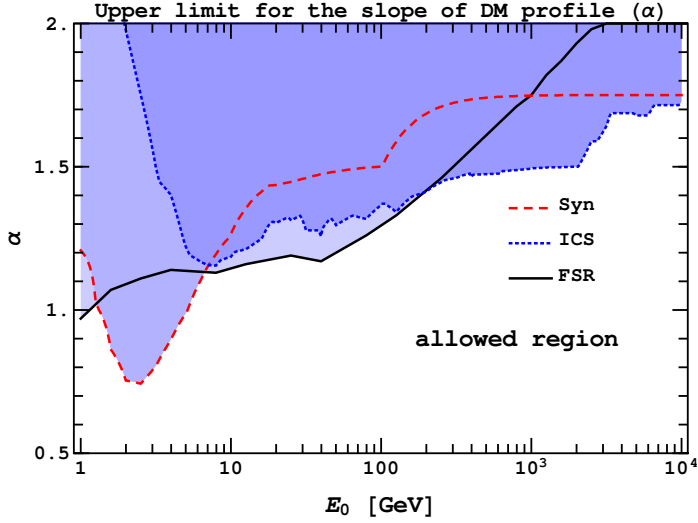


Figure 5.8: Upper limits on the inner logarithmic slope α of dark matter density profile, obtained by imposing that FSR, ICS and synchrotron emission do not overproduce the observed signal (according to the Fermi data) for a thermal dark matter relic (i.e. $\langle \sigma v \rangle_{e^\pm} = 3 \times 10^{-26} \text{ cm}^3 \text{ s}^{-1}$).

lower frequencies would probably make possible to extend these constraints toward lower masses). In particular, the standard case $\alpha = 1$ would be excluded for $E_0 < 5 \text{ GeV}$. At high energies, ICS emission rules out slopes steeper than $\alpha = 1.5$ for dark matter masses below $\sim 2 \text{ TeV}$. The regime $\alpha > 1.8$ seems to be excluded in any case.

The fact that we are considering the total radio and gamma-ray emission, without taking into account the contribution of astrophysical origin, implies that these are a conservative upper limit, and therefore we can conclude that, if dark matter particles annihilate primarily into electrons and positrons (or, more generally, any lepton pair), any scenario where the Milky Way features a steep density profile (due to e.g. adiabatic contraction) may be firmly ruled out.

5.6 Conclusions

We have investigated the constraints on the dark matter annihilation cross-section into electron-positron pairs by comparing the predictions of an analytic model of particle propagation with a multi-wavelength set of observational data obtained from the literature. We have compared the expected emission from synchrotron radiation, inverse Compton scattering and final-state radiation within the Milky Way with 18 maps of the sky at different frequencies: the Haslam radio map at 408 MHz, the 7-year data from the Wilkinson Microwave Anisotropy Probe (WMAP) in its 5 bands (23 GHz, 33 GHz, 41 GHz, 61 GHz, and 94 GHz), and gamma-ray maps from the Fermi Large Area Telescope (LAT) binned in 12 different channels (from 0.3 to 300 GeV). A straightforward statistical criterion has been followed in order to mask the most obvious astrophysical signals (i.e. the emission from the galactic disc and prominent point sources), and observational upper limits are derived from the remaining spherically-symmetric component. In addition, we have also imposed that the predicted abundance of electrons and positrons in the solar neighbourhood does not exceed the measurements by PAMELA, H.E.S.S. and Fermi. Our main results can be summarized as follows:

1. If the density profile of the Milky Way halo is steep ($\alpha > 1$), the exact value of inner logarithmic slope plays a crucial role in the upper limit on the annihilation cross-section. The adiabatic contraction scenario is hardly consistent with any dark matter candidate lighter than ~ 100 GeV and $\langle \sigma v \rangle_{e^\pm} = 3 \times 10^{-26} \text{ cm}^3 \text{ s}^{-1}$.
2. If the density profile of the Milky Way halo is relatively shallow ($\alpha < 1$), the upper limit on the cross-section is set by the local positron spectrum for low values of the injection energy. Combining both types of messenger (photons and positrons) is thus of the utmost importance in this case. Considering the positron spectrum separately makes possible to rule out cross-sections above $3 \times 10^{-26} \text{ cm}^3 \text{ s}^{-1}$ for dark matter particles lighter than a few GeV.
3. These results are fairly robust (by about a factor of two uncertainty) with respect to the propagation parameters. However, a high magnetic field in the Galactic center (above our canonical value of 6 μG) would result in tighter constraints.

Let us conclude by noting that the current upper limits are close to – or have just reached – the expected annihilation cross-section for a thermal relic, and similar constraints (sometimes even stronger, and very robust against uncertainties) have also been obtained from the analysis of the CMB, the gamma-ray emission from nearby dwarf galaxies, and direct detection experiments. Therefore, a better understanding of the production of positrons and gamma rays by astrophysical sources should thus lead to the detection of an exquisite probe of the distribution of dark matter in the innermost regions of the Galactic halo. Otherwise, the most straightforward versions of the leptophilic dark matter scenario would be ruled out completely.

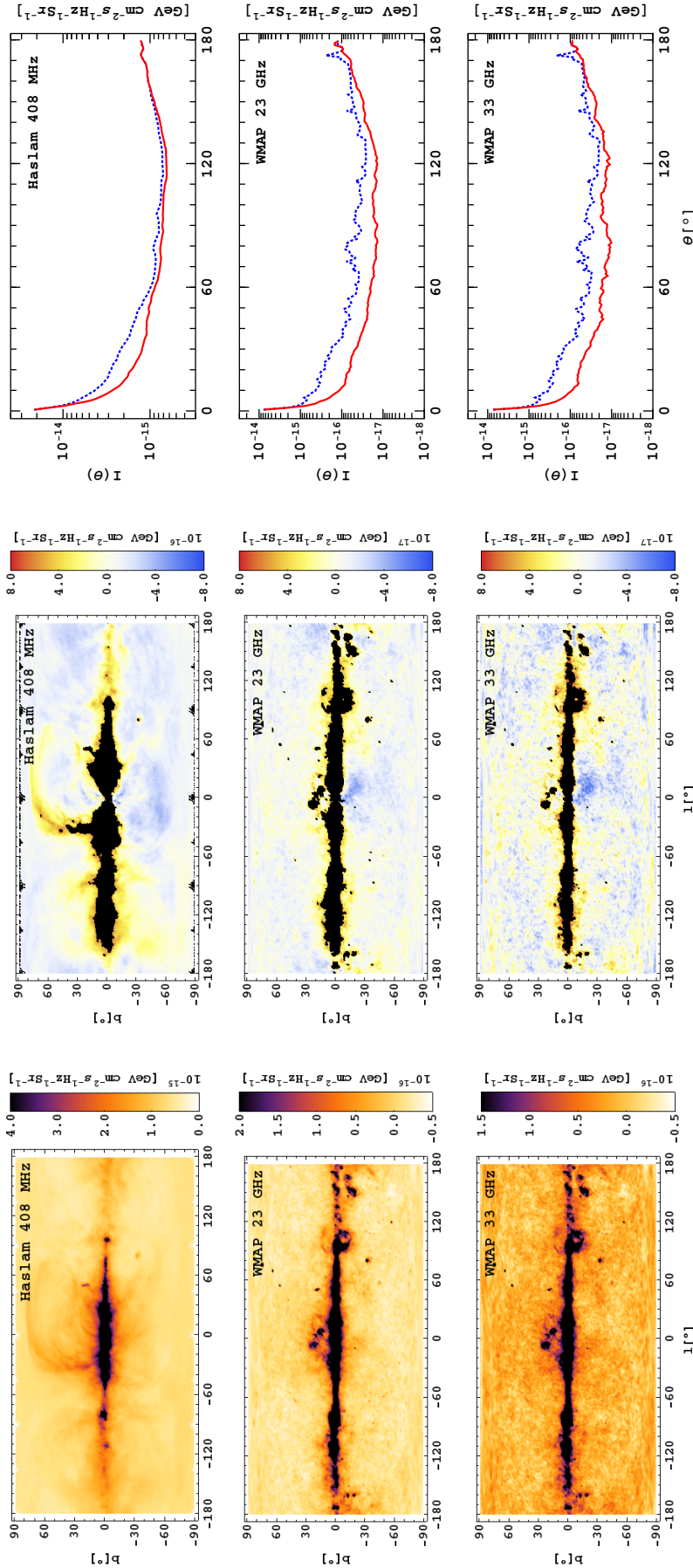


Figure 5.9: Haslam and WMAP intensity maps $I(l, b)$ in Galactic coordinates (left), masked residual maps $I(l, b) - I(\theta)$ (middle), and spherically-averaged intensities (right). Dotted blue lines represent the original mean intensity $I_0(\theta)$, while solid red lines correspond to the final intensity $I(\theta)$ after discarding the outliers (black areas in the masked residual maps).

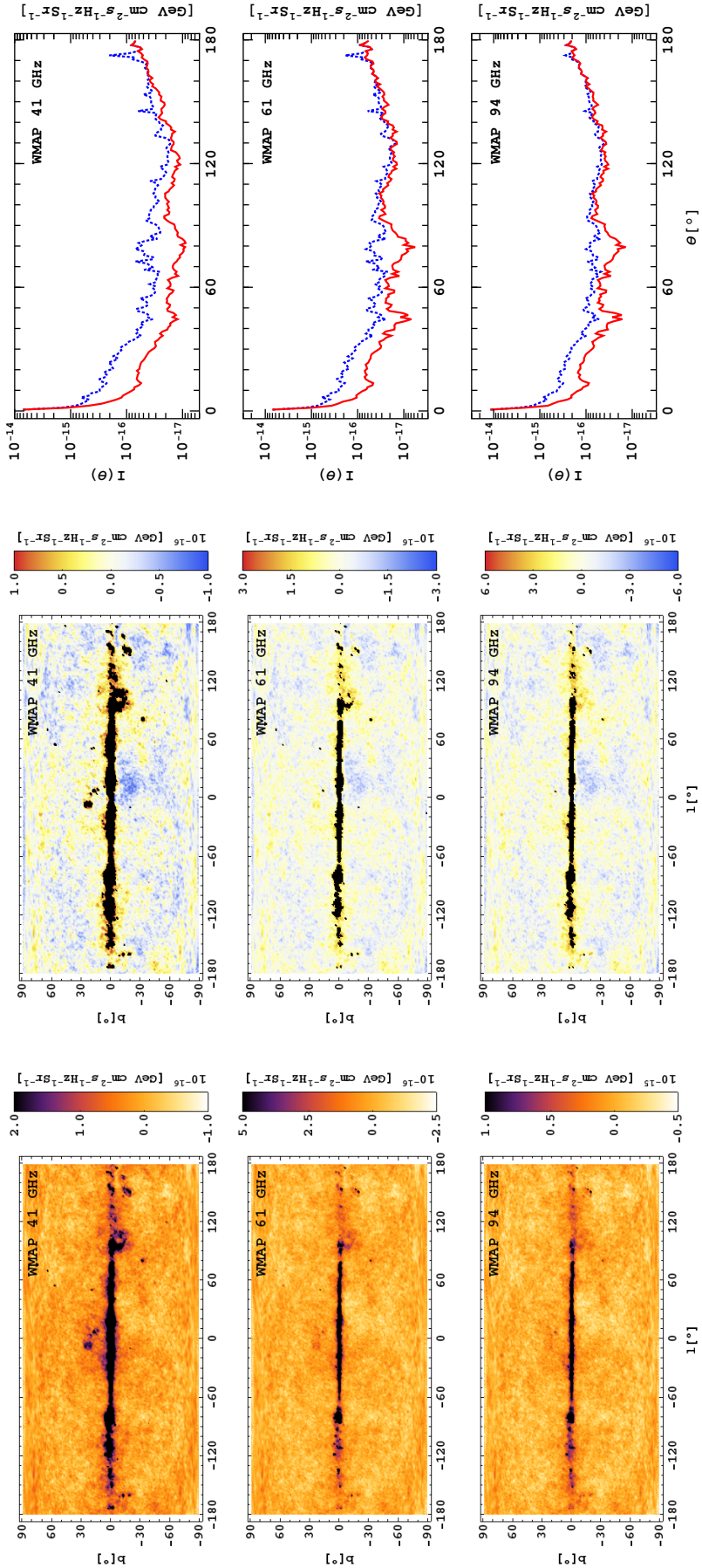


Figure 5.10: WMAP intensity maps $I(l, b)$ in Galactic coordinates (left), masked residual maps $I(l, b) - I(\theta)$ (middle), and spherically-averaged intensities (right). Dotted red lines represent the original mean intensity $I_0(\theta)$, while solid blue lines correspond to the final intensity $I(\theta)$ after discarding the outliers (black areas in the masked residual maps).

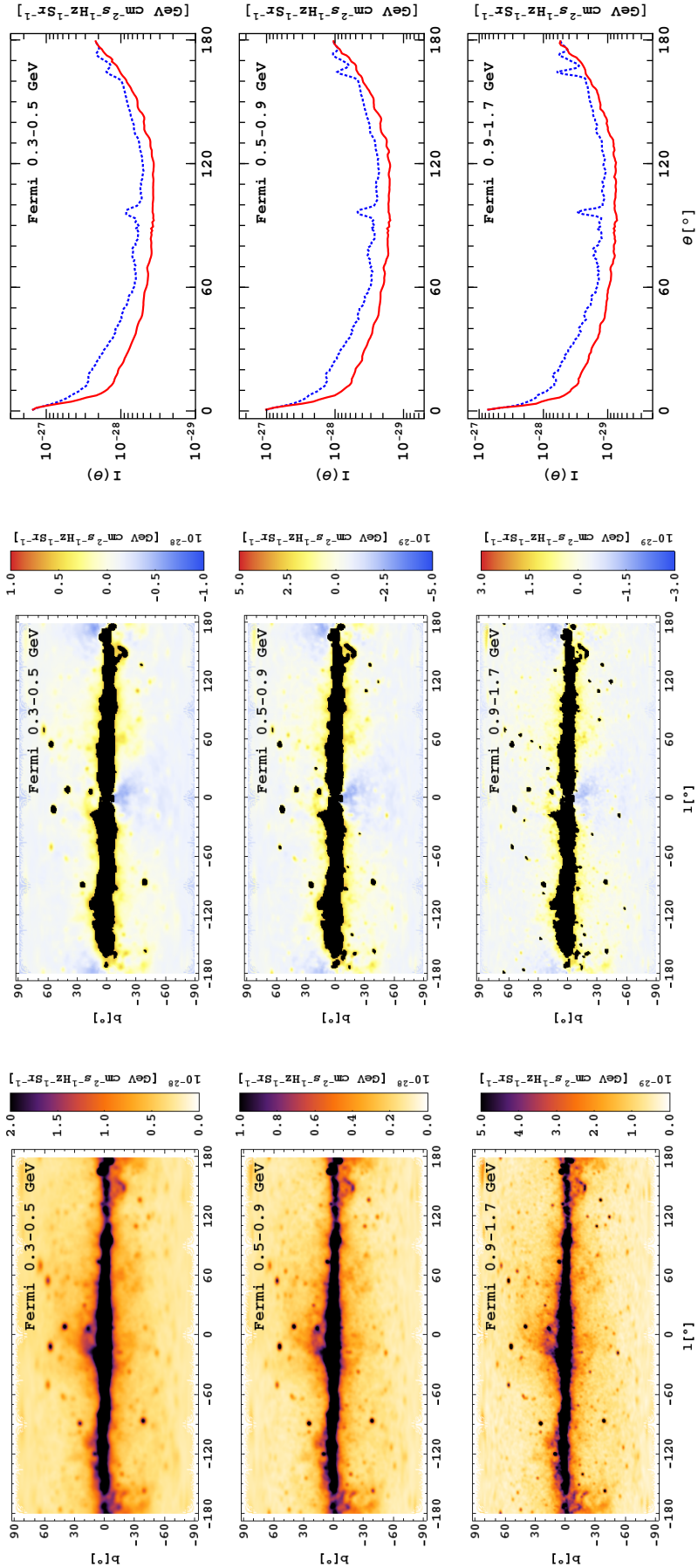


Figure 5.11: Fermi intensity maps $I(l, b)$ in Galactic coordinates (left), masked residual maps $I(l, b) - I(\theta)$ (middle), and spherically-averaged intensities (right). Dotted blue lines represent the original mean intensity $I_0(\theta)$, while solid red lines correspond to the final intensity $I(\theta)$ after discarding the outliers (black areas in the masked residual maps).

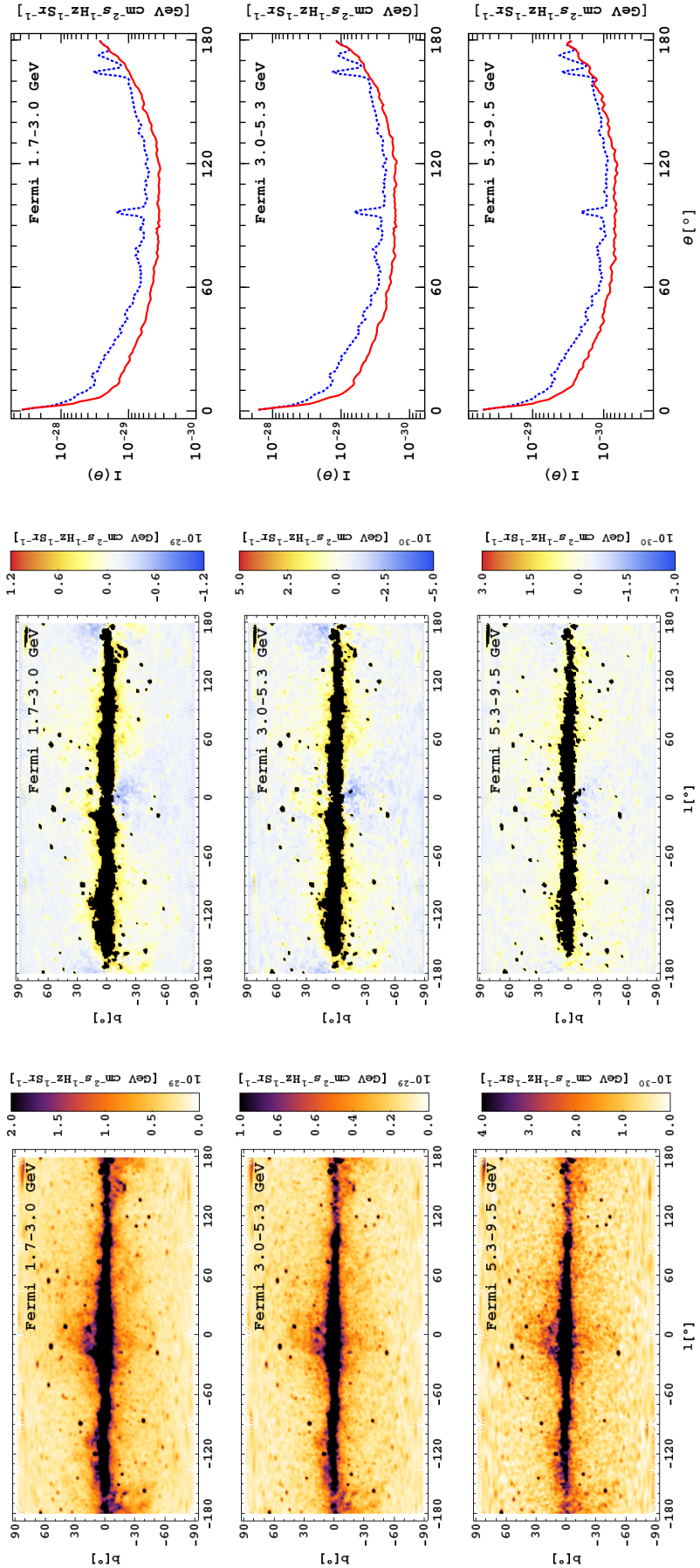


Figure 5.12: Fermi intensity maps $I(l, b)$ in Galactic coordinates (left), masked residual maps $I(l, b) - I(\theta)$ (middle), and spherically-averaged intensities (right). Dotted blue lines represent the original mean intensity $I_0(\theta)$, while solid red lines correspond to the final intensity $I(\theta)$ after discarding the outliers (black areas in the masked residual maps). For the last two bands, we opted to use the original average intensity $I_0(\theta)$ without applying any mask.

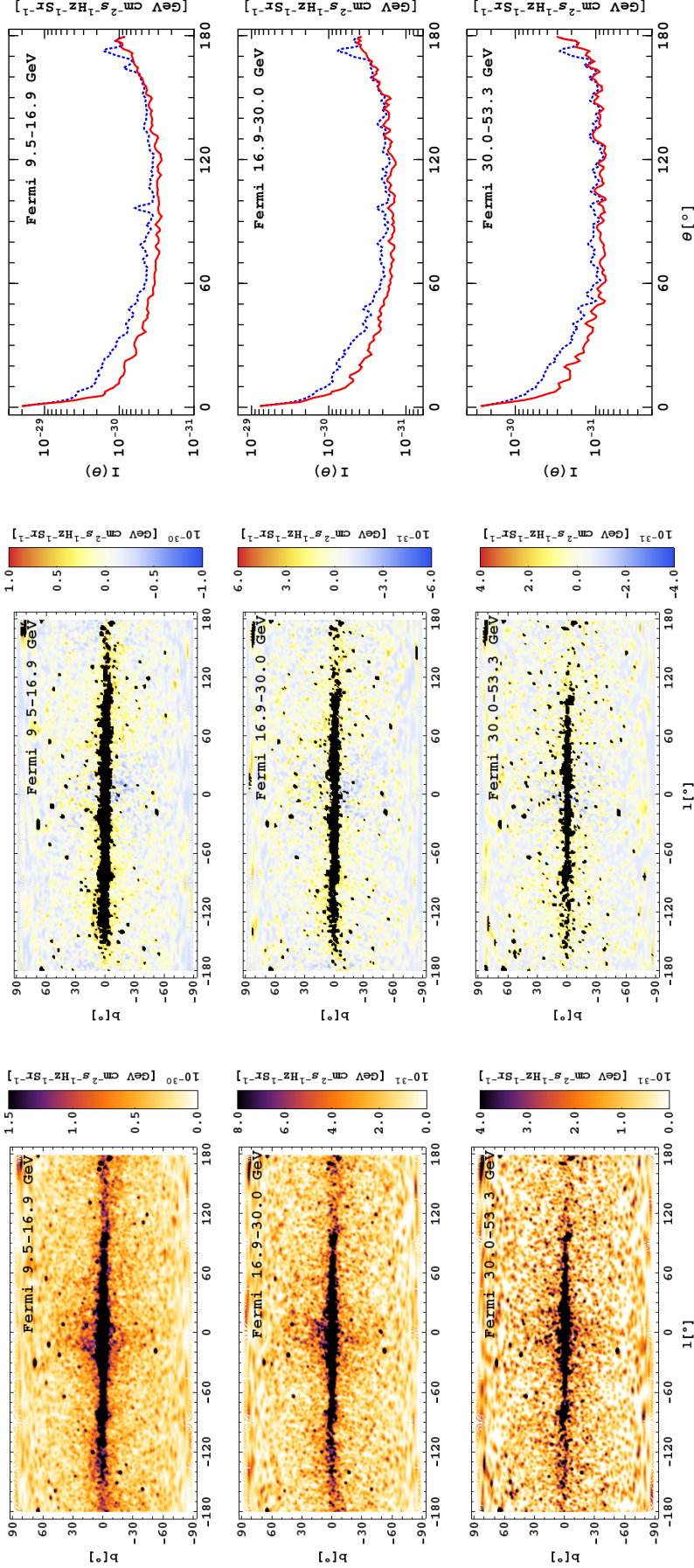


Figure 5.13: Fermi intensity maps $I(l, b)$ in Galactic coordinates (left), masked residual maps $I(l, b) - I(\theta)$ (middle), and spherically-averaged intensities (right). Dotted blue lines represent the original mean intensity $I_0(\theta)$, while solid red lines correspond to the final intensity $I(\theta)$ after discarding the outliers (black areas in the masked residual maps). For the last two bands, we opted to use the original average intensity $I_0(\theta)$ without applying any mask.

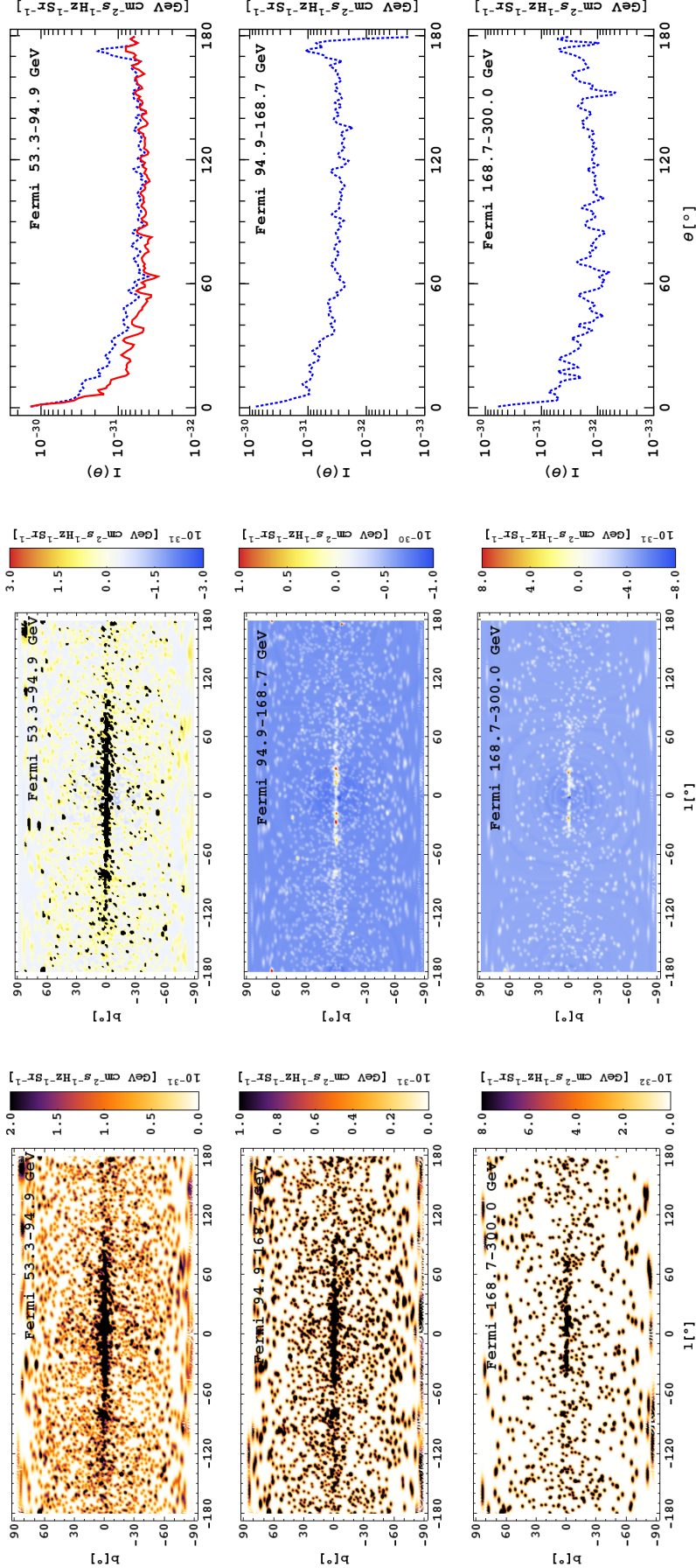


Figure 5.14: Fermi intensity maps $I(l, b)$ in Galactic coordinates (left), masked residual maps $I(l, b) - I(\theta)$ (middle), and spherically-averaged intensities (right). Dotted blue lines represent the original mean intensity $I_0(\theta)$, while solid red lines correspond to the final intensity $I(\theta)$ after discarding the outliers (black areas in the masked residual maps). For the last two bands, we opted to use the original average intensity $I_0(\theta)$ without applying any mask.

θ [$^\circ$]	Haslam				WMAP				
	408 MHz		23 GHz		33 GHz				
	$I_0(\theta)$	$I(\theta)$ $\times 10^{-17}$	$\sigma(\theta)$	$I_0(\theta)$	$I(\theta)$ $\times 10^{-17}$	$\sigma(\theta)$	$I_0(\theta)$	$I(\theta)$ $\times 10^{-17}$	$\sigma(\theta)$
0.5	2092.2	2088.7	33.5	743.9	729.5	3.2	703.8	698.9	5.4
1.5	1476.9	1456.0	35.2	210.4	202.3	3.7	167.8	148.8	4.0
2.5	1034.5	952.1	34.0	116.2	72.0	3.3	92.3	55.2	3.9
3.5	848.1	738.8	35.8	90.6	43.8	2.9	72.5	33.0	3.8
4.5	731.7	544.5	28.9	76.5	35.1	3.2	61.6	22.6	4.1
5.5	648.7	441.3	24.7	67.6	24.2	3.3	54.0	17.9	3.5
6.5	597.5	388.5	24.2	81.1	19.4	2.9	70.9	14.6	3.2
7.5	534.4	343.5	27.3	63.2	17.1	2.9	52.1	12.6	2.8
8.5	493.8	308.8	31.8	56.4	14.4	3.1	48.1	11.2	3.5
9.5	444.1	282.6	28.7	43.6	12.1	3.1	34.8	9.6	3.5
10.5	417.0	260.0	28.2	41.9	10.7	3.1	34.4	8.5	3.8
12.5	363.0	220.9	26.6	34.2	8.6	2.9	27.9	6.7	3.3
14.5	330.8	200.8	23.4	39.3	8.2	3.1	33.2	6.7	3.5
16.5	303.4	182.0	22.8	32.0	7.7	3.1	26.4	6.5	3.5
18.5	294.0	175.6	23.2	33.2	7.3	3.2	28.2	6.2	3.5
20.5	276.5	159.5	22.0	24.5	6.5	3.2	19.7	6.0	3.9
25.5	236.4	136.3	19.4	19.9	5.8	3.0	16.1	4.8	3.3
30.5	212.9	123.1	20.6	17.8	4.4	2.1	14.7	3.5	2.8
40.5	161.0	109.5	25.4	8.5	2.9	1.7	6.4	2.1	2.3
50.5	129.9	103.0	24.9	6.7	2.3	1.4	5.3	1.8	2.0
60.5	97.5	87.3	21.9	4.2	2.0	1.6	3.4	1.7	2.3
70.5	86.6	76.2	16.2	4.7	1.7	1.3	4.0	1.5	2.1
80.5	89.7	75.3	17.2	6.8	1.5	1.4	5.8	1.2	2.0
90.5	80.0	72.3	19.5	4.1	1.4	1.3	3.4	1.3	2.2
100.5	76.3	70.5	16.7	3.5	1.8	1.6	3.0	1.8	2.3
110.5	74.6	66.7	16.9	3.7	1.5	1.6	3.1	1.4	2.5
120.5	72.3	65.0	17.9	2.6	1.4	1.5	2.0	1.2	2.4
130.5	75.0	68.7	20.7	2.6	1.8	1.8	2.0	1.5	2.7
140.5	82.8	77.0	22.9	4.1	2.8	2.2	3.1	2.2	2.7
150.5	94.2	90.0	20.5	5.3	3.0	2.1	4.1	2.4	2.8

Table 5.3: Haslam and WMAP: Original observational mean intensity $I_0(\theta)$, final mean intensity after discard the outliers $I(\theta)$ and standard deviation $\sigma(\theta)$ in the unit of $\text{GeV cm}^{-2} \text{ s}^{-1} \text{ Hz}^{-1} \text{ sr}^{-1}$.

θ [$^\circ$]	WMAP								
	41 GHz			61 GHz			94 GHz		
	$I_0(\theta)$	$I(\theta)$ $\times 10^{-17}$	$\sigma(\theta)$	$I_0(\theta)$	$I(\theta)$ $\times 10^{-17}$	$\sigma(\theta)$	$I_0(\theta)$	$I(\theta)$ $\times 10^{-17}$	$\sigma(\theta)$
0.5	682.0	681.0	4.4	660.2	670.6	8.7	1097.8	1132.3	22.2
1.5	147.8	119.0	5.8	137.3	98.8	11.7	287.4	219.6	24.5
2.5	81.1	47.9	5.4	73.9	36.5	9.3	140.3	66.9	21.4
3.5	64.0	27.9	5.0	58.9	26.6	9.6	114.6	52.3	21.2
4.5	54.1	20.4	5.2	48.0	20.8	10.1	85.1	39.9	21.8
5.5	47.0	15.3	4.3	40.3	13.2	8.6	69.9	25.3	19.2
6.5	65.5	12.3	3.9	60.4	10.5	8.0	86.1	20.6	18.3
7.5	46.4	11.5	4.0	41.1	10.7	7.8	66.6	20.8	17.8
8.5	43.7	9.8	4.2	39.9	9.4	8.2	61.9	18.0	18.1
9.5	30.1	8.4	4.1	25.2	8.0	8.3	43.2	15.7	18.6
10.5	30.3	7.3	4.4	25.9	6.4	8.4	41.6	12.5	19.0
12.5	24.5	6.0	4.2	21.0	4.7	7.5	33.5	9.1	17.5
14.5	29.9	6.2	4.3	26.1	5.8	8.1	39.5	11.7	18.5
16.5	23.5	6.5	4.4	21.4	7.1	8.2	36.6	14.3	18.5
18.5	25.5	6.0	4.4	23.7	6.8	8.5	39.0	15.0	19.4
20.5	17.2	5.9	4.9	15.3	6.2	9.1	27.8	13.2	20.5
25.5	14.2	4.7	4.4	12.8	5.2	8.3	22.9	11.1	18.4
30.5	13.1	3.2	3.7	12.0	3.2	7.6	20.9	7.0	17.4
40.5	5.5	1.8	3.2	4.6	1.6	7.1	9.3	3.5	15.9
50.5	4.6	1.7	2.9	4.5	1.9	6.7	9.4	4.4	15.2
60.5	3.1	1.7	3.2	3.3	2.1	7.1	7.3	4.9	16.1
70.5	3.8	1.5	3.1	3.9	1.8	6.8	7.3	4.0	15.1
80.5	5.3	1.1	3.0	4.9	1.0	6.6	7.7	2.2	14.9
90.5	3.0	1.4	3.3	3.0	1.8	7.0	6.4	3.9	15.6
100.5	3.0	1.9	3.1	3.5	2.8	6.9	7.7	6.2	15.4
110.5	2.9	1.6	3.6	3.2	2.3	7.5	6.9	5.1	16.6
120.5	1.8	1.2	3.4	1.8	1.4	7.4	4.5	3.5	16.6
130.5	1.7	1.4	3.7	1.6	1.4	7.7	4.1	3.7	17.6
140.5	2.7	2.0	3.7	2.7	2.2	8.1	6.8	5.6	18.9
150.5	3.6	2.5	4.0	3.5	2.7	8.2	8.6	7.0	19.0

Table 5.4: WMAP: Original observational mean intensity $I_0(\theta)$, final mean intensity after discard the outliers $I(\theta)$ and standard deviation $\sigma(\theta)$ in the unit of $\text{GeV cm}^{-2} \text{s}^{-1} \text{Hz}^{-1} \text{sr}^{-1}$.

θ [$^\circ$]	Fermi								
	0.3-0.5 GeV			0.5-0.9 GeV			0.9-1.7 GeV		
	$I_0(\theta)$	$I(\theta)$ $\times 10^{-30}$	$\sigma(\theta)$	$I_0(\theta)$	$I(\theta)$ $\times 10^{-30}$	$\sigma(\theta)$	$I_0(\theta)$	$I(\theta)$ $\times 10^{-30}$	$\sigma(\theta)$
0.5	1500.2	1506.8	34.3	989.9	1016.7	18.7	713.6	725.8	9.1
1.5	1295.6	1353.7	37.3	774.3	790.1	16.6	447.3	462.2	9.8
2.5	1037.0	992.3	37.0	553.9	508.8	19.8	275.9	219.7	9.9
3.5	826.8	689.0	34.2	418.4	304.9	16.7	211.3	129.4	8.8
4.5	680.6	460.1	36.1	340.2	208.4	17.8	174.1	107.2	9.1
5.5	585.4	358.1	34.3	293.0	170.4	16.8	146.5	82.5	8.3
6.5	509.1	289.2	32.1	258.2	133.7	16.1	129.9	56.2	9.3
7.5	470.1	213.9	38.6	243.3	101.3	19.3	126.2	47.8	7.7
8.5	415.0	184.3	35.3	211.3	90.0	17.5	107.7	42.6	8.0
9.5	367.1	165.0	33.0	181.9	80.7	16.7	89.5	38.4	8.1
10.5	341.4	150.7	31.9	167.5	74.2	17.0	83.5	36.8	8.6
12.5	285.3	132.9	30.0	137.5	61.5	14.8	67.8	30.3	7.7
14.5	271.2	123.1	31.7	130.1	56.9	15.8	63.7	28.2	8.0
16.5	272.5	117.7	35.1	135.2	55.0	16.8	70.1	27.2	8.3
18.5	264.6	110.3	34.7	132.4	51.7	16.7	66.6	25.7	8.7
20.5	241.1	106.6	33.4	118.3	49.9	16.6	57.9	23.7	8.1
25.5	193.1	89.0	27.0	93.5	40.1	12.4	46.3	19.7	6.7
30.5	160.3	76.2	21.4	78.9	36.0	11.1	39.1	17.7	6.1
40.5	115.6	60.7	19.6	56.0	27.9	10.0	27.8	13.2	5.1
50.5	87.4	50.2	16.8	41.5	22.6	8.3	19.8	10.6	4.5
60.5	65.4	45.1	18.4	30.1	20.0	9.3	14.4	9.5	4.8
70.5	63.3	43.4	16.7	29.2	19.1	8.4	13.6	8.7	4.3
80.5	63.3	39.2	16.0	29.2	17.1	7.7	14.0	8.0	3.9
90.5	59.4	37.4	15.7	27.4	16.3	8.2	13.0	7.8	4.6
100.5	57.8	37.4	15.6	25.9	16.6	7.9	12.0	7.9	4.3
110.5	54.1	36.8	15.0	25.2	15.9	7.6	11.9	7.4	4.0
120.5	51.3	36.3	13.8	23.7	16.0	7.0	11.4	7.4	3.5
130.5	57.2	40.2	15.6	26.1	17.5	7.7	12.3	8.2	3.8
140.5	70.5	49.4	20.4	32.8	21.4	9.6	15.7	10.2	4.9
150.5	83.2	60.0	26.1	39.3	27.2	12.5	19.1	13.4	6.6

Table 5.5: Fermi: Original observational mean intensity $I_0(\theta)$, final mean intensity after discard the outliers $I(\theta)$ and standard deviation $\sigma(\theta)$ in the unit of $\text{GeV}\text{cm}^{-2}\text{s}^{-1}\text{Hz}^{-1}\text{Sr}^{-1}$.

θ [$^{\circ}$]	Fermi								
	1.7-3.0 GeV			3.0-5.3 GeV			5.3-9.5 GeV		
	$I_0(\theta)$	$I(\theta)$ $\times 10^{-31}$	$\sigma(\theta)$	$I_0(\theta)$	$I(\theta)$ $\times 10^{-31}$	$\sigma(\theta)$	$I_0(\theta)$	$I(\theta)$ $\times 10^{-31}$	$\sigma(\theta)$
0.5	3677.0	3711.1	46.4	1554.0	1574.6	19.2	482.4	488.9	7.5
1.5	2301.0	2452.5	46.6	950.3	941.4	17.8	311.6	321.6	7.5
2.5	1397.0	1165.2	48.5	577.1	468.4	20.9	201.6	163.2	7.3
3.5	1067.0	665.6	39.6	443.4	278.5	17.8	158.6	101.2	7.1
4.5	868.0	533.4	42.7	360.0	220.5	18.4	129.0	82.1	7.9
5.5	718.0	366.7	44.3	305.0	181.7	17.6	106.7	60.1	7.3
6.5	634.0	268.7	41.4	274.4	149.0	15.7	93.0	53.1	6.1
7.5	617.0	238.1	39.5	263.3	109.0	21.7	89.9	47.3	6.7
8.5	521.0	215.0	38.3	221.0	94.7	17.7	78.7	41.4	8.0
9.5	429.0	194.7	35.5	182.7	85.8	15.3	67.2	36.6	8.2
10.5	398.0	182.5	39.1	169.4	78.0	17.2	63.0	33.2	7.8
12.5	322.0	148.5	34.9	140.5	66.4	16.2	52.6	27.1	6.7
14.5	315.0	135.5	35.0	132.9	65.9	16.5	49.9	25.6	6.6
16.5	345.0	132.4	39.0	146.3	61.7	16.4	52.4	24.0	7.1
18.5	322.0	123.4	39.8	136.3	53.9	16.5	50.5	22.6	6.6
20.5	280.0	114.6	39.5	116.8	51.4	17.0	44.6	20.4	5.9
25.5	227.0	95.9	32.2	94.5	42.6	15.2	35.2	17.1	5.3
30.5	186.0	83.5	26.6	79.0	36.8	10.6	29.7	14.5	5.0
40.5	134.0	64.1	23.6	57.8	29.6	10.6	21.2	11.2	4.7
50.5	97.0	51.6	22.1	39.8	21.8	8.7	15.7	9.5	4.3
60.5	68.0	45.4	22.7	28.3	19.9	9.5	11.6	8.2	3.6
70.5	65.0	41.1	20.2	27.0	18.1	9.0	11.1	7.8	4.1
80.5	65.0	36.9	18.4	27.7	16.5	7.5	11.3	7.2	3.8
90.5	60.0	35.9	21.0	25.7	16.0	8.6	9.7	6.9	3.5
100.5	57.0	37.6	20.8	23.6	16.2	8.6	9.2	6.7	4.0
110.5	56.0	35.2	19.6	23.8	15.7	8.4	9.3	6.9	3.7
120.5	55.0	36.0	19.4	22.6	15.4	7.9	8.8	6.5	3.4
130.5	58.0	38.2	18.5	24.3	17.8	9.2	9.9	7.8	4.3
140.5	71.8	49.0	24.3	30.0	21.3	11.2	10.9	8.6	4.5
150.5	87.0	60.6	28.6	35.2	26.1	12.5	12.9	10.7	5.3

Table 5.6: Fermi: Original observational mean intensity $I_0(\theta)$, final mean intensity after discard the outliers $I(\theta)$ and standard deviation $\sigma(\theta)$ in the unit of $\text{GeV}\text{cm}^{-2}\text{s}^{-1}\text{Hz}^{-1}\text{Sr}^{-1}$.

θ [$^\circ$]	Fermi								
	9.5-16.9 GeV			16.9-30.0 GeV			30.0-53.3 GeV		
	$I_0(\theta)$	$I(\theta)$ $\times 10^{-31}$	$\sigma(\theta)$	$I_0(\theta)$	$I(\theta)$ $\times 10^{-31}$	$\sigma(\theta)$	$I_0(\theta)$	$I(\theta)$ $\times 10^{-32}$	$\sigma(\theta)$
0.5	188.8	195.6	3.1	74.4	75.7	1.8	253.5	263.1	13.8
1.5	118.7	116.7	3.4	45.9	44.7	2.2	189.2	183.6	14.5
2.5	71.7	60.3	3.7	29.3	23.3	1.9	144.4	113.8	12.9
3.5	51.5	37.5	3.4	23.3	19.1	1.7	115.9	76.8	12.3
4.5	42.7	27.8	3.6	19.3	16.0	2.0	97.8	58.0	13.2
5.5	38.6	16.9	3.2	17.3	11.9	1.9	86.2	47.6	11.4
6.5	36.6	15.6	3.4	15.6	9.4	2.1	71.5	39.8	9.9
7.5	36.2	15.5	3.3	14.9	9.1	2.0	71.0	32.1	12.8
8.5	30.5	13.9	3.4	13.4	7.2	2.2	64.3	29.7	12.5
9.5	24.7	11.9	3.1	11.3	6.1	1.9	55.4	27.6	11.1
10.5	22.4	11.2	3.2	10.4	5.7	1.8	55.1	28.4	11.9
12.5	20.3	10.0	3.2	8.8	4.8	1.8	48.5	25.3	11.8
14.5	19.5	9.5	3.1	9.1	5.4	1.9	44.0	20.9	11.4
16.5	18.9	8.6	2.5	8.8	4.6	1.7	43.7	21.0	10.2
18.5	18.0	8.5	2.8	7.5	3.9	1.7	39.7	21.9	11.1
20.5	17.0	8.5	3.0	7.9	4.0	1.7	39.2	22.7	11.4
25.5	12.9	6.0	2.5	6.0	2.8	1.5	28.9	16.5	9.8
30.5	10.9	6.3	2.2	5.2	3.0	1.4	21.8	13.7	9.4
40.5	8.1	4.8	2.2	3.6	2.2	1.1	19.1	13.4	8.6
50.5	5.9	4.1	2.0	2.7	1.9	1.2	11.1	8.0	6.7
60.5	4.5	3.3	1.7	2.1	1.6	1.1	9.4	7.7	6.9
70.5	4.6	3.3	1.9	2.1	1.5	1.1	11.4	8.9	8.2
80.5	4.5	3.0	1.7	2.2	1.7	1.2	11.6	8.6	7.2
90.5	3.8	2.9	1.8	1.8	1.5	1.0	8.9	7.9	7.7
100.5	3.6	3.0	1.9	1.7	1.4	1.1	8.3	7.5	6.5
110.5	3.9	3.0	1.9	2.1	1.7	1.2	9.4	8.3	7.9
120.5	3.5	2.7	1.7	1.7	1.5	1.0	8.3	7.7	7.0
130.5	4.0	3.0	1.9	1.9	1.8	1.2	11.5	10.6	8.5
140.5	4.4	3.7	2.1	2.0	1.7	1.2	9.6	8.7	8.0
150.5	4.6	3.8	2.1	1.9	1.7	1.2	10.9	9.3	7.9

Table 5.7: Fermi: Original observational mean intensity $I_0(\theta)$, final mean intensity after discard the outliers $I(\theta)$ and standard deviation $\sigma(\theta)$ in the unit of $\text{GeVcm}^{-2}\text{s}^{-1}\text{Hz}^{-1}\text{Sr}^{-1}$.

θ [$^{\circ}$]	Fermi			
	53.3-94.9 GeV		94.9-168.7 GeV	168.7-300.0 GeV
	$I_0(\theta)$ $\times 10^{-32}$	$I(\theta)$ $\times 10^{-32}$	$\sigma(\theta)$	$I_0(\theta)$ $\times 10^{-32}$
0.5	130.5	134.0	8.7	75.5
1.5	96.3	101.4	9.4	50.7
2.5	63.8	50.9	8.6	32.1
3.5	44.4	37.2	9.4	22.3
4.5	37.4	33.1	8.4	17.5
5.5	34.1	27.0	7.5	12.4
6.5	32.1	15.3	9.3	9.6
7.5	32.5	17.3	9.1	10.0
8.5	30.1	18.1	9.3	9.5
9.5	28.2	14.3	8.6	9.6
10.5	29.8	14.0	9.0	11.9
12.5	27.8	12.6	8.4	10.7
14.5	20.1	10.1	6.9	8.8
16.5	17.2	7.3	6.0	8.2
18.5	17.9	8.0	7.0	9.1
20.5	13.4	7.8	6.1	9.5
25.5	14.4	9.1	6.6	7.1
30.5	10.9	6.3	6.0	6.3
40.5	8.5	6.6	6.2	4.2
50.5	6.8	4.4	5.0	4.6
60.5	6.2	5.0	5.5	2.4
70.5	5.9	4.8	5.1	3.6
80.5	5.9	4.1	5.1	2.8
90.5	5.5	4.8	5.5	2.4
100.5	5.2	4.8	5.4	2.7
110.5	5.1	4.0	5.2	2.7
120.5	5.6	5.3	5.4	2.6
130.5	5.0	4.5	5.4	2.4
140.5	6.0	4.9	5.4	3.5
150.5	6.4	5.2	5.4	2.8

Table 5.8: Fermi: Original observational mean intensity $I_0(\theta)$, final mean intensity after discard the outliers $I(\theta)$ and standard deviation $\sigma(\theta)$ in the unit of $\text{GeVcm}^{-2}\text{s}^{-1}\text{Hz}^{-1}\text{Sr}^{-1}$.

Chapter

6

SUMMARY AND FUTURE PROSPECTS

6.1 Summary

The main scientific results of this thesis are the evaluation of the pressure term induced by dark matter annihilations (Wechakama and Ascasibar, 2011) and the multi-messenger constraints on the annihilation cross-section (Wechakama and Ascasibar, 2012). In both cases, we have focused on dark matter annihilation into electron-positron pairs, neglecting other processes, such as dark matter decay, or other annihilation products. Instead of focusing on a specific dark matter annihilation model, we have adopted a model-independent approach, in which all particles are created with the same initial energy E_0 , of the order of the mass of the dark matter particle. The propagation of the electrons and positrons has been determined by the diffusion-loss equation. We have assumed a uniform diffusion coefficient and consider inverse Compton scattering (ICS), synchrotron radiation, Coulomb collisions, bremsstrahlung, and the ionization of neutral hydrogen atoms as the main energy loss mechanisms. Below we summarise the major conclusions of each part.

6.1.1 Pressure from dark matter annihilation

We have estimated the contribution of dark matter annihilation to the total gas pressure and considered its effect on the rotation curve for astrophysical conditions representative of the Milky Way. All the electrons and positrons are injected with an initial energy E_0 between 1 MeV and 1 TeV, and the injection rate is constrained by observations of the electron-positron spectrum in the solar neighbourhood by INTEGRAL, H.E.S.S. and Fermi data. The pressure associated to these particles, i.e. ‘dark matter pressure’, is determined by solving the diffusion-loss equation. For the canonical Milky Way model, the dark matter pressure has a significant effect at the inner regions. The dark matter pressure gradients are strong enough to balance gravity in the central parts within $\sim 10 - 400$ pc as long as the injection energy is lower than 1 GeV. The effect is extremely weak if $E_0 \sim$ GeV and completely negligible for larger values of E_0 .

We have varied the values of astrophysical parameters, namely the intensity of the magnetic field, the density and the ionization fraction of the interstellar medium (ISM) gas, the inner logarithmic slope of the dark matter density profile, and the virial mass of the galaxy. Although the ionization fraction of the ISM and the intensity of the magnetic field determine the energy losses and the shape of the electron-positron spectrum at low

and high values of the Lorentz factor, respectively, they do not affect the rotation curve significantly. These parameters may have a strong impact on other observables, however such as the emission at different wavelengths. However, the details of the gas density play a more important role, and change the results at the significant level. The most relevant astrophysical parameter that affects the rotation curves is the inner logarithmic slope of dark matter density profile α . Since the central dark matter density increases strongly with α , steep logarithmic slopes yield much higher pressures in the central regions. For $\alpha \geq 1.9$, a clear signature of dark matter annihilation on the observed rotation curve is expected even for $E_0 \sim 1$ TeV.

Finally, we have computed the model predictions for constant mass-to-light ratio and maximum disk models of the low surface brightness galaxies compiled by de Blok and Bosma (2002). The results indicate that dark matter pressure may provide a new window to the physical properties of dark matter particles, while bringing the predicted rotation curves into better agreement with observations.

6.1.2 Multi-messenger constraints

We have derived robust upper limits on the dark matter annihilation cross-section into electron-positron pairs by comparing the predictions of an analytic model of particle propagation with a multi-wavelength set of observational data obtained from the literature. Our constraints have been obtained by imposing that the expected emission of synchrotron radiation, ICS and FSR within the Milky Way is consistent with 18 maps of the Galactic sky at different frequencies: the Haslam radio map at 408 MHz, the 5 channels (23 GHz, 33 GHz, 41 GHz, 61 GHz, and 94 GHz) of WMAP 7-year data, and 12 energy bins (from 0.3 to 300 GeV) of gamma-ray maps from the Fermi LAT. In order to mask the most obvious astrophysical signals (i.e. the emission from the galactic disc and prominent point sources), a simple conservative statistical criterion has been followed, and observational upper limits are derived from the remaining spherically-symmetric component. In addition to the photon data, we have also considered the recent measurements of the local electron and positron spectra performed by PAMELA, Fermi, and H.E.S.S.. These constraints, mostly based on the local positron spectrum, have also been derived by imposing that the predicted abundance of these particles does not exceed the observed values for any injection energy E_0 .

For the canonical Milky Way model ($\alpha = 1$), the results show that the the tightest constraints are provided by final-state radiation and inverse Compton scattering for injection energies above $20 - 30$ GeV, whereas the positron spectrum in the solar neighbourhood and synchrotron emission limit the production cross-section at lower energies. The typical value for thermal relics, $\langle \sigma v \rangle_{e^\pm} = 3 \times 10^{-26} \text{ cm s}^{-1}$, is ruled out for particle masses lighter than a few GeV. The tightest constraints are valid for all the values of the magnetic field, diffusion coefficient, and models of the interstellar radiation field that we have considered.

The inner logarithmic slope of the dark matter density profile plays a significant role in the upper limits on $\langle \sigma v \rangle_{e^\pm}$. If the density profile of the Milky Way halo is steep ($\alpha > 1$), the exact value of inner logarithmic slope plays a crucial role in the upper limit on the annihilation cross-section. The adiabatic contraction scenario is hardly consistent with any dark matter candidate lighter than ~ 100 GeV and $\langle \sigma v \rangle_{e^\pm} = 3 \times 10^{-26} \text{ cm}^3 \text{ s}^{-1}$. We have derived a stringent upper limit on the inner logarithmic slope α of the density profile of the Milky Way dark matter halo by setting the dark matter annihilation cross-section into electron-positron pairs to the value expected for a thermally-produced relic, $\langle \sigma v \rangle_{e^\pm} = 3 \times 10^{-26} \text{ cm}^3 \text{ s}^{-1}$, and computing the value of α . Our results show that, for a thermal relic with $m_{\text{dm}} < 100$ GeV, the dark matter density profile of the Milky Way *must*

be shallower than $\alpha \sim 1.3$ in order not to overproduce the observed signal. It is worth noting that, since final-state radiation only depends on the injection rate, this constraint on the inner logarithmic slope α is independent on the other astrophysical parameters. Synchrotron and inverse Compton scattering yield stronger limits than FSR at low and high injection energies, respectively, although of course these results depend much more on the details of the adopted propagation model (most notably, the intensity of the magnetic field). For our canonical set-up, synchrotron radiation imposes extremely tight constraints for a limited range of dark matter masses, around a few GeV (observational data at lower frequencies would probably make possible to extend these constraints toward lower masses). In particular, the standard case $\alpha = 1$ would be excluded for $E_0 < 5$ GeV. At high energies, ICS emission rules out slopes steeper than $\alpha = 1.5$ for dark matter masses below ~ 2 TeV. The regime $\alpha > 1.8$ seems to be excluded in any case.

In any case, detecting an indirect signal from dark matter annihilation into electrons and positrons requires a better understanding of the production of positrons and gamma rays by astrophysical sources, which would also be extremely helpful in constraining the distribution of dark matter in the innermost regions of the Milky Way halo.

6.2 Future prospects

In this thesis, we have provided the methods to investigate the astrophysical signatures of dark matter annihilation into electrons and positrons. The present study can be extended in several different directions, among which we would like to highlight the following:

1. More realistic models of the dark matter halo, the structure of the interstellar medium, intensity of magnetic field, and the propagation of relativistic particles are clearly needed. Rather than using a model-independent approach, it would also be interesting to consider specific dark matter candidates, with their very own photon and particle injection spectra.
2. We have shown that the effect of dark matter pressure on the rotation curves of galaxies is significant enough to be used as a tool to probe the properties of dark matter particles and explore their potential role in the cusp-core problem. In addition to the the Milky Way, the most promising targets are the nearest gas-rich dwarf and low surface brightness galaxies. One can perform a test considering different density profiles and dark matter models, comparing the predicted rotation curves with observational data. An important aspect of this test is that the circular velocity of the gas is sensitive to the dark matter pressure, whereas the stellar dynamics are not.
3. Besides contributing to the total pressure, the energetic particles and photons produced by dark matter annihilation would also heat and ionize the surrounding gas, possibly affecting galaxy formation and evolution. An estimate of the overall impact on the observable properties of galaxies can be obtained from analytical models, while more detailed information can be obtained from self-consistent, three-dimensional gasdynamical simulations. In such simulations, one may compute the local dark matter density and then inject the appropriate amount of heat and pressure to the gas, modifying its chemical composition.

BIBLIOGRAPHY

C. E. Aalseth, P. S. Barbeau, N. S. Bowden, B. Cabrera-Palmer, J. Colaresi, J. I. Collar, S. Dazeley, P. de Lurgio, J. E. Fast, N. Fields, C. H. Greenberg, T. W. Hossbach, M. E. Keillor, J. D. Kephart, M. G. Marino, H. S. Miley, M. L. Miller, J. L. Orrell, D. C. Radford, D. Reyna, O. Tench, T. D. van Wechel, J. F. Wilkerson, and K. M. Yocom. Results from a Search for Light-Mass Dark Matter with a p-Type Point Contact Germanium Detector. *Phys. Rev. Lett.*, 106(13):131301, 2011.

C. E. Aalseth, P. S. Barbeau, J. Colaresi, J. I. Collar, J. Diaz Leon, J. E. Fast, N. E. Fields, T. W. Hossbach, A. Knecht, M. S. Kos, M. G. Marino, H. S. Miley, M. L. Miller, J. L. Orrell, and K. M. Yocom. CoGeNT: A Search for Low-Mass Dark Matter using p-type Point Contact Germanium Detectors. *ArXiv e-prints*, [arXiv: 1208.5737], 2012.

T. Aaltonen, B. Álvarez González, S. Amerio, and et al. [CDF Collaboration]. Search for Dark Matter in Events with One Jet and Missing Transverse Energy in pp Collisions at $s=1.96\text{TeV}$. *Phys. Rev. Lett.*, 108(21):211804, 2012.

M. G. Aartsen, R. Abbasi, Y. Abdou, and et al. [IceCube Collaboration]. Search for dark matter annihilations in the Sun with the 79-string IceCube detector. *ArXiv e-prints*, [arXiv: 1212.4097], 2012.

K. Abazajian. Detection of Dark Matter Decay in the X-ray. In *astro2010: The Astronomy and Astrophysics Decadal Survey*, volume 2010 of *Astronomy*, page 1, 2009.

K. Abazajian and S. M. Koushiappas. Constraints on sterile neutrino dark matter. *Phys. Rev. D*, 74(2):023527, 2006.

K. Abazajian, G. M. Fuller, and W. H. Tucker. Direct Detection of Warm Dark Matter in the X-Ray. *ApJ*, 562:593–604, 2001.

K. N. Abazajian. The consistency of Fermi-LAT observations of the galactic center with a millisecond pulsar population in the central stellar cluster. *JCAP*, 3:010, 2011.

K. N. Abazajian, P. Agrawal, Z. Chacko, and C. Kilic. Conservative constraints on dark matter from the Fermi-LAT isotropic diffuse gamma-ray background spectrum. *JCAP*, 11:41, 2010.

V. M. Abazov, B. Abbott, A. Abdesselam, and et al. [D0 Collaboration]. Search for Large Extra Dimensions in the Monojet+ E_T Channel with the DØ Detector. *Phys. Rev. Lett.*, 90(25):251802, 2003.

R. Abbasi, Y. Abdou, M. Ackermann, and et al. [IceCube Collaboration]. Limits on a Muon Flux from Neutralino Annihilations in the Sun with the IceCube 22-String Detector. *Phys. Rev. Lett.*, 102(20):201302, 2009.

R. Abbasi, Y. Abdou, M. Ackermann, and et al. [IceCube Collaboration]. Search for Neutrinos from Annihilating Dark Matter in the Direction of the Galactic Center with the 40-String IceCube Neutrino Observatory. *ArXiv e-prints*, [arXiv: 1210.3557], 2012.

L. F. Abbott and P. Sikivie. A cosmological bound on the invisible axion. *Phys. Lett. B*, 120:133–136, 1983.

A. A. Abdo, M. Ackermann, M. Ajello, and et al. [The Fermi Collaboration]. Measurement of the Cosmic Ray $e^+ + e^-$ Spectrum from 20GeV to 1TeV with the Fermi Large Area Telescope. *Phys. Rev. Lett.*, 102(18):181101–, 2009.

A. A. Abdo, M. Ackermann, M. Ajello, and et al. [Fermi LAT Collaboration]. Fermi Large Area Telescope Search for Photon Lines from 30 to 200 GeV and Dark Matter Implications. *Phys. Rev. Lett.*, 104(9):091302, 2010a.

A. A. Abdo, M. Ackermann, M. Ajello, and et al. [The Fermi-LAT Collaboration]. Observations of Milky Way Dwarf Spheroidal Galaxies with the Fermi-Large Area Telescope Detector and Constraints on Dark Matter Models. *ApJ*, 712:147–158, 2010b.

A. A. Abdo, M. Ackermann, M. Ajello, and et al. [The Fermi-LAT Collaboration]. Constraints on cosmological dark matter annihilation from the Fermi-LAT isotropic diffuse gamma-ray measurement. *JCAP*, 4:014, 2010c.

A. Abramowski, F. Acero, F. Aharonian, and et al. [H.E.S.S. Collaboration]. H.E.S.S. Observations of the Globular Clusters NGC 6388 and M15 and Search for a Dark Matter Signal. *ApJ*, 735:12, 2011a.

A. Abramowski, F. Acero, F. Aharonian, and et al. [H.E.S.S. Collaboration]. Search for a Dark Matter Annihilation Signal from the Galactic Center Halo with H.E.S.S. *Phys. Rev. Lett.*, 106(16):161301, 2011b.

A. Abramowski, F. Acero, F. Aharonian, and et al. [H.E.S.S. Collaboration]. H.E.S.S. constraints on dark matter annihilations towards the sculptor and carina dwarf galaxies. *Astropart. Phys.*, 34:608–616, 2011c.

A. Abulencia, D. Acosta, J. Adelman, and et al. [CDF Collaboration]. Search for Large Extra Dimensions in the Production of Jets and Missing Transverse Energy in pp Collisions at $s=1.96\text{TeV}$. *Phys. Rev. Lett.*, 97(17):171802, 2006.

V. A. Acciari, T. Arlen, T. Aune, and et al. [VERITAS Collaboration]. VERITAS Search for VHE Gamma-ray Emission from Dwarf Spheroidal Galaxies. *ApJ*, 720:1174–1180, 2010.

M. Ackermann, M. Ajello, W. B. Atwood, and et al. [The Fermi-LAT Collaboration]. Fermi LAT observations of cosmic-ray electrons from 7 GeV to 1 TeV. *Phys. Rev. D*, 82(9):092004, 2010a.

M. Ackermann, M. Ajello, W. B. Atwood, and et al. [The Fermi-LAT Collaboration]. Constraints on dark matter annihilation in clusters of galaxies with the Fermi large area telescope. *JCAP*, 5:025, 2010b.

M. Ackermann, M. Ajello, A. Albert, and et al. [The Fermi-LAT Collaboration]. Constraining Dark Matter Models from a Combined Analysis of Milky Way Satellites with the Fermi Large Area Telescope. *Phys. Rev. Lett.*, 107(24):241302, 2011.

M. Ackermann, M. Ajello, A. Albert, and et al. [Fermi LAT Collaboration]. Fermi LAT search for dark matter in gamma-ray lines and the inclusive photon spectrum. *Phys. Rev. D*, 86(2):022002, 2012a.

M. Ackermann, M. Ajello, A. Allafort, and et al. [The Fermi-LAT Collaboration]. Measurement of Separate Cosmic-Ray Electron and Positron Spectra with the Fermi Large Area Telescope. *Phys. Rev. Lett.*, 108(1):011103, 2012b.

M. Ackermann, M. Ajello, W. B. Atwood, and et al. [The Fermi-LAT Collaboration]. Constraints on the Galactic Halo Dark Matter from Fermi-LAT Diffuse Measurements. *ApJ*, 761:91, 2012c.

O. Adriani, G. C. Barbarino, G. A. Bazilevskaya, and et al. [PAMELA Collaboration]. An anomalous positron abundance in cosmic rays with energies 1.5-100GeV. *Nature*, 458: 607–609, 2009a.

O. Adriani, G. C. Barbarino, G. A. Bazilevskaya, and et al. [PAMELA Collaboration]. New Measurement of the Antiproton-to-Proton Flux Ratio up to 100 GeV in the Cosmic Radiation. *Phys. Rev. Lett.*, 102(5):051101–+, 2009b.

O. Adriani, G. C. Barbarino, G. A. Bazilevskaya, and et al. [PAMELA Collaboration]. A statistical procedure for the identification of positrons in the PAMELA experiment. *Astropart. Phys.*, 34:1–11, 2010a.

O. Adriani, G. C. Barbarino, G. A. Bazilevskaya, and et al. [PAMELA Collaboration]. PAMELA Results on the Cosmic-Ray Antiproton Flux from 60 MeV to 180 GeV in Kinetic Energy. *Phys. Rev. Lett.*, 105(12):121101, 2010b.

O. Adriani, G. C. Barbarino, G. A. Bazilevskaya, and et al. [PAMELA Collaboration]. Cosmic-Ray Electron Flux Measured by the PAMELA Experiment between 1 and 625 GeV. *Phys. Rev. Lett.*, 106(20):201101, 2011.

M. Aguilar, J. Alcaraz, J. Allaby, and et al. [AMS-01 Collaboration]. Cosmic-ray positron fraction measurement from 1 to 30 GeV with AMS-01. *Phys. Lett. B*, 646:145–154, 2007.

F. Aharonian, A. G. Akhperjanian, A. R. Bazer-Bachi, and et al. [HESS Collaboration]. HESS Observations of the Galactic Center Region and Their Possible Dark Matter Interpretation. *Phys. Rev. Lett.*, 97(22):221102–+, 2006.

F. Aharonian, A. G. Akhperjanian, U. Barres de Almeida, and et al. [HESS Collaboration]. Energy Spectrum of Cosmic-Ray Electrons at TeV Energies. *Phys. Rev. Lett.*, 101(26): 261104–+, 2008.

M. Ahlers, P. Mertsch, and S. Sarkar. Cosmic ray acceleration in supernova remnants and the FERMI/PAMELA data. *Phys. Rev. D*, 80(12):123017, 2009.

Z. Ahmed, D. S. Akerib, S. Arrenberg, and et al. [CDMS II Collaboration]. Dark Matter Search Results from the CDMS II Experiment. *Science*, 327:1619–, 2010.

J. Aleksić, E. A. Alvarez, L. A. Antonelli, and et al. [MAGIC-I Collaboration]. Searches for dark matter annihilation signatures in the Segue 1 satellite galaxy with the MAGIC-I telescope. *JCAP*, 6:035, 2011.

R. Aloisio, P. Blasi, and A. V. Olinto. Neutralino annihilation at the galactic centre revisited. *JCAP*, 5:007, 2004.

R. A. Alpher, H. Bethe, and G. Gamow. The Origin of Chemical Elements. *Phys. Rev.*, 73:803–804, 1948.

H. An and M. Pospelov. Dark resonance. *JCAP*, 11:061, 2012.

J. Angle, E. Aprile, F. Arneodo, L. Baudis, A. Bernstein, A. I. Bolozdynya, L. C. C. Coelho, C. E. Dahl, L. Deviveiros, A. D. Ferella, L. M. P. Fernandes, S. Fiorucci, R. J. Gaitskell, K. L. Giboni, R. Gomez, R. Hasty, L. Kastens, J. Kwong, J. A. M. Lopes, N. Madden, A. Manalaysay, A. Manzur, D. N. McKinsey, M. E. Monzani, K. Ni, U. Oberlack, J. Orboeck, G. Plante, R. Santorelli, J. M. F. Dos Santos, S. Schulte, P. Shagin, T. Shutt, P. Sorensen, C. Winant, and M. Yamashita. Search for Light Dark Matter in XENON10 Data. *Phys. Rev. Lett.*, 107(5):051301, 2011.

G. Angloher, M. Bauer, I. Bavykina, A. Bento, C. Bucci, C. Ciemniak, G. Deuter, F. von Feilitzsch, D. Hauff, P. Huff, C. Isaila, J. Jochum, M. Kiefer, M. Kimmerle, J.-C. Lanfranchi, F. Petricca, S. Pfister, W. Potzel, F. Pröbst, F. Reindl, S. Roth, K. Rottler, C. Sailer, K. Schäffner, J. Schmaler, S. Scholl, W. Seidel, M. v. Sivers, L. Stodolsky, C. Strandhagen, R. Strauß, A. Tanzke, I. Usherov, S. Wawoczny, M. Willers, and A. Zöller. Results from 730 kg days of the CRESST-II Dark Matter search. *EPJ C*, 72:1971, 2012.

C. Angulo, M. Arnould, M. Rayet, P. Descouvemont, D. Baye, C. Leclercq-Willain, A. Coc, S. Barhoumi, P. Aguer, C. Rolfs, R. Kunz, J. W. Hammer, A. Mayer, T. Paradellis, S. Kossionides, C. Chronidou, K. Spyrou, S. degl’Innocenti, G. Fiorentini, B. Ricci, S. Zavatarelli, C. Providencia, H. Wolters, J. Soares, C. Grama, J. Rahighi, A. Shottler, and M. Lamehi Rachti. A compilation of charged-particle induced thermonuclear reaction rates. *Nucl. Phys. A*, 656:3–183, 1999.

T. Appelquist, H.-C. Cheng, and B. A. Dobrescu. Bounds on universal extra dimensions. *Phys. Rev. D*, 64(3):035002, 2001.

E. Aprile, K. Arisaka, F. Arneodo, and et al. [XENON100 Collaboration]. Dark Matter Results from 100 Live Days of XENON100 Data. *Phys. Rev. Lett.*, 107(13):131302, 2011.

E. Armengaud, C. Augier, A. Benoît, and et al. [EDELWEISS Collaboration]. Final results of the EDELWEISS-II WIMP search using a 4-kg array of cryogenic germanium detectors with interleaved electrodes. *Phys. Lett. B*, 702:329–335, 2011.

F. Arneodo. Dark Matter Searches. *ArXiv e-prints*, [arXiv: 1301.0441], 2013.

T. Asaka, M. Shaposhnikov, and M. Laine. Lightest sterile neutrino abundance within the ν MSM. *JHEP*, 1:091, 2007.

M. Asano, T. Bringmann, G. Sigl, and M. Vollmann. The 130 GeV gamma-ray line and generic dark matter model building constraints from continuum gamma rays, radio and antiproton data. *ArXiv e-prints*, [arXiv: 1211.6739], 2012.

Y. Ascasibar. Effect of dark matter annihilation on gas cooling and star formation. *A&A*, 462:L65–L68, 2007.

Y. Ascasibar and A. I. Díaz. Photoionized gas in hydrostatic equilibrium: the role of gravity. *MNRAS*, 404:275–282, 2010.

Y. Ascasibar and S. Gottlöber. The dynamical structure of dark matter haloes. *MNRAS*, 386:2022–2030, 2008.

Y. Ascasibar, G. Yepes, S. Gottlöber, and V. Müller. On the physical origin of dark matter density profiles. *MNRAS*, 352:1109–1120, 2004.

Y. Ascasibar, P. Jean, C. Boehm, and J. Knödlseder. Constraints on dark matter and the shape of the Milky Way dark halo from the 511-keV line. *MNRAS*, 368:1695–1705, 2006.

W. B. Atwood, A. A. Abdo, M. Ackermann, and et al. [The Fermi-LAT Collaboration]. The Large Area Telescope on the Fermi Gamma-Ray Space Telescope Mission. *ApJ*, 697:1071–1102, 2009.

H. Baer and A. D. Box. Fine-tuning favors mixed axion/axino cold dark matter over neutralinos in the minimal supergravity model. *EPJ C*, 68:523–537, 2010.

H. Baer and S. Profumo. Low energy antideuterons: shedding light on dark matter. *JCAP*, 12:008, 2005.

J. N. Bahcall and R. M. Soneira. The universe at faint magnitudes. I - Models for the galaxy and the predicted star counts. *ApJS*, 44:73–110, 1980.

E. A. Baltz and J. Edsjö. Positron propagation and fluxes from neutralino annihilation in the halo. *Phys. Rev. D*, 59(2):023511–+, 1999.

E. A. Baltz and L. Wai. Diffuse inverse Compton and synchrotron emission from dark matter annihilations in galactic satellites. *Phys. Rev. D*, 70(2):023512, 2004.

E. A. Baltz, C. Briot, P. Salati, R. Taillet, and J. Silk. Detection of neutralino annihilation photons from external galaxies. *Phys. Rev. D*, 61(2):023514, 2000.

E. A. Baltz, J. Edsjö, K. Freese, and P. Gondolo. Cosmic ray positron excess and neutralino dark matter. *Phys. Rev. D*, 65(6):063511, 2002.

E. A. Baltz, M. Battaglia, M. E. Peskin, and T. Wizansky. Determination of dark matter properties at high-energy colliders. *Phys. Rev. D*, 74(10):103521, 2006.

E. A. Baltz, B. Berenji, G. Bertone, L. Bergström, E. Bloom, T. Bringmann, J. Chiang, J. Cohen-Tanugi, J. Conrad, Y. Edmonds, J. Edsjö, G. Godfrey, R. E. Hughes, R. P. Johnson, A. Lionetto, A. A. Moiseev, A. Morselli, I. V. Moskalenko, E. Nuss, J. F. Ormes, R. Rando, A. J. Sander, A. Sellerholm, P. D. Smith, A. W. Strong, L. Wai, P. Wang, and B. L. Winer. Pre-launch estimates for GLAST sensitivity to dark matter annihilation signals. *JCAP*, 7:013, 2008.

V. Barger, Y. Gao, W.-Y. Keung, D. Marfatia, and G. Shaughnessy. Dark matter and pulsar signals for Fermi LAT, PAMELA, ATIC, HESS and WMAP data. *Phys. Lett. B*, 678:283–292, 2009.

M. Bartelmann and P. Schneider. Weak gravitational lensing. *Phys. Rep.*, 340:291–472, 2001.

S. W. Barwick, J. J. Beatty, A. Bhattacharyya, and et al. [HEAT Collaboration]. Measurements of the Cosmic-Ray Positron Fraction from 1 to 50 GeV. *ApJ*, 482:L191, 1997.

M. Battaglia. The role of an e^+e^- linear collider in the study of cosmic dark matter. *New J. Phys.*, 11(10):105025, 2009.

M. Battaglia, I. Hinchliffe, and D. Tovey. TOPICAL REVIEW: Cold dark matter and the LHC. *Journal of Physics G Nuclear Physics*, 30:217, 2004.

J. F. Beacom and H. Yüksel. Stringent Constraint on Galactic Positron Production. *Phys. Rev. Lett.*, 97(7):071102, 2006.

J. F. Beacom, N. F. Bell, and G. Bertone. Gamma-Ray Constraint on Galactic Positron Production by MeV Dark Matter. *Phys. Rev. Lett.*, 94(17):171301, 2005.

R. Beck. Galactic and Extragalactic Magnetic Fields. *Space Sci. Rev.*, 99:243–260, 2001.

K. G. Begeman, A. H. Broeils, and R. H. Sanders. Extended rotation curves of spiral galaxies - Dark haloes and modified dynamics. *MNRAS*, 249:523–537, 1991.

J. D. Bekenstein. Relativistic gravitation theory for the modified Newtonian dynamics paradigm. *Phys. Rev. D*, 70(8):083509, 2004.

N. F. Bell and T. D. Jacques. Gamma-ray constraints on dark matter annihilation into charged particles. *Phys. Rev. D*, 79(4):043507, 2009.

M. Beltrán, D. Hooper, E. W. Kolb, Z. A. C. Krusberg, and T. M. P. Tait. Maverick dark matter at colliders. *JHEP*, 9:37, 2010.

V. Berezinsky, A. Bottino, and G. Mignola. High energy gamma-radiation from the galactic center due to neutralino annihilation. *Phys. Lett. B*, 325:136–142, 1994.

L. Bergström. Radiative processes in dark matter photino annihilation. *Phys. Lett. B*, 225:372–380, 1989.

L. Bergström. Dark matter candidates. *New J. Phys.*, 11(10):105006, 2009.

L. Bergström and D. Hooper. Dark matter and gamma rays from Draco: MAGIC, GLAST and CACTUS. *Phys. Rev. D*, 73(6):063510, 2006.

L. Bergström and H. Snellman. Observable monochromatic photons from cosmic photino annihilation. *Phys. Rev. D*, 37:3737–3741, 1988.

L. Bergström and P. Ullio. Full one-loop calculation of neutralino annihilation into two photons. *Nucl. Phys. B*, 504:27–44, 1997.

L. Bergström, P. Ullio, and J. H. Buckley. Observability of gamma rays from dark matter neutralino annihilations in the Milky Way halo. *Astropart. Phys.*, 9:137–162, 1998.

L. Bergström, T. Bringmann, M. Eriksson, and M. Gustafsson. Gamma Rays from Kaluza-Klein Dark Matter. *Phys. Rev. Lett.*, 94(13):131301, 2005a.

L. Bergström, T. Bringmann, M. Eriksson, and M. Gustafsson. Gamma Rays from Heavy Neutralino Dark Matter. *Phys. Rev. Lett.*, 95(24):241301, 2005b.

L. Bergström, T. Bringmann, and J. Edsjö. New positron spectral features from supersymmetric dark matter: A way to explain the PAMELA data? *Phys. Rev. D*, 78(10):103520, 2008.

L. Bergström, J. Edsjö, and G. Zaharijas. Dark Matter Interpretation of Recent Electron and Positron Data. *Phys. Rev. Lett.*, 103(3):031103, 2009.

R. Bernabei, P. Belli, F. Cappella, R. Cerulli, C. J. Dai, A. D'Angelo, H. L. He, A. Incicchitti, H. H. Kuang, X. H. Ma, F. Montecchia, F. Nozzoli, D. Prosperi, X. D. Sheng, R. G. Wang, and Z. P. Ye. New results from DAMA/LIBRA. *EPJ C*, 67:39–49, 2010.

N. Bernal and S. Palomares-Ruiz. Constraining Dark Matter Properties with Gamma-Rays from the Galactic Center with Fermi-LAT. *ArXiv e-prints*, [arXiv: 1006.0477], 2010.

G. Bertone. *Particle Dark Matter : Observations, Models and Searches*. Cambridge University Press, 2010.

G. Bertone, E. Nezri, J. Orloff, and J. Silk. Neutrinos from dark matter annihilations at the galactic center. *Phys. Rev. D*, 70(6):063503, 2004.

G. Bertone, D. Hooper, and J. Silk. Particle dark matter: evidence, candidates and constraints. *Phys. Rep.*, 405:279–390, 2005.

G. Bertone, M. Cirelli, A. Strumia, and M. Taoso. Gamma-ray and radio tests of the e^\pm excess from DM annihilations. *JCAP*, 3:009, 2009.

A. Birkedal-Hansen and E. Jeong. Gaugino and higgsino coannihilations I: neutralino-neutralino interactions. *JHEP*, 2:047, 2003.

P. Blasi. Origin of the Positron Excess in Cosmic Rays. *Phys. Rev. Lett.*, 103(5):051104, 2009.

P. Blasi, A. V. Olinto, and C. Tyler. Detecting WIMPs in the microwave sky. *Astropart. Phys.*, 18:649–662, 2003.

G. R. Blumenthal and R. J. Gould. Bremsstrahlung, Synchrotron Radiation, and Compton Scattering of High-Energy Electrons Traversing Dilute Gases. *Rev. Mod. Phys.*, 42:237–271, 1970.

G. R. Blumenthal, S. M. Faber, R. Flores, and J. R. Primack. Contraction of dark matter galactic halos due to baryonic infall. *ApJ*, 301:27–34, 1986.

C. Boehm and Y. Ascasibar. More evidence in favor of light dark matter particles? *Phys. Rev. D*, 70(11):115013, 2004.

C. Boehm, D. Hooper, J. Silk, M. Casse, and J. Paul. MeV Dark Matter: Has It Been Detected? *Phys. Rev. Lett.*, 92(10):101301, 2004.

J. R. Bond, L. Kofman, and D. Pogosyan. How filaments of galaxies are woven into the cosmic web. *Nature*, 380:603–606, 1996.

H. Bonnet, Y. Mellier, and B. Fort. First detection of a gravitational weak shear at the periphery of CL 0024+1654. *ApJ*, 427:L83–L86, 1994.

A. Borriello and P. Salucci. The dark matter distribution in disc galaxies. *MNRAS*, 323:285–292, 2001.

E. Borriello, A. Cuoco, and G. Miele. Radio constraints on dark matter annihilation in the galactic halo and its substructures. *Phys. Rev. D*, 79(2):023518, 2009.

M. Bottino, A. J. Banday, and D. Maino. New insights into the foreground analysis of the WMAP 5-year data using FASTICA. *MNRAS*, 402:207–225, 2010.

R. G. Bower, A. J. Benson, R. Malbon, J. C. Helly, C. S. Frenk, C. M. Baugh, S. Cole, and C. G. Lacey. Breaking the hierarchy of galaxy formation. *MNRAS*, 370:645–655, 2006.

A. Boyarsky, J.-W. den Herder, A. Neronov, and O. Ruchayskiy. Search for the light dark matter with an X-ray spectrometer. *Astropart. Phys.*, 28:303–311, 2007.

A. Boyarsky, D. Malyshev, A. Neronov, and O. Ruchayskiy. Constraining dark matter properties with SPI. *MNRAS*, 387:1345–1360, 2008a.

A. Boyarsky, O. Ruchayskiy, and M. Markevitch. Constraints on Parameters of Radiatively Decaying Dark Matter from the Galaxy Cluster 1E 0657-56. *ApJ*, 673:752–757, 2008b.

A. Boyarsky, O. Ruchayskiy, and M. Shaposhnikov. The Role of Sterile Neutrinos in Cosmology and Astrophysics. *Annual Review of Nuclear and Particle Science*, 59:191–214, 2009.

A. Boyarsky, D. Malyshev, and O. Ruchayskiy. A comment on the emission from the Galactic Center as seen by the Fermi telescope. *Phys. Lett. B*, 705:165–169, 2011.

T. Bringmann and C. Weniger. Gamma ray signals from dark matter: Concepts, status and prospects. *Physics of the Dark Universe*, 1:194–217, 2012.

T. Bringmann, L. Bergström, and J. Edsjö. New gamma-ray contributions to supersymmetric dark matter annihilation. *JHEP*, 1:049, 2008.

P. Brun, T. Delahaye, J. Diemand, S. Profumo, and P. Salati. Cosmic ray lepton puzzle in the light of cosmological N-body simulations. *Phys. Rev. D*, 80(3):035023, 2009.

O. Buchmueller, R. Cavanaugh, D. Colling, A. de Roeck, M. J. Dolan, J. R. Ellis, H. Flächer, S. Heinemeyer, G. Isidori, K. Olive, S. Rogerson, F. Ronga, and G. Weiglein. Implications of initial LHC searches for supersymmetry. *EPJ C*, 71:1634, 2011.

W. Buchmüller, K. Hamaguchi, M. Ratz, and T. Yanagida. Supergravity at colliders. *Phys. Lett. B*, 588:90–98, 2004.

A. Burkert. The Structure of Dark Matter Halos in Dwarf Galaxies. *ApJ*, 447:L25+, 1995.

F. Burnell and G. D. Kribs. The abundance of Kaluza-Klein dark matter with coannihilation. *Phys. Rev. D*, 73(1):015001, 2006.

R. Cen. Decaying Cold Dark Matter Model and Small-Scale Power. *ApJ*, 546:L77–L80, 2001.

D. G. Cerdeño and A. M. Green. *Direct detection of WIMPs*, page 347. Cambridge University Press, 2010.

A. Cesarini, F. Fucito, A. Lionetto, A. Morselli, and P. Ullio. The Galactic center as a dark matter gamma-ray source. *Astropart. Phys.*, 21:267–285, 2004.

J. Chang, J. H. Adams, H. S. Ahn, G. L. Bashindzhyan, M. Christl, O. Ganel, T. G. Guzik, J. Isbert, K. C. Kim, E. N. Kuznetsov, M. I. Panasyuk, A. D. Panov, W. K. H. Schmidt, E. S. Seo, N. V. Sokolskaya, J. W. Watts, J. P. Wefel, J. Wu, and V. I. Zatsepin. An excess of cosmic ray electrons at energies of 300-800GeV. *Nature*, 456:362–365, 2008.

S. Chatrchyan, V. Khachatryan, A. M. Sirunyan, and et al. [CMS Collaboration]. Search for New Physics with a Monojet and Missing Transverse Energy in pp Collisions at $s=7\text{TeV}$. *Phys. Rev. Lett.*, 107(20):201804, 2011.

S. Chatrchyan, V. Khachatryan, A. M. Sirunyan, and et al. [CMS Collaboration]. Search for dark matter and large extra dimensions in monojet events in pp collisions at $\sqrt{s} = 7\text{TeV}$. *JHEP*, 9:94, 2012.

C.-R. Chen and F. Takahashi. Cosmic rays from leptonic dark matter. *JCAP*, 2:004, 2009.

F. Chen, J. M. Cline, A. Fradette, A. R. Frey, and C. Rabideau. Exciting dark matter in the Galactic Center. *Phys. Rev. D*, 81(4):043523, 2010.

X. Chen and M. Kamionkowski. Particle decays during the cosmic dark ages. *Phys. Rev. D*, 70(4):043502–+, 2004.

H.-C. Cheng, J. L. Feng, and K. T. Matchev. Kaluza-Klein Dark Matter. *Phys. Rev. Lett.*, 89(21):211301, 2002.

H.-Y. Chiu. Symmetry Between Particle and Antiparticle Populations in the Universe. *Phys. Rev. Lett.*, 17:712–714, 1966.

Y.-Y. Choi, C. Park, J. Kim, J. R. Gott, III, D. H. Weinberg, M. S. Vogeley, S. S. Kim, and [SDSS Collaboration]. Galaxy Clustering Topology in the Sloan Digital Sky Survey Main Galaxy Sample: A Test for Galaxy Formation Models. *ApJS*, 190:181, 2010.

I. Cholis, D. P. Finkbeiner, L. Goodenough, and N. Weiner. The PAMELA positron excess from annihilations into a light boson. *JCAP*, 12:007, 2009a.

I. Cholis, L. Goodenough, D. Hooper, M. Simet, and N. Weiner. High energy positrons from annihilating dark matter. *Phys. Rev. D*, 80(12):123511, 2009b.

I. Cholis, L. Goodenough, and N. Weiner. High energy positrons and the WMAP haze from exciting dark matter. *Phys. Rev. D*, 79(12):123505, 2009c.

V. Choutko and F. Giovacchini. Cosmic Rays Antideuteron Sensitivity for AMS-02 Experiment. In *International Cosmic Ray Conference*, volume 4 of *International Cosmic Ray Conference*, pages 765–768, 2008.

L. Chuzhoy. Impact of Dark Matter Annihilation on the High-Redshift Intergalactic Medium. *ApJ*, 679:L65–L68, 2008.

M. Cirelli. Indirect searches for dark matter. *Pramana*, 79:1021–1043, 2012.

M. Cirelli and P. Panci. Inverse Compton constraints on the Dark Matter e excesses. *Nucl. Phys. B*, 821:399–416, 2009.

M. Cirelli, F. Iocco, and P. Panci. Constraints on Dark Matter annihilations from reionization and heating of the intergalactic gas. *JCAP*, 10:9–+, 2009a.

M. Cirelli, M. Kadastik, M. Raidal, and A. Strumia. Model-independent implications of the e , p^- cosmic ray spectra on properties of Dark Matter. *Nucl. Phys. B*, 813:1–21, 2009b.

M. Cirelli, P. Panci, and P. D. Serpico. Diffuse gamma ray constraints on annihilating or decaying Dark Matter after Fermi. *Nucl. Phys. B*, 840:284–303, 2010.

M. Cirelli, G. Corcella, A. Hektor, G. Hütsi, M. Kadastik, P. Panci, M. Raidal, F. Sala, and A. Strumia. PPPC 4 DM ID: a poor particle physicist cookbook for dark matter indirect detection. *JCAP*, 3:051, 2011.

J. M. Cline, A. R. Frey, and F. Chen. Metastable dark matter mechanisms for INTEGRAL 511 keV γ rays and DAMA/CoGeNT events. *Phys. Rev. D*, 83(8):083511, 2011.

D. Clowe, M. Bradač, A. H. Gonzalez, M. Markevitch, S. W. Randall, C. Jones, and D. Zaritsky. A Direct Empirical Proof of the Existence of Dark Matter. *ApJ*, 648:L109–L113, 2006.

A. Coc, E. Vangioni-Flam, P. Descouvemont, A. Adahchour, and C. Angulo. Updated Big Bang Nucleosynthesis Compared with Wilkinson Microwave Anisotropy Probe Observations and the Abundance of Light Elements. *ApJ*, 600:544–552, 2004.

A. L. Coil. Large Scale Structure of the Universe. *ArXiv e-prints*, [arXiv: 1202.6633], 2012.

S. Colafrancesco. SZ effect from Dark Matter annihilation. *A&A*, 422:L23–L27, 2004.

S. Colafrancesco and B. Mele. Neutralinos and the Origin of Radio Halos in Clusters of Galaxies. *ApJ*, 562:24–41, 2001.

S. Colafrancesco, S. Profumo, and P. Ullio. Multi-frequency analysis of neutralino dark matter annihilations in the Coma cluster. *A&A*, 455:21–43, 2006.

P. Colín, V. Avila-Reese, and O. Valenzuela. Substructure and Halo Density Profiles in a Warm Dark Matter Cosmology. *ApJ*, 542:622–630, 2000.

M. Colless, G. Dalton, S. Maddox, W. Sutherland, P. Norberg, S. Cole, J. Bland-Hawthorn, T. Bridges, R. Cannon, C. Collins, W. Couch, N. Cross, K. Deeley, R. De Propris, S. P. Driver, G. Efstathiou, R. S. Ellis, C. S. Frenk, K. Glazebrook, C. Jackson, O. Lahav, I. Lewis, S. Lumsden, D. Madgwick, J. A. Peacock, B. A. Peterson, I. Price, M. Seaborne, and K. Taylor. The 2dF Galaxy Redshift Survey: spectra and redshifts. *MNRAS*, 328:1039–1063, 2001.

R. M. Crocker, N. F. Bell, C. Balázs, and D. I. Jones. Radio and gamma-ray constraints on dark matter annihilation in the Galactic center. *Phys. Rev. D*, 81(6):063516–+, 2010.

D. J. Croton, V. Springel, S. D. M. White, G. De Lucia, C. S. Frenk, L. Gao, A. Jenkins, G. Kauffmann, J. F. Navarro, and N. Yoshida. The many lives of active galactic nuclei: cooling flows, black holes and the luminosities and colours of galaxies. *MNRAS*, 365:11–28, 2006.

D. T. Cumberbatch, J. Zuntz, H. K. Kamfjord Eriksen, and J. Silk. Can the WMAP Haze really be a signature of annihilating neutralino dark matter? *ArXiv e-prints*, [arXiv: 0902.0039], 2009.

R. Davé, D. N. Spergel, P. J. Steinhardt, and B. D. Wandelt. Halo Properties in Cosmological Simulations of Self-interacting Cold Dark Matter. *ApJ*, 547:574–589, 2001.

M. Davis, J. Huchra, D. W. Latham, and J. Tonry. A survey of galaxy redshifts. II - The large scale space distribution. *ApJ*, 253:423–445, 1982.

M. Davis, G. Efstathiou, C. S. Frenk, and S. D. M. White. The evolution of large-scale structure in a universe dominated by cold dark matter. *ApJ*, 292:371–394, 1985.

P. de Bernardis, P. A. R. Ade, J. J. Bock, J. R. Bond, J. Borrill, A. Boscaleri, K. Coble, B. P. Crill, G. De Gasperis, P. C. Farese, P. G. Ferreira, K. Ganga, M. Giacometti, E. Hivon, V. V. Hristov, A. Iacoangeli, A. H. Jaffe, A. E. Lange, L. Martinis, S. Masi, P. V. Mason, P. D. Mauskopf, A. Melchiorri, L. Miglio, T. Montroy, C. B. Netterfield, E. Pascale, F. Piacentini, D. Pogosyan, S. Prunet, S. Rao, G. Romeo, J. E. Ruhl, F. Scaramuzzi, D. Sforna, and N. Vittorio. A flat Universe from high-resolution maps of the cosmic microwave background radiation. *Nature*, 404:955–959, 2000.

W. J. G. de Blok. The Core-Cusp Problem. *Advances in Astronomy*, 2010:789293, 2010.

W. J. G. de Blok and A. Bosma. High-resolution rotation curves of low surface brightness galaxies. *A&A*, 385:816–846, 2002.

W. J. G. de Blok, S. S. McGaugh, A. Bosma, and V. C. Rubin. Mass Density Profiles of Low Surface Brightness Galaxies. *ApJ*, 552:L23–L26, 2001.

W. J. G. de Blok, F. Walter, E. Brinks, C. Trachternach, S.-H. Oh, and R. C. Kennicutt. High-Resolution Rotation Curves and Galaxy Mass Models from THINGS. *AJ*, 136: 2648–2719, 2008.

G. De Lucia and J. Blaizot. The hierarchical formation of the brightest cluster galaxies. *MNRAS*, 375:2–14, 2007.

W. Dehnen and J. Binney. Mass models of the Milky Way. *MNRAS*, 294:429–+, 1998.

A. Dekel, I. Arad, J. Devor, and Y. Birnboim. Dark Halo Cusp: Asymptotic Convergence. *ApJ*, 588:680–695, 2003.

T. Delahaye, R. Lineros, F. Donato, N. Fornengo, and P. Salati. Positrons from dark matter annihilation in the galactic halo: Theoretical uncertainties. *Phys. Rev. D*, 77 (6):063527, March 2008.

T. Delahaye, R. Lineros, F. Donato, N. Fornengo, J. Lavalle, P. Salati, and R. Taillet. Galactic secondary positron flux at the Earth. *A&A*, 501:821–833, 2009.

T. Delahaye, C. Böhm, and J. Silk. Can Planck constrain indirect detection of dark matter in our Galaxy? *MNRAS*, 422:L16, 2012.

C. Dickinson, H. K. Eriksen, A. J. Banday, J. B. Jewell, K. M. Górski, G. Huey, C. R. Lawrence, I. J. O’Dwyer, and B. D. Wandelt. Bayesian Component Separation and Cosmic Microwave Background Estimation for the Five-Year WMAP Temperature Data. *ApJ*, 705:1607–1623, 2009.

D. A. Dicus, E. W. Kolb, and V. L. Teplitz. Cosmological upper bound on heavy-neutrino lifetimes. *Phys. Rev. Lett.*, 39:168–171, 1977.

J. Diemand and B. Moore. The Structure and Evolution of Cold Dark Matter Halos. *Adv. Sci. Lett.*, 4:297–310, 2011.

J. Diemand, B. Moore, and J. Stadel. Earth-mass dark-matter haloes as the first structures in the early Universe. *Nature*, 433:389–391, 2005a.

J. Diemand, M. Zemp, B. Moore, J. Stadel, and C. M. Carollo. Cusps in cold dark matter haloes. *MNRAS*, 364:665–673, 2005b.

J. Diemand, M. Kuhlen, P. Madau, M. Zemp, B. Moore, D. Potter, and J. Stadel. Clumps and streams in the local dark matter distribution. *Nature*, 454:735–738, 2008.

M. Dine and W. Fischler. The not-so-harmless axion. *Phys. Lett. B*, 120:137–141, 1983.

G. Dobler and D. P. Finkbeiner. Identification of Spinning Dust in H α -Correlated Microwave Emission. *ApJ*, 680:1235–1242, 2008a.

G. Dobler and D. P. Finkbeiner. Extended Anomalous Foreground Emission in the WMAP Three-Year Data. *ApJ*, 680:1222–1234, 2008b.

G. Dobler, D. P. Finkbeiner, I. Cholis, T. Slatyer, and N. Weiner. The Fermi Haze: A Gamma-ray Counterpart to the Microwave Haze. *ApJ*, 717:825–842, 2010.

S. Dodelson, D. Hooper, and P. D. Serpico. Extracting the gamma ray signal from dark matter annihilation in the galactic center region. *Phys. Rev. D*, 77(6):063512, 2008.

F. Donato, N. Fornengo, and P. Salati. Antideuterons as a signature of supersymmetric dark matter. *Phys. Rev. D*, 62(4):043003, 2000.

F. Donato, N. Fornengo, D. Maurin, P. Salati, and R. Taillet. Antiprotons in cosmic rays from neutralino annihilation. *Phys. Rev. D*, 69(6):063501–, 2004a.

F. Donato, G. Gentile, and P. Salucci. Cores of dark matter haloes correlate with stellar scalelengths. *MNRAS*, 353:L17–L22, 2004b.

F. Donato, D. Maurin, P. Brun, T. Delahaye, and P. Salati. Constraints on WIMP Dark Matter from the High Energy PAMELA \bar{p}/p Data. *Phys. Rev. Lett.*, 102(7):071301, 2009.

B. T. Draine and A. Lazarian. Electric Dipole Radiation from Spinning Dust Grains. *ApJ*, 508:157–179, 1998.

M. Drees and G. Gerbier. Mini-Review of Dark Matter: 2012. *ArXiv e-prints*, [arXiv: 1204.2373], 2012.

M. Drees and M. M. Nojiri. Neutralino relic density in minimal N=1 supergravity. *Phys. Rev. D*, 47:376–408, 1993.

J. Dubinski and R. G. Carlberg. The structure of cold dark matter halos. *ApJ*, 378: 496–503, 1991.

R. Eichler, L. Felawka, N. Kraus, C. Niebuhr, H. K. Walter, S. Egli, R. Engfer, C. Grab, E. A. Hermes, H. S. Pruys, A. van der Schaaf, D. Vermeulen, W. Bertl, N. Lordong, U. Bellgardt, G. Otter, T. Kozlowski, and J. Martino. Limits for short-lived neutral particles emitted in μ^+ or π^+ decay. *Phys. Lett. B*, 175:101–104, 1986.

J. Einasto. On the Construction of a Composite Model for the Galaxy and on the Determination of the System of Galactic Parameters. *Trudy Astrofizicheskogo Instituta Alma-Ata*, 5:87–100, 1965.

J. Einasto. Dark Matter. *ArXiv e-prints*, [arXiv: 0901.0632], 2009.

V. R. Eke, C. M. Baugh, S. Cole, C. S. Frenk, and J. F. Navarro. Galaxy groups in the 2dF Galaxy Redshift Survey: the number density of groups. *MNRAS*, 370:1147–1158, 2006.

A. El-Zant, I. Shlosman, and Y. Hoffman. Dark Halos: The Flattening of the Density Cusp by Dynamical Friction. *ApJ*, 560:636–643, 2001.

J. Ellis, J. S. Hagelin, D. V. Nanopoulos, K. Olive, and M. Srednicki. Supersymmetric relics from the big bang. *Nucl. Phys. B*, 238:453–476, 1984a.

J. Ellis, J. E. Kim, and D. V. Nanopoulos. Cosmological gravitino regeneration and decay. *Phys. Lett. B*, 145:181–186, 1984b.

J. Ellis, D. V. Nanopoulos, and S. Sarkar. The cosmology of decaying gravitinos. *Nucl. Phys. B*, 259:175–188, 1985.

J. Ellis, K. A. Olive, Y. Santoso, and V. C. Spanos. Gravitino dark matter in the CMSSM. *Phys. Lett. B*, 588:7–16, 2004.

J. Ellis, K. A. Olive, and C. Savage. Hadronic uncertainties in the elastic scattering of supersymmetric dark matter. *Phys. Rev. D*, 77(6):065026, 2008.

R. Essig, N. Sehgal, and L. E. Strigari. Bounds on cross sections and lifetimes for dark matter annihilation and decay into charged leptons from gamma-ray observations of dwarf galaxies. *Phys. Rev. D*, 80(2):023506, 2009.

R. Essig, N. Sehgal, L. E. Strigari, M. Geha, and J. D. Simon. Indirect dark matter detection limits from the ultrafaint Milky Way satellite Segue 1. *Phys. Rev. D*, 82(12):123503, 2010.

G. Fahlman, N. Kaiser, G. Squires, and D. Woods. Dark matter in MS 1224 from distortion of background galaxies. *ApJ*, 437:56–62, 1994.

D. Feldman, Z. Liu, and P. Nath. PAMELA positron excess as a signal from the hidden sector. *Phys. Rev. D*, 79(6):063509, 2009.

D. Feldman, Z. Liu, and P. Nath. Low mass neutralino dark matter in the minimal supersymmetric standard model with constraints from B_s to $\mu^+ \mu^-$ and Higgs boson search limits. *Phys. Rev. D*, 81(11):117701, 2010.

J. L. Feng. Dark Matter Candidates from Particle Physics and Methods of Detection. *ARA&A*, 48:495–545, 2010.

J. L. Feng, A. Rajaraman, and F. Takayama. Superweakly Interacting Massive Particles. *Phys. Rev. Lett.*, 91(1):011302, 2003a.

J. L. Feng, A. Rajaraman, and F. Takayama. Superweakly interacting massive particle dark matter signals from the early Universe. *Phys. Rev. D*, 68(6):063504, 2003b.

K. M. Ferrière. The interstellar environment of our galaxy. *Rev. Mod. Phys.*, 73:1031–1066, 2001.

D. P. Finkbeiner. A Full-Sky H α Template for Microwave Foreground Prediction. *ApJS*, 146:407–415, 2003.

D. P. Finkbeiner. Microwave Interstellar Medium Emission Observed by the Wilkinson Microwave Anisotropy Probe. *ApJ*, 614:186–193, 2004a.

D. P. Finkbeiner. WMAP Microwave Emission Interpreted as Dark Matter Annihilation in the Inner Galaxy. *ArXiv e-prints*, [arXiv: astro-ph/0409027], 2004b.

D. P. Finkbeiner and N. Weiner. Exciting dark matter and the INTEGRAL/SPI 511keV signal. *Phys. Rev. D*, 76(8):083519, 2007.

D. P. Finkbeiner, M. Davis, and D. J. Schlegel. Extrapolation of Galactic Dust Emission at 100 Microns to Cosmic Microwave Background Radiation Frequencies Using FIRAS. *ApJ*, 524:867–886, 1999.

D. J. Fixsen. The Temperature of the Cosmic Microwave Background. *ApJ*, 707:916–920, 2009.

D. J. Fixsen, A. Kogut, S. Levin, M. Limon, P. Lubin, P. Mirel, M. Seiffert, J. Singal, E. Wollack, T. Villela, and C. A. Wuensche. ARCADE 2 Measurement of the Extra-Galactic Sky Temperature at 3-90 GHz. *ArXiv e-prints*, [arXiv: 0901.0555], 2009.

R. A. Flores and J. R. Primack. Observational and theoretical constraints on singular dark matter halos. *ApJ*, 427:L1–L4, 1994.

M. Fornasa, L. Pieri, G. Bertone, and E. Branchini. Anisotropy probe of galactic and extra-galactic dark matter annihilations. *Phys. Rev. D*, 80(2):023518–+, 2009.

N. Fornengo, L. Pieri, and S. Scopel. Neutralino annihilation into γ rays in the Milky Way and in external galaxies. *Phys. Rev. D*, 70(10):103529, 2004.

N. Fornengo, R. Lineros, M. Regis, and M. Taoso. Possibility of a Dark Matter Interpretation for the Excess in Isotropic Radio Emission Reported by ARCADE. *Phys. Rev. Lett.*, 107(26):271302, 2011.

N. Fornengo, R. A. Lineros, M. Regis, and M. Taoso. Galactic synchrotron emission from WIMPs at radio frequencies. *JCAP*, 1:005, 2012.

P. J. Fox, R. Harnik, J. Kopp, and Y. Tsai. Missing energy signatures of dark matter at the LHC. *Phys. Rev. D*, 85(5):056011, 2012.

C. S. Frenk and S. D. M. White. Dark matter and cosmic structure. *Ann. Phys. (Berlin)*, 524:507–534, 2012.

C. S. Frenk, S. D. M. White, G. Efstathiou, and M. Davis. Cold dark matter, the structure of galactic haloes and the origin of the Hubble sequence. *Nature*, 317:595–597, 1985.

C. S. Frenk, S. D. M. White, M. Davis, and G. Efstathiou. The formation of dark halos in a universe dominated by cold dark matter. *ApJ*, 327:507–525, 1988.

C. S. Frenk, S. D. M. White, G. Efstathiou, and M. Davis. Galaxy clusters and the amplitude of primordial fluctuations. *ApJ*, 351:10–21, 1990.

Y. Fujita, K. Kohri, R. Yamazaki, and K. Ioka. Is the PAMELA anomaly caused by supernova explosions near the Earth? *Phys. Rev. D*, 80(6):063003, 2009.

T. Fukushige and J. Makino. On the Origin of Cusps in Dark Matter Halos. *ApJ*, 477: L9+, 1997.

T. Fukushige and J. Makino. Structure of Dark Matter Halos from Hierarchical Clustering. *ApJ*, 557:533–545, 2001.

T. Fukushige and J. Makino. Structure of Dark Matter Halos from Hierarchical Clustering. II. Dependence of Cosmological Models in Cluster-sized Halos. *ApJ*, 588:674–679, 2003.

T. Fukushige, A. Kawai, and J. Makino. Structure of Dark Matter Halos from Hierarchical Clustering. III. Shallowing of the Inner Cusp. *ApJ*, 606:625–634, 2004.

S. R. Furlanetto, S. P. Oh, and E. Pierpaoli. Effects of dark matter decay and annihilation on the high-redshift 21cm background. *Phys. Rev. D*, 74(10):103502–+, 2006.

R. J. Gaitskell. Direct Detection of Dark Matter. *Annual Review of Nuclear and Particle Science*, 54:315–359, 2004.

S. Galli, F. Iocco, G. Bertone, and A. Melchiorri. CMB constraints on dark matter models with large annihilation cross section. *Phys. Rev. D*, 80(2):023505–+, 2009.

S. Galli, F. Iocco, G. Bertone, and A. Melchiorri. Updated CMB constraints on dark matter annihilation cross sections. *Phys. Rev. D*, 84(2):027302, 2011.

L. Gao, J. F. Navarro, S. Cole, C. S. Frenk, S. D. M. White, V. Springel, A. Jenkins, and A. F. Neto. The redshift dependence of the structure of massive Λ cold dark matter haloes. *MNRAS*, 387:536–544, 2008.

L. Gao, J. F. Navarro, C. S. Frenk, A. Jenkins, V. Springel, and S. D. M. White. The Phoenix Project: the dark side of rich Galaxy clusters. *MNRAS*, 425:2169–2186, 2012.

M. Garny, A. Ibarra, D. Tran, and C. Weniger. Gamma-ray lines from radiative dark matter decay. *JCAP*, 1:032, 2011.

S. Gelato and J. Sommer-Larsen. On DDO 154 and cold dark matter halo profiles. *MNRAS*, 303:321–328, 1999.

G. B. Gelmini, E. Osoba, and S. Palomares-Ruiz. Inert-sterile neutrino: Cold or warm dark matter candidate. *Phys. Rev. D*, 81(6):063529, 2010.

G. Gentile, P. Salucci, U. Klein, D. Vergani, and P. Kalberla. The cored distribution of dark matter in spiral galaxies. *MNRAS*, 351:903–922, 2004.

G. Gentile, B. Famaey, and W. J. G. de Blok. THINGS about MOND. *A&A*, 527:A76, 2011.

A. Geringer-Sameth and S. M. Koushiappas. Exclusion of Canonical Weakly Interacting Massive Particles by Joint Analysis of Milky Way Dwarf Galaxies with Data from the Fermi Gamma-Ray Space Telescope. *Phys. Rev. Lett.*, 107(24):241303, 2011.

S. Ghigna, B. Moore, F. Governato, G. Lake, T. Quinn, and J. Stadel. Dark matter haloes within clusters. *MNRAS*, 300:146–162, 1998.

S. Ghigna, B. Moore, F. Governato, G. Lake, T. Quinn, and J. Stadel. Density Profiles and Substructure of Dark Matter Halos: Converging Results at Ultra-High Numerical Resolution. *ApJ*, 544:616–628, 2000.

G. Ghisellini, P. W. Guilbert, and R. Svensson. The synchrotron boiler. *ApJ*, 334:L5–L8, 1988.

B. Gold, C. L. Bennett, R. S. Hill, G. Hinshaw, N. Odegard, L. Page, D. N. Spergel, J. L. Weiland, J. Dunkley, M. Halpern, N. Jarosik, A. Kogut, E. Komatsu, D. Larson, S. S. Meyer, M. R. Nolta, E. Wollack, and E. L. Wright. Five-Year Wilkinson Microwave Anisotropy Probe Observations: Galactic Foreground Emission. *ApJS*, 180:265–282, 2009.

B. Gold, N. Odegard, J. L. Weiland, R. S. Hill, A. Kogut, C. L. Bennett, G. Hinshaw, X. Chen, J. Dunkley, M. Halpern, N. Jarosik, E. Komatsu, D. Larson, M. Limon, S. S. Meyer, M. R. Nolta, L. Page, K. M. Smith, D. N. Spergel, G. S. Tucker, E. Wollack, and E. L. Wright. Seven-year Wilkinson Microwave Anisotropy Probe (WMAP) Observations: Galactic Foreground Emission. *ApJS*, 192:15, 2011.

H. Goldberg. Constraint on the photino mass from cosmology. *Phys. Rev. Lett.*, 50: 1419–1422, 1983.

P. Gondolo and J. Silk. Dark Matter Annihilation at the Galactic Center. *Phys. Rev. Lett.*, 83:1719–1722, 1999.

P. Gondolo, J. Edsjö, P. Ullio, L. Bergström, M. Schelke, and E. A. Baltz. DarkSUSY: computing supersymmetric dark matter properties numerically. *JCAP*, 7:008, 2004.

L. Goodenough and D. Hooper. Possible Evidence For Dark Matter Annihilation In The Inner Milky Way From The Fermi Gamma Ray Space Telescope. *ArXiv e-prints*, [arXiv: 0910.2998], 2009.

J. Goodman. Repulsive dark matter. *New Astronomy*, 5:103–107, 2000.

J. Goodman, M. Ibe, A. Rajaraman, W. Shepherd, T. M. P. Tait, and H.-B. Yu. Constraints on dark matter from colliders. *Phys. Rev. D*, 82(11):116010, 2010.

M. W. Goodman and E. Witten. Detectability of certain dark-matter candidates. *Phys. Rev. D*, 31:3059–3063, 1985.

J. R. Gott, III. On the Formation of Elliptical Galaxies. *ApJ*, 201:296–310, 1975.

D. Grasso, S. Profumo, A. W. Strong, and et al. On possible interpretations of the high energy electron-positron spectrum measured by the Fermi Large Area Telescope. *Astropart. Phys.*, 32:140–151, 2009.

K. Griest. Calculations of rates for direct detection of neutralino dark matter. *Phys. Rev. Lett.*, 61:666–669, 1988a.

K. Griest. Cross sections, relic abundance, and detection rates for neutralino dark matter. *Phys. Rev. D*, 38:2357–2375, 1988b.

J. E. Gunn. Massive galactic halos. I - Formation and evolution. *ApJ*, 218:592–598, 1977.

Q. Guo, S. White, M. Boylan-Kolchin, G. De Lucia, G. Kauffmann, G. Lemson, C. Li, V. Springel, and S. Weinmann. From dwarf spheroidals to cD galaxies: simulating the galaxy population in a Λ CDM cosmology. *MNRAS*, 413:101–131, 2011.

W.-L. Guo and Y.-L. Wu. Enhancement of dark matter annihilation via Breit-Wigner resonance. *Phys. Rev. D*, 79(5):055012, 2009.

A. H. Guth. Inflationary universe: A possible solution to the horizon and flatness problems. *Phys. Rev. D*, 23:347–356, 1981.

A. H. Guth and S.-Y. Pi. Fluctuations in the new inflationary universe. *Phys. Rev. Lett.*, 49:1110–1113, 1982.

C. J. Hailey. An indirect search for dark matter using antideuterons: the GAPS experiment. *New J. Phys.*, 11(10):105022, 2009.

S. Hanany, P. Ade, A. Balbi, J. Bock, J. Borrill, A. Boscaleri, P. de Bernardis, P. G. Ferreira, V. V. Hristov, A. H. Jaffe, A. E. Lange, A. T. Lee, P. D. Mauskopf, C. B. Netterfield, S. Oh, E. Pascale, B. Rabii, P. L. Richards, G. F. Smoot, R. Stompor, C. D. Winant, and J. H. P. Wu. MAXIMA-1: A Measurement of the Cosmic Microwave Background Anisotropy on Angular Scales of 10'-5deg. *ApJ*, 545:L5–L9, 2000.

J. P. Harding and K. N. Abazajian. Morphological tests of the pulsar and dark matter interpretations of the WMAP haze. *Phys. Rev. D*, 81(2):023505, 2010.

C. G. T. Haslam, U. Klein, C. J. Salter, H. Stoffel, W. E. Wilson, M. N. Cleary, D. J. Cooke, and P. Thomasson. A 408 MHz all-sky continuum survey. I - Observations at southern declinations and for the North Polar region. *A&A*, 100:209–219, 1981.

C. G. T. Haslam, C. J. Salter, H. Stoffel, and W. E. Wilson. A 408 MHz all-sky continuum survey. II - The atlas of contour maps. *A&AS*, 47:1, 1982.

S. W. Hawking. The development of irregularities in a single bubble inflationary universe. *Phys. Lett. B*, 115:295–297, 1982.

E. Hayashi, J. F. Navarro, C. Power, A. Jenkins, C. S. Frenk, S. D. M. White, V. Springel, J. Stadel, and T. R. Quinn. The inner structure of Λ CDM haloes - II. Halo mass profiles and low surface brightness galaxy rotation curves. *MNRAS*, 355:794–812, 2004.

S. Hilbert and S. D. M. White. Abundances, masses and weak-lensing mass profiles of galaxy clusters as a function of richness and luminosity in Λ CDM cosmologies. *MNRAS*, 404:486–501, 2010.

G. Hinshaw, M. R. Nolta, C. L. Bennett, R. Bean, O. Doré, M. R. Greason, M. Halpern, R. S. Hill, N. Jarosik, A. Kogut, E. Komatsu, M. Limon, N. Odegard, S. S. Meyer, L. Page, H. V. Peiris, D. N. Spergel, G. S. Tucker, L. Verde, J. L. Weiland, E. Wollack, and E. L. Wright. Three-Year Wilkinson Microwave Anisotropy Probe (WMAP) Observations: Temperature Analysis. *ApJS*, 170:288–334, 2007.

J. Hisano, S. Matsumoto, and M. M. Nojiri. Explosive Dark Matter Annihilation. *Phys. Rev. Lett.*, 92(3):031303, 2004.

J. Hisano, S. Matsumot, M. Nagai, O. Saito, and M. Senami. Non-perturbative effect on thermal relic abundance of dark matter. *Phys. Lett. B*, 646:34–38, 2007.

D. Hooper and L. Goodenough. Dark matter annihilation in the Galactic Center as seen by the Fermi Gamma Ray Space Telescope. *Phys. Lett. B*, 697:412–428, 2011.

D. Hooper and G. D. Kribs. Kaluza-Klein dark matter and the positron excess. *Phys. Rev. D*, 70(11):115004, 2004.

D. Hooper and T. Linden. Gamma rays from the Galactic center and the WMAP haze. *Phys. Rev. D*, 83(8):083517, 2011a.

D. Hooper and T. Linden. Origin of the gamma rays from the Galactic Center. *Phys. Rev. D*, 84(12):123005, 2011b.

D. Hooper and K. M. Zurek. PAMELA and ATIC signals from Kaluza-Klein dark matter. *Phys. Rev. D*, 79(10):103529, 2009.

D. Hooper, D. P. Finkbeiner, and G. Dobler. Possible evidence for dark matter annihilations from the excess microwave emission around the center of the Galaxy seen by the Wilkinson Microwave Anisotropy Probe. *Phys. Rev. D*, 76(8):083012, 2007.

D. Hooper, A. V. Belikov, T. E. Jeltema, T. Linden, S. Profumo, and T. R. Slatyer. The isotropic radio background and annihilating dark matter. *Phys. Rev. D*, 86(10):103003, 2012.

W. Hu and S. Dodelson. Cosmic Microwave Background Anisotropies. *ARA&A*, 40: 171–216, 2002.

W. Hu, R. Barkana, and A. Gruzinov. Fuzzy Cold Dark Matter: The Wave Properties of Ultralight Particles. *Phys. Rev. Lett.*, 85:1158–1161, 2000.

A. Huss, B. Jain, and M. Steinmetz. How Universal Are the Density Profiles of Dark Halos? *ApJ*, 517:64–69, 1999.

G. Hütsi, J. Chluba, A. Hektor, and M. Raidal. WMAP7 and future CMB constraints on annihilating dark matter: implications for GeV-scale WIMPs. *A&A*, 535:A26, 2011.

A. Ibarra and D. Tran. Decaying dark matter and the PAMELA anomaly. *JCAP*, 2:021, 2009a.

A. Ibarra and D. Tran. Antideuterons from dark matter decay. *JCAP*, 6:004, 2009b.

A. Ibarra, A. Ringwald, D. Tran, and C. Weniger. Cosmic rays from leptophilic dark matter decay via kinetic mixing. *JCAP*, 8:017, 2009.

M. Ibe, H. Murayama, and T. T. Yanagida. Breit-Wigner enhancement of dark matter annihilation. *Phys. Rev. D*, 79(9):095009, 2009.

F. Iocco, A. Bressan, E. Ripamonti, R. Schneider, A. Ferrara, and P. Marigo. Dark matter annihilation effects on the first stars. *MNRAS*, 390:1655–1669, 2008.

F. Iocco, G. Mangano, G. Miele, O. Pisanti, and P. D. Serpico. Primordial nucleosynthesis: From precision cosmology to fundamental physics. *Phys. Rep.*, 472:1–76, 2009.

K. Ishiwata, S. Matsumoto, and T. Moroi. Synchrotron radiation from the Galactic center in the decaying dark matter scenario. *Phys. Rev. D*, 79(4):043527, 2009.

N. Jarosik, C. L. Bennett, J. Dunkley, B. Gold, M. R. Greason, and et al. Seven-year Wilkinson Microwave Anisotropy Probe (WMAP) Observations: Sky Maps, Systematic Errors, and Basic Results. *ApJS*, 192:14, 2011.

T. E. Jeltema, J. Kehayias, and S. Profumo. Gamma rays from clusters and groups of galaxies: Cosmic rays versus dark matter. *Phys. Rev. D*, 80(2):023005, 2009.

Y. P. Jing and Y. Suto. The Density Profiles of the Dark Matter Halo Are Not Universal. *ApJ*, 529:L69–L72, 2000.

G. Jungman, M. Kamionkowski, and K. Griest. Supersymmetric dark matter. *Phys. Rep.*, 267:195–373, 1996.

M. Kamionkowski and M. S. Turner. Distinctive positron feature from particle dark-matter annihilations in the galactic halo. *Phys. Rev. D*, 43:1774–1780, 1991.

G. L. Kane, L.-T. Wang, and T. T. Wang. Supersymmetry and the cosmic ray positron excess. *Phys. Lett. B*, 536:263–269, 2002a.

G. L. Kane, L.-T. Wang, and J. D. Wells. Supersymmetry and the positron excess in cosmic rays. *Phys. Rev. D*, 65(5):057701, 2002b.

T. Kanzaki, M. Kawasaki, and K. Nakayama. Effects of Dark Matter Annihilation on the Cosmic Microwave Background. *Progress of Theoretical Physics*, 123:853–865, 2010.

M. Kaplinghat, L. Knox, and M. S. Turner. Annihilating Cold Dark Matter. *Phys. Rev. Lett.*, 85:3335–3338, 2000.

M. Kaplinghat, D. J. Phalen, and K. M. Zurek. Pulsars as a source of the WMAP haze. *JCAP*, 12:010, 2009.

B. Katz, K. Blum, J. Morag, and E. Waxman. What can we really learn from positron flux ‘anomalies’? *MNRAS*, 405:1458–1472, 2010.

M. Kilbinger, K. Benabed, J. Guy, P. Astier, I. Tereno, L. Fu, D. Wraith, J. Coupon, Y. Mellier, C. Balland, F. R. Bouchet, T. Hamana, D. Hardin, H. J. McCracken, R. Pain, N. Regnault, M. Schultheis, and H. Yahagi. Dark-energy constraints and correlations with systematics from CFHTLS weak lensing, SNLS supernovae Ia and WMAP5. *A&A*, 497:677–688, 2009.

S. K. Kim. KIMS : Dark Matter Search Experiment in Korea. In K. Choi, J. E. Kim, and D. Son, editors, *Particles, Strings, and Cosmology*, volume 805 of *American Institute of Physics Conference Series*, pages 75–81, 2005.

O. Klein. Quantentheorie und fünfdimensionale Relativitätstheorie. *Zeitschrift fur Physik*, 37:895–906, 1926.

A. Klypin, A. V. Kravtsov, J. S. Bullock, and J. R. Primack. Resolving the Structure of Cold Dark Matter Halos. *ApJ*, 554:903–915, 2001.

A. Klypin, H. Zhao, and R. S. Somerville. Λ CDM-based Models for the Milky Way and M31. I. Dynamical Models. *ApJ*, 573:597–613, 2002.

C. Knobel, S. J. Lilly, C. M. Carollo, T. Contini, J.-P. Kneib, O. Le Fevre, V. Mainieri, A. Renzini, M. Scudeggio, G. Zamorani, S. Bardelli, M. Bolzonella, A. Bongiorno, K. Caputi, O. Cucciati, S. de la Torre, L. de Ravel, P. Franzetti, B. Garilli, A. Iovino, P. Kampczyk, K. Kovač, F. Lamareille, J.-F. Le Borgne, V. Le Brun, C. Maier, M. Mignoli, R. Pello, Y. Peng, E. Perez Montero, V. Presotto, J. Silverman, M. Tanaka, L. Tasca, L. Tresse, D. Vergani, E. Zucca, L. Barnes, R. Bordoloi, A. Cappi, A. Cimatti, G. Coppa, A. M. Koekemoer, C. López-Sanjuan, H. J. McCracken, M. Moresco, P. Nair, L. Pozzetti, and N. Welikala. A Group-galaxy Cross-correlation Function Analysis in zCOSMOS. *ApJ*, 755:48, 2012.

A. Kogut, D. J. Fixsen, S. M. Levin, M. Limon, P. M. Lubin, P. Mirel, M. Seiffert, J. Singal, T. Villela, E. Wollack, and C. A. Wuensche. ARCADE 2 Observations of Galactic Radio Emission. *ApJ*, 734:4, 2011.

K. Kong and K. T. Matchev. Precise calculation of the relic density of Kaluza-Klein dark matter in universal extra dimensions. *JHEP*, 1:038, 2006.

L. M. Krauss. New constraints on “INO” masses from cosmology (I). Supersymmetric “inos”. *Nucl. Phys. B*, 227:556–569, 1983.

A. V. Kravtsov, A. A. Klypin, J. S. Bullock, and J. R. Primack. The Cores of Dark Matter-dominated Galaxies: Theory versus Observations. *ApJ*, 502:48–+, 1998.

M. Kuhlen, J. Diemand, P. Madau, and M. Zemp. The Via Lactea INCITE simulation: galactic dark matter substructure at high resolution. *JPCS*, 125(1):012008, 2008.

R. Kuzio de Naray, S. S. McGaugh, and W. J. G. de Blok. Mass Models for Low Surface Brightness Galaxies with High-Resolution Optical Velocity Fields. *ApJ*, 676:920–943, 2008.

C. Lacey and S. Cole. Merger rates in hierarchical models of galaxy formation. *MNRAS*, 262:627–649, 1993.

M. Laine and M. Shaposhnikov. Sterile neutrino dark matter as a consequence of ν MSM-induced lepton asymmetry. *JCAP*, 6:031, 2008.

D. Larson, J. Dunkley, G. Hinshaw, E. Komatsu, M. R. Nolta, C. L. Bennett, B. Gold, M. Halpern, R. S. Hill, N. Jarosik, A. Kogut, M. Limon, S. S. Meyer, N. Odegard, L. Page, K. M. Smith, D. N. Spergel, G. S. Tucker, J. L. Weiland, E. Wollack, and E. L. Wright. Seven-year Wilkinson Microwave Anisotropy Probe (WMAP) Observations: Power Spectra and WMAP-derived Parameters. *ApJS*, 192:16, 2011.

J. Lavalle. Sunyaev-Zel'dovich effects from annihilating dark matter in the Milky Way: Smooth halo, subhalos, and intermediate-mass black holes. *Phys. Rev. D*, 82(8):083521, 2010.

J. Lavalle and P. Salati. Dark matter indirect signatures. *Comptes Rendus Physique*, 13: 740–782, 2012.

B. W. Lee and S. Weinberg. Cosmological lower bound on heavy-neutrino masses. *Phys. Rev. Lett.*, 39:165–168, 1977.

LeZhang and G. Sigl. Dark matter signatures in the anisotropic radio sky. *JCAP*, 9:027, 2008.

LeZhang, J. Redondo, and G. Sigl. Galactic signatures of decaying dark matter. *JCAP*, 9:012, 2009.

Y.-S. Li and S. D. M. White. Masses for the Local Group and the Milky Way. *MNRAS*, 384:1459–1468, 2008.

A. D. Linde. A new inflationary universe scenario: A possible solution of the horizon, flatness, homogeneity, isotropy and primordial monopole problems. *Phys. Lett. B*, 108: 389–393, 1982a.

A. D. Linde. Scalar field fluctuations in the expanding universe and the new inflationary universe scenario. *Phys. Lett. B*, 116:335–339, 1982b.

T. Linden and S. Profumo. Systematic Effects in Extracting a “Gamma-ray Haze” from Spatial Templates. *ApJ*, 714:L228–L232, 2010.

T. Linden, S. Profumo, and B. Anderson. Morphology of the Galactic dark matter synchrotron emission with self-consistent cosmic-ray diffusion models. *Phys. Rev. D*, 82(6): 063529, 2010.

S. Lombardi, J. Aleksic, J. A. Barrio, A. Biland, M. Doro, D. Elsaesser, M. Gaug, K. Manneheim, M. Mariotti, M. Martinez, D. Nieto, M. Persic, F. Prada, J. Rico, M. Rissi, M. A. Sanchez-Conde, L. S. Stark, F. Zandanel, and for the MAGIC Collaboration. Search for Dark Matter signatures with MAGIC-I and prospects for MAGIC Phase-II. *ArXiv e-prints*, [arXiv: 0907.0738], 2009.

M. S. Longair. *High energy astrophysics: An Informal Introduction for Students of Physics and Astronomy*. Cambridge University Press, 1981.

V. A. Lubimov, E. G. Novikov, V. Z. Nozik, E. F. Tretyakov, and V. S. Kosik. An estimate of the ν_e mass from the β -spectrum of tritium in the valine molecule. *Phys. Lett. B*, 94:266–268, 1980.

D. Malyshev, I. Cholis, and J. Gelfand. Pulsars versus dark matter interpretation of ATIC/PAMELA. *Phys. Rev. D*, 80(6):063005, 2009.

A. Manrique, A. Raig, E. Salvador-Solé, T. Sanchis, and J. M. Solanes. On the Origin of the Inner Structure of Halos. *ApJ*, 593:26–37, 2003.

M. Mapelli, A. Ferrara, and E. Pierpaoli. Impact of dark matter decays and annihilations on reionization. *MNRAS*, 369:1719–1724, 2006.

D. Marchesini, E. D’Onghia, G. Chincarini, C. Firmani, P. Conconi, E. Molinari, and A. Zocchei. $H\alpha$ Rotation Curves: The Soft Core Question. *ApJ*, 575:801–813, 2002.

M. Markevitch. Chandra Observation of the Most Interesting Cluster in the Universe. In A. Wilson, editor, *The X-ray Universe 2005*, volume 604 of *ESA Special Publication*, page 723, 2006.

G. D. Martinez, J. S. Bullock, M. Kaplinghat, L. E. Strigari, and R. Trotta. Indirect Dark Matter detection from Dwarf satellites: joint expectations from astrophysics and supersymmetry. *JCAP*, 6:014, 2009.

S. Mashchenko, H. M. P. Couchman, and J. Wadsley. The removal of cusps from galaxy centres by stellar feedback in the early Universe. *Nature*, 442:539–542, 2006.

S. S. McGaugh and W. J. G. de Blok. Testing the Dark Matter Hypothesis with Low Surface Brightness Galaxies and Other Evidence. *ApJ*, 499:41–+, 1998.

M. McQuinn and M. Zaldarriaga. Testing the dark matter annihilation model for the Wilkinson Microwave Anisotropy Probe haze. *MNRAS*, 414:3577–3589, 2011.

P. Meade, M. Papucci, A. Strumia, and T. Volansky. Dark Matter interpretations of the e^\pm excesses after FERMI. *Nucl. Phys. B*, 831:178–203, 2010.

P. Mertsch and S. Sarkar. Testing Astrophysical Models for the PAMELA Positron Excess with Cosmic Ray Nuclei. *Phys. Rev. Lett.*, 103(8):081104, 2009.

M. Milgrom. A modification of the Newtonian dynamics as a possible alternative to the hidden mass hypothesis. *ApJ*, 270:365–370, 1983.

B. Moore. Evidence against dissipation-less dark matter from observations of galaxy haloes. *Nature*, 370:629–631, 1994.

B. Moore, F. Governato, T. Quinn, J. Stadel, and G. Lake. Resolving the Structure of Cold Dark Matter Halos. *ApJ*, 499:L5+, 1998.

B. Moore, T. Quinn, F. Governato, J. Stadel, and G. Lake. Cold collapse and the core catastrophe. *MNRAS*, 310:1147–1152, 1999.

A. Morselli, A. Lionetto, A. Cesarini, F. Fucito, and P. Ullio. Search for dark matter with GLAST. *Nucl. Phys. B: Proceedings Supplements*, 113:213–220, 2002.

A. Morselli, B. Canadas, and V. Vitale on behalf of the Fermi LAT Collaboration. The Indirect Search for Dark Matter from the centre of the Galaxy with the Fermi LAT. *ArXiv e-prints*, [arXiv: 1012.2292], 2010.

K. Nakamura et al. Review of particle physics. *J. Phys.*, G37:075021, 2010.

D. V. Nanopoulos, K. A. Olive, and M. Srednicki. After primordial inflation. *Phys. Lett. B*, 127:30–34, 1983.

A. Natarajan, J. C. Tan, and B. W. O’Shea. Dark Matter Annihilation and Primordial Star Formation. *ApJ*, 692:574–583, 2009.

P. Natarajan, D. Croton, and G. Bertone. Consequences of dark matter self-annihilation for galaxy formation. *MNRAS*, 388:1652–1666, 2008.

J. F. Navarro, V. R. Eke, and C. S. Frenk. The cores of dwarf galaxy haloes. *MNRAS*, 283:L72–L78, 1996a.

J. F. Navarro, C. S. Frenk, and S. D. M. White. The Structure of Cold Dark Matter Halos. *ApJ*, 462:563–+, 1996b.

J. F. Navarro, C. S. Frenk, and S. D. M. White. A Universal Density Profile from Hierarchical Clustering. *ApJ*, 490:493–+, 1997.

J. F. Navarro, E. Hayashi, C. Power, A. R. Jenkins, C. S. Frenk, S. D. M. White, V. Springel, J. Stadel, and T. R. Quinn. The inner structure of Λ CDM haloes - III. Universality and asymptotic slopes. *MNRAS*, 349:1039–1051, 2004.

J. F. Navarro, A. Ludlow, V. Springel, J. Wang, M. Vogelsberger, S. D. M. White, A. Jenkins, C. S. Frenk, and A. Helmi. The diversity and similarity of simulated cold dark matter haloes. *MNRAS*, 402:21–34, 2010.

A. B. Newman, T. Treu, R. S. Ellis, and D. J. Sand. The Dark Matter Distribution in A383: Evidence for a Shallow Density Cusp from Improved Lensing, Stellar Kinematic, and X-ray Data. *ApJ*, 728:L39, 2011.

T. Nihei, L. Roszkowski, and R. Ruiz de Austri. Towards an accurate calculation of the neutralino relic density. *JHEP*, 5:063, 2001.

T. Nihei, L. Roszkowski, and R. Ruiz de Austri. Exact cross sections for the neutralino WIMP pair-annihilation. *JHEP*, 3:031, 2002.

S.-H. Oh, C. Brook, F. Governato, E. Brinks, L. Mayer, W. J. G. de Blok, A. Brooks, and F. Walter. The Central Slope of Dark Matter Cores in Dwarf Galaxies: Simulations versus THINGS. *AJ*, 142:24, 2011a.

S.-H. Oh, W. J. G. de Blok, E. Brinks, F. Walter, and R. C. Kennicutt, Jr. Dark and Luminous Matter in THINGS Dwarf Galaxies. *AJ*, 141:193, 2011b.

J. H. Oort. The force exerted by the stellar system in the direction perpendicular to the galactic plane and some related problems. *Bull. Astron. Inst. Netherlands*, 6:249, 1932.

N. Padmanabhan and D. P. Finkbeiner. Detecting dark matter annihilation with CMB polarization: Signatures and experimental prospects. *Phys. Rev. D*, 72(2):023508–+, 2005.

A. D. Panov, V. I. Zatsepин, N. V. Sokolskaya, J. H. Adams, Jr., H. S. Ahn, G. L. Bashindzhagyan, J. Chang, M. Christl, T. G. Guzik, J. Isbert, K. C. Kim, E. N. Kouznetsov, M. I. Panasyuk, E. B. Postnikov, E. S. Seo, J. Watts, J. P. Wefel, and J. Wu. Possible structure in the cosmic ray electron spectrum measured by the ATIC-2 and ATIC-4 experiments. *Astrophysics and Space Sciences Transactions*, 7:119–124, 2011.

M. Papucci and A. Strumia. Robust implications on dark matter from the first FERMI sky γ map. *JCAP*, 3:014, 2010.

M. Pato, L. Pieri, and G. Bertone. Multimessenger constraints on the annihilating dark matter interpretation of the positron excess. *Phys. Rev. D*, 80(10):103510–+, 2009.

R. D. Peccei and H. R. Quinn. Constraints imposed by CP conservation in the presence of pseudoparticles. *Phys. Rev. D*, 16:1791–1797, 1977.

P. J. E. Peebles. Fluid Dark Matter. *ApJ*, 534:L127–L129, 2000.

S. Peirani, R. Mohayaee, and J. A. de Freitas Pacheco. Indirect search for dark matter: Prospects for GLAST. *Phys. Rev. D*, 70(4):043503, 2004.

S. Perlmutter, G. Aldering, G. Goldhaber, R. A. Knop, P. Nugent, P. G. Castro, S. Deustua, S. Fabbro, A. Goobar, D. E. Groom, I. M. Hook, A. G. Kim, M. Y. Kim, J. C. Lee, N. J. Nunes, R. Pain, C. R. Pennypacker, R. Quimby, C. Lidman, R. S. Ellis, M. Irwin, R. G. McMahon, P. Ruiz-Lapuente, N. Walton, B. Schaefer, B. J. Boyle, A. V. Filippenko, T. Matheson, A. S. Fruchter, N. Panagia, H. J. M. Newberg, W. J. Couch, and Supernova Cosmology Project. Measurements of Omega and Lambda from 42 High-Redshift Supernovae. *ApJ*, 517:565–586, 1999.

M. E. Peskin and D. V. Schroeder. *An Introduction to Quantum Field Theory*. Westview Press, 1995.

C. Picciotto and M. Pospelov. Unstable relics as a source of galactic positrons. *Phys. Lett. B*, 605:15–25, 2005.

A. Pinzke, C. Pfrommer, and L. Bergström. Prospects of detecting gamma-ray emission from galaxy clusters: Cosmic rays and dark matter annihilations. *Phys. Rev. D*, 84(12):123509, 2011.

T. Piran, N. J. Shaviv, and E. Nakar. Inhomogeneity in the Supernova Remnants as a Natural Explanation of the PAMELA/ATIC Observations. *ArXiv e-prints*, [arXiv: 0905.0904], 2009.

P. P. Ponente, Y. Ascasibar, and J. M. Diego. The contribution of star-forming galaxies to the cosmic radio background. *MNRAS*, 418:691–695, 2011.

T. A. Porter and A. W. Strong. A new estimate of the Galactic interstellar radiation field between 0.1um and 1000um. In *International Cosmic Ray Conference*, volume 4 of *International Cosmic Ray Conference*, page 77, 2005.

T. A. Porter, I. V. Moskalenko, A. W. Strong, E. Orlando, and L. Bouchet. Inverse Compton Origin of the Hard X-Ray and Soft Gamma-Ray Emission from the Galactic Ridge. *ApJ*, 682:400–407, 2008.

M. Pospelov and A. Ritz. The galactic 511 keV line from electroweak scale WIMPs. *Phys. Lett. B*, 651:208–215, 2007.

M. Pospelov, A. Ritz, and M. Voloshin. Secluded WIMP dark matter. *Phys. Lett. B*, 662:53–61, 2008.

C. Power, J. F. Navarro, A. Jenkins, C. S. Frenk, S. D. M. White, V. Springel, J. Stadel, and T. Quinn. The inner structure of Λ CDM haloes - I. A numerical convergence study. *MNRAS*, 338:14–34, 2003.

F. Prada, A. Klypin, J. Flix, M. Martínez, and E. Simonneau. Dark Matter Annihilation in the Milky Way Galaxy: Effects of Baryonic Compression. *Phys. Rev. Lett.*, 93(24):241301–+, 2004.

N. Prantzos, C. Boehm, A. M. Bykov, R. Diehl, K. Ferrière, N. Guessoum, P. Jean, J. Knoedlseder, A. Marcowith, I. V. Moskalenko, A. Strong, and G. Weidenspointner. The 511 keV emission from positron annihilation in the Galaxy. *Rev. Mod. Phys.*, 83:1001–1056, 2011.

J. Preskill, M. B. Wise, and F. Wilczek. Cosmology of the invisible axion. *Phys. Lett. B*, 120:127–132, 1983.

W. H. Press and P. Schechter. Formation of Galaxies and Clusters of Galaxies by Self-Similar Gravitational Condensation. *ApJ*, 187:425–438, 1974.

S. Profumo. TeV γ -rays and the largest masses and annihilation cross sections of neutralino dark matter. *Phys. Rev. D*, 72(10):103521, 2005.

S. Profumo. Dissecting cosmic-ray electron-positron data with Occam’s razor: the role of known pulsars. *Central European Journal of Physics*, 10:1–31, 2012.

S. Profumo and P. Ullio. Multi-wavelength Searches for Particle Dark Matter. *ArXiv e-prints*, [arXiv: 1001.4086], 2010.

A. R. Pullen, R.-R. Chary, and M. Kamionkowski. Search with EGRET for a gamma ray line from the Galactic center. *Phys. Rev. D*, 76(6):063006, 2007.

G. G. Raffelt. Astrophysical methods to constrain axions and other novel particle phenomena. *Phys. Rep.*, 198:1–113, 1990.

A. Rajaraman, W. Shepherd, T. M. P. Tait, and A. M. Wijangco. LHC bounds on interactions of dark matter. *Phys. Rev. D*, 84(9):095013, 2011.

D. Reed, F. Governato, L. Verde, J. Gardner, T. Quinn, J. Stadel, D. Merritt, and G. Lake. Evolution of the density profiles of dark matter haloes. *MNRAS*, 357:82–96, 2005.

M. Regis. Photons from dark matter in a (non-universal) extra dimension model. *Phys. Lett. B*, 663:250–254, 2008.

M. Regis and P. Ullio. Multiwavelength signals of dark matter annihilations at the Galactic center. *Phys. Rev. D*, 78(4):043505–+, 2008.

M. Regis and P. Ullio. Testing the dark matter interpretation of the PAMELA excess through measurements of the galactic diffuse emission. *Phys. Rev. D*, 80(4):043525, 2009.

Y. Rephaeli. Relativistic electrons in the intracluster space of clusters of galaxies - The hard X-ray spectra and heating of the gas. *ApJ*, 227:364–369, 1979.

A. G. Riess, A. V. Filippenko, P. Challis, A. Clocchiatti, A. Diercks, P. M. Garnavich, R. L. Gilliland, C. J. Hogan, S. Jha, R. P. Kirshner, B. Leibundgut, M. M. Phillips, D. Reiss, B. P. Schmidt, R. A. Schommer, R. C. Smith, J. Spyromilio, C. Stubbs, N. B. Suntzeff, and J. Tonry. Observational Evidence from Supernovae for an Accelerating Universe and a Cosmological Constant. *AJ*, 116:1009–1038, 1998.

E. Ripamonti, M. Mapelli, and A. Ferrara. The impact of dark matter decays and annihilations on the formation of the first structures. *MNRAS*, 375:1399–1408, 2007.

E. Ripamonti, F. Iocco, A. Ferrara, R. Schneider, A. Bressan, and P. Marigo. First star formation with dark matter annihilation. *MNRAS*, 406:2605–2615, 2010.

A. C. Robin, C. Reylé, S. Derrière, and S. Picaud. A synthetic view on structure and evolution of the Milky Way. *A&A*, 409:523–540, 2003.

L. J. Rosenberg and K. A. van Bibber. Searches for invisible axions. *Phys. Rep.*, 325:1–39, 2000.

L. Roszkowski, R. Ruiz de Austri, and K.-Y. Choi. Gravitino dark matter in the CMSSM and implications for leptogenesis and the LHC. *JHEP*, 8:080, 2005.

V. C. Rubin and W. K. Ford, Jr. Rotation of the Andromeda Nebula from a Spectroscopic Survey of Emission Regions. *ApJ*, 159:379–+, 1970.

V. C. Rubin, N. Thonnard, and W. K. Ford, Jr. Extended rotation curves of high-luminosity spiral galaxies. IV - Systematic dynamical properties, SA through SC. *ApJ*, 225:L107–L111, 1978.

V. C. Rubin, D. Burstein, W. K. Ford, Jr., and N. Thonnard. Rotation velocities of 16 SA galaxies and a comparison of Sa, Sb, and SC rotation properties. *ApJ*, 289:81–98, 1985.

T. Saab. An Introduction to Dark Matter Direct Detection Searches and Techniques. *ArXiv e-prints*, [arXiv: 1203.2566], 2012.

E. Salvador-Solé, J. Viñas, A. Manrique, and S. Serra. Theoretical dark matter halo density profile. *MNRAS*, 423:2190–2202, 2012.

D. Sautleben, S. Staggs, and B. Winstein. The Cosmic Microwave Background for Pedestrians: A Review for Particle and Nuclear Physicists. *Annual Review of Nuclear and Particle Science*, 57:245–283, 2007.

M. A. Sánchez-Conde, F. Prada, E. L. Lokas, M. E. Gómez, R. Wojtak, and M. Moles. Dark matter annihilation in Draco: New considerations of the expected gamma flux. *Phys. Rev. D*, 76(12):123509, 2007.

M. A. Sánchez-Conde, M. Cannoni, F. Zandanel, M. E. Gómez, and F. Prada. Dark matter searches with Cherenkov telescopes: nearby dwarf galaxies or local galaxy clusters? *JCAP*, 12:11, 2011.

R. H. Sanders and S. S. McGaugh. Modified Newtonian Dynamics as an Alternative to Dark Matter. *ARA&A*, 40:263–317, 2002a.

R. H. Sanders and S. S. McGaugh. Modified Newtonian Dynamics as an Alternative to Dark Matter. *ARA&A*, 40:263–317, 2002b.

C. L. Sarazin. The Energy Spectrum of Primary Cosmic-Ray Electrons in Clusters of Galaxies and Inverse Compton Emission. *ApJ*, 520:529–547, 1999.

D. J. Schlegel, D. P. Finkbeiner, and M. Davis. Maps of Dust Infrared Emission for Use in Estimation of Reddening and Cosmic Microwave Background Radiation Foregrounds. *ApJ*, 500:525, 1998.

M. Seiffert, D. J. Fixsen, A. Kogut, S. M. Levin, M. Limon, P. M. Lubin, P. Mirel, J. Singal, T. Villela, E. Wollack, and C. A. Wuensche. Interpretation of the Extragalactic Radio Background. *ArXiv e-prints*, [arXiv: 0901.0559], 2009.

P. D. Serpico. Astrophysical models for the origin of the positron “excess”. *Astropart. Phys.*, 39:2–11, 2012.

P. D. Serpico and G. Zaharijas. Optimal angular window for observing dark matter annihilation from the Galactic Center region: The case of gamma-ray lines. *Astropart. Phys.*, 29:380–385, 2008.

G. Servant and T. M. P. Tait. Is the lightest Kaluza-Klein particle a viable dark matter candidate? *Nucl. Phys. B*, 650:391–419, 2003.

J. Singal, L. Stawarz, A. Lawrence, and V. Petrosian. Sources of the radio background considered. *MNRAS*, 409:1172–1182, 2010.

P. Sizun, M. Cassé, and S. Schanne. Continuum γ -ray emission from light dark matter positrons and electrons. *Phys. Rev. D*, 74(6):063514, 2006.

T. R. Slatyer, N. Padmanabhan, and D. P. Finkbeiner. CMB constraints on WIMP annihilation: Energy absorption during the recombination epoch. *Phys. Rev. D*, 80(4):043526, 2009.

M. C. Smith, G. R. Ruchti, A. Helmi, R. F. G. Wyse, J. P. Fulbright, K. C. Freeman, J. F. Navarro, G. M. Seabroke, M. Steinmetz, M. Williams, O. Bienaymé, J. Binney, J. Bland-Hawthorn, W. Dehnen, B. K. Gibson, G. Gilmore, E. K. Grebel, U. Munari, Q. A. Parker, R.-D. Scholz, A. Siebert, F. G. Watson, and T. Zwitter. The RAVE survey: constraining the local Galactic escape speed. *MNRAS*, 379:755–772, 2007.

S. Smith. The Mass of the Virgo Cluster. *ApJ*, 83:23, 1936.

Y. Sofue and V. Rubin. Rotation Curves of Spiral Galaxies. *ARA&A*, 39:137–174, 2001.

J. Sommer-Larsen and A. Dolgov. Formation of Disk Galaxies: Warm Dark Matter and the Angular Momentum Problem. *ApJ*, 551:608–623, 2001.

A. Sommerfeld. Über die Beugung und Bremsung der Elektronen. *Ann. Phys. (Berlin)*, 403:257–330, 1931.

M. Spano, M. Marcelin, P. Amram, C. Carignan, B. Epinat, and O. Hernandez. GHASP: an $H\alpha$ kinematic survey of spiral and irregular galaxies - V. Dark matter distribution in 36 nearby spiral galaxies. *MNRAS*, 383:297–316, 2008.

D. N. Spergel and P. J. Steinhardt. Observational Evidence for Self-Interacting Cold Dark Matter. *Phys. Rev. Lett.*, 84:3760–3763, 2000.

D. Spolyar, K. Freese, and P. Gondolo. Dark Matter and the First Stars: A New Phase of Stellar Evolution. *Phys. Rev. Lett.*, 100(5):051101–+, 2008.

V. Springel, S. D. M. White, A. Jenkins, C. S. Frenk, N. Yoshida, L. Gao, J. Navarro, R. Thacker, D. Croton, J. Helly, J. A. Peacock, S. Cole, P. Thomas, H. Couchman, A. Evrard, J. Colberg, and F. Pearce. Simulations of the formation, evolution and clustering of galaxies and quasars. *Nature*, 435:629–636, 2005.

V. Springel, C. S. Frenk, and S. D. M. White. The large-scale structure of the Universe. *Nature*, 440:1137–1144, 2006.

V. Springel, S. D. M. White, C. S. Frenk, J. F. Navarro, A. Jenkins, M. Vogelsberger, J. Wang, A. Ludlow, and A. Helmi. Prospects for detecting supersymmetric dark matter in the Galactic halo. *Nature*, 456:73–76, 2008.

A. A. Starobinsky. Dynamics of phase transition in the new inflationary universe scenario and generation of perturbations. *Phys. Lett. B*, 117:175–178, 1982.

G. Steigman. Cosmology confronts particle physics. *Annual Review of Nuclear and Particle Science*, 29:313–338, 1979.

G. Steigman. Primordial Nucleosynthesis in the Precision Cosmology Era. *Annual Review of Nuclear and Particle Science*, 57:463–491, 2007.

F. Stoehr, S. D. M. White, V. Springel, G. Tormen, and N. Yoshida. Dark matter annihilation in the halo of the Milky Way. *MNRAS*, 345:1313–1322, 2003.

L. E. Strigari, S. M. Koushiappas, J. S. Bullock, and M. Kaplinghat. Precise constraints on the dark matter content of MilkyWay dwarf galaxies for gamma-ray experiments. *Phys. Rev. D*, 75(8):083526, 2007.

L. E. Strigari, S. M. Koushiappas, J. S. Bullock, M. Kaplinghat, J. D. Simon, M. Geha, and B. Willman. The Most Dark-Matter-dominated Galaxies: Predicted Gamma-Ray Signals from the Faintest Milky Way Dwarfs. *ApJ*, 678:614–620, 2008.

M. Su and D. P. Finkbeiner. Strong Evidence for Gamma-ray Line Emission from the Inner Galaxy. *ArXiv e-prints*, [arXiv: 1206.1616], 2012.

D. Syer and S. D. M. White. Dark halo mergers and the formation of a universal profile. *MNRAS*, 293:337, 1998.

M. Tegmark, M. R. Blanton, M. A. Strauss, and et al. [SDSS collaboration]. The Three-Dimensional Power Spectrum of Galaxies from the Sloan Digital Sky Survey. *ApJ*, 606: 702–740, 2004.

The ATLAS Collaboration. Search for dark matter candidates and large extra dimensions in events with a jet and missing transverse momentum with the ATLAS detector. *ArXiv e-prints*, [arXiv: 1210.4491], 2012.

S. Torii, T. Yamagami, T. Tamura, and et al. [PPB-BETS Collaboration]. High-energy electron observations by PPB-BETS flight in Antarctica. *ArXiv e-prints*, [arXiv: 0809.0760], 2008.

R. Trotta, F. Feroz, M. Hobson, L. Roszkowski, and R. Ruiz de Austri. The impact of priors and observables on parameter inferences in the constrained MSSM. *JHEP*, 12: 024, 2008.

M. S. Turner and F. Wilczek. Positron line radiation as a signature of particle dark matter in the halo. *Phys. Rev. D*, 42:1001–1007, 1990.

C. Tyler. Particle dark matter constraints from the Draco dwarf galaxy. *Phys. Rev. D*, 66(2):023509, 2002.

A. J. Tylka. Cosmic-ray positrons from annihilation of weakly interacting massive particles in the Galaxy. *Phys. Rev. Lett.*, 63:840–843, 1989.

J. A. Tyson, R. A. Wenk, and F. Valdes. Detection of systematic gravitational lens galaxy image alignments - Mapping dark matter in galaxy clusters. *ApJ*, 349:L1–L4, 1990.

P. Ullio and L. Bergström. Neutralino annihilation into a photon and a Z boson. *Phys. Rev. D*, 57:1962–1971, 1998.

P. Ullio, L. Bergström, J. Edsjö, and C. Lacey. Cosmological dark matter annihilations into γ rays: A closer look. *Phys. Rev. D*, 66(12):123502–+, 2002.

M. Valdés, A. Ferrara, M. Mapelli, and E. Ripamonti. Constraining dark matter through 21-cm observations. *MNRAS*, 377:245–252, 2007.

T. Vernstrom, D. Scott, and J. V. Wall. Contribution to the diffuse radio background from extragalactic radio sources. *MNRAS*, 415:3641–3648, 2011.

M. Viel, J. Lesgourges, M. G. Haehnelt, S. Matarrese, and A. Riotto. Can Sterile Neutrinos Be Ruled Out as Warm Dark Matter Candidates? *Phys. Rev. Lett.*, 97(7):071301, 2006.

A. C. Vincent, P. Martin, and J. M. Cline. Interacting dark matter contribution to the galactic 511 keV gamma ray emission: constraining the morphology with INTEGRAL/SPI observations. *JCAP*, 4:022, 2012.

M. I. Vysotskii, A. D. Dolgov, and I. B. Zeldovich. Cosmological limits on the masses of neutral leptons. *ZhETF Pis ma Redaktsiiu*, 26:200–202, 1977.

F. Wang and J. M. Yang. SuperWIMP dark matter scenario in light of WMAP. *EPJ C*, 38:129–133, 2004.

J. Wang and S. D. M. White. Are mergers responsible for universal halo properties? *MNRAS*, 396:709–717, 2009.

M. Wechakama and Y. Ascasibar. Pressure from dark matter annihilation and the rotation curve of spiral galaxies. *MNRAS*, 413:1991–2003, 2011.

M. Wechakama and Y. Ascasibar. Multi-messenger constraints on dark matter annihilation into electron-positron pairs. *ArXiv e-prints*, [arXiv: 1212.2583], 2012.

G. Weidenspointner, G. Skinner, P. Jean, J. Knödlseder, P. von Ballmoos, G. Bignami, R. Diehl, A. W. Strong, B. Cordier, S. Schanne, and C. Winkler. An asymmetric distribution of positrons in the Galactic disk revealed by γ -rays. *Nature*, 451:159–162, 2008.

S. Weinberg. A new light boson? *Phys. Rev. Lett.*, 40:223–226, 1978.

C. Weniger. A tentative gamma-ray line from Dark Matter annihilation at the Fermi Large Area Telescope. *JCAP*, 8:007, 2012.

M. J. White. SUSY and Dark Matter Constraints from the Lhc. *International Journal of Modern Physics A*, 22:5771–5784, 2007.

S. D. M. White, C. S. Frenk, and M. Davis. Clustering in a neutrino-dominated universe. *ApJ*, 274:L1–L5, 1983.

S. D. M. White, M. Davis, G. Efstathiou, and C. S. Frenk. Galaxy distribution in a cold dark matter universe. *Nature*, 330:451–453, 1987a.

S. D. M. White, C. S. Frenk, M. Davis, and G. Efstathiou. Clusters, filaments, and voids in a universe dominated by cold dark matter. *ApJ*, 313:505–516, 1987b.

F. Wilczek. Problem of strong P and T invariance in the presence of instantons. *Phys. Rev. Lett.*, 40:279–282, 1978.

M. Wood, G. Blaylock, S. M. Bradbury, and et al. A Search for Dark Matter Annihilation with the Whipple 10 m Telescope. *ApJ*, 678:594–605, 2008.

X. X. Xue, H. W. Rix, G. Zhao, P. Re Fiorentin, T. Naab, M. Steinmetz, F. C. van den Bosch, T. C. Beers, Y. S. Lee, E. F. Bell, C. Rockosi, B. Yanny, H. Newberg, R. Wilhelm, X. Kang, M. C. Smith, and D. P. Schneider. The Milky Way’s Circular Velocity Curve to 60 kpc and an Estimate of the Dark Matter Halo Mass from the Kinematics of \sim 2400 SDSS Blue Horizontal-Branch Stars. *ApJ*, 684:1143–1158, 2008.

P.-F. Yin, Q. Yuan, J. Liu, J. Zhang, X.-J. Bi, S.-H. Zhu, and X. Zhang. PAMELA data and leptonically decaying dark matter. *Phys. Rev. D*, 79(2):023512, 2009.

N. Yoshida, V. Springel, S. D. M. White, and G. Tormen. Weakly Self-interacting Dark Matter and the Structure of Dark Halos. *ApJ*, 544:L87–L90, 2000.

H. Yüksel, S. Horiuchi, J. F. Beacom, and S. Ando. Neutrino constraints on the dark matter total annihilation cross section. *Phys. Rev. D*, 76(12):123506, 2007.

G. Zaharijas and D. Hooper. Challenges in detecting gamma-rays from dark matter annihilations in the galactic center. *Phys. Rev. D*, 73(10):103501, 2006.

J. Zavala, M. Vogelsberger, T. R. Slatyer, A. Loeb, and V. Springel. Cosmic X-ray and gamma-ray background from dark matter annihilation. *Phys. Rev. D*, 83(12):123513, 2011.

Ya. B. Zeldovich. *Adv. Astron. Astrophys.*, (3):241, 1965.

L. Zhang, X. Chen, Y.-A. Lei, and Z.-G. Si. Impacts of dark matter particle annihilation on recombination and the anisotropies of the cosmic microwave background. *Phys. Rev. D*, 74(10):103519–+, 2006.

L. Zhang, X. Chen, M. Kamionkowski, Z.-G. Si, and Z. Zheng. Constraints on radiative dark-matter decay from the cosmic microwave background. *Phys. Rev. D*, 76(6):061301–+, 2007.

F. Zwicky. Die Rotverschiebung von extragalaktischen Nebeln. *Helvetica Physica Acta*, 6:110–127, 1933.

F. Zwicky. On the Masses of Nebulae and of Clusters of Nebulae. *ApJ*, 86:217, 1937.

ACKNOWLEDGMENTS

First of all I would like to thank my supervisors:

Dr. Yago Ascáibar from Departamento de Física Teórica, Universidad Autónoma de Madrid, for giving me the opportunity to work with him on dark matter during my PhD. I am deeply grateful for his guidance, patience and inspiring ideas. Although he worked in Madrid, I have never lacked of his advise and support. I am very glad I had such a committed, diligent, and encouraging supervisor and want to express my deepest gratitude to him.

PD. Dr. Volker Müller and Prof. Matthias Steinmetz from the Leibniz-Institut für Astrophysik Potsdam for their interest in my work and their valuable financial and scientific support with which this project and thesis could be realized. I am very thankful for the opportunity I owe to them and the excellent research environment and scientific exchange they provided me with during my time as a PhD student at their institute. Especially, PD. Dr. Volker Müller has granted me the freedom I wanted and given me the guidance I needed, providing the completion of this thesis.

Second I would like to thank my former astrophysics teachers in Thailand who provided the early foundations for this work by open my eyes for the universe. Especial I want to name Dr. Michael A. Allen and Prof. David Ruffolo, who both taught me a lot about astrophysics. I would also like to thanks Dr. Piyabut Burikham who always pushed and supported me to study abroad.

Next I would like to thank my current and former colleagues at the AIP for their support during the recent years, for the nice working environment to which they contributed and for the good times we had during lunch, German classes, at “Gleis 6” and at many other occasions. In particular I want to name my office mates Adrian Partl, Isabel Suarez Velasquez, Kristin Riebe, Timur Doumler and Simona Bekeraite; moreover from the cosmology group J.-C. Muñoz-Cuartas, Jochen Klar, Anne Hutter, Steffen Knollmann, Claudio Llinares, Christian Wagner, Jaime Forero-Romero, Heike Modest, Fran Martínez, Metin Ata, Maria del Pilar Bonilla Tobar, Tae-Sun Kim, Alexander Knebe, Noam Libeskind, Pratika Dayal, Sebastian Nuza, Cecilia Scannapieco, Steffen Heß, Arman Khalatyan, and Francisco Shu Kitaura Joyanes ; the seniors scientists Stefan Gottlöber, Jan Mückel, Axel Schwope, and Lutz Wisotzki; and friends from other groups; Sebastian Kamann, Andreas Schulze, Dasha Dubinovska, Christian Herenz, Pierre-Antoine Poulhazan, Iliya Nickelt, Daniel Kupko, Claudia Conrad, Todor Kondic, Christian Vock, Hakan Önel, Omar Choudhury, Ugur Ural, Peter Creasey and Yazmin Padilla Michel.

In addition I would like to thank Noam Libeskind, Peter Creasey, Simona Bekeraite and Frank Breitling for helping with proofreading; Karl-Heinz Böning from the computer division for his kind support in all hardware issues; Oliver Gressel for his thesis template; and Frank Breitling for his advice in many aspects of my work such as programming, presenting and publishing. His loving support has been invaluable to me.

Finally I want to thank my family, my parents, my sisters, relatives and friends for their continuous support beyond science, including Frank’s family, Ingrid and Peter, Tante Kätkchen and Onkel Heinz, and my Thai friends in Germany, e.g. Athassawat Kam-

manee and Decha Dechtrirat who took care of me so well after I arrived in Potsdam, and also Rakporn Dokchan, Saifon Krueger, Jarungjit Parnjai, Thada Keawprasert, Patcharee Larpsuriyakul, Nutsawadee Apichatwatana, Dara Phusanga, Korakot Wichitsa-nguan and Wannarut Rungrottheera for a great time we spent together in Germany.

I was supported by the DFG Research Grant AS 312/1-1 (Germany) and by the Brückenstipendium of the Universität Potsdam.

